EBM Experimental Biology and Medicine

Volume 251 | Issue 3

Experimental Biology and Medicine

Editor-in-Chief

Nicola Conran
University of Campinas, Brazil

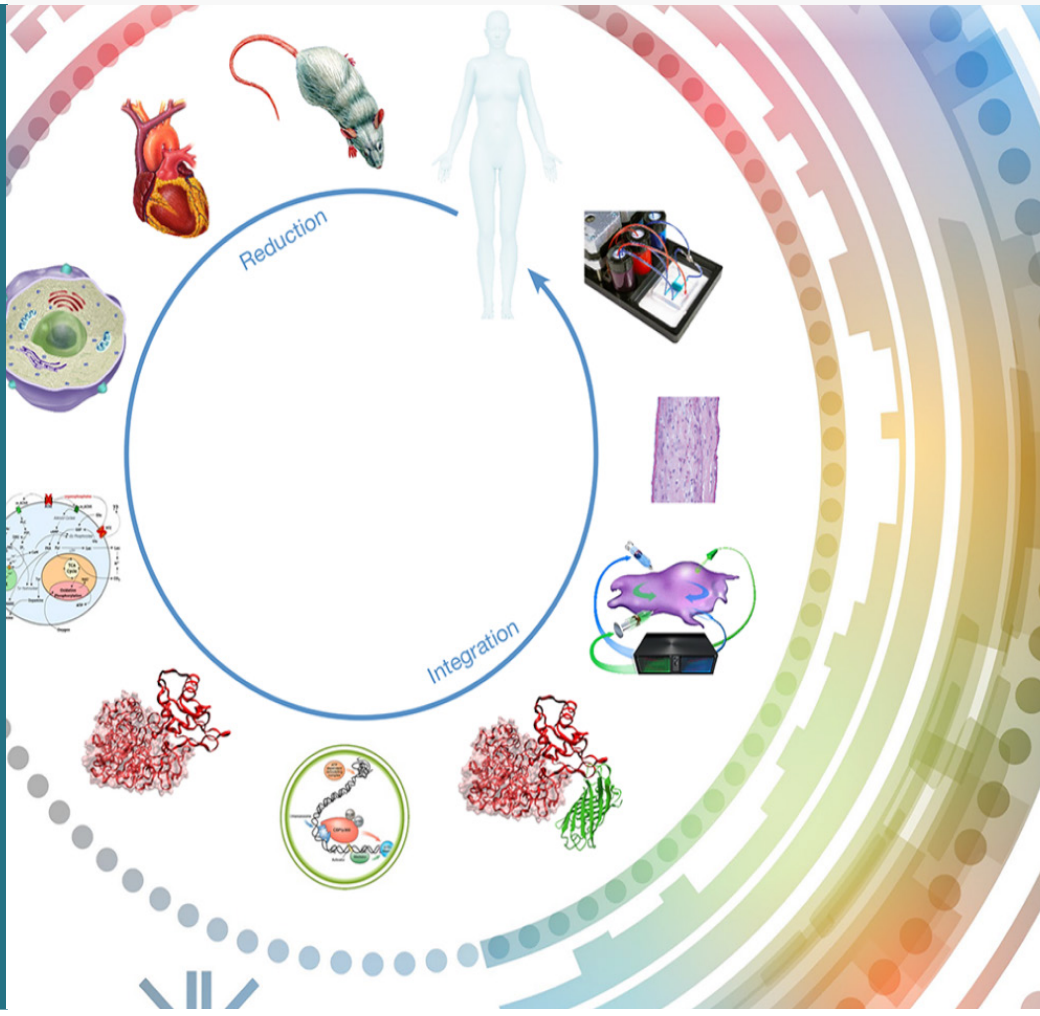

ISBN 978-2-8325-7770-7
DOI 10.3389/978-2-8325-7770-7

frontiers | Publishing Partnerships

Society for Experimental Biology and Medicine
3220 N Street NW, #179
Washington DC 20007, USA
Executive Director – ed@sebm.org

www.sebm.org

EBM Experimental Biology and Medicine

Editorial Board

ISSN 1535-3699
ISBN 978-2-8325-7770-7
DOI 10.3389/978-2-8325-7770-7

Generative AI statement
Any alternative text (Alt text) provided alongside figures in the articles in this ebook has been generated by Frontiers with the support of artificial intelligence and reasonable efforts have been made to ensure accuracy, including review by the authors wherever possible. If you identify any issues, please contact us.

EBM Experimental Biology and Medicine

2026 | Volume 251 | Issue 3 | ISSN 1535-3699

Table of contents

EBM Experimental Biology and Medicine

TYPE Original Research
PUBLISHED 02 March 2026
DOI 10.3389/ebm.2026.10709

OPEN ACCESS

*CORRESPONDENCE
Chrismis Novalinda Ginting,
chrismis@unprimdn.ac.id

RECEIVED 13 June 2025
REVISED 12 January 2026
ACCEPTED 20 February 2026
PUBLISHED 02 March 2026

CITATION
Wang X, Ginting CN and Leslie W (2026) Identification of potential hub genes related to ferroptosis and hypoxia in dilated cardiomyopathy: a bioinformatic analysis with preliminary experimental validation.
Exp. Biol. Med. 251:10709.
doi: 10.3389/ebm.2026.10709

Identification of potential hub genes related to ferroptosis and hypoxia in dilated cardiomyopathy: a bioinformatic analysis with preliminary experimental validation

Xiqin Wang, Chrismis Novalinda Ginting* and William Leslie

Medicine, Dentistry, and Health Science, Universitas Prima Indonesia, Medan, Indonesia

Abstract

The study aims to explore the potential role of ferroptosis and hypoxia in dilated cardiomyopathy (DCM). GSE120895, GSE17800, GSE112556, ferroptosis-related genes (FRGs), and hypoxia-related genes (HRGs) were downloaded from the public dataset. Ferroptosis- and hypoxia-related differentially expressed genes (DEGs) and DCM-related genes were obtained. Subsequentially, hub genes were identified, and their diagnostic values were assessed. Next, immune cell infiltration analysis, drug prediction and molecular docking were carried out based on the hub genes. Finally, the hub gene TGM2 was preliminarily verified *in vitro*. A total of 18 ferroptosis- and hypoxia-related DEGs and 315 DCM-related genes were acquired. Subsequently, 6 hub genes (PPP1R15A, TGM2, MAP3K5, USP7, SESN2, and ADAM23) were obtained and have potential diagnostic value. Immune infiltration analysis showed that CD56dim natural killer (NK) cells, macrophages, monocytes, NK cells, and NK T cells were significantly infiltrated in DCM patients. Furthermore, the lncRNA-miRNA-mRNA network was constructed. Moreover, 16 drugs were predicted, and the binding energy between atorvastatin and TGM2 was −2.79 kcal/mol. *In vitro* verification showed that TGM2, PPP1R15A and SESN2 were up-regulated in DOX-induced AC16 cardiomyocyte injury. After knocking down TGM2, the expressions of α-actinin and cTnT were increased, and the expression level of HIF-1α was inhibited. Dual luciferase assay showed that hsa-miR-291-5p exerted its regulatory effect by directly binding to TGM2. Flow cytometry results showed that TGM2 had no significant effect on the apoptosis of AC16 cells. Our findings may provide new ideas for the diagnosis and treatment of DCM.

KEYWORDS

dilated cardiomyopathy, ferroptosis, hypoxia, immune infiltration, lncRNA-miRNA-mRNA network

Impact statement

DCM is a disease that primarily affects the myocardium, causing the heart to become dilated and reducing its ability to pump blood. As the condition progresses, heart function further deteriorates, potentially leading to heart failure, arrhythmias, or other complications. Recent evidence suggests that ferroptosis and hypoxia play important roles in cardiomyopathies. Our study employs bioinformatics methods to identify the hub genes related to ferroptosis and hypoxia in dilated cardiomyopathy. Through bioinformatical analysis, 6 hub genes were identified, and these genes exhibited better performance in distinguishing DCM from healthy controls. After knockdown TGM2, the expressions of α-actinin and cTnT were increased. Flow cytometry results showed that TGM2 had no significant effect on the apoptosis of AC16 cells. Our findings may provide new insights into understanding the role of ferroptosis and hypoxia in the development of DCM and may offer new treatment targets.

Introduction

Dilated cardiomyopathy (DCM), a heart muscle disease, is defined as the dilation of the left ventricular (LV) or biventricular and impaired contractility [1]. DCM is a primary risk factor for developing heart failure (HF) and severe arrhythmia [2]. In clinical practice, echocardiography is employed to evaluate ventricular dilatation, cardiac magnetic resonance imaging is used to assess fibrosis and oedema, and myocardial biopsy is performed to examine inflammation. The pathophysiology of DCM is various, including genetic mutations, inflammation, autoimmunity, infections, and chemical and toxin exposure. However, the etiology and pathogenesis of DCM remain unclear and require further investigation.

Recent evidence suggests that ferroptosis plays an important role in cardiomyopathies [3, 4]. Ferroptosis, an iron-dependent form of non-apoptotic cell death, is caused by lipid peroxidation and reactive oxygen species (ROS) accumulation [5]. Fang et al. demonstrated that mitochondrial oxidative damage is a key mechanism underlying ferroptosis-induced cardiac injury in cardiomyopathy [6]. Additionally, hypoxia usually causes an increase in ROS and oxidative stress, which is strongly associated with cardiomyopathy [7, 8]. Intermittent hypoxia causes high blood pressure, LV remodeling, and dysfunction in rodent models [8]. Chick embryos exposed to hypoxia exhibited LV dilatation, decreased LV ejection fractions, and diastolic dysfunction [9]. In ischemia/reperfusion (I/R) injury myocardium, liproxstatin-1, a ferroptosis inhibitor, could decrease myocardial infarct sizes and mitochondrial ROS production to protect the myocardium [10]. Another ferroptosis inhibitor, dexrazoxane, impedes myocardial cell death caused by ROS and iron [11]. The above results indicate that ferroptosis and hypoxia were involved in cardiomyopathy, yet the potential role of ferroptosis and hypoxia in DCM remains unclear.

In this study, based on ferroptosis- and hypoxia-related genes, the hub genes in DCM were identified using weighted gene co-expression network analysis (WGCNA) and the least absolute shrinkage and selection operator (LASSO) regression analysis. Our findings may provide new insights into understanding the role of ferroptosis and hypoxia in the development of DCM and may offer new treatment targets.

Materials and methods

Data collection and preprocessing

GSE120895 (platform: GPL570) and GSE17800 (platform: GPL570) datasets were collected from the Gene Expression Omnibus (GEO) database[1]. The GSE120895 dataset contained 8 control samples and 47 cases of endomyocardial biopsies (EMBs) from DCM patients, which is used as the training set to identify hub genes. The GSE17800 included 8 control samples and 40 cases of EMBs from DCM patients, which is used as the validation set to verify hub genes. The "affy" (version 1.68.0) package in R was used for data processing. Gene expression data were normalized by Robust Multi-array Average (RMA) algorithm, which included background correction, quantile normalization, probe summarization and log2 transformation. All subsequent statistical analyses were performed based on the expression values after log2 transformation.

A total of 564 ferroptosis-related genes (FRGs) were acquired from the Ferroptosis database V2 (FerrDb,[2]). A total of 200 hypoxia-related genes (HRGs) were collected from the Molecular Signatures Database (MSigDB,[3]). All data and statistical analyses were performed in R software (version 4.0.5).

Differential expression analysis and functional enrichment analysis

The DCM-related differential expressed genes (DEGs) with false discovery rate (FDR) <0.05 were identified in the GSE120895 dataset using the "limma" (version 3.46.0) package in R. Then, 564 FRGs, 200 HRGs, and DCM-related DEGs were intersected to obtain ferroptosis- and hypoxia-related DEGs. The volcano plot was used to visualize these results. Subsequently, Gene Ontology (GO) and Kyoto Encyclopedia of Genes and

1 https://www.ncbi.nlm.nih.gov/geo/
2 http://www.zhounan.org/ferrdb/current/
3 https://www.gsea-msigdb.org/gsea/msigdb/

Genome (KEGG) functional enrichment analysis of ferroptosis- and hypoxia-related DEGs were carried out through the DAVID database[4]. The screening criterion for terms was p-value <0.05.

WGCNA

The "WGCNA" package in R was utilized to perform WGCNA in the GSE120895. First, the "hclust" function was used to cluster all samples and detect the outliers. The high degree was set to 0.9, and the function "pickSoftThreshold" was utilized to calculate the soft threshold to construct a scale-free co-expression network. The weighted adjacency matrix was transferred into the topological overlap matrix (TOM) and 1-TOM. Genes with similar expression patterns were clustered, and modules were divided by default parameters according to the "cutreeDynamic" function. Since the modules identified by the dynamic tree cutting algorithm may be similar, these modules were merged at a height cutoff of 0.25. The "moduleEigengenes" function was used to calculate module eigengene (ME) and Pearson analysis was employed to identify DCM-related ME. Genes with |gene significance (GS)| >0.4 and |module membership (MM)| >0.4 in the hub module were selected as the DCM-related genes.

Identification of hub genes

DCM-related genes, ferroptosis-related DEGs, and hypoxia-related DEGs were intersected to acquire intersection genes. Then, LASSO regression analysis was utilized to select the hub genes through the "glmnet" (version 4.1–1) package. Additionally, receiver operating characteristic (ROC) analysis was performed to evaluate the diagnostic value of hub genes in distinguishing DCM from healthy controls using the "pROC" (version 1.17.0.1) package. Area under the curve (AUC) was used to evaluate the diagnostic accuracy of hub genes.

Immune cell infiltration analysis

The relative abundance of each immune cell was calculated using the single-sample GSEA (ssGSEA) algorithm. Signature gene sets marking various types of infiltrating immune cells were obtained from Charoentong's study [12, 13], which covers a range of human immune cell subtypes, including activated CD8 T cell, activated dendritic cell, macrophages, monocyte, natural killer cell, and regulatory T cells. The difference in immune cell infiltration between DCM patients and healthy controls was compared using the Wilcox test. Furthermore, the correlation between differentially infiltrating immune cells and hub genes was explored.

Construction of competing endogenous RNA (ceRNA) network

The miRNA-expressed dataset GSE112556 comprised 3 healthy controls and 3 heart tissue samples from DCM patients. The differentially expressed miRNAs (DEmiRNAs) with p-value <0.05 between DCM patients and controls were obtained. The Encyclopedia of RNA Interactomes (ENCORI,[5]) dataset was used to select hub gene-related miRNAs. Next, the predicted miRNAs were intersected with DEmiRNAs, and their intersection was taken to obtain miRNA-mRNA targeting pairs with negative regulatory relationships. Additionally, the miRNAs-related lncRNAs were attained through the ENCORI dataset. Next, the lncRNAs associated with the hub genes were defined as DCM-related lncRNAs by correlation analysis (p-value <0.05). Finally, the lncRNA-miRNA-mRNA network was constructed using the Cytoscape.

Drug prediction and molecular docking

The Drug Gene Interaction Database (DGIdb,[6]) was utilized to obtain hub genes-related drugs. Molecular docking technology is to place small molecules (ligands) in the binding region of macromolecular targets (receptors) by computer simulation, and predict the binding energy (binding affinity) and binding mode (conformation) of the two by calculating physical and chemical parameters, and then identifies the lowest-energy conformations of ligand-receptor binding. Low binding energy is the basis of stable binding between molecules. The 3D structures of target proteins (receptors) and drugs (ligands) were downloaded from the RCSB PDB[7] and the PubChem database[8], respectively. Subsequently, proteins and drug molecules were hydrogenated and other pretreated in AutoDockTools, followed by molecular docking. In the docking results, binding energy was used as a reference to screen the most active ligand molecules and target genes. Binding energy <0 means that the ligand and receptor can bind spontaneously. The smaller the binding energy, the more stable the binding between ligand and receptor. Binding energy less than −5.0 kJ/mol (Note: −5.0 kJ/mol = −1.19423 kcal/mol) is the basis for screening candidate targets of active ingredients/

4 https://david.ncifcrf.gov/

5 http://starbase.sysu.edu.cn/index.php

6 https://dgidb.org/

7 http://www.rcsb.org/pdb/home/home.do

8 https://pubchem.ncbi.nlm.nih.gov/

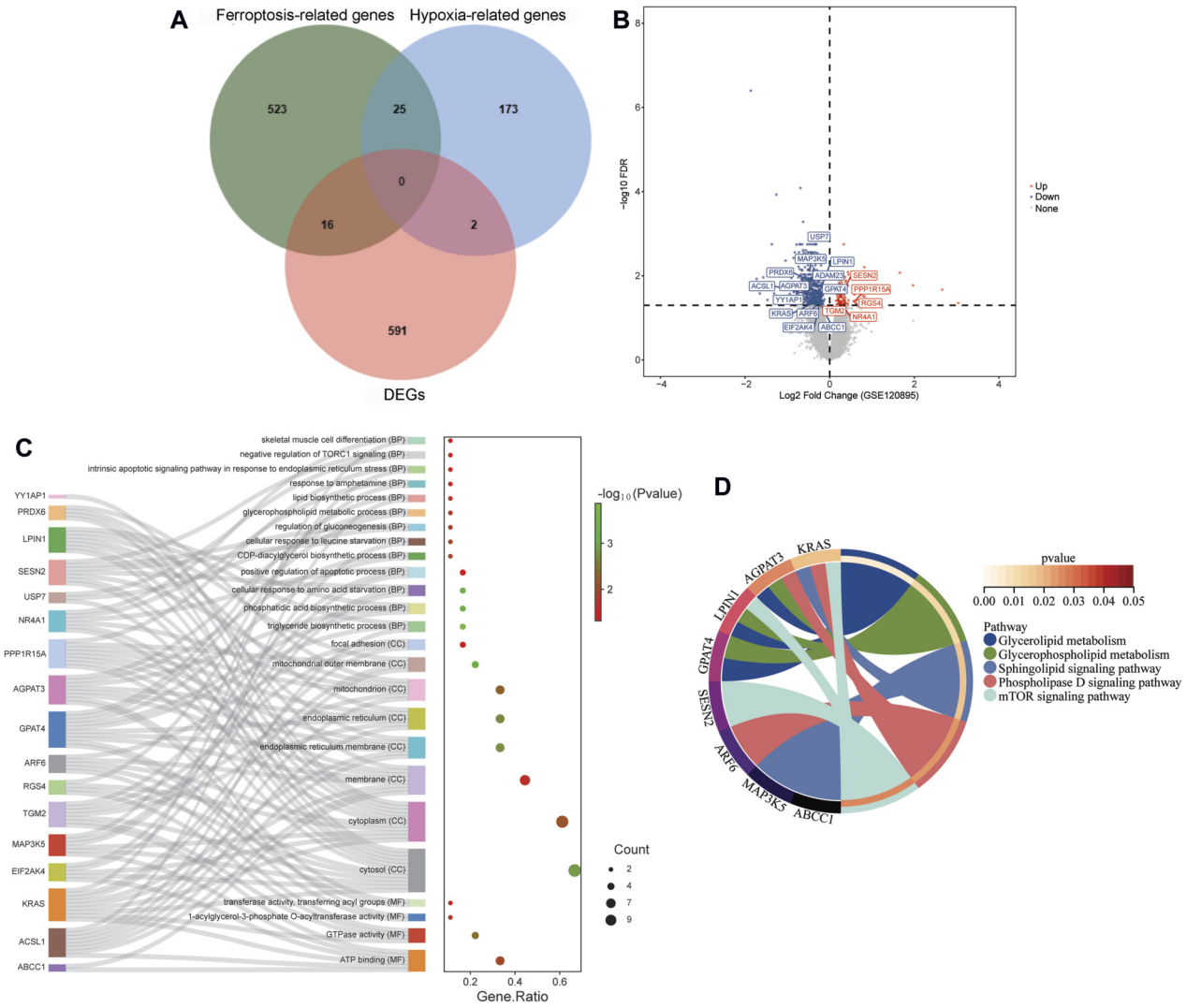

FIGURE 1
Identification of ferroptosis- and hypoxia-related DEGs. **(A)** Venn plot among ferroptosis-related genes, hypoxia-related genes, and DEGs in the GSE120895 dataset. **(B)** The volcano of ferroptosis- and hypoxia-related DEGs. **(C,D)** GO **(C)** and KEGG **(D)** analysis of ferroptosis- and hypoxia-related DEGs.

drugs. Finally, the molecular docking results were visualized by the PyMol software.

In vitro verification

The human cardiomyocyte AC16 was purchased from Wuhan Pricella Biotechnology Co., Ltd. Doxorubicin (DOX; 0.3 μM) was used to stimulate AC16 cells at 37 ˚C in a humidified atmosphere of 5% CO2 for 24 h to induce cardiomyocyte injury model. ATrizol (TIANGEN, DP424), FastQuant cDNA first strand synthesis (TIANGEN, KR106) and SuperReal PreMix Plus (SYBR Green) (TIANGEN, FP205) kits were used for RNA extraction, reverse transcription and RT-qPCR, respectively. The hub gene TGM2 was selected for knockdown experiments, and the expression of TGM2 was detected by RT-qPCR and western blotting. The sequence of siRNA is shown in Supplementary Table S1. According to the manufacturer's instructions, apoptotic cells were evaluated using the Annexin V-FITC/PI apoptosis detection kit (Solarbio, CA1020). In addition, immunofluorescence staining was performed on cardiomyocytes in each group. After fixing and permeabilizing cells, incubate them with mouse anti-α-actinin monoclonal antibody (Biodragon, BD-PM3612) and rabbit anti-troponin T-C polyclonal antibody (Biodragon, BD-PT5362), followed

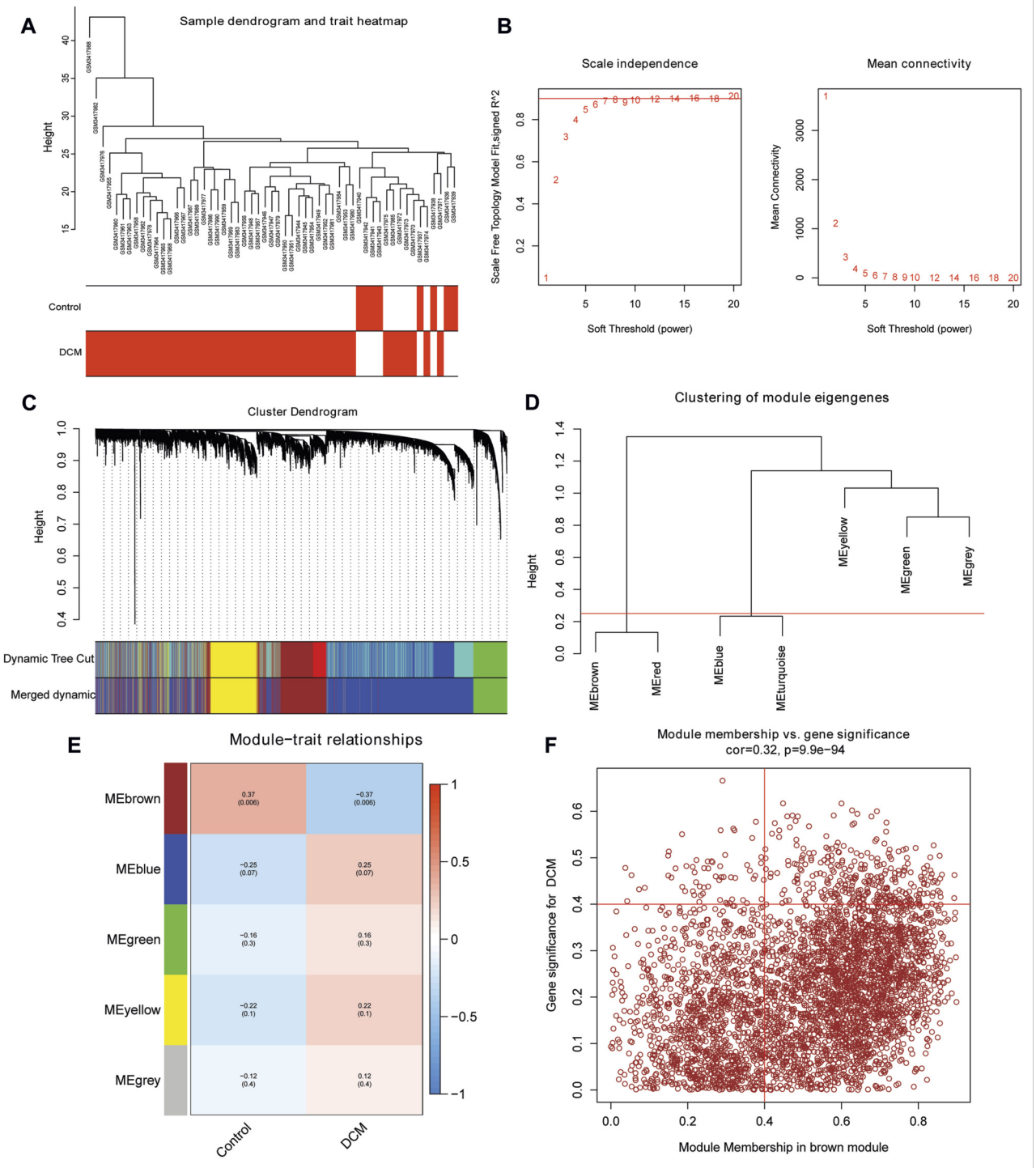

FIGURE 2
WGCNA. **(A)** Clustering dendrogram of all samples in the GSE120895 dataset. **(B)** Scale independence and mean connectivity analysis. **(C)** Clustering dendrogram of genes. **(D)** Clustering of module eigengenes. **(E)** The correlation between modules and groups. **(F)** The scatterplot of MM and GS in the brown module.

by fluorescently labeled goat anti-mouse IgG (red, Biodragon, BD9276) and goat anti-rabbit IgG (green, Bioss, bs-0295G-FITC). Finally, stain the nuclei with DAPI and observe under a fluorescence microscope. In addition, the dual-luciferase reporter assay was used to investigate the association between hsa-miR-296-5p and TGM2.

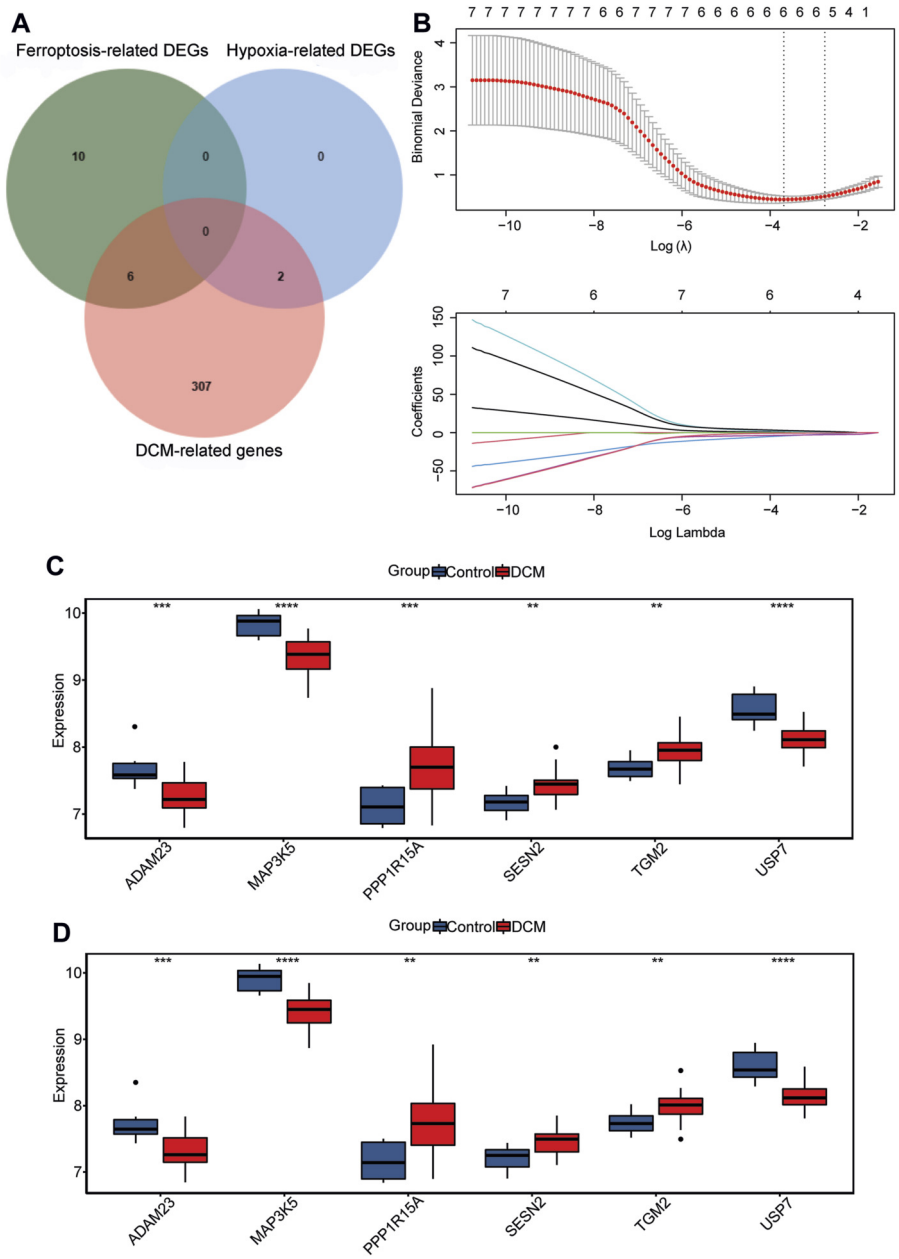

FIGURE 3
Identification of hub genes. **(A)** Venn plot among DCM-related genes, ferroptosis-related DEGs, and hypoxia-related DEGs. **(B)** LASSO regression analysis is used to identify hub genes. **(C,D)** The expression levels of hub genes between healthy controls and DCM patients in the GSE120895 **(C)** and GSE17800 datasets **(D)**.

Results

Identification of ferroptosis- and hypoxia-related DEGs and functional enrichment analysis

A total of 609 DEGs were identified in DCM patients compared to healthy controls in the GSE120895 dataset, including 102 up- and 507 down-regulated DEGs. Then, 564 ferroptosis-related genes, 200 hypoxia-related genes, and 609 DEGs were intersected (Figure 1A). Finally, 16 ferroptosis-related DEGs (SESN2, AGPAT3, MAP3K5, EIF2AK4, PRDX6, NR4A1, ARF6, KRAS, ABCC1, RGS4, LPIN1, YY1AP1, USP7, GPAT4, ACSL1, and ADAM23) and 2 hypoxia-related DEGs (PPP1R15A and TGM2) were acquired (Figure 1B).

In the GO:BP terms, these 18 genes were significantly enriched in triglyceride biosynthetic process, phosphatidic acid biosynthetic process and cellular response to amino acid starvation (Figure 1C). In the GO:CC terms, these 18 genes significantly enriched in cytosol, cytoplasm and membrane (Figure 1C). In the GO:MF terms, these 18 genes were significantly enriched in ATP binding, GTPase activity and 1-acylglycerol-3-phosphate O-acyltransferase activity (Figure 1C). The KEGG results showed that the DEGs were significantly enriched in mTOR signaling pathway, Glycerophospholipid metabolism and Glycerolipid metabolism (Figure 1D).

Identification of DCM-related genes

The GSE120895 dataset was used to carry out WGCNA. All samples were clustered, and the sample clustering tree is displayed in Figure 2A. Then, the soft threshold was set as 6 to construct the scale-free network (Figure 2B). The minimum number of genes in the module was set to 500, and 7 modules were attained (Figure 2C). Next, the brown and red modules were merged, as were the blue and turquoise modules (Figure 2D). Finally, 5 modules were identified. Subsequently, we found that the brown module was significantly correlated with DCM (Figure 2E). Then, a total of 315 DCM-related genes with |GS| >0.4 & |MM| >0.4 were acquired (Figure 2F).

Identification of hub genes

The 315 DCM-related genes, 16 ferroptosis-related DEGs, and 2 hypoxia-related DEGs were intersected, and 8 intersection genes were acquired (Figure 3A). Subsequently, 6 hub genes (PPP1R15A and TGM2 for hypoxia and MAP3K5, USP7, SESN2, and ADAM23 for ferroptosis) were identified using LASSO regression analysis (Figure 3B). The expression levels of ADAM23, MAP3K5, and USP7 were significantly decreased in DCM patients, while the expression levels of PPP1R15A, TGM2, and SESN2 were significantly increased in DCM patients in both GSE120895 and GSE17800 datasets (Figures 3C,D). Additionally, ROC analysis showed that the AUC values of 6 hub genes were all more than 0.8 in both the GSE120895 and GSE17800 datasets (Figure 4; Supplementary Figure S1). Furthermore, a diagnostic model for DCM was constructed via LASSO regression based on the 6 hub genes. Results showed that the AUC of the model exceeded 0.9 in both the GSE120895 (Supplementary Figure S1A) and GSE17800 (Supplementary Figure S1B) datasets.

Immune cell infiltration analysis

Immune cell infiltration analysis results showed that CD56dim natural killer (NK) cells, macrophages, monocytes, NK cells, and NK T cells were significantly highly infiltrated in DCM patients in the GSE120895 dataset (Figure 5A). Additionally, the correlation between differentially infiltrating immune cells and hub genes was explored. CD56dim NK cells were significantly correlated with 6 hub genes (Figure 5B). Macrophages were significantly associated with SESN2 and ADAM23 (Figure 5C). Monocytes showed significant correlations with PPP1R15A, TGM2, and SESN2 (Figure 5D). NK cells and NK T cells were significantly correlated with MAP3K5 and ADAM23 (Figures 5E,F). Additionally, NK cells exhibited a significant correlation with SESN2.

Construction of ceRNA network

A total of 21 DEmiRNAs were acquired in the GSE112556 dataset, including 7 up- and 14 down-regulated DEmiRNAs (Figure 6A). Then, 11 miRNA-mRNA negative regulatory relationship pairs were obtained, including 8 DEmiRNAs. Subsequently, 11 lncRNAs were identified that interacted with 7 DEmiRNAs (hsa-miR-770-5p, hsa-miR-16-5p, hsa-miR-139-5p, hsa-miR-296-5p, hsa-miR-338-3p, hsa-miR-148a-3p, and hsa-miR-363-3p) and 3 hub genes (ADAM23, SESN2, and TGM2). Finally, the ceRNA network, including 11 lncRNAs, 7 miRNAs, and 3 mRNAs, was constructed (Figure 6B).

Drug prediction and molecular docking

A total of 16 drugs were obtained (Figure 7A). Among these, 1 drug may target the MAP3K5 gene, 15 drugs may target the TGM2 gene, and the remaining genes were not matched to drugs. Literature retrieval revealed that atorvastatin, a drug associated with TGM2, has significant benefits in treating DCM, and low-dose use significantly reduces levels of inflammatory cytokines and uric acid, improves hemodynamic parameters, and increases the 5-year survival rate of DCM patients [14, 15]. Subsequently, molecular docking between atorvastatin and TGM2 was performed. Molecular docking between atorvastatin and TGM2 was performed. The binding energy was −2.79 kcal/mol by binding LYS-173 with 1 hydrogen bond (Figure 7B).

In vitro verification of the hub gene TGM2

The expression of the highly expressed hub genes (TGM2, PPP1R15A, and SESN2) in the DCM group was verified through RT-qPCR in AC16 cells treated with DOX. Compared with the control group, the expression levels of TGM2, PPP1R15A, and SESN2 in the DOX group were significantly increased (Figures 8A–C), which was

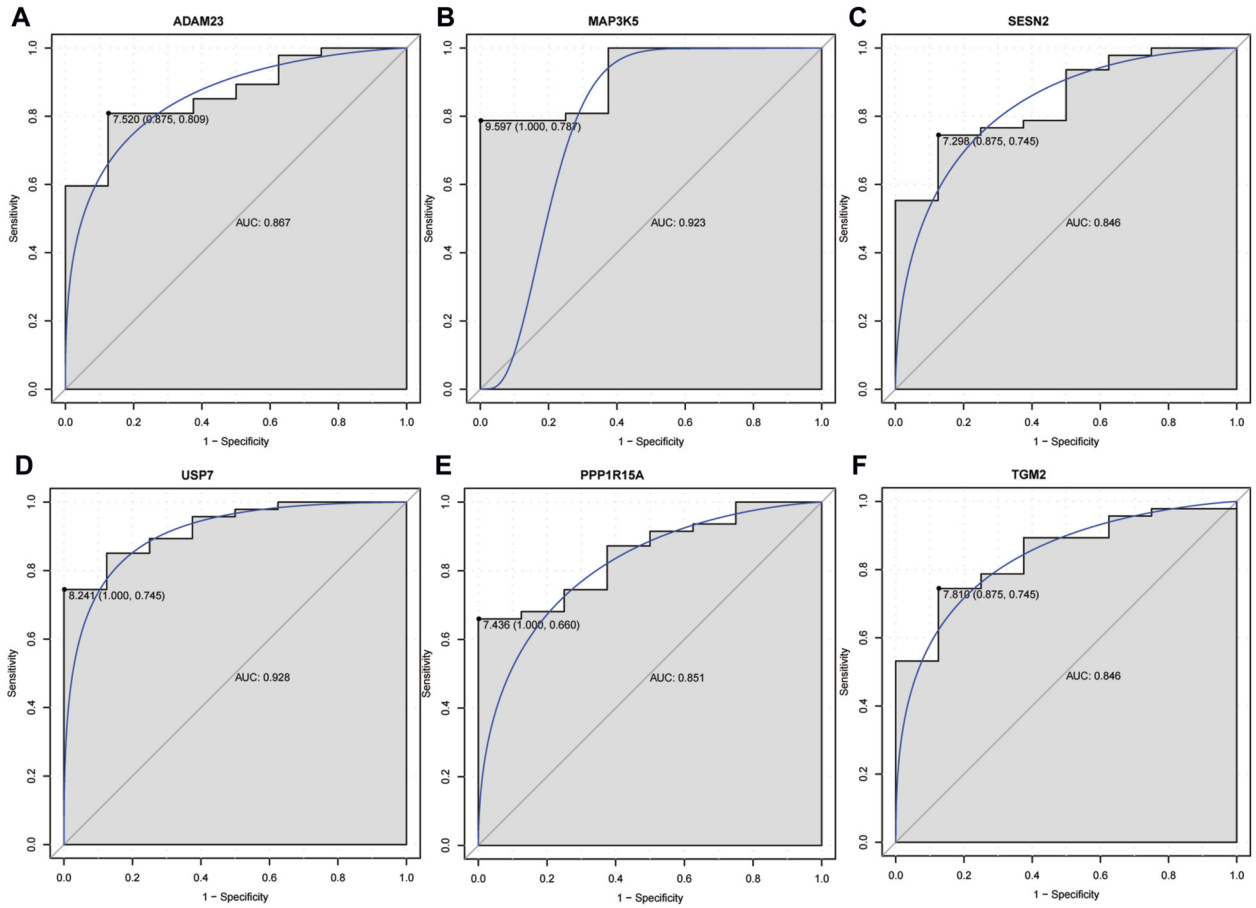

FIGURE 4
The ROC analysis of ADAM23 **(A)**, MAP3K5 **(B)**, SESN2 **(C)**, USP7 **(D)**, PPP1R15A **(E)**, and TGM2 **(F)** in the GSE120895 dataset. In ROC analysis, the greater the AUC, the higher the diagnostic accuracy. The AUC value of 0.8–0.9 indicated very good diagnostic accuracy, and 0.9–0.1 indicated excellent diagnostic accuracy.

consistent with the expression trend in the public database. Hub gene TGM2, a potential diagnostic biomarker, is not only associated with immune cell infiltration but also may play a crucial regulatory role in DCM via the lncRNA-miRNA-TGM2 axis. Moreover, drug prediction revealed that atorvastatin, a drug associated with TGM2, has significant benefits in treating DCM. Therefore, TGM2 was selected for subsequent experiments.

TGM2 was knockdown via siRNA transfection, and TGM2 expression was quantified by RT-qPCR to identify effective siRNA targets. The results showed that the knockdown effect of target 2 was the best (Figure 8D). Therefore, siRNA-2 was selected for subsequent knockdown experiments. Subsequently, the expression of TGM2 in each group was detected by RT-qPCR and western blotting. The results showed that the expression of TGM2 was significantly increased after DOX treatment, while the expression of TGM2 was significantly decreased in the knockdown group (Figures 8E–G). Subsequently, immunofluorescence staining was performed to investigate the effects of TGM2 on cTnT and α-actinin (Figure 9). Compared with the control group, the expressions of α-actinin and cTnT in the DOX group were decreased. After knocking down TGM2, the expressions of α-actinin and cTnT were increased. Furthermore, after knockdown of TGM2, the expression level of HIF-1α was inhibited (Figures 10A,B). The complementary binding sites between hsa-miR-296-5p and the 3′ UTR of TGM2 were predicted through the ENCORI database (Figure 10C). Based on the psiCHECK 2 vector, we constructed TGM2-WT (wild-type) and TGM2-Mut (mutant) dual-luciferase reporter plasmids. Dual luciferase assay showed that hsa-miR-291-5p exerted its regulatory effect by directly binding to TGM2 (Figure 10D). In addition, flow cytometry results showed that TGM2 had no significant effect on the apoptosis of AC16 cells (Figures 11A–E).

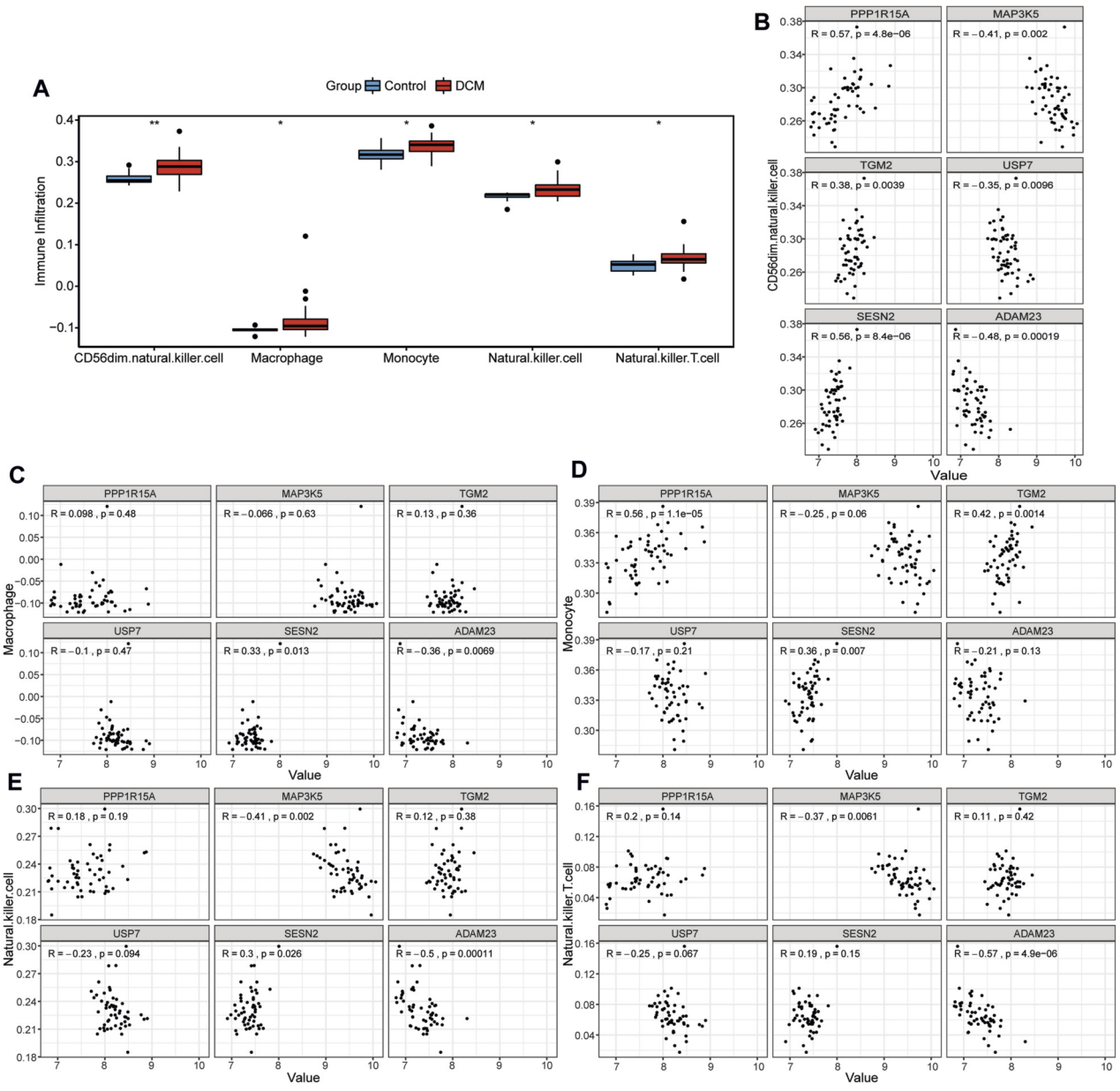

FIGURE 5
Immune cell infiltration analysis. **(A)** The box plot shows the difference in immune infiltration between DCM and healthy controls. **(B–F)** The correlation between hub genes and CD56dim NK cells **(B)**, macrophages **(C)**, monocytes **(D)**, NK cells **(E)**, and NK T cells **(F)** respectively.

Discussion

DCM is a cardiac disease that eventually leads to HF and sudden cardiac death [16]. Ferroptosis is regulated necrosis and plays a crucial role in cardiovascular disease. Cardiomyocyte ferroptosis is involved in the pathogenesis and progression of DCM, and inhibition of ferroptosis can improve DCM-related pathological phenotypes [17]. Interleukin 27 may exert a protective effect in DCM by inhibiting ferroptosis [18]. Furthermore, hypoxia is the major risk factor for cardiovascular diseases. Hypoxia is associated with DCM [9], and asprosin protects cardiomyocytes by enhancing cardiac mitochondrial function under hypoxia, reducing the risk of adverse cardiovascular events in DCM patients [19]. Hypoxia can also regulate ferroptosis under certain conditions [20]. This study screened and identified hypoxia- and ferroptosis-related hub genes via bioinformatics analysis, providing new insights for subsequent related research.

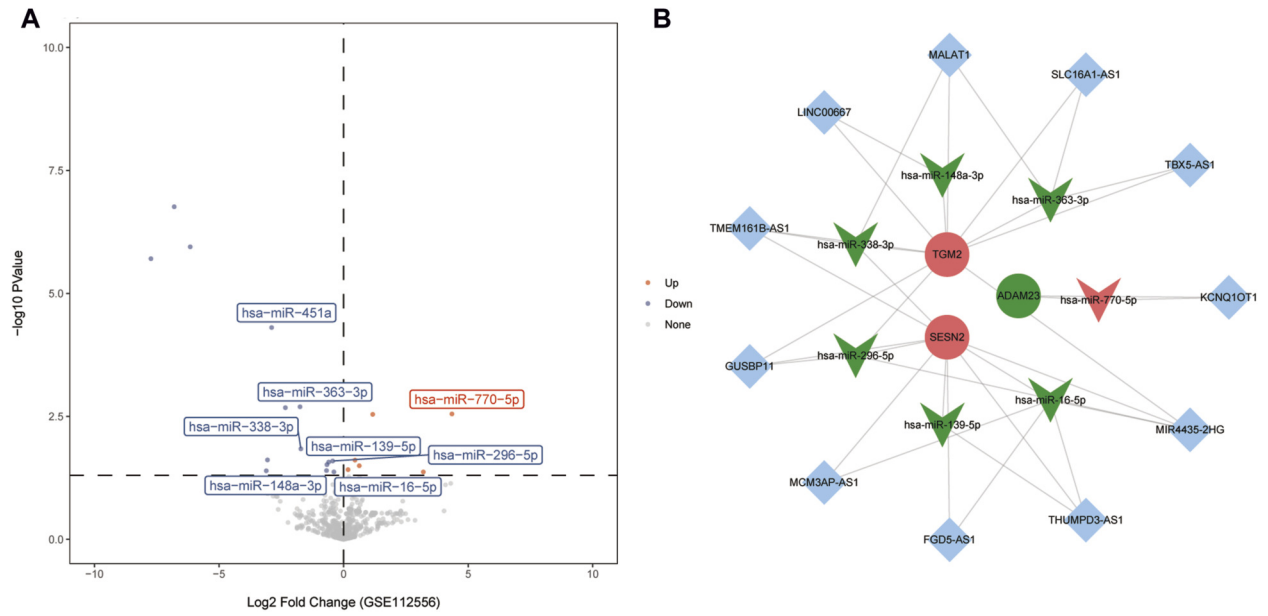

FIGURE 6
Construction of ceRNA network. **(A)** The volcano plot of DEmiRNAs in the GSE112556 dataset. **(B)** A ceRNA network in DCM. The rhombus represented lncRNA, the V type denoted miRNA, and the circle indicated mRNA. Red and green indicated upregulation and downregulation, respectively. The lines between nodes indicate predicted targeted regulatory relationships.

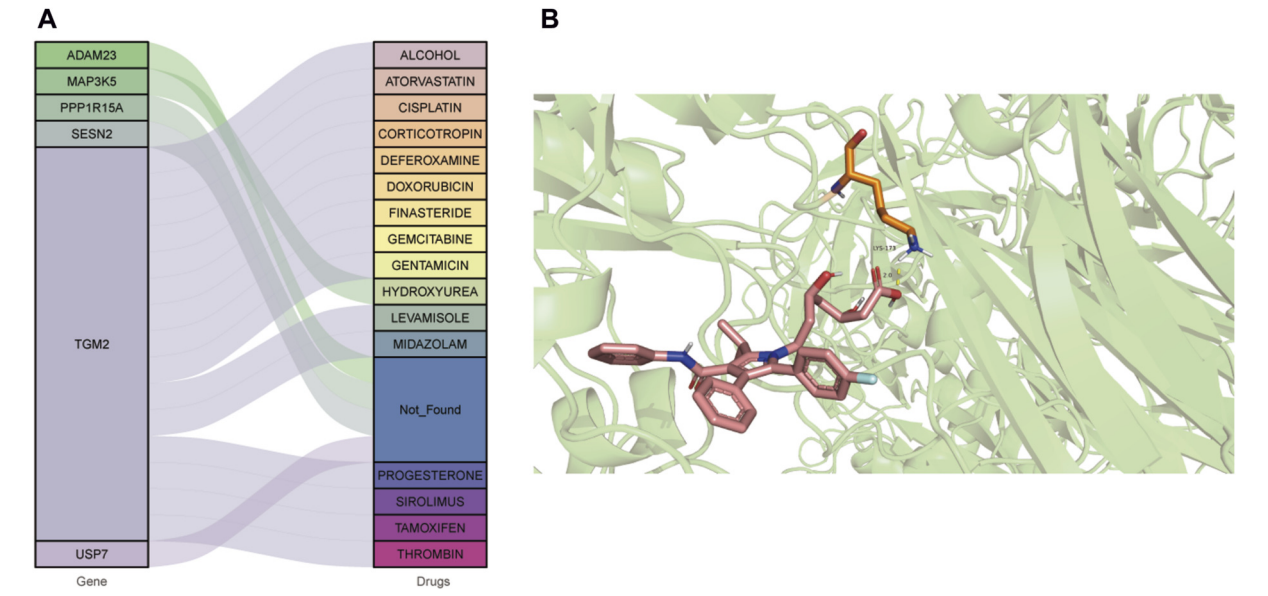

FIGURE 7
Drug prediction and molecular docking. **(A)** Drug prediction for hub genes. **(B)** The molecular docking between TGM2 and atorvastatin.

In this study, a total of 6 hub genes (MAP3K5, USP7, SESN2, ADAM23, PPP1R15A, and TGM2) were acquired in DCM patients. Mitogen-activated protein kinase kinase kinase 5 (MAP3K5), also known as apoptosis signal-regulating kinase 1 (ASK1), participates in regulating cell fate in HF and reperfusion injury [21, 22]. Its abnormal expression is related to DCM [23].

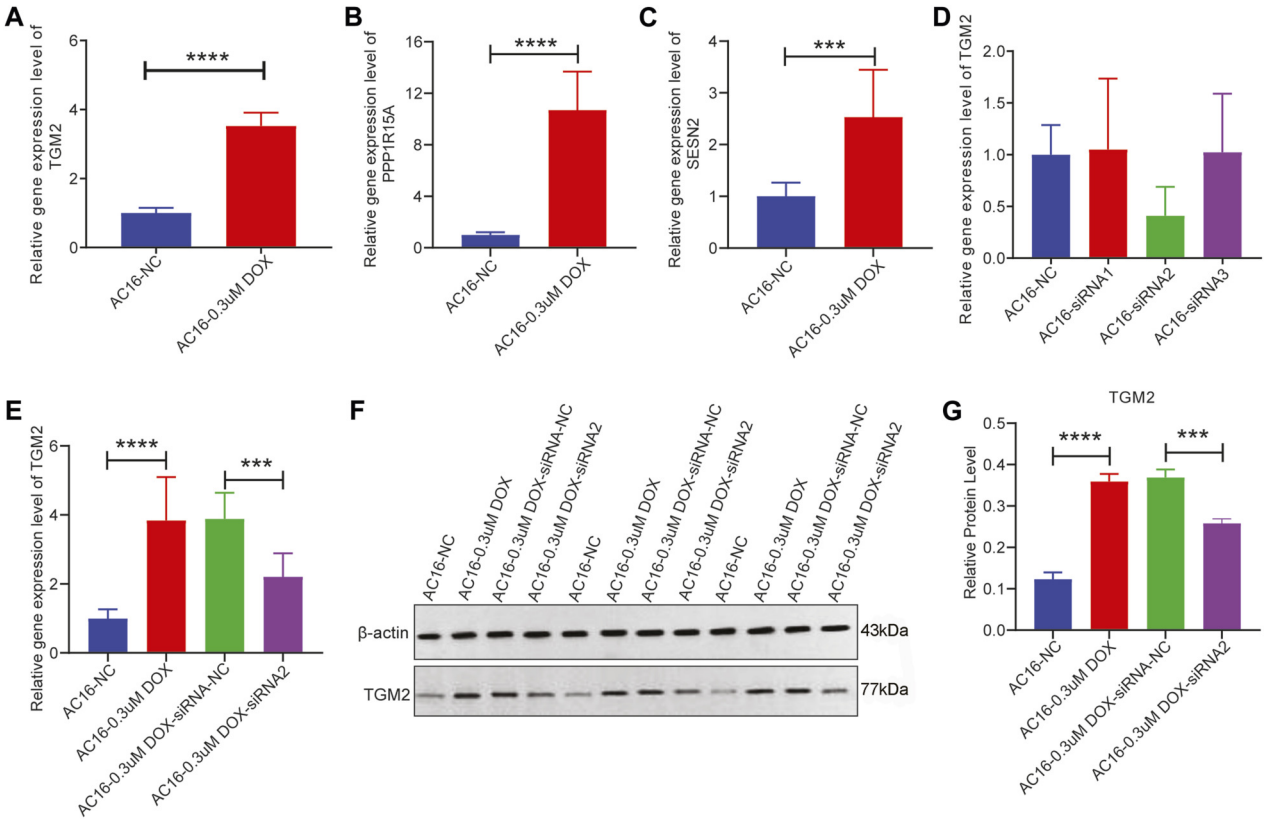

FIGURE 8
The expression of TGM2 in the DOX-induced AC16 cardiomyocyte injury model. **(A–C)** mRNA expression levels of TGM2, PPP1R15A, and SESN2 in DOX-induced AC16 cardiomyocyte injury. **(D)** The knockdown effect of 3 interference plasmids on TGM2 was detected by RT-qPCR. **(E)** mRNA expression levels of TGM2 in AC16-NC, AC16-0.3uM DOX, AC16-0.3uM DOX-siRNA-NC and AC16-0.3uM DOX-siRNA2 cells were detected by RT-qPCR. **(F)** The expression bands of TGM2 protein in AC16-NC, AC16-0.3uM DOX, AC16-0.3uM DOX-siRNA-NC and AC16-0.3uM DOX-siRNA2 cells were detected by western blotting. **(G)** The relative expression levels of TGM2 protein in AC16-NC, AC16-0.3uM DOX, AC16-0.3uM DOX-siRNA-NC and AC16-0.3uM DOX-siRNA2 cells.

Ubiquitin-specific protease 7 (USP7) is a component of the ubiquitin-proteasome system and plays a role in cardiomyocyte injury [24, 25]. Increasing USP7 could enhance ferroptosis in myocardial I/R rats [26]. Sestrin 2 (SESN2) is a stress-inducible protein associated with various stress conditions [27]. SESN2 can regulate cardiomyopathy by modulating mitophagy and mitochondrial function [28]. A disintegrin and metalloprotease 23 (ADAM23) belong to the transmembrane protein family, and its expression is down-regulated in heart tissues in DCM patients [29]. Transglutaminase 2 (TGM2) is a potential risk gene related to DCM [30]. Inhibiting TGM2 can alleviate myocardial fibrosis after myocardial infarction [31]. However, Protein phosphatase 1 regulatory subunit 15A (PPP1R15A) has not been reported in DCM. In this study, these hub genes have good performance in distinguishing DCM patients from healthy controls, suggesting that these hub genes may serve as potential biomarkers for DCM.

cTnT, as an important component of cardiac troponin, is a specific regulatory protein of cardiomyocytes. It collaborates with troponin I and C to regulate the contraction and relaxation of the myocardium, playing a key role in the excitation-contraction coupling mechanism of cardiomyocytes [32]. α-actinin is an actin-binding protein that is abundant in muscle tissues, and its main function is to maintain the structural stability of actin filaments. In cardiomyocytes, it is involved in the formation of the Z-line of the sarcomere, which is crucial for maintaining the contractile function and structural integrity of cells [33]. Previous studies have shown that cTnT and α-actinin play an indispensable role in the occurrence and development of DCM [34–36]. In this study, we found that TGM2 affected the expressions of cTnT and α-actinin. This revealed a novel mechanism by which TGM2 participates in the regulation of cardiomyocytes function by influencing the expression of cardiac structural proteins cTnT and α-actinin, providing potential molecular targets for understanding the pathological process of DCM. As a core molecule in the hypoxic response, existing studies have confirmed that HIF-1α is involved in the regulation of cardiac hypertrophy and heart failure [37, 38]. In this study, we also found

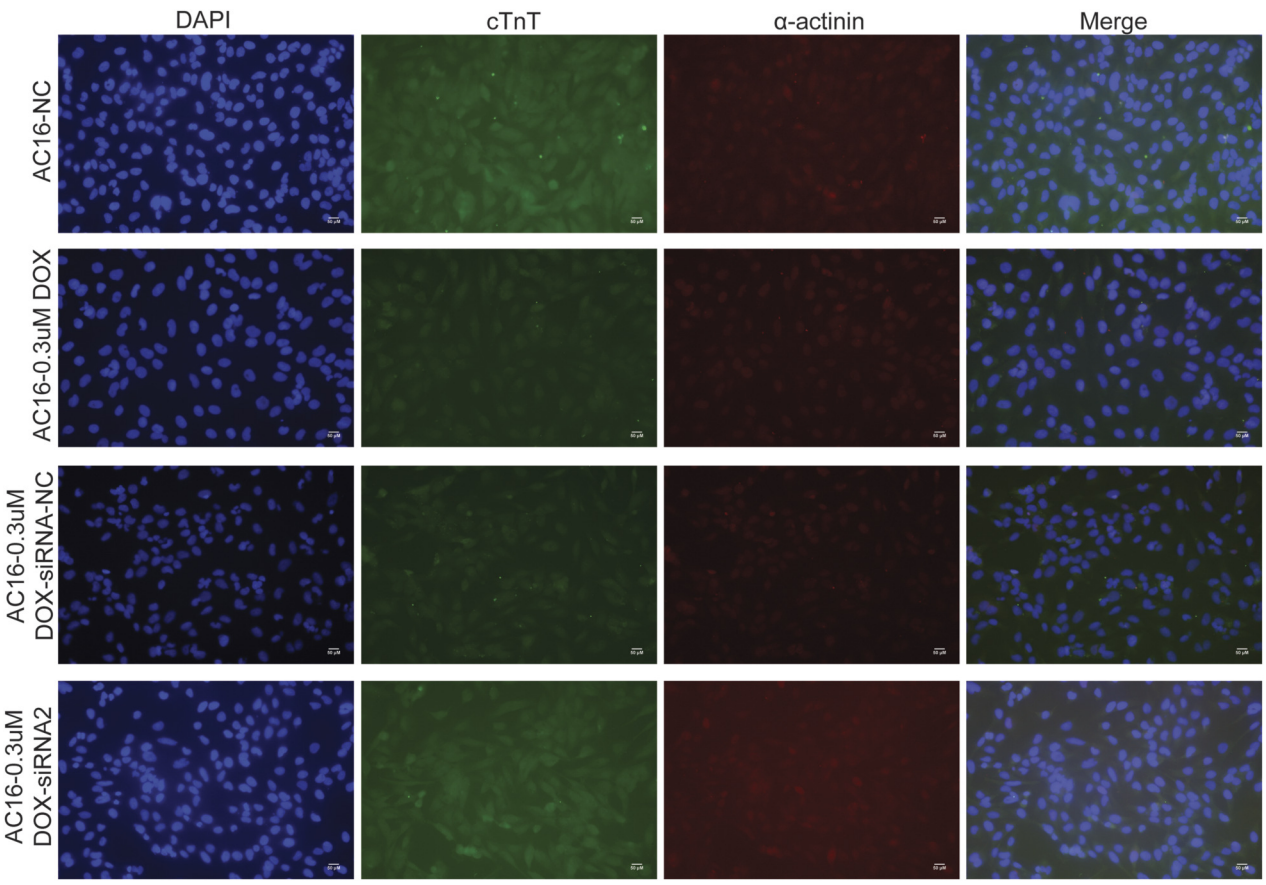

FIGURE 9
The influence of TGM2 on the expressions of cTnT and α-actinin was detected by immunofluorescence staining in DOX-induced AC16 cardiomyocyte injury.

that TGM2 affected the expression of HIF-1α. This result confirms that TGM2 plays a significant role in the hypoxia pathway of DCM. HIF-1α has been confirmed in previous studies to be involved in the ferroptosis process by regulating genes related to iron metabolism and lipid peroxidation [39, 40]. This provides potential associative clues for TGM2 to possibly intervene in ferroptosis regulation. Based on this, it is worth further study to explore the specific role and mechanism of TGM2 in the process of ferroptosis.

The immune response and its regulatory mechanisms play an important role in the occurrence and development of DCM [41]. Higher infiltrating levels of CD56dim NK cells, macrophages, monocytes, NK cells, and NK T cells were observed in DCM patients compared to healthy controls in this study. Stettner et al. demonstrated that the number of NK cells is significantly decreased, whereas the frequency of NK T-like cells is significantly increased in peripheral blood patients with idiopathic DCM [42]. However, NK cell activity in blood samples in DCM patients is decreased [43]. Among cardiac resident immune cells, macrophages, comprising approximately 7% of nonmyocytes, regulate cardiac impulse conduction, promote angiogenesis and vascular development, and maintain mitochondrial homeostasis [44, 45]. In the clinical study, DCM patients with higher infiltration levels of macrophage exhibited worse outcomes [46]. In DCM patients, increased expression of myeloid differentiation factor-2 (MD-2) could promote monocyte chemotactic protein 1 (MCP-1) secretion and monocyte recruitment, resulting in the progression of DCM [47]. The implantation of bone marrow-derived mononuclear cells into the LV anterior wall significantly relieves LV remodeling in DCM rats [48]. The Pearson correlation analysis revealed a certain degree of correlation between these immune cells and hub genes. Therefore, we speculate that the functions of these immune cells in DCM may be regulated via hub genes, and the specific molecular mechanisms deserve further investigation.

To further explore the possible molecular mechanisms involved in hub genes, a ceRNA network was constructed. The ceRNA network comprising 3 hub genes, 7 miRNAs, and 11 lncRNAs was constructed. Previous studies have shown that the abnormal expressions of hsa-miR-770-5p [49, 50], hsa-miR-16-5p [51], hsa-miR-338-3p [52] and hsa-miR-363-3p [49, 50]

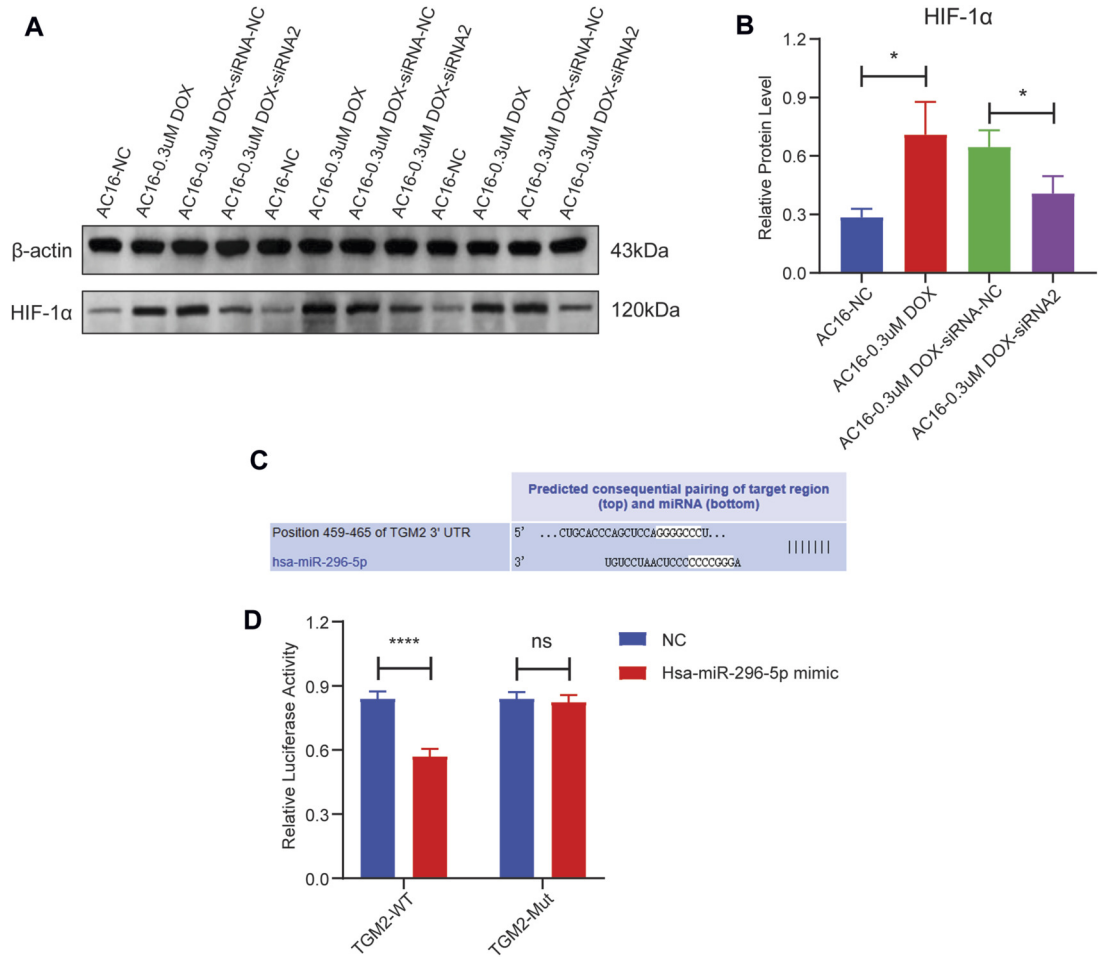

FIGURE 10
The effect of HIF-1α by TGM2 and validation of hsa-miR-296-5p targeting TGM2 via dual-luciferase reporter assay. **(A)** The expression bands of HIF-1α protein AC16-NC, AC16-0.3uM DOX, AC16-0.3uM DOX-siRNA-NC, AC16-0.3uM DOX-siRNA2. **(B)** The relative expression levels of HIF-1α protein in AC16-NC, AC16-0.3uM DOX, AC16-0.3uM DOX-siRNA-NC and AC16-0.3uM DOX-siRNA2 cells. **(C)** Bioinformatic prediction of the binding site between hsa-miR-296-5p and TGM2. **(D)** Validation of the targeted regulation of TGM2 by hsa-miR-296-5p using dual-luciferase reporter assay.

are involved in regulating the development of DCM. LncRNA KCNQ1OT1 can participate in regulating myocardial ischemia/reperfusion injury in mice and mediate apoptosis of myocardial cells [53, 54]. Inhibition of lncRNA MIR4435-2HG improved infarction volume, ejection fraction, and cardiomyocyte apoptosis [55]. LncRNA FGD5-AS1 is abnormally expressed in DCM and is involved in the regulation of cardiomyocyte apoptosis and cardiac fibrosis [56, 57]. LncRNA MALAT1 can regulate the microvascular function after myocardial infarction in mice by modulating mitochondrial dynamics [58]. Moreover, it can also mediate high glucose-induced cardiomyocyte apoptosis through the RhoA/ROCK pathway [59]. Based on the previous studies mentioned above, we speculated that the KCNQ1OT1-hsa-miR-770-5p-ADAM23, MIR4435-2HG/FGD5-AS1-hsa-miR-16-5p-SESN2 and MALAT1-hsa-miR-338-3p-TGM2 axes identified in this study may play an important regulatory role in the progression of DCM. To date, no studies have been reported on hsa-miR-139-5p, hsa-miR-296-5p, and hsa-miR-148a-3p in DCM. In this study, hsa-miR-296-5p was selected for dual-luciferase reporter assay, and the results showed that it had a direct targeting binding relationship with TGM2. This suggests that hsa-miR-296-5p may exert its function in DCM by targeting and regulating TGM2, while its specific mechanism remains to be further explored.

TGM2 is a Ca^{2+}-dependent transglutaminase that participates in apoptosis, cell survival, phagocytosis, cell adhesion and migration, and cell signaling [60]. Drug prediction results showed that atorvastatin, sirolimus, and thrombin were predicted to target TGM2. Atorvastatin improves left ventricular ejection fraction in DCM patients in the meta-analysis [14]. Sirolimus, also known as rapamycin, relieves

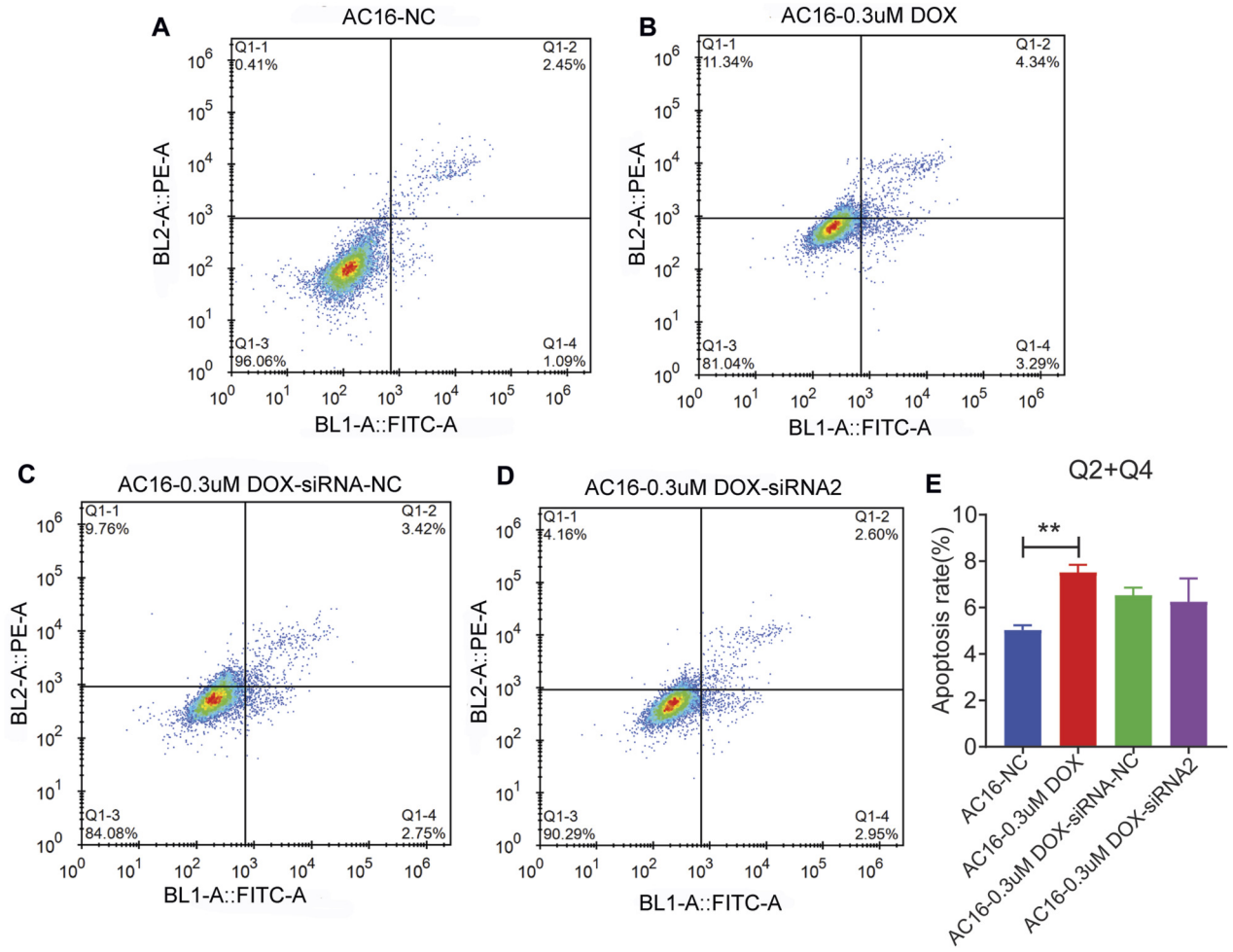

FIGURE 11
Flow cytometry was used to detect the effect of TGM2 on apoptosis of AC16 cardiomyocyte. **(A)** Flow cytometry was used to detect AC16-NC cell apoptosis. **(B)** Flow cytometry was used to detect AC16-0.3uM DOX cell apoptosis. **(C)** Flow cytometry was used to detect AC16-0.3uM DOX-siRNA-NC cell apoptosis. **(D)** Flow cytometry was used to detect AC16-0.3uM DOX-siRNA2 cell apoptosis. **(E)** Statistical histogram of apoptosis in flow cytometry.

oxidative stress, protects mitochondria, and restores energy homeostasis in DCM mice [61]. Additionally, sirolimus improves heart function in various cardiomyopathies, including alcoholic cardiomyopathy, cirrhotic cardiomyopathy, and hypertrophic cardiomyopathy [62–64]. Noteworthily, the mTOR (mammalian target of rapamycin) pathway was found to be enriched in our study. Wang et al. reported that inhibition of the AMPK/mTOR pathway reduces myocardial damage and attenuates diabetic cardiomyopathy [65]. Thrombin expression was significantly up-regulated in DCM patients compared to healthy controls through immunohistochemical [66]. After inhibition of thrombin, left ventricular function and poor outcomes in DCM mice were significantly improved [66]. From the perspective of transformation, atorvastatin and sirolimus have been clinically used for cardiovascular indications, and if their efficacy through TGM2 targeted therapy is confirmed, it may contribute to their use in DCM. Although the regulation of thrombin has shown promising application prospects in preclinical studies, its safety and efficacy characteristics still need to be strictly evaluated in cardiomyopathy. Overall, these predicted drugs offer testable candidates for future translational studies aimed at DCM therapy.

Conclusion

Through bioinformatical analysis, 6 hub genes (PPP1R15A, TGM2, MAP3K5, USP7, SESN2, and ADAM2) were identified, which may be potential diagnostic biomarkers for DCM. Preliminary *in vitro* verification showed that TGM2 was up-regulated in DOX-induced AC16 cardiomyocyte injury. After knocking down TGM2, the expressions of α-actinin and cTnT

were increased, and the expression level of HIF-1α was inhibited. Dual luciferase assay showed that hsa-miR-291-5p exerted its regulatory effect by directly binding to TGM2. Our findings may facilitate understanding the potential pathogenesis of DCM and provide new insights for the treatment of DCM.

Author contributions

XW: Designed the study, performed data analysis, drafted the manuscript, and interpreted the results; WL: Collected data, contributed to data analysis, and made significant revisions to the manuscript; CG: Supervised the study, provided theoretical guidance, and reviewed and edited the final. All authors contributed to the article and approved the submitted version.

Data availability

The datasets presented in this study can be found in the GEO database (http://www.ncbi.nlm.nih.gov/geo). The accession numbers are GSE120895, GSE17800, and GSE112556, respectively.

Ethics statement

Publicly available datasets used in this study were obtained from previously published research, all of which had received approval from the respective Institutional Review Boards (IRBs) in the original studies.

Funding

The author(s) declared that financial support was not received for this work and/or its publication.

Conflict of interest

The author(s) declared no potential conflicts of interest with respect to the research, authorship, and/or publication of this article.

Generative AI statement

The author(s) declared that generative AI was not used in the creation of this manuscript.

Any alternative text (alt text) provided alongside figures in this article has been generated by Frontiers with the support of artificial intelligence and reasonable efforts have been made to ensure accuracy, including review by the authors wherever possible. If you identify any issues, please contact us.

Supplementary material

The Supplementary Material for this article can be found online at: https://www.ebm-journal.org/articles/10.3389/ebm.2026.10709/full#supplementary-material

References

1. Sinagra G, Elliott PM, Merlo M. Dilated cardiomyopathy: so many cardiomyopathies. *Eur Heart J* (2020) **41**:3784–6. doi:10.1093/eurheartj/ehz908

2. McNally EM, Mestroni L. Dilated cardiomyopathy: genetic determinants and mechanisms. *Circ Res* (2017) **121**:731–48. doi:10.1161/circresaha.116.309396

3. Sun H, Chen D, Xin W, Ren L, Li Q, Han X. Targeting ferroptosis as a promising therapeutic strategy to treat cardiomyopathy. *Front Pharmacol* (2023) **14**: 1146651. doi:10.3389/fphar.2023.1146651

4. Ruan Y, Zhang L, Zhang L, Zhu K. Therapeutic approaches targeting ferroptosis in cardiomyopathy. *Cardiovasc Drugs Ther* (2025) **39**:595–613. doi:10.1007/s10557-023-07514-4

5. Tang D, Chen X, Kang R, Kroemer G. Ferroptosis: molecular mechanisms and health implications. *Cell Res* (2021) **31**:107–25. doi:10.1038/s41422-020-00441-1

6. Fang X, Wang H, Han D, Xie E, Yang X, Wei J, et al. Ferroptosis as a target for protection against cardiomyopathy. *Proc Natl Acad Sci U S A* (2019) **116**:2672–80. doi:10.1073/pnas.1821022116

7. D'Aiuto N, Hochmann J, Millán M, Di Paolo A, Bologna-Molina R, Sotelo Silveira J, et al. Hypoxia, acidification and oxidative stress in cells cultured at large distances from an oxygen source. *Sci Rep* (2022) **12**:21699. doi:10.1038/s41598-022-26205-y

8. Zhou S, Yin X, Jin J, Tan Y, Conklin DJ, Xin Y, et al. Intermittent hypoxia-induced cardiomyopathy and its prevention by Nrf2 and metallothionein. *Free Radic Biol Med* (2017) **112**:224–39. doi:10.1016/j.freeradbiomed.2017.07.031

9. Tintu A, Rouwet E, Verlohren S, Brinkmann J, Ahmad S, Crispi F, et al. Hypoxia induces dilated cardiomyopathy in the chick embryo: mechanism, intervention, and long-term consequences. *PLoS One* (2009) **4**:e5155. doi:10.1371/journal.pone.0005155

10. Feng Y, Madungwe NB, Imam Aliagan AD, Tombo N, Bopassa JC. Liproxstatin-1 protects the mouse myocardium against ischemia/reperfusion injury by decreasing VDAC1 levels and restoring GPX4 levels. *Biochem Biophys Res Commun* (2019) **520**:606–11. doi:10.1016/j.bbrc.2019.10.006

11. Ryabov VV, Maslov LN, Vyshlov EV, Mukhomedzyanov AV, Kilin M, Gusakova SV, et al. Ferroptosis, a regulated form of cell death, as a target for the development of novel drugs preventing ischemia/reperfusion of cardiac injury, cardiomyopathy and stress-induced cardiac injury. *Int J Mol Sci* (2024) **25**:897. doi:10.3390/ijms25020897

12. Charoentong P, Finotello F, Angelova M, Mayer C, Efremova M, Rieder D, et al. Pan-cancer immunogenomic analyses reveal genotype-immunophenotype relationships and predictors of response to checkpoint blockade. *Cell Rep* (2017) **18**: 248–62. doi:10.1016/j.celrep.2016.12.019

13. Barbie DA, Tamayo P, Boehm JS, Kim SY, Moody SE, Dunn IF, et al. Systematic RNA interference reveals that oncogenic KRAS-driven cancers require TBK1. *Nature* (2009) **462**:108–12. doi:10.1038/nature08460

14. Fu L, Shang X, Zhang X. The impact of atorvastatin on cardiac performance for dilated cardiomyopathy: a meta-analysis of randomized controlled studies. *Heart Surg Forum* (2020) **23**:E329–e34. doi:10.1532/hsf.2787

15. Bielecka-Dabrowa A, Mikhailidis DP, Rizzo M, von Haehling S, Rysz J, Banach M. The influence of atorvastatin on parameters of inflammation left ventricular function, hospitalizations and mortality in patients with dilated cardiomyopathy--5-year follow-up. *Lipids Health Dis* (2013) **12**:47. doi:10.1186/1476-511x-12-47

16. Pérez-Serra A, Toro R, Sarquella-Brugada G, de Gonzalo-Calvo D, Cesar S, Carro E, et al. Genetic basis of dilated cardiomyopathy. *Int J Cardiol* (2016) **224**: 461–72. doi:10.1016/j.ijcard.2016.09.068

17. She G, Hai XX, Jia LY, Zhang YJ, Ren YJ, Pang ZD, et al. Hippo pathway activation mediates cardiomyocyte ferroptosis to promote dilated cardiomyopathy through downregulating NFS1. *Redox Biol* (2025) **82**:103597. doi:10.1016/j.redox.2025.103597

18. Zhao Y, Dai J, Gong A, Jin S, Guan C, Wang K, et al. Interleukin 27 deficiency drives dilated cardiomyopathy by ferroptosis. *Clin Transl Med* (2025) **15**:e70269. doi:10.1002/ctm2.70269

19. Wen MS, Wang CY, Yeh JK, Chen CC, Tsai ML, Ho MY, et al. The role of asprosin in patients with dilated cardiomyopathy. *BMC Cardiovasc Disord* (2020) **20**:402. doi:10.1186/s12872-020-01680-1

20. Wang Z, Yao M, Jiang L, Wang L, Yang Y, Wang Q, et al. Dexmedetomidine attenuates myocardial ischemia/reperfusion-induced ferroptosis *via* AMPK/GSK-3β/Nrf2 axis. *Biomed Pharmacother* (2022) **154**:113572. doi:10.1016/j.biopha.2022.113572

21. Wang T, Pang L, He M, Wang Z. Small-molecule inhibitors targeting apoptosis signal-regulated kinase 1. *Eur J Med Chem* (2023) **262**:115889. doi:10.1016/j.ejmech.2023.115889

22. Song J, Cho KJ, Cheon SY, Kim SH, Park KA, Lee WT, et al. Apoptosis signal-regulating kinase 1 (ASK1) is linked to neural stem cell differentiation after ischemic brain injury. *Exp Mol Med* (2013) **45**:e69. doi:10.1038/emm.2013.134

23. Huang Q, Zhou HJ, Zhang H, Huang Y, Hinojosa-Kirschenbaum F, Fan P, et al. Thioredoxin-2 inhibits mitochondrial reactive oxygen species generation and apoptosis stress kinase-1 activity to maintain cardiac function. *Circulation* (2015) **131**:1082–97. doi:10.1161/circulationaha.114.012725

24. Xue Q, Yang D, Zhang J, Gan P, Lin C, Lu Y, et al. USP7, negatively regulated by miR-409-5p, aggravates hypoxia-induced cardiomyocyte injury. *Apmis* (2021) **129**:152–62. doi:10.1111/apm.13100

25. Xu Q, Liu M, Gu J, Ling S, Liu X, Luo Z, et al. Ubiquitin-specific protease 7 regulates myocardial ischemia/reperfusion injury by stabilizing Keap1. *Cell Death Discov* (2022) **8**:291. doi:10.1038/s41420-022-01086-2

26. Tang LJ, Zhou YJ, Xiong XM, Li NS, Zhang JJ, Luo XJ, et al. Ubiquitin-specific protease 7 promotes ferroptosis *via* activation of the p53/TfR1 pathway in the rat hearts after ischemia/reperfusion. *Free Radic Biol Med* (2021) **162**:339–52. doi:10.1016/j.freeradbiomed.2020.10.307

27. Liu Y, Li M, Du X, Huang Z, Quan N. Sestrin 2, a potential star of antioxidant stress in cardiovascular diseases. *Free Radic Biol Med* (2021) **163**:56–68. doi:10.1016/j.freeradbiomed.2020.11.015

28. Wang P, Lan R, Guo Z, Cai S, Wang J, Wang Q, et al. Histone demethylase JMJD3 mediated doxorubicin-induced cardiomyopathy by suppressing SESN2 expression. *Front Cell Dev Biol* (2020) **8**:548605. doi:10.3389/fcell.2020.548605

29. Xiang M, Luo H, Wu J, Ren L, Ding X, Wu C, et al. ADAM23 in cardiomyocyte inhibits cardiac hypertrophy by targeting FAK - AKT signaling. *J Am Heart Assoc* (2018) **7**:e008604. doi:10.1161/jaha.118.008604

30. Wang H, Wang Y, Huang D, Jiang X, Li C, Xia X, et al. Potential risk factors and therapeutic targets for dilated cardiomyopathy identified through Mendelian randomization analysis. *J Am Heart Assoc* (2026) **15**:e038088. doi:10.1161/jaha.124.038088

31. Sun R, Li H, Chen Y, Hu M, Wang J. Tubuloside A alleviates postmyocardial infarction cardiac fibrosis by inhibiting TGM2: involvement of inflammation and mitochondrial pathway apoptosis. *Int Immunopharmacol* (2024) **143**:113324. doi:10.1016/j.intimp.2024.113324

32. Chaulin A. Cardiac troponins: Contemporary biological data and new methods of determination. *Vasc Health Risk Manag* (2021) **17**:299–316. doi:10.2147/vhrm.s300002

33. Ribeiro Ede A, Jr, Pinotsis N, Ghisleni A, Salmazo A, Konarev PV, Kostan J, et al. The structure and regulation of human muscle α-actinin. *Cell* (2014) **159**: 1447–60. doi:10.1016/j.cell.2014.10.056

34. Ye L, Liu J, Lei W, Ni B, Han X, Zhang Y, et al. *Disruption of cTnT-Mediated sarcomere-mitochondrial communication results in dilated cardiomyopathy* (2025). doi:10.1161/circulationaha.125.071523

35. O'Sullivan ML, O'Grady MR, Pyle WG, Dawson JF. Evaluation of 10 genes encoding cardiac proteins in doberman pinschers with dilated cardiomyopathy. *Am J Vet Res* (2011) **72**:932–9. doi:10.2460/ajvr.72.7.932

36. Hein S, Block T, Zimmermann R, Kostin S, Scheffold T, Kubin T, et al. Deposition of nonsarcomeric alpha-actinin in cardiomyocytes from patients with dilated cardiomyopathy or chronic pressure overload. *Exp Clin Cardiol* (2009) **14**: e68–75.

37. Kumar S, Wang G, Liu W, Ding W, Dong M, Zheng N, et al. Hypoxia-induced mitogenic factor promotes cardiac hypertrophy *via* calcium-dependent and hypoxia-inducible Factor-1α mechanisms. *Hypertension* (2018) **72**:331–42. doi:10.1161/hypertensionaha.118.10845

38. Zolk O, Solbach TF, Eschenhagen T, Weidemann A, Fromm MF. Activation of negative regulators of the hypoxia-inducible factor (HIF) pathway in human end-stage heart failure. *Biochem Biophys Res Commun* (2008) **376**:315–20. doi:10.1016/j.bbrc.2008.08.152

39. Yuan S, Wei C, Liu G, Zhang L, Li J, Li L, et al. Sorafenib attenuates liver fibrosis by triggering hepatic stellate cell ferroptosis *via* HIF-1α/SLC7A11 pathway. *Cell Prolif* (2022) **55**:e13158. doi:10.1111/cpr.13158

40. Wang D, Zhang H, Liao X, Li J, Zeng J, Wang Y, et al. Oral administration of Robinia pseudoacacia L. flower exosome-like nanoparticles attenuates gastric and small intestinal mucosal ferroptosis caused by hypoxia through inhibiting HIF-1α- and HIF-2α-mediated lipid peroxidation. *J Nanobiotechnology* (2024) **22**:479. doi:10.1186/s12951-024-02663-6

41. Wang E, Zhou R, Li T, Hua Y, Zhou K, Li Y. *The molecular role of immune cells in dilated cardiomyopathy* (2023). p. 59. doi:10.3390/medicina59071246

42. Stettner-Leonkiewicz D, Grywalska E, Zhang ZY, Rolinski J, Wysokinski A, Idcm P. The expression of NKT like cells and NK cells in the peripheral blood among patients with idiopathic dilated cardiomyopathy (IDCM). *Eur Heart J* (2020) **41**:41. doi:10.1093/ehjci/ehaa946.1006

43. Anderson JL, Carlquist JF, Hammond EH. Deficient natural killer cell activity in patients with idiopathic dilated cardiomyopathy. *Lancet* (1982) **2**(2):1124–7. doi:10.1016/s0140-6736(82)92786-6

44. Banerjee D, Tian R, Cai S. The role of innate immune cells in cardiac injury and repair: a metabolic perspective. *Curr Cardiol Rep* (2023) **25**:631–40. doi:10.1007/s11886-023-01897-4

45. Pinto AR, Ilinykh A, Ivey MJ, Kuwabara JT, D'Antoni ML, Debuque R, et al. Revisiting cardiac cellular composition. *Circ Res* (2016) **118**:400–9. doi:10.1161/circresaha.115.307778

46. Nakayama T, Sugano Y, Yokokawa T, Nagai T, Matsuyama TA, Ohta-Ogo K, et al. Clinical impact of the presence of macrophages in endomyocardial biopsies of patients with dilated cardiomyopathy. *Eur J Heart Fail* (2017) **19**:490–8. doi:10.1002/ejhf.767

47. Feldtmann R, Kümmel A, Chamling B, Strohbach A, Lehnert K, Gross S, et al. Myeloid differentiation factor-2 activates monocytes in patients with dilated cardiomyopathy. *Immunology* (2022) **167**:40–53. doi:10.1111/imm.13490

48. Sun CK, Chang LT, Sheu JJ, Chiang CH, Lee FY, Wu CJ, et al. Bone marrow-derived mononuclear cell therapy alleviates left ventricular remodeling and improves heart function in rat-dilated cardiomyopathy. *Crit Care Med* (2009) **37**:1197–205. doi:10.1097/CCM.0b013e31819c0667

49. Wang LJ, Qiu BQ, Yuan MM, Zou HX, Gong CW, Huang H, et al. Identification and validation of dilated cardiomyopathy-related genes *via* bioinformatics analysis. *Int J Gen Med* (2022) **15**:3663–76. doi:10.2147/ijgm.s350954

50. Huang K, Wen S, Huang J, Wang F, Pang L, Wang Y, et al. Integrated analysis of hub genes and miRNAs in dilated cardiomyopathy. *Biomed Res Int* (2020) **2020**: 8925420. doi:10.1155/2020/8925420

51. Toro R, Pérez-Serra A, Mangas A, Campuzano O, Sarquella-Brugada G, Quezada-Feijoo M, et al. miR-16-5p suppression protects human cardiomyocytes against endoplasmic reticulum and oxidative stress-induced injury. *Int J Mol Sci* (2022) **23**:1036. doi:10.3390/ijms23031036

52. Huang C, Wang R, Lu J, He Y, Wu Y, Ma W, et al. MicroRNA-338-3p as a therapeutic target in cardiac fibrosis through FGFR2 suppression. *J Clin Lab Anal* (2022) **36**:e24584. doi:10.1002/jcla.24584

53. Rong J, Pan H, He J, Zhang Y, Hu Y, Wang C, et al. Long non-coding RNA KCNQ1OT1/microRNA-204-5p/LGALS3 axis regulates myocardial ischemia/reperfusion injury in mice. *Cell Signal* (2020) **66**:109441. doi:10.1016/j.cellsig.2019.109441

54. Lai L, Xu Y, Kang L, Yang J, Zhu G. LncRNA KCNQ1OT1 contributes to cardiomyocyte apoptosis by targeting FUS in heart failure. *Exp Mol Pathol* (2020) **115**:104480. doi:10.1016/j.yexmp.2020.104480

55. Wang X, Ren L, Chen S, Tao Y, Zhao D, Wu C. Long non-coding RNA MIR4435-2HG/microRNA-125a-5p axis is involved in myocardial ischemic injuries. *Bioengineered* (2022) **13**:10707–20. doi:10.1080/21655979.2022.2051259

56. Chen YX, Ding J, Zhou WE, Zhang X, Sun XT, Wang XY, et al. Identification and functional prediction of long non-coding RNAs in dilated cardiomyopathy by bioinformatics analysis. *Front Genet* (2021) **12**:648111. doi:10.3389/fgene.2021.648111

57. Zhao Y, Wang C, Cui T, Wang Q, Xu Y, Miao C, et al. LncRNA FGD5-AS1 reduces cardiomyocyte apoptosis and inflammation by modulating Akt and miR-223-3p expression. *Am J Transl Res* (2022) **14**:6175–86.

58. Chen Y, Li S, Zhang Y, Wang M, Li X, Liu S, et al. The lncRNA Malat1 regulates microvascular function after myocardial infarction in mice *via* miR-26b-5p/Mfn1 axis-mediated mitochondrial dynamics. *Redox Biol* (2021) **41**: 101910. doi:10.1016/j.redox.2021.101910

59. Wang T, Li N, Yuan L, Zhao M, Li G, Chen Y, et al. MALAT1/miR-185-5p mediated high glucose-induced oxidative stress, mitochondrial injury and cardiomyocyte apoptosis *via* the RhoA/ROCK pathway. *J Cell Mol Med* (2023) **27**:2495–506. doi:10.1111/jcmm.17835

60. Zakrzewicz A, Atanasova S, Padberg W, Grau V. Monocytic tissue transglutaminase in a rat model for reversible acute rejection and chronic renal allograft injury. *Mediators Inflamm* (2015) **2015**:429653. doi:10.1155/2015/429653

61. Zhang S, Wei X, Zhang H, Wu Y, Jing J, Huang R, et al. Doxorubicin downregulates autophagy to promote apoptosis-induced dilated cardiomyopathy *via* regulating the AMPK/mTOR pathway. *Biomed Pharmacother* (2023) **162**: 114691. doi:10.1016/j.biopha.2023.114691

62. Tu X, Wang C, Ru X, Jing L, Zhou L, Jing L. Therapeutic effects of rapamycin on alcoholic cardiomyopathy. *Exp Ther Med* (2017) **14**:2763–70. doi:10.3892/etm.2017.4901

63. Saeedi Saravi SS, Ghazi-Khansari M, Ejtemaei Mehr S, Nobakht M, Mousavi SE, Dehpour AR. Contribution of mammalian target of rapamycin in the pathophysiology of cirrhotic cardiomyopathy. *World J Gastroenterol* (2016) **22**: 4685–94. doi:10.3748/wjg.v22.i19.4685

64. Dhandapany PS, Kang S, Kashyap DK, Rajagopal R, Sundaresan NR, Singh R, et al. Adiponectin receptor 1 variants contribute to hypertrophic cardiomyopathy that can be reversed by rapamycin. *Sci Adv* (2021) **7**:7. doi:10.1126/sciadv.abb3991

65. Wang H, Wang L, Hu F, Wang P, Xie Y, Li F, et al. Neuregulin-4 attenuates diabetic cardiomyopathy by regulating autophagy *via* the AMPK/mTOR signalling pathway. *Cardiovasc Diabetol* (2022) **21**:205. doi:10.1186/s12933-022-01643-0

66. Ito K, Hongo K, Date T, Kashiwagi Y, Yoshino T, Nagoshi T, et al. Thrombin is a novel target of the treatment of dilated cardiomyopathy. *Circulation* (2015) **132**:A10260–A.

EBM Experimental Biology and Medicine

TYPE Original Research
PUBLISHED 03 February 2026
DOI 10.3389/ebm.2026.10869

OPEN ACCESS

*CORRESPONDENCE
Lezan Medhat Mohammed,
loay.altaay@gmail.com

RECEIVED 21 October 2025
REVISED 16 December 2025
ACCEPTED 22 January 2026
PUBLISHED 03 February 2026

CITATION
Mohammed LM, Ali PS, Taha AQ and Mohammad LM (2026) Expression of MicroRNA-155 and its associations with EBV serological markers and inflammatory cytokines in young lymphoma patients with evidence of active EBV infection.
Exp. Biol. Med. 251:10869.
doi: 10.3389/ebm.2026.10869

Expression of MicroRNA-155 and its associations with EBV serological markers and inflammatory cytokines in young lymphoma patients with evidence of active EBV infection

Lezan Medhat Mohammed[1]*, Payman S. Ali[2], Ali Qasim Taha[2] and Luay M. Mohammad[3]

[1]Medical Technical Institute/Kirkuk, Northern Technical University, Ministry of Higher Education and Scientific Research, Kirkuk, Iraq, [2]Department of Nurse, Medical Technical Institute/Kirkuk, Northern Technical University, Ministry of Higher Education and Scientific Research, Kirkuk, Iraq, [3]Department of Public Health, Kirkuk Health Directorate, Iraqi Ministry of Health (MOH), Kirkuk, Iraq

Abstract

The Epstein–Barr virus (EBV) is implicated in several lymphoproliferative disorders, particularly among children and adolescents who frequently experience primary EBV infection. MicroRNA-155 (miR-155), an oncogenic and immunoregulatory molecule, is known to participate in EBV-related immune modulation; however, its expression profile and relationship with EBV serological markers and inflammatory cytokines in young lymphoma patients remain insufficiently characterized. This cross-sectional observational study included 80 participants, comprising 40 young lymphoma patients with serological evidence of active EBV infection and 40 healthy controls. Serum EBV IgM and IgG levels were measured using ELISA, as were IL-18 and IL-32 concentrations, while serum miR-155 levels were quantified using qRT-PCR with an absolute quantification approach. The mean age of participants was 13.19 $\pm$ 2.51 years, and 55% were male. Serum miR-155 levels were significantly higher in lymphoma patients compared with controls (median: 1.13 vs. 0.43 ng/mL; $p = 0.012$). Elevated miR-155 expression was significantly associated with EBV IgM positivity ($p < 0.001$), IL-18 ($p = 0.001$), and IL-32 ($p < 0.001$). In multivariate logistic regression analysis, IL-32 positivity emerged as a strong independent predictor of elevated miR-155 levels (AOR = 19.02, $p = 0.001$). Receiver operating characteristic curve analysis demonstrated good discriminative performance of miR-155 (AUC = 0.87), with 87% sensitivity and 90% specificity at a cutoff value of ≥1.11 ng/mL. These findings indicate that serum miR-155 is significantly elevated in young lymphoma patients with serological evidence of active EBV infection and is statistically associated with inflammatory cytokines, particularly IL-32. miR-155 may represent a

promising non-invasive biomarker reflecting EBV-related immune activation, although tissue-based EBV confirmation and mechanistic studies are required to establish causality.

KEYWORDS

cytokines (IL-18 and IL-32), Epstein–Barr virus, Iraq, microRNA-155, young lymphoma patients

Impact statement

This study addresses a clinically relevant gap in understanding how Epstein–Barr virus–related immune activity is reflected in young lymphoma patients. While microRNA-155 has been widely studied in adult malignancies and experimental models, its circulating expression profile in pediatric and adolescent lymphoma patients with active EBV serology has remained poorly defined. By demonstrating that serum microRNA-155 is significantly elevated in affected patients and closely associated with inflammatory signaling—particularly interleukin-32—this work advances the field by linking viral serological activity to a measurable, non-invasive biomarker. These findings provide new insight into the interaction between EBV infection and immune-mediated pathways in early-onset lymphoma. Importantly, this study supports the clinical relevance of serum microRNA-155 as a candidate biomarker for future risk stratification and monitoring in EBV-associated lymphoproliferative disorders, thereby informing both translational research and clinical investigation.

Introduction

The Epstein-Barr virus (EBV) is a prevalent gamma-herpesvirus that infects more than 90% of people globally. It primarily targets B-lymphocytes and establishes lifelong latency within these cells. EBV is recognized as the first oncogenic pathogen linked to various cancers [1].

EBV contributes to the development of several lymphoproliferative disorders, including Hodgkin's lymphoma, Burkitt lymphoma, diffuse large B-cell lymphoma, and post-transplant lymphoproliferative diseases. In these cases, weakened immune surveillance permits unchecked proliferation of B-cells [2–4]. EBV infections usually occur during childhood and are often asymptomatic. Following the initial infection, the virus enters a dormant state, with memory B-lymphocytes becoming infected and establishing latency. This process involves the expression of latent genes and changes in the host's immune responses in humans [5, 6].

MicroRNA-155 (miR-155), are encoded by the B-cell integration cluster gene (BIC) and play a crucial role in regulating inflammation, T-cell proliferation, and apoptosis [7]. Dysregulation of miR-155 is associated with various cancers [8].

MiR-155 is an upregulated microRNA in EBV-associated malignant B-lymphocytes, and the EBV genes LMPI and EBNA2 promote the expression of microRNA-155 through enhancer elements. This upregulation is particularly necessary for the proliferation of EBV-infected B-lymphocytes [9]. The miR-155 influences the production of both anti-inflammatory and pro-inflammatory cytokines [10].

Additionally, the expression of immune checkpoints enhances EBV infection, leading to the release of immunosuppressive cytokines and the efflux of regulatory T cells in the tumor microenvironment [11]. Furthermore, interleukin-18 (IL-18) stimulates the expression of interferon-gamma, which is a key cytokine for controlling viral infections [12]. Moreover, interleukin-32 (IL-32) is recognized as a pro-inflammatory cytokine produced by T lymphocytes, natural killer cells, monocytes, and epithelial cells. It has been emphasized that IL-32 plays a significant role in the pathophysiology of the disease [13].

The association between miR-155 and cytokine expression may indicate an underlying immune-regulatory interaction, as suggested by previous research, especially in pediatric populations where immune responses and microRNA regulatory networks are still evolving [10, 12–15]. However, these interactions were not directly assessed in the current study.

Children and adolescents exhibit immunological characteristics that are notably different from those of adults. They have a higher likelihood of experiencing primary EBV infections and possess a more dynamic immune environment that is regulated by developmental factors. Notably, microRNA-155 regulatory networks, which include those that control lymphocyte function, undergo ontogenetic changes. The expression patterns of microRNA-155 shift during lymphopoiesis and transition from childhood to adulthood [14–16]. These developmental changes can result in different baseline and responsive levels of microRNA-155, like miR-155, in younger individuals compared to adults. Such variations highlight the importance of investigating miR-155 expression specifically within pediatric cohorts of EBV-associated lymphomas. Our discussion of EBV-related mechanisms is based on previously published experimental studies; these regulatory interactions were not directly evaluated in the present cohort.

Despite increasing evidence of miR-155s involvement in EBV-related oncogenesis, few studies have focused on its expression in young patients with lymphoma and serological evidence of active EBV infection and its correlation with viral serological markers

(IgM and IgG) and inflammatory cytokines. Understanding these relationships could offer valuable insights into the diagnostic and prognostic significance of miR-155 in early-onset lymphoma and may aid in identifying new therapeutic targets.

This study aimed to examine the expression levels of miR-155 in young patients with lymphoma who demonstrated serological evidence of active EBV infection, investigate its association with EBV IgM/IgG serological markers and inflammatory cytokines (IL-18 and IL-32), and evaluate its diagnostic potential.

Materials and methods

Study design and setting

This cross-sectional observational was carried out between November 2024 and May 2025 at the Teaching Oncology Hospital in Baghdad, Iraq. The objective of the study was to evaluate the expression of microRNA-155 (miR-155) and its relationship with Epstein-Barr virus (EBV) serological markers and inflammatory cytokines in young lymphoma patients with serological evidence of active EBV infection.

Sample size determination

The required sample size was estimated using the formula for comparing two independent means [17]:

$$n = \frac{\left(Z_{\alpha/2} + Z_{\beta}\right)^2 \cdot 2\sigma^2}{\delta^2}$$

Where:

- $Z\alpha/2 = 1.96$ (95% confidence)
- $Z\beta = 0.84$ (80% power)
- δ = expected difference in miR-155 levels
- σ = pooled standard deviation

The sample size calculation utilized $\delta = 0.45$ ng/mL as the expected difference in serum miR-155 levels between patients and controls, and $\sigma = 0.62$ ng/mL as the estimated pooled standard deviation based on previous studies of miR-155 in B-cell lymphomas [18, 19]. Using these parameters along with $\alpha = 0.05$ and $\beta = 0.20$ determined a minimum required sample size of 39 participants per group. To account for potential missing data and maintain balanced groups, the sample was rounded to include 40 patients and 40 controls, totaling 80 participants.

Sensitivity analysis revealed that with 40 participants per group, the study could detect a minimum standardized effect size of 0.58 (considered a moderate effect) with 80% power.

Participant selection criteria

- Inclusion Criteria
  - The study involved pediatric and adolescent patients aged 8 to 17, in line with established definitions of children and early adolescents with lymphoma. This age range was chosen due to the notable differences in immune responses, EBV infection patterns, and microRNA regulation compared to adults.
  - Diagnosed lymphoma based on clinical and hematological assessment.
  - Serological evidence of active EBV infection (positive EBV IgM and/or high EBV IgG titers).
- Exclusion Criteria
  - Recent infections other than EBV.
  - Co-infection with HIV, HBV, or HCV.
  - Autoimmune disorders or immunosuppressive therapy.
  - Previous malignancy.
  - Incomplete laboratory data.
- Controls

  Age- and sex-matched healthy individuals with negative EBV serology (IgM/IgG) and no history of malignancy.

Data collection and laboratory procedures

Demographic and clinical data

Data regarding age, gender, and residency were gathered through structured interviews and medical records. Comprehensive histopathological subtype information (such as Hodgkin lymphoma, Burkitt lymphoma, and DLBCL) was not accessible for all patients in the clinical records; consequently, a subtype-specific analysis could not be conducted.

Serological testing

EBV serology was evaluated by detecting IgM and IgG antibodies using enzyme-linked immunosorbent assay (ELISA) kits from MyBioSource (USA), according to the manufacturer's protocols (IgM: Cat# MBS029816; IgG: Cat# MBS285442). ELISA is a sensitive and validated method for diagnosing EBV serologically [20]. According to manufacturer data, both kits demonstrate sensitivities >95% and specificities >97%. Positivity was determined using the manufacturer-defined index values (≥1.1 = positive, 0.9–1.1 = equivocal, <0.9 = negative). All samples were analyzed in duplicate, and internal quality controls supplied with each kit were included on every assay plate. Laboratory personnel performing the ELISA assays were blinded to case/control status to minimize measurement bias.

Cytokine measurement

Serum levels of IL-18 and IL-32 were assessed using commercially available ELISA kits from MyBioSource (USA) (IL-18: Cat# MBS281497; IL-32: Cat# MBS580104).

Classification as positive or negative was determined based on kit-specific cutoffs. These cytokines play a crucial role as inflammatory mediators in viral pathogenesis and lymphoproliferative disorders [21, 22]. The manufacturer reports assay sensitivities of 4.8 pg/mL for IL-18 and 9.38 pg/mL for IL-32, with specificities >95% and no notable cross-reactivity. All samples were run in duplicate with internal low- and high-control wells. Technicians conducting cytokine measurements were blinded to participant group allocation.

MicroRNA-155 expression quantification

Peripheral blood samples were collected in EDTA tubes, and total RNA was extracted using the miRNeasy Mini Kit (Qiagen, Germany). Quantitative reverse transcription polymerase chain reaction (qRT-PCR) was conducted using the miScript SYBR Green PCR Kit (Qiagen, Germany) according to the manufacturer's instructions. Serum miR-155 levels were quantified using an absolute quantification method based on a standard curve provided by the kit, with results reported directly in ng/mL. Following MIQE recommendations [23, 24], an internal reaction control included in the assay ensured amplification quality; however, no endogenous reference gene was necessary for normalization. Raw Ct values were monitored to ensure amplification efficiency and reaction quality; however, they were not used for ΔCt or relative quantification because the assay followed an absolute quantification protocol. The optimal diagnostic cut-off value of ≥1.11 ng/mL was established based on ROC curve analysis.

Statistical analysis

- The Shapiro-Wilk test was employed to evaluate the normality of the data.
- Mann-Whitney U (two groups) were utilized to compare miR-155 levels among different groups.
- Chi-square tests were conducted to examine associations between categorical variables and miR-155 positivity.
- Binary logistic regression was performed to identify predictors of elevated miR-155 levels, reporting both crude odds ratios (ORs) and adjusted odds ratios (AORs) with 95% confidence intervals.
- Receiver Operating Characteristic (ROC) curve analysis was carried out to evaluate the diagnostic performance of miR-155, with the Area Under the Curve (AUC) calculated to determine sensitivity and specificity.
- All analyses were performed using SPSS version 27, with a p-value of less than 0.05 considered statistically significant.

Ethical considerations

The study received approval from the Technical Medical Institute, Kirkuk Northern Technical University, Ministry of Higher Education and Scientific Research, under approval IRB 73/21/11-2024. Written informed consent was obtained from the guardians of all participants.

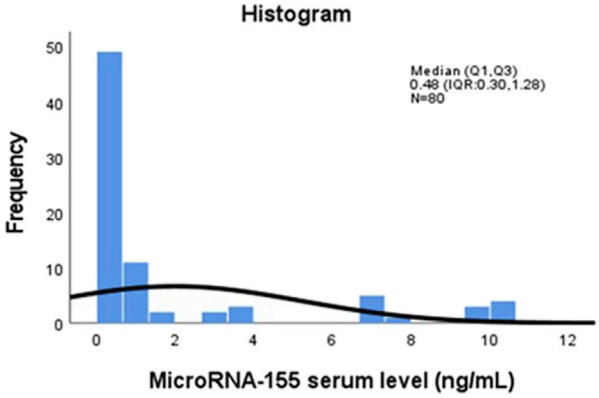

FIGURE 1
Distribution of serum MicroRNA-155 (miR-155) levels (ng/mL) among study participants (n = 80). The histogram displays the distribution of serum miR-155 concentrations measured by qRT-PCR. The x-axis represents serum miR-155 levels in ng/mL, and the y-axis represents the frequency of observations across the study population (n = 80).

Results

A total of 80 participants were included in this study, comprising 40 young lymphoma patients with serological evidence of active EBV infection and 40 healthy controls matched for age and sex. The overall mean age of the study population was 13.19 ± 2.51 years (range: 8–17), with a median age of 13 years (IQR: 11–15), and 55% of the participants were male. Demographic, serological, and molecular characteristics were analyzed to assess serum microRNA-155 (miR-155) expression and its associations with EBV serological markers and proinflammatory cytokines. Figure 1 illustrates the distribution of serum miR-155 levels (ng/mL) among all participants. The histogram reveals significant variability in expression, with some individuals displaying much higher concentrations of miR-155. This visualization emphasizes the differences in miR-155 levels throughout the study population.

Table 1 presented a comparison of miR-155 expression between patients with lymphoma patients with serological evidence of active EBV infection and healthy controls. Lymphoma patients demonstrated a significantly median miR-155 expression level (1.13 ng/mL) compared to healthy controls (0.43 ng/mL), with a wide interquartile range and a maximum value exceeding 10 ng/mL. This difference was statistically significant (p = 0.012).

Table 2 summarizes the association between demographic and clinical variables and miR-155 positivity, defined as levels

TABLE 1 Comparison of microRNA-155 expression levels between lymphoma patients with serological evidence of active EBV infection and healthy controls (n = 80).

Study groups	microRNA-155 (n = 80)				
	n	Median (Q1, Q3[a])	Minimum	Maximum	P-value
Healthy controls	40	0.43 (0.29, 0.61)	0.11	0.77	0.012[b]
Patient groups	40	1.13 (0.32, 7.22)	0.12	10.53	
Total	80	0.48 (0.30, 1.28)	0.11	10.53	

[a]Q1 is quantile one and, Q3 is quantile three.
[b]P value obtained from Mann-Whitney Test.

TABLE 2 Association of participant demographics and clinical characteristics by microRNA-155 positivity status (n = 80).

Variables	Total (%)	Negative microRNA155 n (%)[a]	Positive microRNA155 n (%)	P-value[b]
Total sample	80	60 (75.0)	20 (25.0)	
Gender Female Male	36 (45.0) 44 (55.0)	28 (77.8) 32 (72.7)	8 (22.2) 12 (27.3)	0.004
Age group (years) (mean ± SD) 8–12 13–17	13.19 ± 2.51 32 (40.0) 48 (60.0)	13.27 ± 2.43 23(71.9) 37 (77.1)	13.00 ± 2.71 9 (28.1) 11 (22.9)	0.598
Residency Rural Urban	47 (58.8) 33 (41.3)	35 (74.5) 25 (75.8)	12 (25.5) 8 (24.2)	0.896
EVBIgM Negative Positive	41 (51.2) 39 (48.8)	41 (100.0) 19 (48.7)	0 (0.0) 20 (51.3)	<0.001
EVBIgG Negative Positive	66 (82.5) 14 (17.5)	51 (77.3) 9 (64.3)	15 (22.7) 5 (35.7)	0.308
Interleukin-18 Negative Positive	67 (83.8) 13 (16.3)	55 (82.1) 5 (38.5)	12 (17.9) 8 (61.5)	0.001
Interleukin-32 Negative Positive	41 (51.2) 39 (48.8)	40 (97.6) 20 (51.3)	1 (2.4) 19 (48.7)	<0.001

[a]Frequency (%).
[b]Chi-Square Tests.

of ≥1.11 ng/mL. The dichotomous analysis (miR-155 positive vs. negative) revealed several significant relationships.

Males exhibited a higher rate of miR-155 positivity (27.3%) compared to females (22.2%), and this difference was statistically significant ($p = 0.004$). A statistically significant association was also noted between EBV IgM positivity and miR-155 positivity ($p < 0.001$); all IgM-negative participants were miR-155 negative, whereas 51.3% of IgM-positive individuals were miR-155 positive.

Similarly, positivity for IL-18 and IL-32 showed statistically significant association with miR-155 positivity ($p = 0.001$ and $p < 0.001$, respectively). These findings suggest that elevated miR-155 levels are more closely related to EBV serological activity and inflammatory cytokine expression rather than demographic factors.

No significant associations were found for age or residency, indicating that the variability in miR-155 levels within this cohort is primarily influenced by immunological factors rather than demographic characteristics.

Table 3 presented a comparison of median miR-155 levels across subgroups (non-parametric analysis) and explores subgroup differences using continuous miR-155 values.

In terms of gender, males exhibited significantly higher median miR-155 expression than females ($p = 0.006$).

TABLE 3 Comparison of microRNA-155 expression levels across demographic and laboratory subgroups (n = 80).

Variables	microRNA-155 (n = 80)				
	n	Median (Q1, Q3)[a]	Minimum	Maximum	P-value
Gender Female Male	36 44	0.50 (0.25, 0.74) 0.45 (0.31, 1.49)	0.11 0.11	10.53 10.53	0.006[b]
Age group (years) 8–12 13–17	32 48	0.50 (0.32, 3.19) 0.47 (0.28, 0.75)	0.12 0.11	10.46 10.40	0.576
Residency Rural Urban	47 33	0.55 (0.30, 1.16) 0.47 (0.31, 0.74)	0.11 0.11	10.53 9.85	0.594
EVBIgM Negative Positive	41 39	0.43 (0.29, 0.61) 1.12 (0.32, 7.22)	0.11 0.11	0.77 10.53	0.004
EVBIgG Negative Positive	66 14	0.51 (0.30, 0.77) 0.39 (0.17, 3.19)	0.11 0.12	10.46 10.53	0.785
Interleukin-18 Negative Positive	67 13	0.44 (0.28, 0.72) 3.98 (0.67, 7.21)	0.11 0.11	10.46 10.53	0.008
Interleukin-32 Negative Positive	41 39	0.44 (0.30, 0.62) 0.77 (0.32, 7.20)	0.11 0.11	10.40 10.53	0.031

[a]Q1 is quantile one and, Q3 is quantile three.
[b]P value obtained from Mann-Whitney test.

A notable difference was observed between IgM-negative individuals (0.43 ng/mL) and IgM-positive individuals (1.12 ng/mL), with a p-value of 0.004.

Both interleukin-18 and IL-32 showed significant associations with miR-155 levels ($p = 0.008$ and $p = 0.031$, respectively), with particularly high miR-155 levels found in IL-18-positive individuals (median 3.98).

No significant differences were noted for age groups or residency, indicating that biological factors related to inflammation and infection are the primary drivers of miR-155 expression.

The binary logistic regression analysis for predictors of elevated miR-155 expression (≥1.11 ng/mL) is presented in Table 4. The model identified IL-32 positivity as a good predictor of high miR-155 levels, with a crude odds ratio (OR) of 18.01 and an adjusted odds ratio (AOR) of 19.02 (95% CI: 7.72–36.92, $p = 0.001$). This association indicates that IL-32 is closely linked to elevated miR-155 expression in this cohort.

IL-18 positivity was also significantly associated with higher miR-155 levels in univariate analysis (OR = 7.33, $p = 0.002$), but it did not remain significant in the final multivariable model. This may reflect biological overlap between IL-18 and IL-32 pathways or limited statistical power for multiple predictors.

The ROC curve illustrating the diagnostic performance of serum miR-155 in distinguishing lymphoma patients with serological evidence of EBV infection from healthy controls is shown in Figure 2. The analysis yielded an Area Under the Curve (AUC) of 0.87 (95% CI: 0.77–0.94, $p < 0.001$), demonstrating good ability to differentiate between the two groups. Bootstrap cross-validation using 1,000 resamples produced a bias-corrected AUC of approximately 0.87, confirming the robustness of the ROC estimate. Using a cut-off value of ≥1.11 ng/mL, miR-155 demonstrated a sensitivity of 87% and a specificity of 90%. These findings suggest that serum miR-155 may have potential utility as a non-invasive marker for identifying EBV-associated lymphoma risk, although validation in larger and independent cohorts is required.

Discussion

This study examined serum microRNA-155 (miR-155) expression and its associations with Epstein–Barr virus (EBV) serological markers and proinflammatory cytokines (IL-18 and IL-32) in young lymphoma patients with evidence of active EBV infection. Our results indicate that serum miR-155 levels were significantly higher in patients than in healthy controls, suggesting that miR-155 may serve as a marker of EBV-

TABLE 4 Predictors of elevated microRNA-155 expression among study participants: Logistic Regression Analysis (n = 80).

Variables	microRNA-155 (n = 80)				
	n	OR (95% CI)[a]	P-value	AOR (95% CI)[b]	P-value
Gender Female Male	36 44	Ref. 1.31 (0.47–3.67)	0.004	3.02 (0.63–11.43)	0.022
Age group (years) 8–12 13–17	32 48	Ref. 0.76 (0.27–2.11)	0.599	-	-
Residency Rural Urban	47 33	Ref. 0.93 (0.33–2.62)	0.933	-	-
EVBIgM Negative Positive	41 39	Ref. 1.05(0.49–3.59)	0.060	-	-
EVBIgG Negative Positive	66 14	Ref. 1.37 (0.54–3.53)	0.505	-	-
Interleukin-18 Negative Positive	67 13	Ref. 7.33 (2.03–26.38)	0.002	-	-
Interleukin-32 Negative Positive	41 39	Ref. 18.01 (4.74–30.56)	0.001	19.02 (7.72–36.92)	0.001

[a]Crude odds ratio obtains from binary logistic regression.
[b]Adjusted odds ratio obtains from Forward Stepwise (Likelihood Ratio).

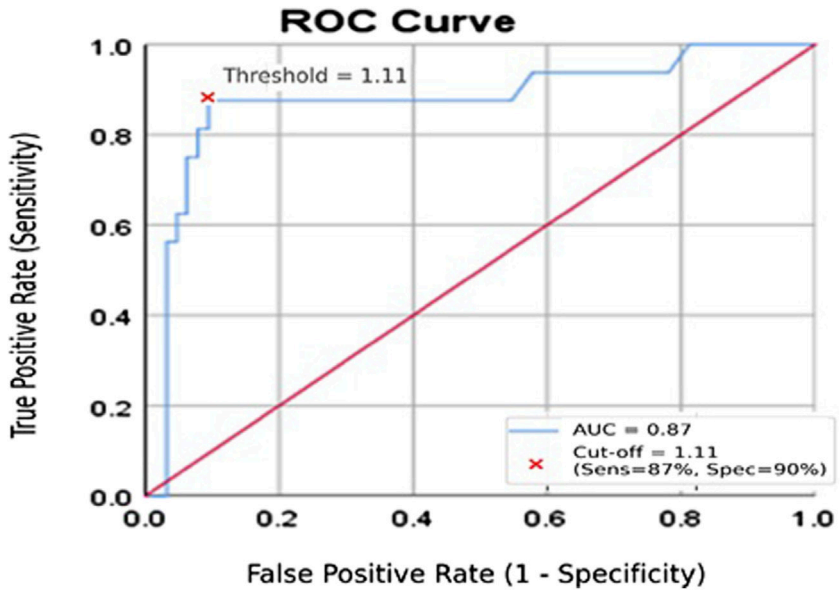

FIGURE 2
Receiver operating characteristic (ROC) curve for serum miR-155 in distinguishing lymphoma patients from healthy controls. The ROC curve depicts the diagnostic performance of serum miR-155 (ng/mL). The y-axis represents sensitivity, and the x-axis represents 1 – specificity. The analysis yielded an AUC of 0.87, indicating good discriminative ability.

related immune activity and systemic inflammation in this group.

In line with earlier reports that identify miR-155 as an oncogenic and immunoregulatory microRNA commonly upregulated in B-cell malignancies [7, 8], the median miR-155 concentration was significantly higher in the patient group. miR-155 has been linked to oncogenic processes through the regulation of pathways such as NF-κB, PI3K/AKT, and JAK/STAT [8, 9]. However, our findings are associative and do not establish a mechanistic role in the development of lymphoma.

A notable finding in this study was the statistically significant association between miR-155 overexpression and EBV IgM positivity, suggesting that elevated miR-155 may correlate with an active or recent EBV serological response. Experimental studies have demonstrated that EBV latent proteins—especially latent membrane protein-1 (LMP1)—activate NF-κB signaling and enhance the transcription of the BIC gene, which produces miR-155 [25, 26]. While these mechanisms are biologically plausible, this study cannot determine whether EBV directly induces miR-155 expression in tumor tissue, as gold-standard tissue-based confirmation methods (such as EBER-ISH or LMP1 IHC) were not employed.

Additionally, significant correlations were observed between elevated miR-155 levels and positivity for IL-18 and IL-32. Both cytokines play key roles in mediating inflammatory and antiviral immune responses. IL-18 enhances Th1-type immunity and activates MyD88-dependent NF-κB and STAT4 signaling [12, 27], while IL-32 stimulates the NF-κB, AP-1, and p38 MAPK pathways [13, 28, 29]. These signaling pathways have been implicated in the regulation of miR-155 expression. Although these findings suggest an association between inflammatory activation and increased miR-155 levels, they remain correlational, as functional experiments were not included in the current study design.

The associations observed between miR-155 expression and IL-18/IL-32 positivity may reflect previously described mechanistic interactions between cytokine-driven inflammatory signaling and the transcriptional regulation of miR-155. IL-18 activates NF-κB and STAT4 through MyD88-dependent pathways [12, 27], while IL-32 induces NF-κB, AP-1, and p38 MAPK activation [28, 29], and has been reported to enhance miR-155 expression via JAK1-dependent mechanisms [13]. These cytokine-driven pathways intersect with EBV latency-associated signaling: EBV latent proteins like LMP1 and EBNA2 activate NF-κB, AP-1, and JAK/STAT pathways [25, 26], and LMP1 can increase miR-155 transcription through BIC gene enhancers [9]. Collectively, these findings provide a biologically plausible framework that may explain the observed associations, although our study did not directly evaluate these mechanisms. Our findings are therefore consistent with previously described EBV- and cytokine-mediated regulatory pathways, but they do not establish mechanistic causality in this cohort. Future studies incorporating *in-vitro* LMP1/EBNA2 functional assays or analysis of EBV latency transcripts in tumor tissue are needed to experimentally validate these pathways.

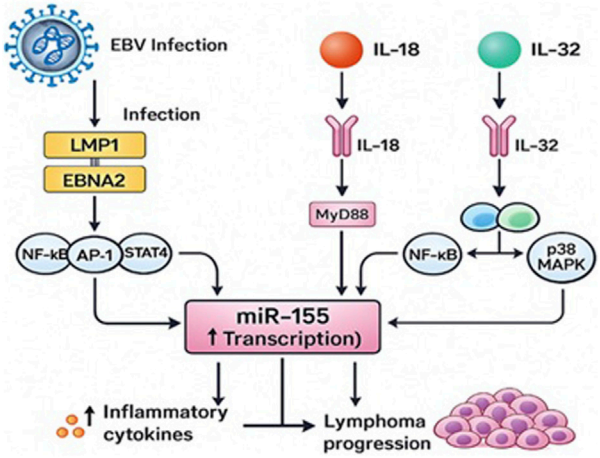

FIGURE 3
Proposed Mechanisms Linking EBV Infection, IL-18 and IL-32 Signaling, and miR-155 Upregulation in Young Lymphoma Patients.

The conceptual model presented in Figure 3 integrates previously reported mechanistic data regarding EBV-related signaling and cytokine-mediated regulation of miR-155. This diagram serves as a theoretical synthesis based on existing literature [9, 10, 25, 26, 29], rather than as direct evidence from this cohort.

Multivariate analysis identified IL-32 positivity as a good independent predictor of elevated miR-155 expression (AOR = 19.02), highlighting the robust association between IL-32 and miR-155 in this cohort. Male sex also remained independently associated with elevated miR-155 expression (AOR = 3.02, p = 0.022). While the biological basis is unclear, prior studies have reported gender-based differences in immune responses and microRNA regulation [30], which may contribute to this finding. However, given the modest sample size and the absence of lymphoma subtype data, this sex-related association should be interpreted cautiously and considered exploratory.

Receiver operating characteristic (ROC) analysis revealed that serum miR-155 has good discriminatory ability (AUC = 0.87) for distinguishing patients from controls. With a cutoff value of ≥1.11 ng/mL, miR-155 effectively separated the groups, in line with the sensitivity and specificity estimates derived from the ROC analysis. These results are consistent with earlier studies suggesting that miR-155 could be a potential biomarker for hematologic malignancies [7, 31]. However, because EBV

status in tumor tissue was not validated and the cohort size was relatively small, diagnostic interpretations should be approached with caution.

Overall, the findings suggest that elevated serum miR-155 is linked to EBV serological activity and systemic inflammation, particularly with regard to IL-18 and IL-32, in young lymphoma patients. miR-155 may serve as a promising non-invasive biomarker indicative of EBV-related immune activation. However, confirmation of EBV in tissue samples and functional studies are necessary to establish whether EBV directly causes miR-155 dysregulation in lymphoma.

Limitations

Although this study presents valuable findings, several limitations must be acknowledged. First, the cross-sectional design prevents assessment of temporal changes in miR-155 expression or its behavior during treatment or disease progression. Second, although the sample size was adequate to detect significant associations, it limits generalizability and reduces statistical power for subgroup analyses. Third, our cytokine analysis focused only on IL-18 and IL-32; evaluating a broader cytokine profile would have provided a more comprehensive view of the inflammatory microenvironment.

A major limitation is the absence of tissue-based confirmation of EBV tumor positivity. EBV status was determined solely by serology (IgM/IgG), as diagnostic tumor blocks were not available for EBER *in situ* hybridization, LMP1 immunohistochemistry, or EBV DNA PCR. Therefore, the cohort should be interpreted as lymphoma patients with serological evidence of active EBV infection, and not as confirmed EBV-positive lymphomas.

Another limitation is the lack of complete histopathological subtype information. Because subtype details were inconsistently documented in the clinical records, we were unable to stratify miR-155 expression according to lymphoma subtype, which may differ in biology and EBV association. Future studies should incorporate comprehensive subtype classification.

Finally, the mechanistic interpretations provided in this study are based on correlational findings. Although the observed associations are consistent with known EBV- and cytokine-related signaling pathways, functional experiments were not performed. Future longitudinal and mechanistic studies are required to validate these pathways and determine their clinical relevance. The ROC analysis was conducted in a single dataset without external validation; although bootstrap resampling supported the stability of the AUC, larger multicenter cohorts are required to validate the discriminative performance of miR-155.

Conclusion

This study demonstrates that serum microRNA-155 (miR-155) is significantly elevated in young lymphoma patients with serological evidence of active EBV infection. miR-155 levels showed statistically significant association with EBV IgM positivity and with the proinflammatory cytokines IL-18 and IL-32, with IL-32 emerging as a good independent predictor of elevated miR-155. These findings suggest that heightened inflammatory signaling may contribute to the increased miR-155 expression observed in this cohort.

Serum miR-155 also demonstrated good discriminatory performance in distinguishing patients from healthy controls in this dataset. While this indicates potential utility as a non-invasive marker of EBV-related immune activation, it should not be interpreted as a diagnostic test because EBV tumor positivity was not confirmed using tissue-based methods. Larger studies with tissue confirmation and external validation are required to establish its diagnostic or prognostic value.

Overall, the results highlight a relevant relationship between EBV serological activity, inflammatory cytokines, and miR-155 expression in young lymphoma patients, supporting further investigation of miR-155 within EBV-associated immune and oncogenic pathways.

Author contributions

LM: Supervision, Writing – review and editing, Visualization, Validation and Methodology. PS: Writing – review and editing, Visualization, and Validation. AQ: Writing – review and editing, and Validation. LM: Writing – original draft, Methodology, Conceptualization, Data curation, Formal analysis, and Project administration.

Data availability

The data generated in this study consist of targeted qRT-PCR measurements of a single microRNA (miR-155) and associated clinical variables from human participants. These data are not suitable for deposition in public gene-expression repositories and are not publicly available due to ethical and privacy restrictions. De-identified data supporting the findings of this study are available from the corresponding author upon reasonable request.

Ethics statement

Ethics approval and consent to participate Ethical approval has been obtained from the Iraqi Research Ethics Committee at the Kirkuk Northern Technical University, Ministry of Higher Education and Scientific

Research, Iraq, IRB 73/21/11-2024. The studies were conducted in accordance with the local legislation and institutional requirements. The participants provided their written informed consent to participate in this study.

Funding

The author(s) declared that financial support was not received for this work and/or its publication.

Acknowledgements

The authors wish to express their sincere gratitude to the Technical Medical Institute at Northern Technical University and the Public Health Department at the Teaching Oncology Hospital in Baghdad, Iraq for their dedication and efforts.

Conflict of interest

The author(s) declared no potential conflicts of interest with respect to the research, authorship, and/or publication of this article.

Generative AI statement

The author(s) declared that generative AI was used in the creation of this manuscript. The authors used Poe (Quora, 2025) to assist with language refinement and summarization during manuscript preparation. The authors reviewed and approved all generated content and are fully responsible for the final text.

Any alternative text (alt text) provided alongside figures in this article has been generated by Frontiers with the support of artificial intelligence and reasonable efforts have been made to ensure accuracy, including review by the authors wherever possible. If you identify any issues, please contact us.

References

1. Solares S, León J, García-Gutiérrez L. The functional interaction between epstein-barr virus and MYC in the pathogenesis of burkitt lymphoma. *Cancers (Basel)* (2024) **16**(24):4212. doi:10.3390/cancers16244212

2. Bednarska K, Chowdhury R, Tobin JWD, Swain F, Keane C, Boyle S, et al. Epstein-barr virus-associated lymphomas decoded. *Br J Haematol* (2024) **204**(2): 415–33. doi:10.1111/bjh.19255

3. Ihsan EA, Mohammed LM, Ali WM. Prevalence of epstein-barr virus among hemodialysis patients in Kirkuk city. *NTU J Pure Sci* (2023) **2**(4):17–22. doi:10.56286/ntujps.v2i4

4. Ihsan EA, Mohammed LM, Ali WM. Correlation of interleukin-10 and interleukin-8 with cytomegalovirus. *Med J Babylon* (2024) **21**:S195–8. doi:10.4103/mjbl.mjbl_780_23

5. Huang W, Bai L, Tang H. Epstein-barr virus infection: the micro and macro worlds. *Virol J* (2023) **20**(1):220. doi:10.1186/s12985-023-02187-9

6. Teshome S, Zealiyas K, Abubeker A, Tadesse F, Balakrishna J, Weigel C, et al. Detection and quantification of the epstein-barr virus in lymphoma patients from Ethiopia: molecular and serological approaches. *Microorganisms* (2023) **11**:2606. doi:10.3390/microorganisms11102606

7. Koumpis E, Georgoulis V, Papathanasiou K, Papoudou-Bai A, Kanavaros P, Kolettas E, et al. The role of microRNA-155 as a biomarker in diffuse large B-Cell lymphoma. *Biomedicines* (2024) **12**(12):2658. doi:10.3390/biomedicines12122658

8. Wang J, Wang Q, Guan Y, Sun Y, Wang X, Lively K, et al. Breast cancer cell-derived microRNA-155 suppresses tumor progression via enhancing immune cell recruitment and antitumor function. *J Clin Invest* (2022) **132**(19):e157248. doi:10.1172/JCI157248

9. Wood CD, Carvell T, Gunnell A, Ojeniyi OO, Osborne C, West MJ. Enhancer control of MicroRNA miR-155 expression in epstein-barr virus-infected B cells. *J Virol* (2018) **92**(19):e00716–18. doi:10.1128/JVI.00716-18

10. Kurowska-Stolarska M, Alivernini S, Ballantine LE, Asquith DL, Millar NL, Gilchrist DS, et al. MicroRNA-155 as a proinflammatory regulator in clinical and experimental arthritis. *Proc Natl Acad Sci U S A* (2011) **108**(27):11193–8. doi:10.1073/pnas.1019536108

11. Tsotridou E, Hatzipantelis E. Epstein-barr infection, hodgkin's lymphoma, and the immune System: insights into the molecular mechanisms facilitating immune evasion. *Cancers (Basel)* (2025) **17**(9):1481. doi:10.3390/cancers17091481

12. Zalinger ZB, Elliott R, Weiss SR. Role of the inflammasome-related cytokines Il-1 and Il-18 during infection with murine coronavirus. *J Neurovirol* (2017) **23**(6): 845–54. doi:10.1007/s13365-017-0574-4

13. Chang J, Zhou B, Wei Z, Luo Y. IL-32 promotes the occurrence of atopic dermatitis by activating the JAK1/microRNA-155 axis. *J Transl Med* (2022) **20**(1): 207. doi:10.1186/s12967-022-03375-x

14. Huen K, Lizarraga D, Kogut K, Eskenazi B, Holland N. Age-related differences in miRNA expression in Mexican-American newborns and children. *Int J Environ Res Public Health* (2019) **16**(4):524. doi:10.3390/ijerph16040524

15. Yu HR, Hsu TY, Huang HC, Kuo HC, Li SC, Yang KD, et al. Comparison of the functional microRNA expression in immune cell subsets of neonates and adults. *Front Immunol* (2016) **7**:615. doi:10.3389/fimmu.2016.00615

16. Kuchen S, Resch W, Yamane A, Kuo N, Li Z, Chakraborty T, et al. Regulation of microRNA expression and abundance during lymphopoiesis. *Immunity* (2010) **32**(6):828–39. doi:10.1016/j.immuni.2010.05.009

17. Lwanga SK, Lemeshow S. Sample size determination in health studies: a practical manual. Geneva, Switzerland: World Health Organization (1992). Available online at: https://lib.umku.ac.id/wp-content/uploads/2022/06/Sample-size-determination-in-health-studies-a-practical-manual.pdf (Accessed June 17, 2025).

18. Eis PS, Tam W, Sun L, Chadburn A, Li Z, Gomez MF, et al. Accumulation of miR-155 and BIC RNA in human B cell lymphomas. *Proc Natl Acad Sci U S A* (2005) **102**(10):3627–32. doi:10.1073/pnas.0500613102

19. Rai D, Karanti S, Jung I, Dahia PL, Aguiar RC. Coordinated expression of microRNA-155 and predicted target genes in diffuse large B-cell lymphoma. *Cancer Genet Cytogenet* (2008) **181**(1):8–15. doi:10.1016/j.cancergencyto.2007.10.008

20. Human Epstein-barr virus IgG (EBv-IgG) ELISA kit, *MyBioSource,* San Diego (CA), USA (2025). Available online at: https://www.mybiosource.com/ebv-igg-human-elisa-kits/epstein-barr-virus-igg/285442 (Accessed June 17, 2025).

21. Human IL-18(Interleukin 18) ELISA kit (E-EL-H0253). Elabscience Biotechnology Co., Ltd., Wuhan, Hubei, China (2025). Available online at: https://www.elabscience.com/p/human-il-18-interleukin-18-elisa-kit–e-el-h0253 (Accessed June 17, 2025).

22. Human IL-32(Interleukin 32) ELISA kit (E-EL-H0216). Elabscience Biotechnology Co., Ltd., Wuhan, Hubei, China (2025) Available online at: https://www.elabscience.com/p/human-il-32-interleukin-32-elisa-kit–e-el-h0216 (Accessed June 17, 2025).

23. *miRNeasy kit for miRNA purification*. Hilden, Germany: QIAGEN N.V. (2025). Available online at: https://www.qiagen.com/us/products/discovery-and-translational-research/dna-rna-purification/rna-purification/mirna/mirneasy-kits (Accessed June 17, 2025).

24. *Reverse transcription & cDNA synthesis for qPCR*, (2025). Hilden, Germany: QIAGEN N.V. Available online at: https://www.qiagen.com/us/product-categories/discovery-and-translational-research/pcr-qpcr-dpcr/real-time-pcr-enzymes-and-kits/reverse-transcription-cdna-synthesis-qpcr (Accessed June 17, 2025).

25. Cheerathodi MR, Meckes DG, Jr. The epstein-barr virus LMP1 interactome: biological implications and therapeutic targets. *Future Virol* (2018) **13**(12):863–87. doi:10.2217/fvl-2018-0120

26. Zhao Y, Zhang Q, Zhang B, Dai Y, Gao Y, Li C, et al. Epstein-barr viruses: their immune evasion strategies and implications for autoimmune diseases. *Int J Mol Sci* (2024) **25**(15):8160. doi:10.3390/ijms25158160

27. Dinarello CA. Overview of the IL-1 family in innate inflammation and acquired immunity. *Immunol Rev* (2018) **281**(1):8–27. doi:10.1111/imr.12621

28. Meng D, Dong H, Wang C, Zang R, Wang J. Role of interleukin-32 in cancer progression. *Oncol Lett* (2023) **27**(2):54. doi:10.3892/ol.2023.14187

29. Kim SH, Han SY, Azam T, Yoon DY, Dinarello CA. Interleukin-32: a cytokine and inducer of TNFalpha. *Immunity* (2005) **22**(1):131–42. doi:10.1016/j.immuni.2004.12.003

30. Sharma S, Eghbali M. Influence of sex differences on microRNA gene regulation in disease. *Biol Sex Differ* (2014) **5**(1):3. doi:10.1186/2042-6410-5-3

31. Imig J, Motsch N, Zhu JY, Barth S, Okoniewski M, Reineke T, et al. microRNA profiling in epstein-barr virus-associated B-cell lymphoma. *Nucleic Acids Res* (2011) **39**(5):1880–93. doi:10.1093/nar/gkq1043

EBM Experimental Biology and Medicine

TYPE Original Research
PUBLISHED 14 January 2026
DOI 10.3389/ebm.2025.10849

OPEN ACCESS

*CORRESPONDENCE
Mustafa Abdulkareem Salman,
salman@uodiyala.edu.iq

RECEIVED 03 October 2025
REVISED 12 December 2025
ACCEPTED 31 December 2025
PUBLISHED 14 January 2026

CITATION
Salman MA, Jameel TY, Ayvaz A and Abdullah AR (2026) The correlation between pro- and anti-inflammatory cytokines and anti-spike IgG antibody responses induced by the SARS-CoV-2 coronavirus vaccine.
Exp. Biol. Med. 250:10849.
doi: 10.3389/ebm.2025.10849

The correlation between pro- and anti-inflammatory cytokines and anti-spike IgG antibody responses induced by the SARS-CoV-2 coronavirus vaccine

Mustafa Abdulkareem Salman[1,2]*, Thowiba Yousif Jameel[1,3], Abdurrahman Ayvaz[4] and Ahmed Rushdi Abdullah[5]

[1]Department of Biology, Graduate School of Natural and Applied Science, Erciyes University, Kayseri, Türkiye, [2]Department of Anatomy, College of Medicine, University of Diyala, Diyala, Iraq, [3]Department of Biology, Faculty of Science, Tikrit University, Tikrit, Iraq, [4]Department of Biology, Faculty of Science, Erciyes University, Kayseri, Türkiye, [5]Head of the Microbiology Department, Medical College, Aliraqia University, Baghdad, Iraq

Abstract

Even with the development of the Pfizer-BioNTech BNT162b2 vaccine, which provides protection against COVID-19 and demonstrates high efficacy in generating immune responses, the complexities of the dynamics linking pro- and anti-inflammatory cytokine profiles with anti-spike IgG production remain unclear. The study aims to elucidate these immune dynamics after vaccination. This prospective cohort research was done at the University of Diyala from January 2022 to January 2023, evaluating the immunological response to the Pfizer-BNT162b2 mRNA vaccine in 180 healthy students. Pro- and anti-inflammatory cytokines and anti-spike IgG antibodies were measured before vaccination, 1 month after the second dose, and 4 months after the second dose. Biomarkers were analyzed via ELISA and CRP assays. The study involved 180 healthy participants (80 males, 100 females; median age, 21 years; BMI, 25.7 kg/m^2). After the first Pfizer-BNT162b2 vaccine dose, the level of anti-spike IgG increased by 330-fold, and the levels of pro- and anti-inflammatory markers, such as IL-1β, IL-10, and CRP, increased significantly. Four months after the second dose, anti-spike IgG levels were 136-fold above baseline. Significant correlations emerged between cytokine and IgG levels, with anti-spike IgG/IL-10 ratios elevated and sustained over the long term. Pfizer-BNT162b2 vaccine elicits a significant immune response associated with changes in pro-inflammatory cytokines, and the interaction between these cytokines and anti-spike IgG suggests a potential role for immune regulation in

enhancing humoral immunity. Based on these findings, the IgG/IL-17 ratio may serve as a viable exploratory biomarker for assessing short- and medium-term vaccination efficacy.

KEYWORDS

anti-inflammatory, anti-spike IgG, BNT162b2 mRNA, Pfizer-BioNTech, pro-inflammatory

Impact statement

This study investigates the paradoxical interplay between pro- and anti-inflammatory cytokines and anti-spike IgG responses following administration of the Pfizer-BioNTech BNT162b2 vaccine. A prospective cohort of 180 healthy, unvaccinated medical students (median age: 21 years) was followed from January 2022 to January 2023. Cytokine and antibody levels were measured before vaccination, one month after the first dose, and four months after the second dose using ELISA and CRP assays. The first vaccine dose elicited a robust 330% increase in anti-spike IgG alongside significant elevations in both pro- and anti-inflammatory cytokines. Four months after the second dose, IgG levels remained 137.6% above baseline, with distinct correlations emerging between cytokine and antibody dynamics. Notably, anti-IgG/IL-10 ratios remained consistently elevated, suggesting a potential biomarker of durable immune response. These findings highlight the complex but clinically relevant relationships between cytokine regulation and antibody production, offering insights into immunological mechanisms underlying COVID-19 vaccination.

Introduction

The global community witnessed a comprehensive scientific response to the COVID-19 pandemic, characterized by the use of many technological platforms to develop viable vaccines. The Pfizer-BioNTech BNT162b2 vaccine was one of the first approved and most widely used vaccines globally [1]. This vaccine utilizes mRNA technology, which stimulates the immune system to produce the viral spike protein, leading to integrated humoral and cellular immune responses [2].

Studies indicate that mRNA vaccines initially activate innate immunity by increasing inflammatory cytokines such as IL-1β, IL-2, IL-8, IL-17, and IFN-γ. They also activate the non-cytokine inflammatory biomarker C-reactive protein (CRP). Thus, preparing the immune system to mount an effective adaptive response [3, 4]. These cytokines exhibit distinct temporal patterns post-vaccination, with some increasing in the first days and others peaking thereafter [4, 5]. Conversely, anti-inflammatory cytokines, such as IL-10 and IL-13, play a crucial regulatory role in reducing excessive inflammation and modulating immune system activity after vaccination [6, 7].

Although multiple investigations have elucidated the impact of the BNT162b2 vaccination on immune cell activation and antibody synthesis, the correlation between pro- and anti-inflammatory cytokine dynamics and anti-spike IgG levels remains ambiguous, especially in healthy young individuals. Comprehending the interplay among these immunological indicators is essential for evaluating the quality and durability of the immune response. From this standpoint, this study aims to evaluate changes in the inflammatory cytokines IL-1β, IL-2, IL-8, IL-17 and IFN-γ, and the anti-inflammatory cytokines IL-10 and IL-13, in addition to levels of anti-spik IgG, as well as to analyze the relationship between these immune changes after receiving the Pfizer-BNT162b2 mRNA vaccine in a group of healthy young people.

Materials and methods

Study design and participants

This prospective cohort study was conducted at the Postgraduate Research Laboratory, College of Medicine, University of Diyala, in Baqubah, Iraq, between January 2022 and January 2023. The authors interviewed each participant and explained the study's objective and protocol. A total of 460 students took part in the study. To ensure the reliability of our findings, we rigorously monitored participants through weekly follow-ups for 4 months, during which we assessed complete blood counts (CBC) and C-reactive protein (CRP) levels. This allowed us to detect and exclude participants with any signs of inflammation or infection, maintaining the integrity of the cohort and ensuring that the observed cytokine responses were specifically related to vaccination.

Before their participation, they underwent IgG/IgM testing using VIDAS® SARS-CoV-2 IgG & IgM (Specificity 100%, Sensitivity 99.6%, and Sensitivity) from bioMérieux company/FRANCH. To ensure that they were not previously infected or vaccinated. Among the 460 students initially screened before the study, after confirmatory testing to exclude prior SARS-CoV-2 infection or COVID-19 vaccination, 180 participants were identified as previously uninfected and unvaccinated. These individuals consented to participate in the current study and to receive two doses of the Pfizer-BNT162b2 mRNA vaccine under our supervision and follow-up, with their health monitored throughout the study period. Pro- and anti-

inflammatory cytokines were assessed before vaccination, 1 month after the second dose, and 4 months after the second dose. Informed consent was obtained from the participants to collect blood samples.

Infection monitoring during the study period

To ensure the exclusion of asymptomatic SARS-CoV-2 infection during the follow-up period, all participants underwent continuous assessment of their immune and overall health status after vaccination. Anti-nucleocapsid protein IgG antibodies were checked using the SARS-CoV-2 Nucleocapsid Protein IgG ELISA qualitative kit (Elabscience®) at post-vaccination follow-up points to detect any new natural infections that could not be caused by the Pfizer-BNT162b2 spike protein-only vaccine.

In addition, participants were followed up weekly through structured post-class meetings, during which they were clinically assessed for any symptoms consistent with COVID-19 infection, including fever, runny nose, fatigue, lethargy, headache, and increased sleepiness. Weekly blood samples were also collected in EDTA tubes for complete blood count (CBC) testing to monitor any hematological changes that might indicate infection. This integrated system of immunological, clinical, and laboratory monitoring made it possible to rule out the occurrence of new infections during the study period and to ensure that the measured immune responses were related only to vaccination without the influence of natural infection.

Inclusion and exclusion criteria

The eligible participants were adults aged 18–23 years, all genders, in general good health, with no history of acute (within 2 weeks) or chronic pathological conditions. Participants with a history of COVID-19 infection or who received the COVID-19 vaccine or had autoimmune diseases, e.g., systemic lupus erythematosus, and pregnant women were excluded from the study.

Vaccination of the participants

The Pfizer-BioNTech COVID-19 vaccine (Comirnaty® BNT162b2) is recommended in our community. It is an mRNA vaccine developed by Pfizer, Inc. (USA) and BioNTech SE (Germany). The primary vaccination series consisted of 2 doses, administered 21 days apart, each containing 0.3 mL of the mRNA vaccine. The vaccine is supplied as a preservative-free frozen suspension (0.45 mL) in multi dose vials. The reconstitution protocol involved adding 1.8 mL of sterile 0.9% sodium chloride solution to each vial. Post reconstitution, each vial provides six standard doses. Participants were asked to report any signs or symptoms that developed after vaccination, including pain at the injection site, fever, fatigue, headache, and excessive sleepiness.

Determination of biomarkers

Blood samples were obtained from all participants before vaccination and at 1 and 4 months' post-vaccination. The sera were separated by centrifugation at 1,000 × g for 10 min.

Anti-spike IgG antibodies were measured using the EPITOPE DIAGNOSTIC, INC (EDI) Quantitative SARS-CoV-2 Spike Protein IgG ELISA Kit, USA, according to the manufacturer's instructions. This assay was used to assess the quality and quantity of the anti-spike IgG response.

Pro-inflammatory cytokines, including IL-1β, IL-2, IL-8, IL-17, IFN-γ, and non-cytokine inflammatory biomarker CRP, as well as anti-inflammatory cytokines, including IL-10, and IL-13, were measured as biomarkers of the immune response. The interleukins (IL-1β, IL-2, IL-8, IL-10, IL-13, and IL-17) were quantified using ELISA kits from ELK Biotechnology Co. Ltd., Wuhan, China. The detection ranges were as follows: IL-1β, 7.82–500 pg/mL; IL-10, 0.15–800 pg/mL; IL-2, IL-8, IL-13, and IL-17, 15.63–1,000 pg/mL.

CRP levels were measured using a Cobas C-111 analyzer (Roche, Germany) according to the manufacturer's instructions.

Statistical analysis

The results are presented as numbers, percentages, medians, and interquartile ranges (Q1 and Q3). The significant differences between the data before and after vaccination were determined via Wilcoxon's paired signed rank test. The correlations between the included variables were determined via a two-tailed Spearman's correlation test. All statistical analyses were performed using IBM SPSS Statistics for Windows (version 26, IBM Corp., Chicago). A p-value of ≤0.05 is the cutoff for a significant value.

Results

A total of 180 healthy subjects (80 males and 100 females) with a median (interquartile range) age of 21 years (20 and 21.5) and a body mass index of 25.7 kg/m2 (24.3 and 26.6) were included.

The immune response to the first vaccination dose is characterized by significant increases in both pro-inflammatory and inflammatory biomarkers, as indicated in Table 1. Relative to the pre-vaccination baseline (0.21), the

TABLE 1 Baseline data of 180 participants vaccinated with two doses of Pfizer-BNT162b2 mRNA vaccine.

Variables	Before	After 1 month	After 4 months	P1	P2	P3
Age, year	21.0 (20.0, 21.5)					
Body mass index, kg/m^2	24.7 (24.3, 26.6)					
Anti-spike IgG antibody (DU/mL)	0.21 (0.08, 0.45)	69.3 (67.3, 73.4)	28.9 (25.3, 31.0)	<0.001	<0.001	<0.001
Interleukin 1β (pg/mL)	5.3 (4.4, 5.8)	316.2 (296.6, 348.2)	67.0 (60.1, 76.3)	<0.001	<0.001	<0.001
Interleukin 2 (pg/mL)	14.0 (11.3, 16.0)	540.1 (511.8, 613.3)	57.3 (51.7, 64.6)	<0.001	<0.001	<0.001
Interleukin 8 (pg/mL)	16.0 (13.2, 17.9)	611.1 (449.7, 707.2)	45.4 (35.2, 51.3)	<0.001	<0.001	<0.001
Interleukin 10 (pg/mL)	6.6 (4.9, 8.5)	349.4 (263.6, 398.6)	141.8 (109.8, 206.4)	<0.001	<0.001	<0.001
Interleukin 13 (pg/mL)	14.6 (12.3, 17.3)	481.7 (406.1, 515.2)	199.3 (117.0, 210.8)	<0.001	<0.001	<0.001
Interleukin 17 (pg/mL)	9.9 (8.3, 10.4)	349.6 (284.6, 427.4)	129.4 (103.3, 180.6)	<0.001	<0.001	<0.001
Interferon-γ (pg/mL)	11.7 (10.1, 12.6)	651.5 (585.7, 699.3)	208.6 (189.8, 216.6)	<0.001	<0.001	<0.001
C-reactive protein (mg/L)	0.82 (0.67, 0.91)	12.0 (10.5, 12.4)	2.4 (1.9, 2.8)	<0.001	<0.001	<0.001

The results are presented as median (Q1 and Q3). The P-value was calculated using Wilcoxon's paired signed rank test. P1: comparison before and after 1 month, P2: comparison between before and after 4 months, P3: comparison between after one and 4 months.

TABLE 2 Bivariate Spearman's correlations showed inter-relationships between pro-inflammatory, anti-inflammatory markers, and anti-immunoglobulin spike antibodies as a marker of immune response to mRNA vaccine after 1 month.

Biomarkers	IL10	IL13	INF-γ	IL1β	IL2	IL8	IL17	CRP
Anti-spike IgG	−0.231 (0.128)	0.043 (0.780)	−0.004 (0.977)	0.199 (0.189)	−0.001 (0.995)	−0.021 (0.892)	0.182 (0.23)	−0.064 (0.675)
IL10		−0.086 (0.574)	0.167 (0.274)	−0.307* (0.040)	0.213 (0.160)	−0.091 (0.552)	−0.190 (0.211)	−0.050 (0.744)
IL13			−0.041 (0.787)	−0.081 (0.599)	0.207 (0.172)	−0.028 (0.855)	−0.268 (0.072)	0.328* (0.028)
INF-γ				0.120 (0.432)	0.038 (0.805)	0.313* (0.036)	−0.005 (0.975)	−0.149 (0.328)
IL1β					−0.244 (0.106)	0.122 (0.426)	−0.016 (0.918)	−0.096 (0.529)
IL2						−0.091 (0.551)	0.027 (0.861)	0.071 (0.642)
IL8							0.208 (0.171)	0.013 (0.935)
IL17								0.060 (0.694)

The results are presented as a correlation factor (p-value). * Significant correlation. IL: interleukin, INF: interferon, and CRP: C-reactive protein.

anti-spike IgG level exhibited an approximately 330-fold increase at 1 month post-vaccination, reaching 69.3. C-reactive protein showed a 14.6-fold increase. The concentrations of the pro-inflammatory cytokines IL-1β, IL-2, IL-8, and IL-17 increased by 59.7-fold, 38.6-fold, 38.2-fold, and 35.3-fold, respectively. The anti-inflammatory markers IL-10, IL-13, and IFN-γ increased by 52.9-fold, 33-fold, and 55.7-fold, respectively.

Four months after the second vaccination, the immune response remained elevated: anti-spike IgG, IL-1β, IL-2, IL-8, IL-17, IL-10, IL-13, IFN-γ, and CRP exhibited increases of 136-fold, 12.6-fold, 4.1-fold, 2.8-fold, 13.1-fold, 21.5-fold, 13.7-fold, 17.8-fold, and 2.9-fold, respectively, relative to baseline. Anti-spike IgG antibodies do not correlate with pro-inflammatory or anti-inflammatory cytokines after the first vaccination dose. The anti-inflammatory cytokines were inconsistently and significantly correlated with the pro-inflammatory cytokines, with inverse correlations between IL-10 and IL-1β, IL-13 and CRP, and INF-γ and IL-8 4 months after the second vaccination, as indicated in Table 2.

The anti-spike IgG antibody level is significantly and directly correlated with the level of IL-17 (Figures 1A–C). The study demonstrated a strong positive correlation between interleukin-17 (IL-17) concentrations and anti-spike IgG levels at 1 month and 4 months after the second vaccine dose. The scatter plots in Figures 1A–C show the clustering of data points near the regression line. Figure 1A, represents the relationship between IL-17 concentrations and anti-spike IgG levels before vaccination, where the regression line indicates a negative association, as reflected by the coefficient of determination (R^2 = 0.200). This value represents a noticeable but weak

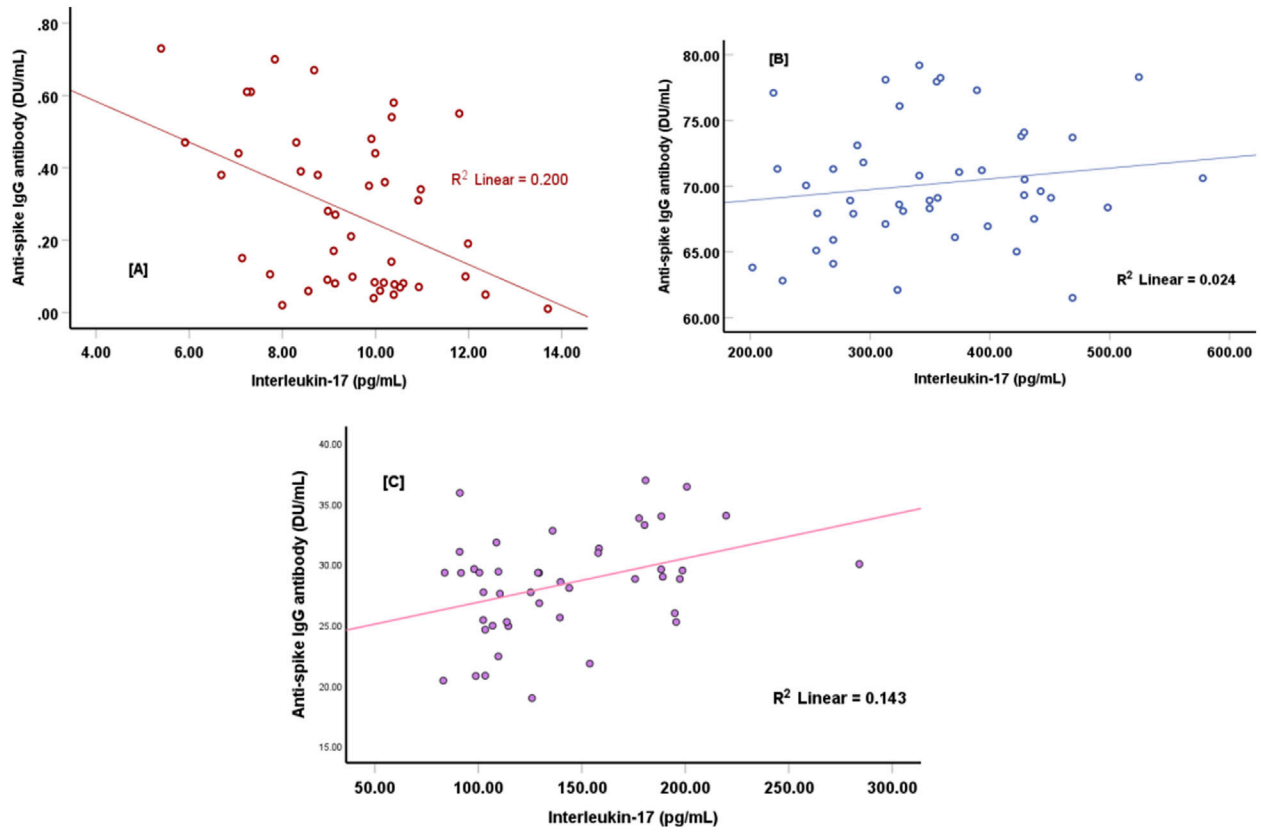

FIGURE 1
Correlations between anti-Spike-IgG antibody titers and interleukin-17 at baseline **(A)** (r = – 447, p < 0.001), after 1 month of the vaccination **(B)** (r = +0.182, p = 0.230), and after 4 months of the vaccination **(C)** (r = +0.337, p = 0.024).

negative relationship between IL-17 concentrations and anti-spike IgG levels. Additionally, Figure 1B, illustrates the positive relationship between IL-17 concentrations and anti-spike IgG levels 1 month after receiving the two COVID-19 vaccine doses. The regression line shows a moderate positive association, supported by the coefficient of determination (R^2 = 0.024).

Moreover, 4 months' post-vaccination, a strong positive correlation was observed between IL-17 concentrations and anti-spike IgG levels, as indicated by the higher coefficient of determination (R^2 = 0.143), as shown in Figure 1C.

An inverse and significant correlation was observed with IL-10 and IL-2, IL-13 and INF-γ, and IL-1β and IL-8. In contrast, significant direct correlations were observed between IL-13 and IL-2, and between INF-γ and IL-8 (Table 3). Interestingly, the ratio of anti-spike IgG antibody level to IL10 level was significantly higher than the baseline ratio and remained elevated after 4 months following the second vaccination dose (Table 4; Figure 3). The highest ratios were observed for CRP (Figure 2) Where Before vaccination, the IgG/CRP ratio was very low because antibodies were not present. At the same time, CRP levels were normal and low. One month after vaccination, the ratio rose significantly, reflecting a considerable increase in IgG relative to CRP. Four months later, the ratio increased further as IgG continued to mature and rise, along with an increase in CRP, followed by the pro-inflammatory cytokines IL8, IL2, and IL1β.

Discussion

The findings of the present study demonstrated that, after 1 month of immunization, both cytokine and anti-spike IgG antibody levels were higher and tended to decrease. The immune response to the Pfizer vaccine develops progressively with each dose. According to studies of all genders after the first dose, there is a measurable increase in antibody levels (IgG antibodies specific to the spike protein), providing partial immunity, primarily against severe disease [8]. This initial response usually peaks approximately 2–3 weeks after the first dose. Following the second dose, there was a significant increase in neutralizing antibody and IgG levels, with peak immunity occurring approximately 7–14 days after the second dose [9]. Additionally, the second dose triggers robust activation of T cells, which are crucial for long-term immunity and immune memory [10]. Over the next 3–6 months, antibody levels gradually

TABLE 3 Bivariate Spearman's correlations showed inter-relationships between pro-inflammatory, anti-inflammatory markers and anti-immunoglobulin spike antibodies as a marker of immune response to mRNA vaccine after 4 months.

Biomarkers	Anti-spike IgG	IL10	IL13	INF-γ	IL1β	IL2	IL8	IL17
IL10	−0.129 (0.398)							
IL13	−0.136 (0.372)	−0.068 (0.658)						
INF-γ	−0.028 (0.854)	−0.169 (0.266)	−0.326* (0.029)					
IL1β	0.103 (0.501)	0.279 (0.064)	−0.177 (0.245)	−0.099 (0.517)				
IL2	−0.236 (0.118)	−0.328* (0.028)	+0.300* (0.046)	−0.022 (0.884)	−0.211 (0.165)			
IL8	−0.156 (0.307)	−0.028 (0.856)	−0.060 (0.695)	+0.342* (0.021)	−0.317* (0.034)	0.273 (0.070)		
IL17	+0.337* (0.024)	−0.170 (0.264)	−0.190 (0.212)	0.027 (0.860)	0.099 (0.517)	0.073 (0.635)	−0.051 (0.739)	
CRP	0.159 (0.298)	0.026 (0.868)	0.065 (0.671)	−0.039 (0.797)	0.081 (0.596)	0.072 (0.637)	−0.008 (0.960)	0.143 (0.350)

The results are presented as a correlation factor (p-value). * Significant correlation. IL: interleukin, INF: interferon, and CRP: C-reactive protein.

TABLE 4 The ratio of anti-spike IgG antibody value to the cytokines and CRP levels.

Ratios	Before	After 1 month	After 4 months	P1	P2	P3
Anti-spike IgG/IL10	0.035 (0.012–0.079)	0.202 (0.167–0.278)	0.190 (0.138–0.267	<0.001	<0.001	0.001
Anti-spike IgG/IL-13	0.015 (0.006–0.035)	0.147 (0.134–0.176)	0.151 (0.127–0.230)	<0.001	<0.001	0.029
Anti-spike IgG/INF-γ	0.021 (0.007–0.038)	0.107 (0.099–0.121)	0.140 (0.126–0.161)	<0.001	<0.001	0.001
Anti-spike IgG/IL1β	0.039 (0.016–0.096)	0.224 (0.211–0.236)	0.399 (0.360–0.514)	<0.001	<0.001	0.001
Anti-spike IgG/IL2	0.014 (0.006–0.039)	0.131 (0.116–0.140)	0.481 (0.410–0.557)	<0.001	<0.001	0.001
Anti-spike IgG/IL-8	0.016 (0.005–0.029)	0.115 (0.099–0.158)	0.621 (0.527–0.818)	<0.001	<0.001	0.001
Anti-spike IgG/IL17	0.022 (0.008–0.050)	0.208 (0.166–0.244)	0.204 (0.172–0.247)	<0.001	<0.001	0.329
Anti-spike IgG/CRP	0.250 (0.110–0.561)	5.902 (5.560–6.754)	12.008 (9.668–14.479)	<0.001	<0.001	<0.001

The results are presented as median (interquartile Q1, Q3). The P-value was calculated using Wilcoxon's paired signed rank test.

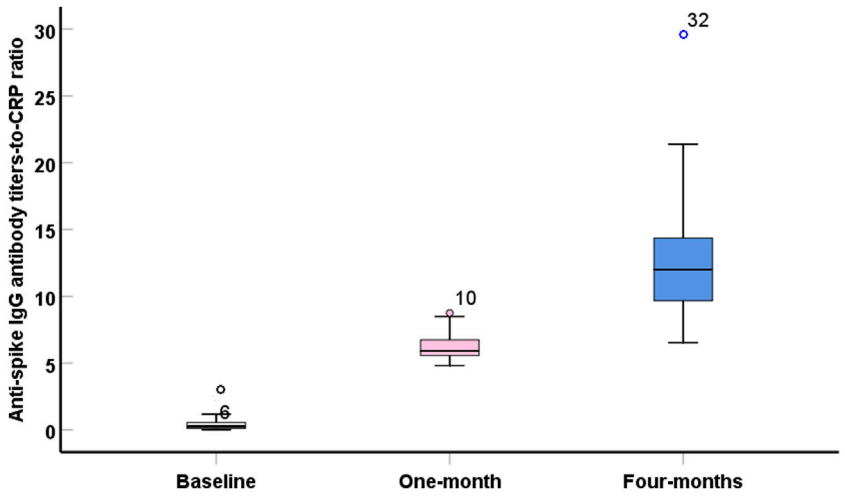

FIGURE 2
Boxplot showed significant ($p < 0.001$) high values of anti-spike IgG antibody titers- to – C-reactive protein ratio during the post-vaccination intervals.

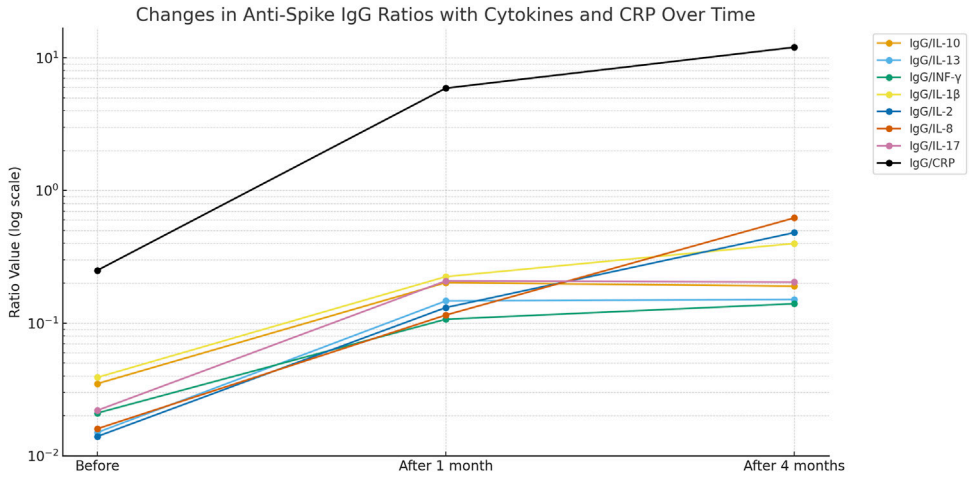

FIGURE 3
Changes in anti-Spike-IgG ratios with cytokines and CRP over time.

decline, which is normal. Still, memory B cells and T cells continue to offer protection against severe illness. Pro-inflammatory and anti-inflammatory markers do not significantly correlate with anti-spike IgG antibodies after 1-month post-immunization; however, 4 months after immunization, there is a significant positive correlation between anti-spike IgG antibodies and IL-17. The relationship between IL-17 and anti-spike IgG suggests that activation of the Th17 pathway may contribute to enhanced humoral response and increased antibody production against the sclerosing antigen. This can be explained by IL-17 supporting an inflammatory environment conducive to B cell maturation and activation via helper T-B signaling, in addition to its role in stimulating cytokines and chemokines that promote B cell differentiation and transformation to produce higher levels of IgG [11]. A study measuring IL-17 levels in the saliva of Pfizer vaccine recipients found a significant increase after two doses, without causing an excessive cytokine storm [12], which is consistent with our current study. Therefore, IL-17 activation is not necessarily harmful; it may be part of the environment conducive to B-cell maturation. Furthermore, another study on the role of the Th17 response suggested that IL-17 (produced by Th17 cells) may contribute to the severe inflammatory response in COVID-19 infection [13].

Therefore, it can be argued that IL-17 may play a role in stimulating the immune response, not just in harmful inflammation. The cytokine storm that follows COVID-19 infection is comparable to the picture of elevated pro-inflammatory and anti-inflammatory cytokine levels observed after COVID-19 immunization, albeit to a lesser extent, and is linked to a sharp rise in anti-spike IgG antibody titers [14]. A higher level of IL-1β indicates a response to vaccination, as immunization failure may occur in patients who use IL-1 inhibitors [15]. IL-2 is a pro-inflammatory cytokine that stimulates T cells, particularly $CD8^{+}$ T cells, thereby playing an essential role in antibody production. Participants in the current study exhibited a significant response to IL-2, thereby enhancing the production of anti-spike IgG antibodies. This conclusion aligns with the findings of Alhajjat et al. (2023) [16]. Despite showing no significant correlation with anti-spike IgG antibodies, interleukin-8 levels were substantially elevated, suggesting an enhanced inflammatory response. According to a recent study, post-acute COVID-19 vaccination syndrome is associated with higher levels of the pro-inflammatory cytokine IL-8 [17]. According to the cytokine profile of COVID-19 patients, those with longer COVID-19 disease exhibited higher IL-17 levels [18].

Consequently, persistent immunization may be indicated by a greater level of IL-17 and its association with anti-spike IgG antibodies. A noticeably elevated level of IL-10, which is typically reduced in long-term chronic COVID-19 infection, supports this hypothesis [18]. A significant association with IL-13 was observed 1 month after immunization. No significant correlation was found after 4 months, indicating that changes in C-reactive protein levels mirrored the profile seen in long-term COVID-19 syndrome, which tends to return to normal levels over time [19].

According to these findings, elevated CRP levels during the first month after vaccination may reflect an enhanced post-vaccination immune response. In addition, the positive correlations between CRP and the ratios of anti-spike IgG antibodies with each pro- or anti-inflammatory biomarker support this assumption. The anti-spike IgG antibody level is elevated by more than 10 DU/mL, indicating a persistent positive

immune response for 4 months, which explains why we used the anti-spike IgG-to-other-cytokine ratio, which declined briskly within 4 months [20].

The ratio of anti-spike IgG antibody levels to cytokine levels could serve as a new, valuable parameter for assessing the positive immune response, with cytokine levels normalized to baseline. Table 4; Figure 3 show a greater ratio of anti-spike IgG antibodies to CRP after 4 months, suggesting a more pronounced humoral-to-inflammatory balance. Anti-inflammatory markers, including IL-10, IL-13, and IFN-γ, are decreased in severe COVID-19 infection. Their dynamic changes can determine the degree of protection against the lung damage induced by SARS [21, 22].

Therefore, Higher levels of anti-inflammatory biomarkers were observed; however, these findings reflect an association only and do not imply a protective effect or enhanced immunization. The strength of this study lies in the simultaneous assessment of pro- and anti-inflammatory cytokines at different time points. Another important finding is that The ratio of anti-spike IgG to CRP may serve as an indicator of changes in humoral and inflammatory status over time following vaccination, although its relevance to immunization outcomes remains uncertain. The limitations of this study include its small sample size and the exclusion of individuals with risk factors, e.g., diabetes mellitus, to illustrate differences in immune responses between healthy individuals and those at risk of contracting COVID-19.

Conclusion

The present findings suggest that the pattern of cytokine alterations post-vaccination influences the potency and longevity of the humoral response. The IgG/IL-17 ratio may serve as a viable exploratory biomarker for assessing short- and medium-term vaccination efficacy, functioning as a hypothesis-generating indication rather than a validated clinical metric. The results demonstrate that immune response dynamics to the Pfizer-BNT162b2 vaccine involve coordinated inflammatory and anti-inflammatory activity alongside antibody responses.

Author contributions

MS (Conceptualization, Investigation, Methodology, Resources, Writing – original draft), TJ (Methodology, Writing – review and editing), AbA (Supervision, Methodology), AhA (Supervision, Methodology). All authors contributed to the article and approved the submitted version.

Data availability

The original contributions presented in the study are included in the article/supplementary material, further inquiries can be directed to the corresponding author.

Ethics statement

The studies involving humans were approved by the scientific and ethical committees in the University of Diyala, College of Medicine, Iraq. The studies were conducted in accordance with the local legislation and institutional requirements. The participants provided their written informed consent to participate in this study. Following the Declaration of Helsinki, the institutional ethical and scientific committee of the College of Medicine at the University of Diyala approved this study (code 2022 MAS260 in 2022, number 158, dated 4 April 2024), including the consent from each participant enrolled in the study. It is pertinent to note that, during the timeframe of the study, the administration of the vaccine was mandated by the government for all citizens.

Funding

The author(s) declared that financial support was not received for this work and/or its publication.

Conflict of interest

The author(s) declared no potential conflicts of interest with respect to the research, authorship, and/or publication of this article.

Generative AI statement

The author(s) declared that generative AI was not used in the creation of this manuscript.

Any alternative text (alt text) provided alongside figures in this article has been generated by Frontiers with the support of artificial intelligence and reasonable efforts have been made to ensure accuracy, including review by the authors wherever possible. If you identify any issues, please contact us.

References

1. Singh RB, Parmar UPS, Kahale F, Agarwal A, Tsui E. Vaccine-associated Uveitis after COVID-19 vaccination: Vaccine adverse event reporting system database analysis. *Ophthalmology* (2023) **130**:179–86. doi:10.1016/j.ophtha.2022.08.027

2. Xia X. Detailed dissection and critical evaluation of the Pfizer/BioNTech and moderna mRNA vaccines. *Vaccines* (2021) **9**:734. doi:10.3390/vaccines9070734

3. Kim S, Jeon JH, Kim M, Lee Y, Hwang Y-H, Park M, et al. Innate immune responses against mRNA vaccine promote cellular immunity through IFN-β at the injection site. *Nat Commun* (2024) **15**:7226. doi:10.1038/s41467-024-51411-9

4. Rosati M, Terpos E, Homan P, Bergamaschi C, Karaliota S, Ntanasis-Stathopoulos I, et al. Rapid transient and longer-lasting innate cytokine changes associated with adaptive immunity after repeated SARS-CoV-2 BNT162b2 mRNA vaccinations. *Front Immunol* (2023) **14**:1292568. doi:10.3389/fimmu.2023.1292568

5. Zhu X, Gebo KA, Abraham AG, Habtehyimer F, Patel EU, Laeyendecker O, et al. Dynamics of inflammatory responses after SARS-CoV-2 infection by vaccination status in the USA: a prospective cohort study. *The Lancet Microbe* (2023) **4**:e692–e703. doi:10.1016/S2666-5247(23)00171-4

6. Bergamaschi C, Terpos E, Rosati M, Angel M, Bear J, Stellas D, et al. Systemic IL-15, IFN-γ, and IP-10/CXCL10 signature associated with effective immune response to SARS-CoV-2 in BNT162b2 mRNA vaccine recipients. *Cell Rep* (2021) **36**:109504. doi:10.1016/j.celrep.2021.109504

7. Hofbauer SI, Fink LA, Young RE, Vijayakumar T, Nelson KM, Bellopede N, et al. Cytokine mRNA delivery and local immunomodulation in the placenta using lipid nanoparticles. *Adv Ther* (2025) **8**:e00148. doi:10.1002/adtp.202500148

8. Li C, Lee A, Grigoryan L, Arunachalam PS, Scott MKD, Trisal M, et al. Mechanisms of innate and adaptive immunity to the Pfizer-BioNTech BNT162b2 vaccine. *Nat Immunol* (2022) **23**:543–55. doi:10.1038/s41590-022-01163-9

9. Chu L, Vrbicky K, Montefiori D, Huang W, Nestorova B, Chang Y, et al. Immune response to SARS-CoV-2 after a booster of mRNA-1273: an open-label phase 2 trial. *Nat Med* (2022) **28**:1042–9. doi:10.1038/s41591-022-01739-w

10. Mateus J, Dan JM, Zhang Z, Rydyznski Moderbacher C, Lammers M, Goodwin B, et al. Low-dose mRNA-1273 COVID-19 vaccine generates durable memory enhanced by cross-reactive T cells. *Science* (2021) **374**(80-):eabj9853. doi:10.1126/science.abj9853

11. Zhang S. The role of transforming growth factor β in T helper 17 differentiation. *Immunology* (2018) **155**:24–35. doi:10.1111/imm.12938

12. Ali DM, Taha GI. Effect of Covid-19 vaccine on some immunological salivary biomarkers (sIgA and Interleukine-17). *J Fac Med Baghdad* (2023) **65**:86–92. doi:10.32007/jfacmedbagdad.2039

13. Kang YW, Lee SC, Jeon SM, Jo E-K. Roles of interleukin-17 and th17 responses in COVID-19. *J Bacteriol Virol* (2021) **51**:89–102. doi:10.4167/jbv.2021.51.3.089

14. Zanza C, Romenskaya T, Manetti AC, Franceschi F, La Russa R, Bertozzi G, et al. Cytokine storm in COVID-19: immunopathogenesis and therapy. *Medicina (Kaunas)* (2022) **58**:144. doi:10.3390/medicina58020144

15. Atagündüz P, Keser G, Soy M. Interleukin-1 inhibitors and vaccination including COVID-19 in inflammatory rheumatic diseases: a nonsystematic review. *Front Immunol* (2022) **12**:734279. doi:10.3389/fimmu.2021.734279

16. Alhajjat AM, Redden CR, Langereis M, Papastefan ST, Ito JAS, Ott KC, et al. CD4 and IL-2 mediated NK cell responses after COVID-19 infection and mRNA vaccination in adults. *Immunobiology* (2023) **228**:152304. doi:10.1016/j.imbio.2022.152304

17. Mundorf AK, Semmler A, Heidecke H, Schott M, Steffen F, Bittner S, et al. Clinical and diagnostic features of post-acute COVID-19 vaccination syndrome (PACVS). *Vaccines* (2024) **12**:790. doi:10.3390/vaccines12070790

18. Queiroz MAF, Neves PFM, Lima SS, Lopes Jda C, Torres MKda S, Vallinoto IMVC, et al. Cytokine profiles associated with acute COVID-19 and long COVID-19 syndrome. *Front Cell Infect Microbiol* (2022) **12**:922422. doi:10.3389/fcimb.2022.922422

19. García-Abellán J, Fernández M, Padilla S, García JA, Agulló V, Lozano V, et al. Immunologic phenotype of patients with long-COVID syndrome of 1-year duration. *Front Immunol* (2022) **13**:920627. doi:10.3389/fimmu.2022.920627

20. Abdul-Wahab KA, Rushdi AA, Mujahid A. Increasing levels of serum anti-spike S1-RBD IgG after 120 days of the Pfizer-BioNTech-mRNA second dose vaccination. *Arch Razi Inst* (2023) **78**:1071–5. doi:10.22092/ARI.2022.359934.2517

21. Lindner HA, Velásquez SY, Thiel M, Kirschning T. Lung protection vs. infection resolution: interleukin 10 suspected of double-dealing in COVID-19. *Front Immunol* (2021) **12**:602130. doi:10.3389/fimmu.2021.602130

22. Sasson J, Moreau GB, Petri WA. The role of interleukin 13 and the type 2 immune pathway in COVID-19: a review. *Ann Allergy Asthma Immunol* (2023) **130**:727–32. doi:10.1016/j.anai.2023.03.009

EBM Experimental Biology and Medicine

TYPE Original Research
PUBLISHED 03 March 2026
DOI 10.3389/ebm.2026.10834

OPEN ACCESS

*CORRESPONDENCE
Caiyun Ma,
caiyun_ma@bbmu.cn
Dawei Yang,
bbyangdawei@163.com

RECEIVED 22 September 2025
REVISED 18 December 2025
ACCEPTED 06 February 2026
PUBLISHED 03 March 2026

CITATION
Zang H, Yang X, Liu Y, Ma C and Yang D (2026) A novel *de novo ATP2B1* variant causes autosomal dominant intellectual developmental disorder 66 by disrupting calcium homeostasis via impaired membrane trafficking.
Exp. Biol. Med. 251:10834.
doi: 10.3389/ebm.2026.10834

A novel *de novo ATP2B1* variant causes autosomal dominant intellectual developmental disorder 66 by disrupting calcium homeostasis via impaired membrane trafficking

Huanhuan Zang[1,2], Xiaoyun Yang[1], Yucai Liu[1], Caiyun Ma[2]* and Dawei Yang[3]*

[1]Department of Pediatrics, The First Affiliated Hospital of Bengbu Medical University, Bengbu, China, [2]Anhui Engineering Research Centre for Neural Regeneration Technology and Medical New Materials, Bengbu Medical University, Bengbu, Anhui, China, [3]Department of Rheumatology and Immunology, Bengbu Hospital of Shanghai General Hospital/The Second Affiliated Hospital of Bengbu Medical University, Bengbu, China

Abstract

Heterozygous pathogenic variants in *ATP2B1* (encoding PMCA1) cause autosomal dominant intellectual developmental disorder 66 (MRD66; OMIM #619910). To date, only 12 pathogenic *de novo ATP2B1* variants have been reported in MRD66. This study aimed to identify the genetic etiology in a Chinese infant with a neurodevelopmental disorder characterized by early-onset seizures and global developmental delay (GDD) and functionally characterize a novel *ATP2B1* missense variant. Trio-based whole-exome sequencing revealed a heterozygous *de novo ATP2B1* variant (c.2140A>C, p.Thr714Pro) in the proband. The proband presented with infantile spasms, GDD (Gesell Developmental Quotient: 65–74), and severe growth restriction (height/weight <–2 SD). To investigate the variant's pathogenicity, the wild-type (WT) and mutant *ATP2B1* constructs, N-terminally tagged with mScarlet, were transfected into HEK293T cells. Confocal imaging demonstrated profound cytoplasmic mislocalization of the p.Thr714Pro mutant protein, contrasting sharply with the characteristic plasma membrane localization of WT ATP2B1. Measurement of intracellular Ca^{2+} levels using Fluo-4 AM showed a significant 2.07-fold increase in basal Ca^{2+} levels in cells expressing the mutant compared to WT. This finding expands the spectrum of ATP2B1 variants associated with MRD66 and confirms calcium dyshomeostasis as the core pathomechanism.

This case of MRD66 demonstrates a very early onset of seizures, consistent with the recognized phenotypic variability and the critical role of PMCA1 in early neurodevelopment.

KEYWORDS

ATP2B1, calcium homeostasis, *de novo* variant, intellectual developmental disorder 66, neurodevelopmental disorder

Impact statement

This manuscript contributes significantly to understanding genetic causes of early-onset epileptic encephalopathy and developmental delay. It identifies a novel ATP2B1 variant in a patient with severe developmental impairment and infantile spasms, demonstrating how this genetic change disrupts calcium balance in cells through two mechanisms: improper protein localization and reduced calcium export. This work expands the spectrum of known ATP2B1 variants linked to neurodevelopmental disorders and highlights the critical role of calcium regulation in early brain development and function. By providing new insights into the genetic architecture and pathophysiology of these conditions, the study advances diagnostic approaches and points toward potential therapeutic strategies targeting calcium homeostasis. The findings also underscore the variability in clinical presentation associated with ATP2B1 variants, offering valuable information for genetic counseling and clinical management.

Introduction

Neurodevelopmental disorders (NDDs) with early-onset seizures and associated developmental delay represent a genetically heterogeneous group of neurodevelopmental disorders (NDDs) [1]. While environmental factors like gestational infections or teratogen exposure can contribute, pathogenic *de novo* variants (DNMs) in critical developmental genes are a major etiology, particularly in undiagnosed cases, roughly divided equally between loss-of-function (LoF) and altered-function variants, which are often missense and can confer gain-of-function, dominant-negative, or other pathogenic mechanisms [2]. Disrupted intracellular Ca^{2+} signaling has emerged as a key pathological mechanism underlying both neurodevelopmental deficits and epilepsy.

Calcium ions (Ca^{2+}) function as universal second messengers essential for fundamental neuronal processes. They regulate diverse functions including signal transduction cascades, gene expression, cellular metabolism, neurotransmitter release, synaptic plasticity, and membrane excitability [3]. Within neurons, precise Ca^{2+} homeostasis is critical for a suite of processes indispensable for learning and memory, such as neurotransmitter release, neurite outgrowth, synaptogenesis, and synaptic efficacy. Dysregulation of Ca^{2+} signaling is implicated in neurodegeneration (e.g., Alzheimer's, Parkinson's, Huntington's diseases) and is a well-established driver of epileptogenesis. Pathogenic variants in voltage-gated calcium channel genes, such as *CACNA1H* which encodes T-type channels, can lower activation thresholds and prolong channel opening, causing pathological Ca^{2+} influx, neuronal hyperexcitability, and seizures [4]. Elevated intracellular Ca^{2+} potentiates presynaptic glutamate release [5], while simultaneously desensitizing postsynaptic GABAergic receptors, thereby impairing inhibitory neurotransmission despite normal GABA levels [6]. This dual action disrupts the critical excitatory-inhibitory (E/I) balance within neuronal networks, facilitating seizure initiation and propagation. Clinically, the efficacy of Ca^{2+} channel-targeting antiepileptic drugs (e.g., ethosuximide, zonisamide) provides strong validation for the proposed pathomechanism of calcium dyshomeostasis [7].

Plasma membrane Ca^{2+}-ATPase type 1 (PMCA1), encoded by the *ATP2B1* gene (OMIM #108731, Chr12q21.33), is a P-type ATPase crucial for maintaining low resting cytosolic Ca^{2+} levels. It actively exports Ca^{2+} against its steep concentration gradient, utilizing energy derived from ATP hydrolysis, forming a characteristic aspartyl phosphate intermediate during its catalytic cycle [8]. PMCA1 belongs to a family of four calmodulin-dependent Ca^{2+} pumps in mammals (*ATP2B1*, *ATP2B2* [Chr3p26], *ATP2B3* [ChrXq28], *ATP2B4* [Chr1q25]). Functional diversity within this family is further expanded by extensive alternative splicing and tissue-specific expression patterns (PMCA1 is ubiquitously expressed, with high levels in the brain and bone marrow). The 1,220-amino acid PMCA1 protein features a C-terminal calmodulin-binding autoinhibitory domain and contains consensus sites for phosphorylation by cAMP-dependent kinase. Beyond its primary role in calcium extrusion, PMCA1 regulates insulin sensitivity in endothelial cells through Ca^{2+}/calmodulin-dependent activation of AKT1 and NOS3 signaling pathways [9]. The embryonic lethality observed in *Atp2b1* homozygous knockout mice underscores its essential non-redundant role in development [10].

Autosomal dominant intellectual developmental disorder 66 (MRD66; OMIM#619910) is caused by heterozygous pathogenic *de novo* variants in *ATP2B1*. Characterized by variable expressivity, the core phenotypic features include global developmental delay (GDD), mild-to-moderate intellectual disability (ID), and seizures, which occur in ~50% of patients.

The other accompanying features include autism spectrum disorder (ASD), subtle dysmorphic features, and others. To date, only 12 distinct pathogenic *de novo ATP2B1* variants have been conclusively associated with MRD66 [8], limiting the understanding of robust genotype-phenotype correlations. This knowledge gap underscores the critical importance of functional validation for novel variants to elucidate their specific pathomechanisms.

In the current study, we report an infant with a neurodevelopmental disorder featuring infantile spasms and GDD harboring a novel *de novo ATP2B1* missense variant (p.Thr714Pro). Structural modeling predicts that this variant disrupts critical hydrogen bonding within the catalytic P-domain. We then employed confocal microscopy and live-cell calcium imaging to functionally validate that this alteration causes PMCA1 mislocalization away from the plasma membrane and ablates Ca2+ efflux capacity, leading to cytotoxic calcium overload. These findings significantly expand the mutational spectrum of MRD66 and provide direct mechanistic evidence implicating calcium dyshomeostasis as the central neuropathogenic process.

Materials and methods

Patient recruitment

We recruited a proband with epilepsy from non-consanguineous parents. The legal guardian of the proband provided informed consent and was aware of the anonymous publication of clinical and genetic information of the proband. The medical ethics of this study have been approved by the Institutional Review Board of the First Affiliated Hospital of Bengbu Medical University (ID: 2025049).

Genetic analysis

Genomic DNA was extracted from peripheral blood lymphocytes of the proband and both parents using a Blood Genomic DNA Extraction Kit (CWBIO Biotechnology). DNA concentration and quality were assessed using a Qubit® 3.0 Fluorometer (Thermo Fisher Scientific). Whole-exome sequencing (WES) libraries were prepared using the IDT xGen Exome Research Panel v2.0 and sequenced on an Illumina NovaSeq 6000 platform (2 × 150 bp paired-end reads), achieving a mean coverage depth of >100× across the exome. Raw sequencing data underwent standard preprocessing: adapter sequences were trimmed, and low-quality reads were filtered using Illumina's bcl2fastq software. Cleaned reads were aligned to the GRCh37/hg19 human reference genome using BWA-MEM (v0.7.17). Post-alignment processing included duplicate marking, local realignment around insertions/deletions, and base quality score recalibration using the Genome Analysis Toolkit (GATK v4.1.8.1). Variant calling was performed using GATK HaplotypeCaller. Trio-based variant prioritization employed the following sequential filters: 1) Annotation using ANNOVAR, filtering against population allele frequencies [dbSNP, 1000 Genomes, Exome Aggregation Consortium (ExAC), Genome Aggregation Database (gnomAD)]; 2) Assessment of predicted functional impact using multiple algorithms (MutationTaster, SIFT, PolyPhen-2, PROVEAN, CADD, REVEL, and M-CAP) and evolutionary conservation scores (GERP++, phyloP, phastCons); 3) Classification according to the American College of Medical Genetics and Genomics/Association for Molecular Pathology (ACMG/AMP) guidelines [11]; 4) Correlation with known disease phenotypes using curated databases [Human Gene Mutation Database (HGMD), ClinVar, Online Mendelian Inheritance in Man (OMIM)]. Candidate variants identified through this pipeline were validated by bidirectional Sanger sequencing using specific primers. For detailed experimental procedures, see the Supplementary Material.

Protein structural analysis

Our analysis of the canonical human ATP2B1 isoform (UniProt ID: P20020) was based primarily on the high-resolution cryo-EM structure of a homologous P-type ATPase (PDB ID: 6A69) [12]. Subsequently, to introduce the specific variant, the atomic coordinates for c.2140A>C (p.Thr714Pro) were modeled by performing residue substitution within the UCSF ChimeraX software package (v1.7.1). This enabled comparative visualization and analysis of the wild-type (WT) and mutant protein conformations.

Plasmid construction and site-directed mutagenesis

The functional experimental strategy, including the assessment of calcium homeostasis, was designed based on established methods for investigating *ATP2B1* variant pathogenicity [8]. The full-length coding sequence of wild-type (WT) human *ATP2B1* (RefSeq NM_001366521.1) was PCR-amplified from commercial human brain cDNA (BioCat GmbH, Heidelberg, Germany) using high-fidelity Phanta Max Super-Fidelity DNA Polymerase (#P505, Vazyme Biotech). The amplicon was subsequently fused in-frame to the N-terminus of the mScarlet-I fluorescent protein using the ClonExpress Ultra One Step Cloning Kit (#C115, Vazyme Biotech), generating the WT ATP2B1-mScarlet construct. The T714P mutant (c.2140A>C) was generated using the WT ATP2B1-mScarlet plasmid as a template and mutation-specific

primers via overlap extension PCR. All constructs (WT and T714P) were directionally cloned into the mammalian expression vector pcDNA3.1(+) (Thermo Fisher Scientific) using NotI and EcoRI restriction sites. PCR products and restriction digests were electrophoresed on 1.5% agarose gels (#SH441-01, Biosharp) stained with GelRed Nucleic Acid Gel Stain (#41005, Biotium). Bands of the correct size were excised and purified using a Gel Extraction Kit (#DP209, Tiangen Biotech). Purified inserts were ligated into EcoRI/NotI-digested pcDNA3.1(+) vector using T4 DNA Ligase (New England Biolabs). Recombinant plasmids were transformed into chemically competent *E. coli* DH5α cells. Positive clones were selected on LB agar plates containing 100 μg/mL ampicillin and screened by colony PCR. Plasmid DNA from positive clones was purified (#DP103, Tiangen Biotech) and the entire ATP2B1 insert was validated by bidirectional Sanger sequencing (Tsingke Biotech).

Cell culture and transient transfection

HEK293T cells (Shanghai Cell Bank of the Chinese Academy of Sciences) were cultured in Dulbecco's Modified Eagle Medium (#11965092, DMEM; Gibco) supplemented with 10% fetal bovine serum (FBS; Gibco, 10099141) and 1% penicillin-streptomycin (#15140122, Gibco). Cells were maintained at 37 °C in a humidified incubator with 5% CO_2. For transient transfection, cells were seeded onto poly-L-lysine-coated coverslips in 6-well plates or directly into plates and grown to 50–60% confluence. Transfection complexes were prepared by mixing 2 μg of plasmid DNA (WT ATP2B1-mScarlet, T714P ATP2B1-mScarlet, or empty pcDNA3.1 vector control) with 7 μL Lipofectamine 3000 reagent and 4 μL P3000 Enhancer Reagent (#L3000015, Thermo Fisher Scientific) in 250 μL Opti-MEM I Reduced Serum Medium (#31985070, Gibco). The mixture was incubated for 15 min at room temperature before adding dropwise to the cells. After 6 h of incubation, the transfection mixture was replaced with fresh complete growth medium. Cells were analyzed 48 h post-transfection.

Subcellular localization analysis by confocal microscopy

At 48 h post-transfection, cells grown on coverslips were washed twice with phosphate-buffered saline (PBS) and fixed with 4% paraformaldehyde in PBS for 15 min at room temperature. After fixation, cells were washed three times with PBS and permeabilized with 0.1% Triton X-100 in PBS for 10 min. Nuclei were counterstained with 10 μg/mL Hoechst 33342 (#C1028, Beyotime Biotech) in PBS for 15 min at room temperature. Coverslips were mounted onto glass slides using ProLong Gold Antifade Mountant (#P36930, Thermo Fisher Scientific). Fluorescence imaging was performed using a Leica TCS SP8 confocal microscope equipped with a ×63 oil immersion objective (NA 1.4). Excitation/emission settings were optimized for mScarlet (excitation: 569 nm, emission: 593–620 nm) and Hoechst 33342 (excitation: 405 nm, emission: 410–480 nm). Z-stacks were acquired with a step size of 0.5 μm. Plasma membrane localization was quantified using ImageJ software (NIH). The EzColocalization plugin was used to generate line-scan intensity profiles across cell peripheries from maximum intensity projections. The ratio of plasma membrane fluorescence intensity (peak) to adjacent cytoplasmic fluorescence intensity (trough) was calculated for at least 30 cells per condition from three independent experiments.

Measurement of intracellular calcium levels

This assay was performed to assess the impact of the *ATP2B1* variant on basal cytosolic calcium concentration, a key indicator of calcium homeostasis. The approach of measuring resting Ca^{2+} levels in transfected cells aligns with the functional validation methodology employed in prior studies of *ATP2B1*-related disorders [8]. Transfected HEK293T cells in 6-well plates were washed twice with pre-warmed PBS and loaded with 5 μM Fluo-4, AM (#KGE3103-1, KeyGEN BioTECH) dissolved in PBS containing 0.02% pluronic F-127 (#P3000MP, Thermo Fisher Scientific) for 30 min at 37 °C in the dark. After loading, cells were washed three times with PBS to remove excess dye and incubated in dye-free PBS for an additional 20 min at 37 °C to allow complete de-esterification of the AM ester. Cells were then gently trypsinized, resuspended in fresh PBS, and transferred to glass-bottom dishes for immediate imaging. Intracellular Ca^{2+} levels were quantified by measuring Fluo-4 fluorescence intensity using an Olympus IX83 fluorescence microscope equipped with a FITC filter set (excitation: 494 nm, emission: 516 nm) and a cooled CCD camera. Images were acquired using identical exposure times (200 ms) and gain settings to allow direct comparison. Baseline fluorescence intensity was measured in the absence of any stimulation for ≥100 individual cells per condition (WT, T714P, empty vector) from three independent biological replicates. To minimize photobleaching and dye leakage, cells were imaged rapidly, and exposure time was strictly limited. Fluorescence intensity values were background-subtracted using cell-free regions. Mean fluorescence intensity per cell was calculated.

Statistical analysis

All experiments were performed with a minimum of three independent biological replicates, each consisting of technical triplicates where applicable. Data are presented as mean ± standard error of the mean (SEM). Statistical significance between two groups was determined using unpaired, two-tailed Student's t-tests. Analyses were performed using

TABLE 1 Developmental assessment of the proband using Gesell Developmental Schedules at 8 months.

Domain	Developmental quotient (DQ)	Severity classification
Adaptive	70	Mild delay
Gross motor	68	Mild delay
Fine motor	65	Mild delay
Personal-social	74	Mild delay
Language	69	Mild delay

GraphPad Prism software (v8.0). A p-value <0.05 was considered statistically significant. $^{**}p < 0.01$, $^{***}p < 0.001$.

Results

Patient and clinical evaluation

An 8-month-old female infant was the first child (G1P1) of non-consanguineous Chinese parents. She was delivered vaginally at 35^{+3} weeks of gestation following preterm premature rupture of membranes. Severe intrauterine growth restriction was evident [birth weight 2,260 g (<3rd percentile, Z-score −2.8), length 49 cm (<3rd percentile, Z-score −2.3)]. A comprehensive review of the perinatal records revealed no clinical or biochemical indicators of asphyxia. At 2 months of age, she developed acute-onset infantile spasms. The seizures manifested as 10–15 daily clusters, each cluster comprising 20–30 individual flexor-dominant events. Semiology included repetitive head-nodding ("salaam attacks"), bilateral shoulder elevation, asymmetric tonic limb posturing, and axial hyperextension, predominantly occurring during sleep-wake transitions. The infant exhibited consistent post-ictal irritability. Concurrently, a developmental plateau was observed. Furthermore, brain MRI revealed no evidence of structural abnormalities or patterns indicative of hypoxic-ischemic injury. Systemic investigations (ECG, abdominal ultrasound) were normal. Video-EEG monitoring demonstrated significant abnormalities: Interictally, there was diffuse background slowing (4–5 Hz) with multifocal epileptiform discharges. During wakefulness, bilateral occipital-dominant sharp waves showed a right-greater-left asymmetry. Sleep stages featured prominent midline spike-wave complexes (2.5–3 Hz). Growth parameters remained severely restricted at 8 months (weight 7.5 kg [<−2 SD], length 68 cm [<−2 SD]). Gesell Developmental Schedules assessment at 8 months confirmed global impairment across all domains (Table 1): Adaptive skills (Developmental Quotient [DQ] = 70) revealed deficits in object permanence and cause-effect understanding; Gross motor function (DQ = 68) manifested as an inability to sit independently; Fine motor abilities (DQ = 65) showed an immature palmar grasp without object transfer; Personal-social interaction (DQ = 74) demonstrated poor eye contact and limited social referencing; Language development (DQ = 69) was restricted to reduplicated babbling ("ba-ba", "ma-ma") without communicative gestures. This constellation of findings prompted comprehensive genetic investigation: refractory epileptic spasms, persistent microsomatism, and developmental arrest in the absence of structural lesions.

Identification of a novel *de novo* *ATP2B1* variant

Trio-based WES identified a heterozygous missense variant in *ATP2B1* (NM_001366521.1: c.2140A>C) in the proband, resulting in the substitution of proline for threonine at amino acid position 714 (p.Thr714Pro; chr12:90005077, GRCh37/hg19). Bidirectional Sanger sequencing confirmed that this variant was absent in both unaffected parents (Figure 1A; PS2) and in major population databases (gnomAD v4.1.0, dbSNP v155, 1000 Genomes Phase 3, ExAC v0.3.1; PM2_Supporting). *ATP2B1* exhibits strong intolerance to missense variation, as evidenced by a high gnomAD missense Z-score (7.01; constraint threshold ≥3.09; PP2). Computational prediction tools unanimously supported a deleterious effect: Provean (−5.63), SIFT (0.0), PolyPhen-2 (1.0), MutationTaster (1), M-CAP (0.52), REVEL (0.96), CADD (27.5) (PP3). Thr714 residue is highly conserved across diverse species (Figure 1B). This variant represents a novel addition to the 12 previously reported *ATP2B1* variants associated with MRD66 (Figure 1C; Table 2). No other pathogenic variants or copy-number variations explaining the proband's phenotype were detected. Based on ACMG/AMP guidelines (PS2 + PM2_Supporting + PP2 + PP3), the *ATP2B1* c.2140A>C (p.Thr714Pro) variant was classified as Likely Pathogenic.

Structural impact of the p.Thr714Pro variant

Homology modeling based on the human ATP2B1 cryo-EM structure (PDB: 6A69) positioned Thr714 within the P domain, specifically on a solvent-exposed α-helix (Figure 2A). This residue participates in essential hydrogen bonding networks that stabilize the local P-domain structure: the sidechain hydroxyl group of

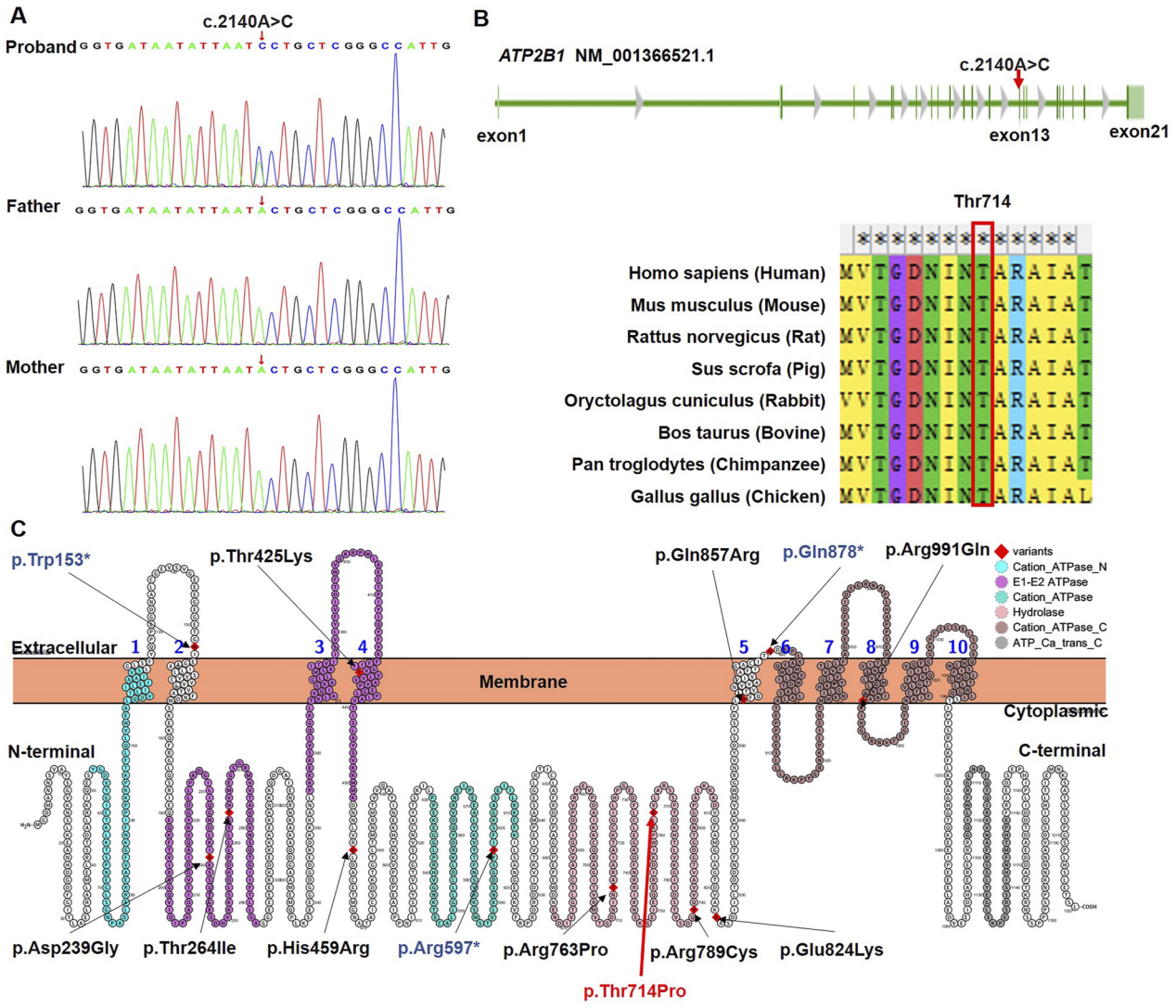

FIGURE 1
Genetic characterization of the novel *ATP2B1* variant. **(A)** Sanger sequencing chromatograms confirming the *de novo* heterozygous *ATP2B1* c.2140A>C variant (arrow) in the proband and its absence in both parents. **(B)** Evolutionary conservation analysis of Thr714 residue across diverse species (analyzed using MEGA12), highlighting its critical conservation. The mutated residue is indicated by the red box. **(C)** Schematic representation of the ATP2B1 protein domain architecture (generated using Protter) depicting the novel p.Thr714Pro variant (red) alongside the 12 previously reported MRD66-associated *de novo* variants (black: missense; dark blue: nonsense). Functional domains are annotated: 10 transmembrane helices (TM1-10), N-terminal cation transport ATPase region, catalytic E1-E2 ATPase, P-type cation transport ATPase domain, haloacid dehalogenase-like hydrolase (location of Thr714), C-terminal cation transport ATPase region, and C-terminal calmodulin-binding autoinhibitory region.

Thr714 forms a hydrogen bond with the backbone carbonyl oxygen of Asn711 and another with the backbone amide nitrogen of Ile718 (Figure 2B). The substitution of proline for threonine at position 714 induces significant structural perturbations: 1) Steric Incompatibility: Proline's rigid cyclic side chain generates steric clashes (minimum atomic distance ~1.8 Å) with the side chain of the adjacent Asn711 residue; 2) Loss of Critical Hydrogen Bonds: The absence of the hydroxyl group in proline ablates the hydrogen bonds normally formed between Thr714 and Asn711 (Figure 2C). These structural modifications destabilize the P domain interface required for calcium-dependent conformational changes during pump activation.

The p.Thr714Pro variant disrupts plasma membrane trafficking of ATP2B1

Confocal microscopy analysis revealed stark differences in the subcellular distribution of WT and mutant ATP2B1-mScarlet fusion proteins expressed in HEK293T cells (Figure 3A).

Experimental Biology and Medicine

TABLE 2 Clinical features of the proband and previously reported patients with *ATP2B1* vriants (NM_001366521.1).

Patient (Ref.)	Variant	Inheritance	Age	Sex	DD/ID	Epilepsy	Growth	Brain MRI	Facial/Skeletal features	Additional features	Functional evidence
This study	c.2140A>C (p.Thr714Pro)	*De novo*	8 ms	F	Mild DD	Infantile spasms	Ht/Wt SD <−2	Normal	Normal	Normal	↓ Ca^{2+} export, mislocalization
P1 [8]	c.716A>G (p.Asp239Gly)	*De novo*	6 ys	F	Moderate ID	Yes	Normal	NA	Facial dysmorphism, toe clinodactyly	Hypotonia, secundum atrial septal defect	↓ Ca^{2+} export, mislocalization
P2 [8]	c.791C>T (p.Thr264Ile)	*De novo*	8 ys	M	Mild ID	No	Normal	NA	Low-set ears	ASD, transposition of great vessels	↓ Ca^{2+} export
P3 [8]	c.1274C>A (p.Thr425Lys)	*De novo*	9 ys	M	Mild ID	Abnormal EEG	Normal	Abnormal	Sparse hair	Cerebral cavernous malformation	↓ Ca^{2+} export, mislocalization
P4 [8]	c.1376A>G (p.His459Arg)	*De novo*	17 ys	M	Mild ID	Yes	Normal	NA	Marfanoid habitus, arachnodactyly	ASD, scoliosis, hypermobile thumb	↓ Ca^{2+} export
P5 [8]	c.2288G>C (p.Arg763Pro)	*De novo*	21 ys	M	Mild ID	No	Normal	NA	Facial dysmorphism	ASD	↓ Ca^{2+} export, mislocalization
P6 [8]	c.2365C>T (p.Arg789Cys)	*De novo*	3 ys	M	ID	Yes	Normal	NA	Facial dysmorphism, hypotonia	Sleeping difficulties	↓ Ca^{2+} export
P7 [8]	c.2470G>A (p.Glu824Lys)	*De novo*	22 ys	F	Moderate ID	Yes	Normal	NA	–	Compulsive behavior	↓ Ca^{2+} export, mislocalization
P8 [8]	c.2570A>G (p.Gln857Arg)	*De novo*	3 ys	F	ID	No	Normal	NA	Brachycephaly, facial dysmorphism, 5th-finger clinodactyly	Normal	↓ Ca^{2+} export, mislocalization
P9 [8]	c.2972G>A (p.Arg991Gln)	Unknown	51 ys	M	Mild ID	No	Normal	NA	Marfanoid habitus, facial dysmorphism	ASD, aortic dilation, pectus carinatum, scoliosis	↓ Ca^{2+} export, mislocalization
P10 [8]	c.2632C>T (p.Gln878*)	*De novo*	6 ys	M	Mild ID	No	Normal	NA	Facial dysmorphism	Hyperactivity	Nonsense (NMD predicted)
P11 [8]	c.458G>A (p.Trp153*)	Unknown	6 ys	F	Moderate ID	No	Short stature	NA	–	NA	Nonsense (NMD predicted)
P12 [8]	c.1789C>T (p.Arg597*)	Unknown	5 ys	M	ID	Infantile spasms	Short stature	NA	Pectus excavatum, plagiocephaly	ASD	Nonsense (NMD predicted)
[13]	c.2938G>T (p.Val980Leu) c.3060 + 2T>G	Compound heterozygous	14 ys	M	Moderate ID (WISC:50)	No	Short stature	PVNH	Distinct craniofacial gestalt, microretrognathia, cleft palate	PVNH, brachydactyly, syndactyly, hypoparathyroidism	↓ ATP2B1 protein, ↓ Ca^{2+} export; splicing defect (NMD)

Abbreviations: DD: developmental delay, ID: intellectual disability, ASD: autism spectrum disorder, NA: Not Available/Absent, PVNH: periventricular nodular heterotopia, WISC: wechsler intelligence scale for children, SD: standard deviation, EEG: electroencephalogram, MRI: magnetic resonance imaging, mo: months, yrs: years, Ht: Height, Wt: Weight, TGV: transposition of great vessels, NMD: Nonsense-Mediated Decay.

Published by Frontiers
Society for Experimental Biology and Medicine

10.3389/ebm.2026.10834

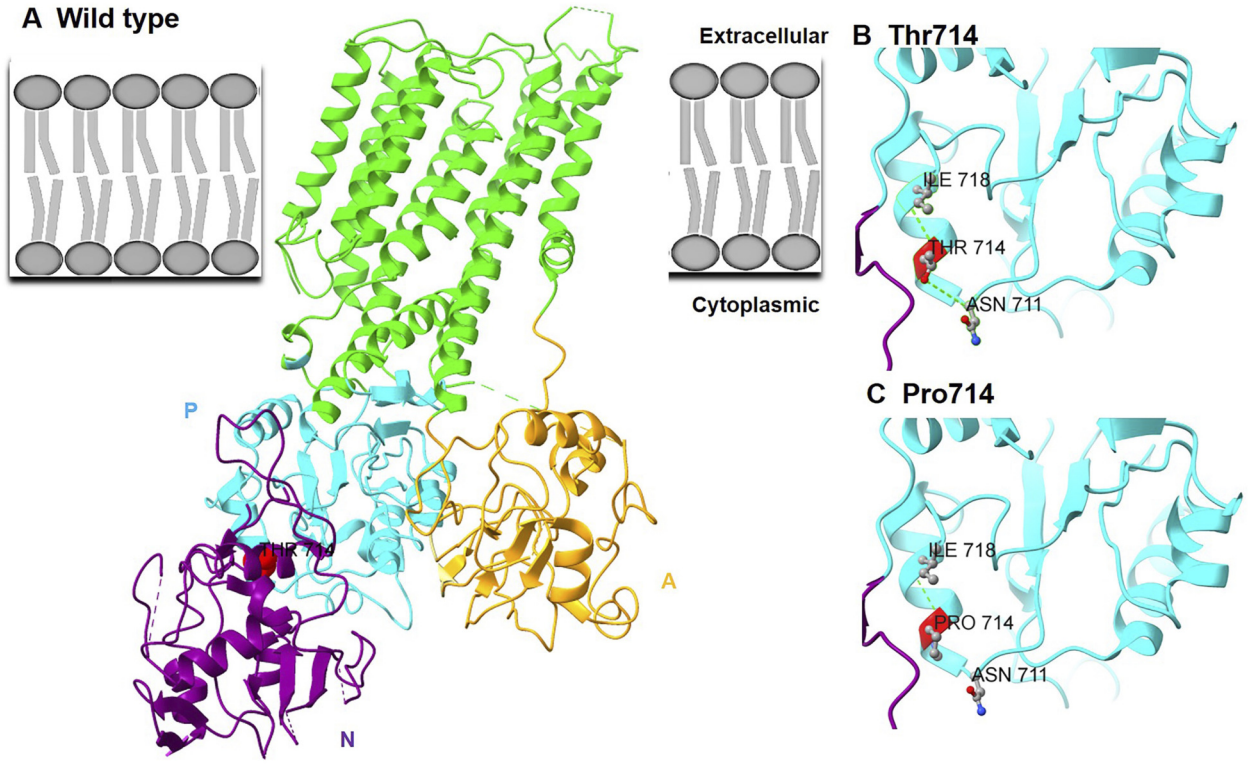

FIGURE 2
Structural impact of the p.Thr714Pro variant in *ATP2B1*. **(A)** 3D structure of wild-type ATP2B1 (based on PDB: 6A69): Phosphorylation (P) domain (blue), nucleotide-binding (N) domain (purple), and actuator (A) domain (gold). Thr714 (highlighted as red spheres) resides at the P-N domain interface within the P domain. The approximate location of the plasma membrane is indicated. **(B)** Close-up view of wild-type interactions involving Thr714: Hydrogen bonds (green dashed lines) between the Thr714 sidechain hydroxyl and the backbone carbonyl of Asn711 and the backbone amide of Ile718 stabilize the local α-helix. **(C)** Mutant conformation (p.Thr714Pro): Substitution with proline eliminates the hydroxyl group, preventing hydrogen bond formation with Asn711.

ATP2B1-WT-mScarlet exhibited robust localization primarily at the plasma membrane, characterized by sharp, continuous fluorescence outlining the cellular periphery. In stark contrast, the T714P mutant displayed a predominantly diffuse cytoplasmic distribution, with significantly diminished fluorescence signal at the plasma membrane. Line-scan intensity profile analysis across cell boundaries confirmed a substantial reduction in membrane-associated fluorescence intensity for the T714P mutant (peak/trough ratio = 1.2 ± 0.3, mean ± SEM) compared to the WT construct (4.3 ± 0.5) ($p < 0.001$), representing a 72.3% decrease. This mislocalization phenotype demonstrates that the p.Thr714Pro substitution severely impairs the trafficking of PMCA1 to its functional site on the plasma membrane.

Impaired calcium homeostasis in cells expressing the p.Thr714Pro variant

Given the critical role of PMCA1 in calcium extrusion, we assessed the functional consequence of mislocalization by measuring resting cytosolic Ca^{2+} levels using Fluo-4 AM fluorescence imaging (Figure 3B). Cells expressing the ATP2B1-T714P mutant exhibited profoundly elevated basal intracellular Ca^{2+} levels. The mean Fluo-4 fluorescence intensity was 2.07-fold higher in mutant-expressing cells compared to cells expressing WT ATP2B1 ($p < 0.001$). Cells transfected with the empty vector control exhibited fluorescence intensity between that of WT and T714P-expressing cells, and the differences were statistically significant compared to both (WT vs. empty vector, $p < 0.01$; T714P vs. empty vector, $p < 0.001$). This aberrant accumulation of cytosolic calcium provides direct functional evidence that the p.Thr714Pro variant compromises the Ca^{2+} extrusion capacity of PMCA1, leading to calcium dyshomeostasis. While this single-timepoint measurement reflects the net outcome of calcium influx, buffering, and efflux, a significant elevation in basal cytosolic Ca^{2+} is a consistent functional hallmark of pathogenic *ATP2B1* missense variants [8], indicating disrupted calcium homeostasis.

Discussion

We identified a novel *de novo ATP2B1* missense variant, c.2140A>C (p.Thr714Pro), in a Chinese infant presenting with

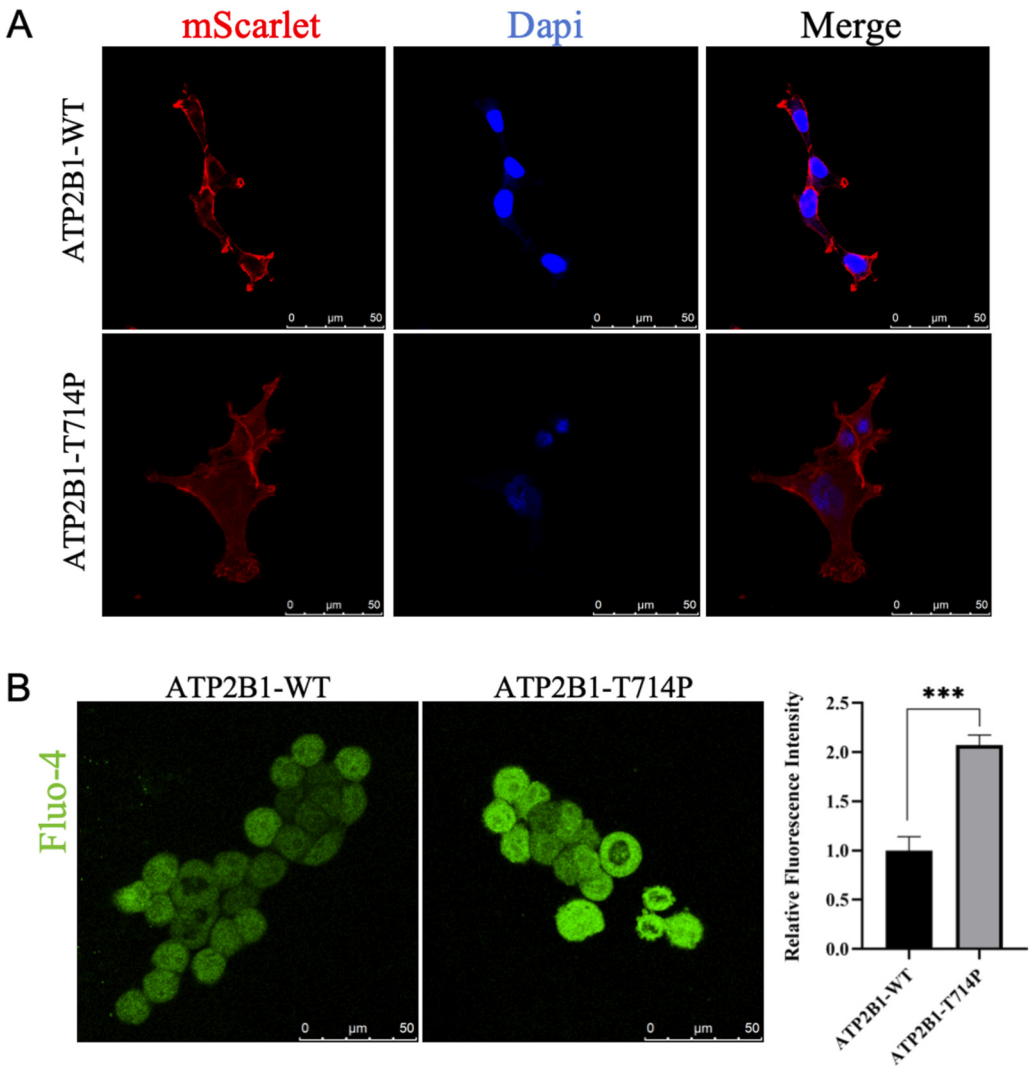

FIGURE 3
Functional Validation of the p.Thr714Pro Variant. **(A)** Confocal microscopy images of HEK293T cells expressing mScarlet-tagged ATP2B1 constructs (red). Nuclei are counterstained with Hoechst 33342 (blue). ATP2B1-WT-mScarlet localizes predominantly to the plasma membrane. ATP2B1-T714P-mScarlet shows diffuse cytoplasmic distribution with minimal plasma membrane signal. Scale bars: 20 μm. Insets show x3 magnified regions of interest. **(B)** Quantification of basal intracellular Ca^{2+} levels using Fluo-4 AM fluorescence intensity. Data represent mean fluorescence intensity ±SEM from three independent experiments (n ≥ 100 cells per condition per experiment). ***$p < 0.001$ vs. WT ATP2B1 (unpaired t-test). EV: Empty Vector control.

the core features of MRD66, including early-onset seizures and severe global developmental delay. Functional characterization demonstrates that the variant impairs *ATP2B1* function by causing its mislocalization away from the plasma membrane. This reduction in properly localized protein leads to a consequent loss of calcium efflux capacity. These findings establish that p.Thr714Pro causes haploinsufficiency via combined mislocalization and loss of catalytic activity, resulting in elevated cytosolic calcium (Ca^{2+}), neuronal hyperexcitability, and the observed phenotype of global developmental delay with infantile spasms.

ATP2B1 encodes the plasma membrane Ca^{2+}-ATPase isoform 1 (PMCA1), a ubiquitously expressed P-type ATPase. PMCA1 is characterized by large cytoplasmic domains [Actuator (A), Nucleotide-binding (N), Phosphorylation (P)] and ten transmembrane helices (M1-M10) that form the ion transport pathway, making it essential for maintaining intracellular Ca^{2+} homeostasis via Ca^{2+} extrusion [12, 14] (Figures 1C, 2A). Its critical role in development is underscored by embryonic lethality in homozygous *Atp2b1* knockout mice [15], whereas heterozygous knockouts exhibit systemic alterations such as

hypertension and abnormal bone metabolism [16]. In neurodevelopment, PMCA1 is particularly vital. Murine studies show a surge in its expression during key events like neural tube closure and neuronal migration [17], and it is expressed in the developing cerebral cortex [18]. This pattern is consistent with the established role of spatially and temporally regulated Ca^{2+} signaling in coordinating neurogenesis, neuronal differentiation, and circuit formation. In humans, biallelic *ATP2B1* variants are associated with a neurodevelopmental malformation syndrome with primary hypoparathyroidism [13], whereas *de novo* variants are the predominant cause of MRD66, a disorder defined by neurodevelopmental delay [8].

Deleterious heterozygous *ATP2B1* variants were first linked to MRD66 by Rahimi et al., who identified 12 patients with GDD, variable ID (mild to severe), and behavioral abnormalities (including ASD in 42%); seizures (infantile spasms, myoclonic, absence) were present in 50% of cases [8]. Phenotypic heterogeneity was notable, ranging from ambulatory patients with mild learning deficits to severely affected non-ambulatory and nonverbal individuals. Our patient's presentation aligns with these core features of MRD66, exhibiting GDD and early-onset infantile spasms. Notably, the pronounced and persistent growth retardation (height and weight consistently below −2 SD) observed in our case represents a more severe manifestation of this feature compared to most previously reported heterozygous cases, thereby expanding the known phenotypic spectrum of MRD66 (Table 2). This degree of growth delay, although variable across reported patients, underscores the potential role of PMCA1 dysfunction in somatic growth pathways beyond neurodevelopment. In contrast to patients with biallelic *ATP2B1* variants who often present with multi-system malformations [13], our patient lacked overt dysmorphic features, structural brain anomalies, or biochemical evidence of hypocalcemia, further supporting haploinsufficiency as the primary disease mechanism in heterozygous carriers.

Thr714 resides within the conserved TGES motif of the haloacid dehalogenase-like hydrolase (HAD) domain, which is integral to the dephosphorylation step of the catalytic cycle during Ca^{2+} transport. Notably, two other MRD66 variants within this catalytic domain (p.Arg763Pro, p.Arg789Cys) also cause loss-of-function [8], highlighting the functional sensitivity of this region. The severe functional deficit caused by p.Thr714Pro aligns perfectly with *ATP2B1* 's documented high intolerance to variation (gnomAD pLI = 1.0, missense Z = 5.29). Currently, only ~12 pathogenic *de novo* heterozygous variants (missense [75%], with nonsense [25%]) are associated with MRD66, distributed throughout the gene without clear genotype-phenotype correlations [8]. The existence of asymptomatic heterozygous carriers (e.g., the mother carrying the c.3060 + 2T>G splicing variant reported by Yap et al. [13]) underscores that the pathogenicity of ATP2B1 variants is not determined by inheritance pattern alone, but by the extent of functional impairment. This observation supports the concept of a threshold effect, whereby clinical manifestations arise only when the resultant calcium dyshomeostasis exceeds a physiological compensatory capacity. Notably, some missense variants may exert a more profound dominant-negative or toxic gain-of-function effect compared to alleles leading to simple haploinsufficiency, thereby reaching this pathogenic threshold more readily. Altered Ca^{2+} dynamics could also disrupt the E/I balance, possibly involving modulation of purinergic signaling pathways (e.g., P2X7 receptors impacting GABAergic function) [19]. Our functional characterization demonstrates that the p.Thr714Pro variant impairs PMCA1 function through a dual mechanism: defective trafficking to the plasma membrane and consequent failure to maintain low resting cytosolic Ca^{2+}. This mislocalization phenotype is reminiscent of several pathogenic missense variants reported by Rahimi et al. (e.g., p.Asp239Gly, p.Thr264Ile, p.Arg991Gln) [8]. The significant elevation of basal intracellular Ca^{2+} we observed is a consistent finding across all nine missense variants functionally tested in that study. Importantly, the p.Thr714Pro variant resides within the critical P-domain. Our structural modeling suggests it disrupts key hydrogen bonds (Thr714-Asn711), likely destabilizing the local structure. This provides a plausible molecular explanation for both the mislocalization (due to protein misfolding) and the loss of calcium transport activity. Combined, our genetic, cellular, and *in silico* data robustly support the pathogenicity of the novel p.Thr714Pro variant via a loss-of-function mechanism.

Our findings have immediate clinical implications. *ATP2B1* sequencing should be prioritized in infants presenting with a neurodevelopmental disorder with early-onset seizures, even in the absence of dysmorphism or overt systemic features. This notion aligns with the concept of a pathogenic threshold, where the severity of clinical presentation correlates with the degree of functional impairment [13]. Heterozygous variants, particularly those that cause Haploinsufficiency, are associated predominantly with neurodevelopmental deficits, while biallelic genotypes lead to multi-system malformations, including primary hypoparathyroidism, distinctive craniofacial and skeletal features, and periventricular heterotopia [13]. The central role of calcium dyshomeostasis in pathogenesis supports the careful consideration of calcium channel modulators (e.g., ethosuximide for absence seizures, nimodipine) as adjunctive therapy for seizure control, although efficacy specifically in *ATP2B1*-related epilepsy requires further study. Early intensive developmental intervention is critical. Our patient's severe growth restriction necessitates proactive management, including endocrine evaluation, quarterly anthropometric monitoring, high-calorie nutritional supplementation, and surveillance of serum calcium and parathyroid hormone levels, even in the absence of current hypocalcemia [13]. Proactive neurodevelopmental support is warranted, potentially including the Early Start Denver Model for

ASD prevention given the high co-occurrence [8], and consideration of the ketogenic diet, which demonstrates ~40% efficacy in infantile spasms, potentially via ketone-mediated reduction of neuronal excitability and attenuation of P2X7 receptor-mediated neuroinflammation [19]. Prognostically, uncontrolled infantile spasms persisting beyond 12 months confer a >70% risk of significant cognitive impairment; our patient may progress to moderate ID, particularly given the persistent background EEG abnormalities. Study limitations include reliance on the HEK293T cell model; future studies utilizing neuronal models (e.g., patient-derived iPSCs differentiated into neurons) and longitudinal natural history studies of larger *ATP2B1*-variant cohorts are essential to fully elucidate pathomechanisms, define genotype-phenotype correlations, and optimize clinical management strategies.

This study has several limitations. First, the calcium imaging assay measured basal Ca^{2+} levels rather than dynamically quantifying *ATP2B1*-mediated extrusion kinetics. While elevated resting Ca^{2+} is a validated indicator of *ATP2B1* dysfunction [8], future studies employing time-resolved efflux assays (e.g., measuring the exponential decline of Ca^{2+} after a load) would provide more direct insight into pump activity. Second, our functional analysis was conducted in a heterologous system (HEK293T cells). Although this model is well-established for the initial characterization of ion transporter variants, studies using patient-derived neurons would more accurately reflect the pathomechanism in the relevant cell type. Finally, the clinical cohort of individuals with pathogenic *ATP2B1* variants remains small. Larger studies are needed to establish definitive genotype-phenotype correlations and the full clinical spectrum of MRD66.

In conclusion, we identified a novel *de novo* *ATP2B1* p.Thr714Pro variant causing MRD66 through a dual-stage pathomechanism: defective plasma membrane trafficking and intrinsic impairment of catalytic function, culminating in calcium dysregulation. This case significantly expands the phenotypic spectrum of MRD66 by demonstrating the earliest seizure onset reported to date and reinforces haploinsufficiency as the primary mechanism underlying heterozygous *ATP2B1* variants. Our integrated genetic, structural, and functional findings underscore the indispensable role of PMCA1 in neurodevelopment and calcium homeostasis, providing a foundation for developing targeted therapeutic strategies aimed at mitigating calcium dyshomeostasis in this disorder.

Author contributions

HZ: investigation, data curation, and writing – review and editing. XY: conceptualization, methodology, and writing – original draft. YL: data curation, investigation, and visualization. DY: project administration, supervision, and writing – review and editing. CM: data curation, writing – review and editing. All authors contributed to the article and approved the submitted version.

Data availability

The data generated in this study are available from the corresponding author upon reasonable request. The variant data from this study have been submitted to the ClinVar database (Submission ID: SUB15908833).

Ethics statement

The studies involving humans were approved by The First Affiliated Hospital of Bengbu Medical University (2025049). The studies were conducted in accordance with the local legislation and institutional requirements. Written informed consent for participation in this study was provided by the participants' legal guardians/next of kin. Written informed consent was obtained from the individual(s), and minor(s)' legal guardian/next of kin, for the publication of any potentially identifiable images or data included in this article.

Funding

The author(s) declared that financial support was received for this work and/or its publication. The work was supported by the Opening Project of Anhui Engineering Research Center for Neural Regeneration Technology and Medical New Materials (AHNR2025W002); Bengbu Social Science Planning Project (BB22C029); Anhui Provincial Young Backbone Teachers' Domestic Visiting and Research Training Program (JNFX2025034).

Acknowledgements

We extend our sincere appreciation to the patient and her families for their invaluable contributions to this research.

Conflict of interest

The author(s) declared no potential conflicts of interest with respect to the research, authorship, and/or publication of this article.

Generative AI statement

The author(s) declared that generative AI was not used in the creation of this manuscript.

Any alternative text (alt text) provided alongside figures in this article has been generated by Frontiers with the support of artificial intelligence and reasonable efforts have been made to ensure accuracy, including review by the authors wherever possible. If you identify any issues, please contact us.

Supplementary material

The Supplementary Material for this article can be found online at: https://www.ebm-journal.org/articles/10.3389/ebm.2026.10834/full#supplementary-material

References

1. Guerrini R, Conti V, Mantegazza M, Balestrini S, Galanopoulou AS, Benfenati F. Developmental and epileptic encephalopathies: from genetic heterogeneity to phenotypic continuum. *Physiol Rev* (2023) **103**:433–513. doi:10.1152/physrev.00063.2021

2. Wang T, Kim CN, Bakken TE, Gillentine MA, Henning B, Mao Y, et al. Integrated gene analyses of *de novo* variants from 46,612 trios with autism and developmental disorders. *Proc Natl Acad Sci U S A* (2022) **119**:e2203491119. doi:10.1073/pnas.2203491119

3. Pikor D, Hurła M, Słowikowski B, Szymanowicz O, Poszwa J, Banaszek N, et al. Calcium ions in the physiology and pathology of the central nervous system. *Int J Mol Sci* (2024) **25**:13133. doi:10.3390/ijms252313133

4. Proft J, Rzhepetskyy Y, Lazniewska J, Zhang FX, Cain SM, Snutch TP, et al. The Cacna1h mutation in the GAERS model of absence epilepsy enhances T-type Ca(2+) currents by altering calnexin-dependent trafficking of Ca(v)3.2 channels. *Sci Rep* (2017) **7**:11513. doi:10.1038/s41598-017-11591-5

5. Chen TS, Huang TH, Lai MC, Huang CW. The role of glutamate receptors in epilepsy. *Biomedicines* (2023) **11**:783. doi:10.3390/biomedicines11030783

6. Feng Y, Wei ZH, Liu C, Li GY, Qiao XZ, Gan YJ, et al. Genetic variations in GABA metabolism and epilepsy. *Seizure* (2022) **101**:22–9. doi:10.1016/j.seizure.2022.07.007

7. Li X, Tao AL, Wu N, Zhang X, Xiao F, Wang J, et al. Calcium-iron crosstalk in epileptogenesis: unraveling mechanisms and therapeutic opportunities. *Neurobiol Dis* (2025) **212**:106989. doi:10.1016/j.nbd.2025.106989

8. Rahimi MJ, Urban N, Wegler M, Sticht H, Schaefer M, Popp B, et al. *De novo* variants in ATP2B1 lead to neurodevelopmental delay. *Am J Hum Genet* (2022) **109**:944–52. doi:10.1016/j.ajhg.2022.03.009

9. Long Y, Xia JY, Chen SW, Gao CL, Liang GN, He XM, et al. ATP2B1 gene silencing increases insulin sensitivity through facilitating akt activation *via* the Ca(2+)/calmodulin signaling pathway and Ca(2+)-associated eNOS activation in endothelial cells. *Int J Biol Sci* (2017) **13**:1203–12. doi:10.7150/ijbs.19666

10. Okunade GW, Miller ML, Pyne GJ, Sutliff RL, O'Connor KT, Neumann JC, et al. Targeted ablation of plasma membrane Ca2+-ATPase (PMCA) 1 and 4 indicates a major housekeeping function for PMCA1 and a critical role in hyperactivated sperm motility and male fertility for PMCA4. *J Biol Chem* (2004) **279**:33742–50. doi:10.1074/jbc.M404628200

11. Richards S, Aziz N, Bale S, Bick D, Das S, Gastier-Foster J, et al. Standards and guidelines for the interpretation of sequence variants: a joint consensus recommendation of the American college of medical Genetics and genomics and the association for molecular pathology. *Genet Med* (2015) **17**:405–24. doi:10.1038/gim.2015.30

12. Gong D, Chi X, Ren K, Huang G, Zhou G, Yan N, et al. Structure of the human plasma membrane Ca(2+)-ATPase 1 in complex with its obligatory subunit neuroplastin. *Nat Commun* (2018) **9**:3623. doi:10.1038/s41467-018-06075-7

13. Yap P, Riley LG, Kakadia PM, Bohlander SK, Curran B, Rahimi MJ, et al. Biallelic ATP2B1 variants as a likely cause of a novel neurodevelopmental malformation syndrome with primary hypoparathyroidism. *Eur J Hum Genet* (2024) **32**:125–9. doi:10.1038/s41431-023-01484-9

14. Chen J, Sitsel A, Benoy V, Sepúlveda MR, Vangheluwe P. Primary active Ca(2+) transport systems in health and disease. *Cold Spring Harb Perspect Biol* (2020) **12**:a035113. doi:10.1101/cshperspect.a035113

15. Dickinson ME, Flenniken AM, Ji X, Teboul L, Wong MD, White JK, et al. High-throughput discovery of novel developmental phenotypes. *Nature* (2016) **537**:508–14. doi:10.1038/nature19356

16. Ehara Y, Hirawa N, Sumida K, Fujiwara A, Kagimoto M, Ooki-Okuyama Y, et al. Reduced secretion of parathyroid hormone and hypocalcemia in systemic heterozygous ATP2B1-null hypertensive mice. *Hypertens Res* (2018) **41**:699–707. doi:10.1038/s41440-018-0067-8

17. Chen M, Laursen SH, Habekost M, Knudsen CH, Buchholdt SH, Huang J, et al. Central and peripheral nervous system progenitors derived from human pluripotent stem cells reveal a unique temporal and cell-type specific expression of PMCAs. *Front Cell Dev Biol* (2018) **6**:5. doi:10.3389/fcell.2018.00005

18. Bouron A. Transcriptomic profiling of Ca2+ transport systems during the formation of the cerebral cortex in mice. *Cells* (2020) **9**:1800. doi:10.3390/cells9081800

19. Chen YH, Lin S, Jin SY, Gao TM. Extracellular ATP is a homeostatic messenger that mediates cell-cell communication in physiological processes and psychiatric diseases. *Biol Psychiatry* (2025) **97**:41–53. doi:10.1016/j.biopsych.2024.04.013

EBM Experimental Biology and Medicine

TYPE Review
PUBLISHED 02 March 2026
DOI 10.3389/ebm.2026.10835

OPEN ACCESS

*CORRESPONDENCE
Zairong Wei,
zairongwei@163.com
Shaoying Gao,
729414738@qq.com

RECEIVED 25 September 2025
REVISED 06 February 2026
ACCEPTED 12 February 2026
PUBLISHED 02 March 2026

CITATION
Long F, Pan X, He A, Wang X, Wei Z and Gao S (2026) Skeletal muscle reprogramming in peripheral nerve injury: mechanisms, therapeutic roles, and complication management. *Exp. Biol. Med.* 251:10835. doi: 10.3389/ebm.2026.10835

Skeletal muscle reprogramming in peripheral nerve injury: mechanisms, therapeutic roles, and complication management

Fuqiang Long[1], Xiaoru Pan[1], Anxin He[1], Xinlu Wang[1], Zairong Wei[1,2,3]* and Shaoying Gao[1]*

[1]Department of Burns and Plastic Surgery, Affiliated Hospital of Zunyi Medical University, Zunyi, China, [2]The 2011 Collaborative Innovation Center of Tissue Damage Repair and Regeneration Medicine, Affiliated Hospital of Zunyi Medical University, Zunyi, China, [3]The Collaborative Innovation Center of Tissue Damage Repair and Regeneration Medicine, Zunyi Medical University, Zunyi, China

Abstract

Peripheral nerve injury (PNI) presents a significant clinical challenge, frequently leading to long-term neuromuscular dysfunction, muscle atrophy, fibrosis, and chronic pain. Traditional repair strategies, including microsurgical reconnection and neurotrophic support, often yield limited functional recovery, especially in cases of delayed or incomplete reinnervation. In this context, skeletal muscle reprogramming—defined as the intentional modulation of cellular fate, function, or metabolic state in muscle-resident cells—has emerged as a promising strategy to enhance regenerative outcomes. This process involves transcriptional, epigenetic, and metabolic interventions targeting myogenic progenitors, fibro-adipogenic progenitors (FAPs), satellite cells (MuSCs), and the broader muscle microenvironment. Recent studies demonstrate that reprogramming strategies can mitigate denervation-induced muscle atrophy, delay fibrotic remodeling, promote neuromuscular junction (NMJ) reconstruction, and even stimulate endogenous nerve regrowth via retrograde signaling. Mechanistic insights have uncovered pivotal roles for signaling pathways such as Wnt/β-catenin, TGF-β, Notch, and HDAC-regulated chromatin dynamics. Furthermore, innovations in small molecule cocktails, CRISPR-based transcriptional reactivation, and metabolic rewiring have expanded the therapeutic toolkit for muscle preservation and regeneration. This review comprehensively examines the molecular mechanisms, therapeutic roles, and translational challenges of skeletal muscle reprogramming in the context of PNI. We explore how muscle-targeted interventions can address complications of denervation, improve the efficacy of nerve repair, and offer a synergistic axis

of regeneration when integrated with nerve-centric strategies. Finally, we identify key knowledge gaps and outline future research directions required to translate reprogramming-based therapies into clinical practice.

KEYWORDS

skeletal muscle reprogramming, peripheral nerve injury, therapeutic strategies, complications, regeneration medicine

Impact statement

This work introduces skeletal muscle reprogramming as a transformative approach for managing peripheral nerve injuries (PNIs), offering a novel perspective by targeting muscle regeneration, rather than solely focusing on nerve repair. The insights provided here bridge a critical gap in current therapeutic strategies, addressing the complications of denervation-induced muscle atrophy, fibrosis, and chronic pain.

The article advances the field by synthesizing the latest molecular, epigenetic, and metabolic approaches to skeletal muscle reprogramming, particularly in PNI contexts. It highlights how muscle-targeted therapies, integrated with nerve-centered strategies, can improve regenerative outcomes and functional recovery. This work presents new insights into the mechanisms underlying muscle reprogramming, such as the role of signaling pathways (e.g., Wnt/β-catenin, TGF-β) and small molecule cocktails. It introduces the potential for retrograde signaling to stimulate nerve regrowth and neuromuscular junction (NMJ) reconstruction, expanding the therapeutic toolkit for PNI recovery.

The new information shifts the paradigm from treating muscle and nerve damage separately to adopting a synergistic approach. By focusing on muscle reprogramming, this work may lead to more effective, holistic treatments for PNI, particularly for cases with poor recovery due to prolonged or incomplete reinnervation.

Introduction

Peripheral nerve injuries (PNIs) affect millions globally and are commonly associated with trauma, surgery, or chronic compression syndromes [1]. Despite advances in microsurgical techniques and neurotrophic factor delivery, the functional recovery following PNI remains suboptimal—particularly in proximal or delayed repairs—largely due to irreversible changes in the denervated skeletal muscle [2]. Denervation triggers a cascade of degenerative events in muscle tissue, including fiber atrophy, fibrosis, mitochondrial dysfunction, and motor endplate destabilization, all of which significantly compromise reinnervation and functional restitution [3, 4]. Historically, therapeutic interventions for PNI have centered on promoting axonal regrowth and guiding nerve regeneration. However, emerging evidence underscores the critical importance of preserving or reactivating the denervated target tissue—primarily skeletal muscle—as an equally essential component of successful nerve repair. Indeed, the muscle environment plays an active role in modulating neuromuscular regeneration [5–7], through retrograde signaling, extracellular matrix remodeling, and trophic support for regenerating axons [6, 8, 9]. Skeletal muscle reprogramming represents a paradigm shift in the treatment of PNI and its complications [10]. Rather than focusing solely on neuronal repair, reprogramming strategies aim to convert, preserve, or rejuvenate muscle-resident cells—such as satellite cells, fibro-adipogenic progenitors (FAPs), and even mature myofibers—via targeted molecular interventions [11, 12]. This approach not only prevents muscle degeneration but may also transform the injured muscle into a more permissive and instructive environment for axonal regeneration. In this review, we systematically explore the concept of skeletal muscle reprogramming in the context of peripheral nerve injury. We provide an overview of its underlying cellular and molecular mechanisms, examine current experimental and translational strategies, and evaluate its potential to mitigate PNI-associated complications such as muscle fibrosis and chronic pain. Additionally, we highlight the intersection between muscle biology and nerve regeneration, proposing skeletal muscle not merely as a passive target but as an active participant in neuromuscular repair.

Pathophysiology of peripheral nerve injury and complications

Peripheral nerve injury (PNI) initiates a complex and time-sensitive cascade of degenerative and regenerative events, impacting both the nervous system and its target organs, primarily skeletal muscle. Understanding the cellular and molecular basis of PNI is critical to identifying the therapeutic window for skeletal muscle reprogramming and its role in functional recovery (Figure 1).

Classification and etiology of PNI

Peripheral nerve injuries (PNIs) are stratified by severity according to Seddon's and Sunderland's systems. Seddon's scheme distinguishes three types—neurapraxia (transient conduction block), axonotmesis (axon disruption with intact connective sheaths), and neurotmesis (complete nerve transection)—while Sunderland refines this into five grades, specifying the extent of damage to axons, endoneurium,

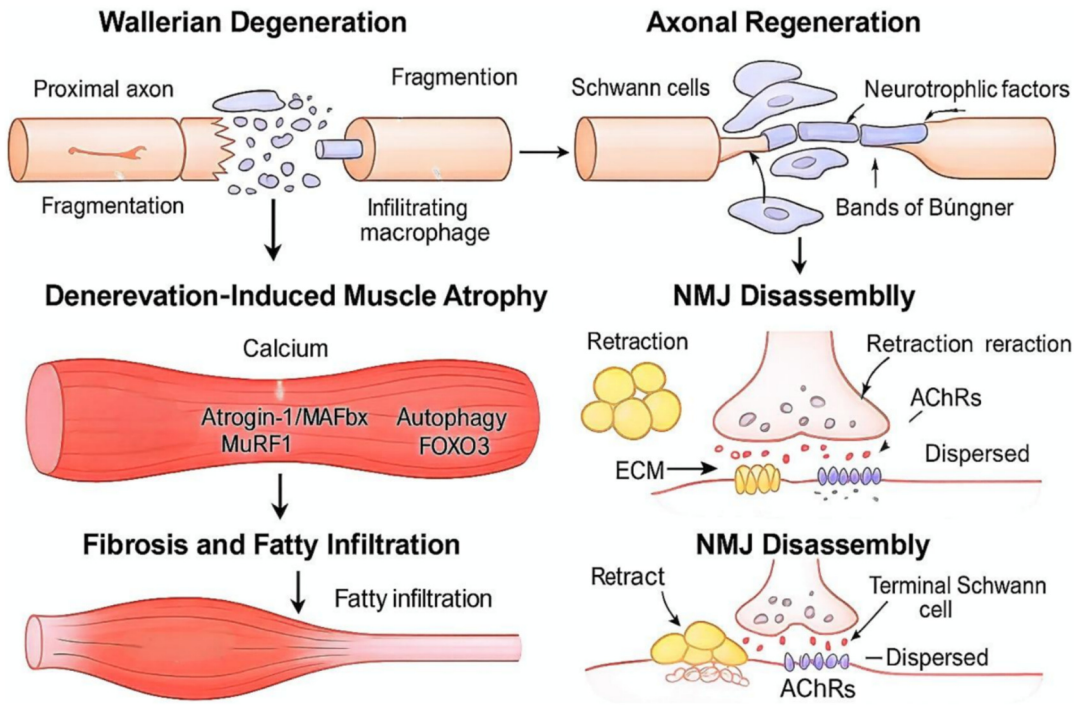

FIGURE 1
Pathophysiology of Peripheral Nerve Injury and Muscle Degeneration. This figure illustrates the sequential pathological cascade triggered by peripheral nerve injury, encompassing nervous system changes and target muscle degeneration. The section on Wallerian degeneration depicts the fragmentation of the distal axon and the subsequent clearance of debris by Schwann cells and macrophages. Denervation-induced muscle atrophy is highlighted through the activation of proteolytic and autophagic pathways, such as those involving Atrogin-1, MuRF1, and FOXO3, which lead to a rapid loss of muscle mass. Furthermore, the figure reveals the aberrant activation of fibro-adipogenic progenitors (FAPs) and their differentiation into fibroblastic and adipogenic lineages, ultimately resulting in tissue fibrosis and fatty infiltration.

perineurium, and epineurium [13, 14]. Etiologies range from blunt trauma and sharp lacerations to iatrogenic injury during surgery [15], tumor compression, and inflammatory neuropathies. The potential for regeneration diminishes as injury severity increases and as the interval to reinnervation lengthens; hence, prompt diagnosis and intervention are critical to maintain muscle responsiveness and prevent irreversible atrophic changes [16].

Wallerian degeneration and axonal regeneration

Following axonal transection, Wallerian degeneration ensues within hours: the distal axon and myelin sheath fragment and are cleared by Schwann cells and infiltrating macrophages [17]. Concurrently, Schwann cells adopt a reparative phenotype, upregulating neurotrophic factors such as NGF, GDNF, and BDNF, and aligning into Bands of Büngner that channel regrowing axonal sprouts [18]. Despite this orchestrated response, axonal regrowth proceeds slowly—typically 1–3 mm per day—and often fails to bridge long gaps, especially in proximal injuries or when surgery is delayed [19]. Such delays exacerbate target muscle atrophy and highlight the necessity of preserving the muscle niche to optimize reinnervation [20].

Denervation-induced skeletal muscle atrophy

Denervated muscle fibers rapidly undergo atrophy driven by disrupted calcium homeostasis, oxidative stress, and activation of proteolytic systems such as the ubiquitin–proteasome pathway (via atrogin-1/MAFbx and MuRF1) [21]. Autophagy–lysosome activity is also upregulated early after denervation, facilitating removal of damaged organelles but becoming insufficient at later stages of atrophy [22]. FOXO3-mediated transcriptional upregulation of atrophy-related genes further amplifies catabolic signaling [23]. Concurrently, the IGF-1/Akt/mTOR axis is downregulated, reducing anabolic drive and protein synthesis [24]. Loss of neural stimuli also triggers sarcomere disassembly, shifts fiber-type composition toward fast-twitch phenotypes, and exacerbates mitochondrial dysfunction [25].

Fibrosis and fatty infiltration

With prolonged denervation, myofibers are progressively replaced by fibrotic and adipose tissue [26]. Fibro-adipogenic progenitors (FAPs), normally transiently activated after injury, proliferate unchecked in the absence of reinnervation, driving extracellular matrix (ECM) deposition through TGF-β signaling [27]. This process is exacerbated by a dysregulated balance of matrix metalloproteinases and their inhibitors (MMPs and TIMPs), leading to ECM stiffening that impedes myogenic repair and creates a physical barrier to regenerating axons [28]. Simultaneously, ectopic lipid accumulation from FAPadipogenic differentiation further degrades muscle architecture and metabolic homeostasis [29].

Neuromuscular junction (NMJ) disassembly

The NMJ, comprising the presynaptic motor terminal, the postsynaptic muscle membrane with clustered acetylcholine receptors (AChRs), and terminal Schwann cells, deteriorates rapidly after denervation [30]. AChR clusters disperse and synaptic folds flatten as presynaptic terminals retract; myonuclei drift from the subsynaptic region [31]. Initially, terminal Schwann cells extend processes that guide regenerating axons, but prolonged denervation leads to Schwann cell apoptosis, undermining reinnervation fidelity [32]. Restoring NMJ architecture thus requires coordinated nerve and muscle repair strategies [33].

Pain and sensory complications

PNI frequently precipitates neuropathic pain, marked by ectopic neuronal firing and central sensitization [34]. Denervated muscle contributes to pain through increased proinflammatory cytokines (e.g., IL-6, TNF-α), altered metabolic signaling, and heightened peripheral nociceptor sensitivity [35]. Effective management of sensory symptoms therefore demands both neurocentric interventions and strategies that modulate the denervated muscle environment, further supporting a role for muscle reprogramming in comprehensive PNI management [36].

Concept and classification of skeletal muscle reprogramming

Definition and scope

Skeletal muscle reprogramming encompasses deliberate interventions that alter the fate or functional phenotype of muscle-resident or stromal cells to restore or enhance regeneration after injury. Unlike classical myogenesis, which relies solely on activation of endogenous satellite cells, reprogramming employs transcriptional, epigenetic, and metabolic cues to override impaired regenerative programs [37–39]. By reinforcing myogenic commitment in senescent MuSCs [40], converting fibro-adipogenic progenitors into myogenic-like cells [26, 41], or modulating the niche to support reinnervation, angiogenesis, and antifibrotic remodeling [42], this approach extends beyond mere muscle repair. In the setting of peripheral nerve injury (PNI), where denervated muscle rapidly atrophies and undergoes fibrosis and synaptic loss, skeletal muscle reprogramming serves as a critical adjunct to nerve-centered therapies.

Key target cell populations

Muscle satellite cells (MuSCs), marked by Pax7, are the principal drivers of myofiber regeneration. Under chronic denervation or aging, MuSCs enter senescence or apoptosis, depleting the progenitor pool [43]. Reprogramming strategies restore MuSC function bysuppressing oxidative stress [44], inhibiting NF-κB–mediated inflammatory suppression [45], and remodeling histone marks (H3K27ac) to revive stemness [46]. Fibro-adipogenic progenitors (FAPs) normally support acute repair but drive fibrosis and fatty infiltration under chronic insult. Redirecting FAP fate through TGF-β/Smad blockade and IL-4/STAT6 activation promotes secretion of pro-myogenic factors such as follistatin while suppressing adipogenesis [8, 47]. Moreover, epigenetic remodeling ofFAP-derived extracellular vesicles with miR-206/133 cargo enhances MuSC activity and niche rewiring via M2 macrophage polarization or GDNF-mediated innervation further restrains FAP dysregulation. Fibroblasts and myofibroblasts, which contribute to ECM deposition and scarring after PNI, can be transdifferentiated into induced myogenic progenitor cells (iMPCs) using MyoD overexpression, small-molecule cocktails, and HDAC inhibition; yet this conversion is limited by TGF-β–driven epigenetic barriers, matrix stiffness, and inflammation [48]. Although not direct reprogramming targets, immune and vascular cells are reshaped by muscle-centric interventions, with M2 macrophages and neovessels forming supportive niches [49]. Lastly, mature myofibers exhibit metabolic and structural plasticity: interventions such as AMPK activation or NAD^+ supplementation stimulate mitochondrial biogenesis and shift fiber-type profiles, creating a substrate more conducive to reinnervation [50].

Inductive modalities

Transcriptional reprogramming via overexpression of myogenic factors like MyoD or Pax7 can restart myogenesis in fibroblasts or senescent MuSCs; however, the balance between these factors is critical, as Pax7 overexpression may inhibit MyoD-driven differentiation [51]. Epigenetic modulation uses HDAC

TABLE 1 Mechanistic Classification of skeletal muscle reprogramming approaches.

Strategy	Mechanism	Advantages	Limitations	References
Transcriptional	Forced expression or activation of myogenic transcription factors (e.g., MyoD, Pax7)	High efficiency in direct lineage conversion and myogenic commitment Pt	Potential risk of oncogenic transformation and formation of immature or unstable myofibers [s]	[58]
Epigenetic Mc	Modulation of chromatin accessibility via HDAC inhibitors, DNA demethylases, or CRISPRa-effectors Fs	Facilitates activation of endogenous muscle-specific genes without introducing exogenous sequences Rs	Risk of unintended global epigenetic shifts and potential for off-target gene activation [n]	[59, 60]
Metabolic Ac	Alteration of cellular bioenergetics to boost mitochondrial function (e.g., AMPK agonists, NAD+) m	Mitochondrial function (e.g., AMPK agonists, NAD+) high clinical feasibility and safety; addresses the metabolic decline associated with denervation n	Primarily addresses bioenergetics; may be insufficient to drive full structural regeneration in chronic injury [y]	[61]
Pharmacological Ul	Use of cytokines and small molecules to influence signaling pathways (e.g., IGF-1, Wnt agonists)	Highly translatable and compatible with injectable delivery systems or smart biomaterials ss	Short molecular half-life requires sustained release systems to maintain therapeutic levels [s]	[62, 63, 131]

This table systematically classifies skeletal muscle reprogramming strategies based on their molecular intervention levels and includes a critical evaluation of their advantages and limitations to address reviewer recommendations. Transcriptional reprogramming utilizes the forced expression of myogenic regulatory factors such as MyoD to achieve high-efficiency lineage conversion, though it carries risks of oncogenic transformation and the formation of immature myofibers. Epigenetic reprogramming modulates chromatin accessibility to activate endogenous genes without introducing exogenous sequences, but it must be carefully monitored for off-target modifications. Metabolic reprogramming targets the bioenergetic decline in denervated muscle, offering high clinical safety and feasibility, yet it may be insufficient to drive full structural regeneration independently. Pharmacological reprogramming employs small molecules to flexibly modulate signaling pathways with high local controllability, but its efficacy is often limited by the short half-life of these molecules.

inhibitors and DNA methylation inhibitors such as 5-azacytidine to relax chromatin, facilitating activation of muscle-specific genes [52]. Chemical cocktails that recapitulate developmental signals—combining forskolin, CHIR99021, FGF2, and IGF-1—activate Wnt/β-catenin and PI3K/AKT pathways to induce reprogramming without genetic manipulation [53]. CRISPR-mediated activation (CRISPRa) employs dCas9 fused to transcriptional activators to upregulate endogenous Myod1 and Myf5 with spatial and temporal precision [54]. Finally, metabolic and mechanical cues such as hypoxia-induced ROS, ECM stiffness, and cyclic stretch modulate mechanotransduction pathways (e.g., YAP/TAZ) to influence cell fate decisions [55].

Classification of reprogramming strategies

Reprogramming approaches can be categorized mechanistically into four classes (Table 1). Transcriptional reprogramming involves forced expression or activation of myogenic transcription factors, exemplified by MyoD-driven conversion of fibroblasts [56]. Epigenetic reprogramming modulates chromatin accessibility via HDAC inhibitors, DNA demethylases like 5-aza, or CRISPRa/dCas9 tethered to epigenetic effectors [57, 58]. Metabolic reprogramming alters bioenergetic states through AMPK activation or NAD^+ supplementation, enhancing mitochondrial function and oxidative capacity [50]. Pharmacological reprogramming utilizes cytokines and small molecules—such as IGF-1, Wnt agonists, and TGF-β inhibitors—to shift cell fate trajectories [53, 59]. This framework informs tailored therapy design for specific PNI-related pathologies, whether combating atrophy, fibrosis, or NMJ instability.

Combinatorial and sequential modalities

To maximize efficacy, emerging studies advocate for integrated, staged interventions. In a murine denervation model, sequential administration of CHIR99021 and HDAC inhibitors followed by MyoD-CRISPRa achieved superior myofiber regeneration compared to any single modality, illustrating the synergism of metabolic priming, epigenetic opening, and transcriptional activation [60]. Such combinatorial regimens may be delivered via smart biomaterials that release agents in response to enzymatic or pH changes in the injured niche, providing temporal control aligned with endogenous repair phases [61, 62].

Molecular mechanisms of skeletal muscle reprogramming

Skeletal muscle reprogramming involves a complex interplay of transcriptional activation, chromatin remodeling, metabolic reconfiguration, and cell–cell signaling. These molecular mechanisms determine whether denervated muscle undergoes regeneration, fibrosis, or irreversible degeneration. Understanding these processes provides a basis for the rational design of reprogramming therapies in the context of peripheral nerve injury (PNI) (Figure 2).

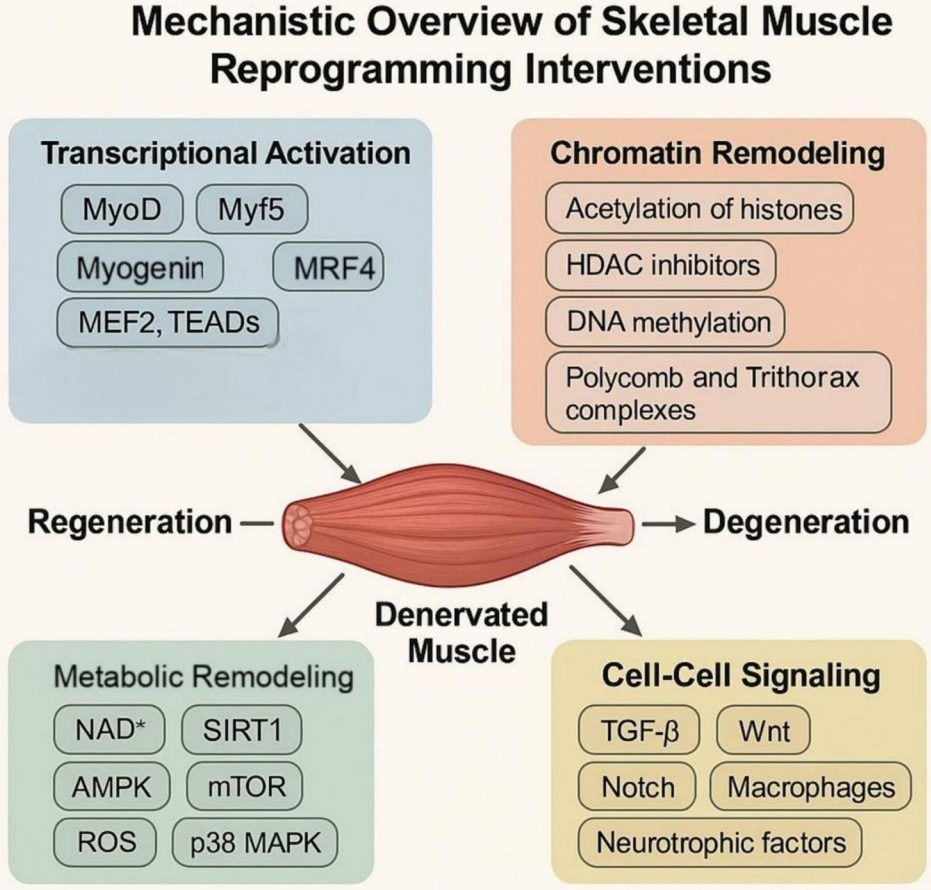

FIGURE 2
Mechanistic Overview of Skeletal Muscle Reprogramming Interventions. This figure provides a comprehensive mechanistic framework for reprogramming interventions in the context of peripheral nerve injury. It details the synergistic interplay between transcriptional activation, chromatin remodeling, metabolic reconfiguration, and intercellular signaling pathways such as Wnt, Notch, and TGF-β. These reprogramming strategies do not only target mature myofibers to improve contractile performance but also reshape the regenerative microenvironment by modulating extracellular matrix (ECM) components and inducing M2 macrophage polarization, aiming to transform the degenerated muscle niche into a supportive environment for axonal regeneration.

Transcriptional control of myogenic identity

Transcription factors (TFs) are primary regulators of cellular identity and lineage reprogramming. In skeletal muscle, the core myogenic regulatory factors (MRFs)— MyoD, Myf5, Myogenin, and MRF4—coordinate muscle-specific gene expression and lineage commitment. MyoD, in particular, can convert non-myogenic cells, such as fibroblasts, into myoblast-like cells by binding to E-box elements and recruiting epigenetic coactivators [63]. Pax7 is another key TF that maintains the self-renewal and quiescence of satellite cells; its acetylation status regulates muscle stem cell function and differentiation potential [64]. TF networks are further modulated by context-specific cofactors such as MEF2, TEADs, and YAP/TAZ, which integrate developmental cues and mechanical signals to fine-tune myogenic outputs [65, 66].

Epigenetic remodeling and chromatin dynamics

Epigenetic modifications govern the accessibility of myogenic loci, influencing a cell's responsiveness to reprogramming signals. Histone acetylation, such as H3K9ac mediated by p300/CBP, facilitates open chromatin at myogenic enhancers, while histone deacetylation by HDACs represses myogenic genes. HDAC inhibitors, like trichostatin A, have been shown to enhance MyoD-induced conversion efficiency [67]. DNA methylation also plays a crucial role; hypermethylation of muscle-specific promoters (e.g., Myf5)

can block myogenic differentiation, whereas inhibitors like 5-azacytidine demethylate these regions and restore transcriptional competency [68]. Chromatin regulators, such as the Polycomb and Trithorax complexes, dynamically repress or activate gene loci. EZH2, a methyltransferase in PRC2, represses Pax7 and MyoD; its inhibition reactivates satellite cell proliferation in aged or denervated muscle [69]. CRISPRa/i systems, employing engineered dCas9-fused activators or repressors, offer locus-specific epigenetic modulation, enabling fine control over endogenous gene expression without genome editing [69].

Metabolic regulation and mitochondrial rewiring

Muscle regeneration and cell fate decisions are tightly coupled to metabolic states. Oxidative metabolism favors MuSC quiescence and self-renewal, whereas glycolytic flux supports proliferation and differentiation [70]. Denervation leads to mitochondrial fragmentation and oxidative stress, impairing regenerative potential [71]. Boosting NAD^+ levels through nicotinamide riboside or SIRT1 activation improves mitochondrial function and enhances myogenic capacity in aging and injury [72]. The AMPK and mTOR pathways are also pivotal; AMPK promotes autophagy and metabolic resilience, while mTORC1 drives protein synthesis and muscle hypertrophy [73, 74]. Their balanced modulation is essential in reprogramming strategies. Reactive oxygen species (ROS) play dual roles; while excessive ROS is damaging, moderate levels act as signaling molecules to stimulate regeneration via p38 MAPK and NRF2 pathways [75].

Crosstalk with the extracellular niche

The extracellular matrix (ECM), vasculature, and immune system shape the reprogramming landscape via paracrine and mechanical cues. TGF-β signaling is a central inhibitor of regeneration, promoting FAP differentiation into fibrotic and adipogenic lineages; its blockade with agents such as losartan or TGF-β–neutralizing antibodies reduces fibrosis and enhances muscle regeneration in injury models [76, 77]. The Wnt/β-catenin pathway plays a dual role: canonical Wnt signaling promotes MuSC activation, whereas non-canonical ligands (e.g., Wnt5a) can impair myogenic reprogramming by inducing pro-inflammatory cascades [78]. Notch signaling maintains satellite cell quiescence and is essential during early regeneration; modulating Notch–Delta interactions (for example, via γ-secretase inhibitors or Delta-like ligand mimetics) improves functional recovery after PNI [79]. Finally, macrophage polarization from M1 to M2 phenotypes supports regenerative myogenesis—delivery of IL-4 or IL-10 to injured muscle skews macrophages toward an M2 profile, creating a pro-regenerative microenvironment that synergizes with reprogramming cues [80].

Synaptic and neurotrophic interactions

Recent findings suggest that reprogrammed muscle can exert retrograde effects on the regenerating nerve. Muscle-restricted overexpression of neurotrophic factors—including IGF-1, BDNF and GDNF—enhances neuronal survival and axonal elongation in models of peripheral nerve injury [81]. Myogenic reprogramming also restores the expression of key synaptic organizers, such as Rapsyn, Agrin and MuSK, which are essential for neuromuscular junction integrity [82]. Additionally, axon-guidance molecules—including Netrin-1, Semaphorins and Slit-Robo ligands—are modulated in reprogrammed muscle, influencing reinnervation fidelity and guiding regenerating axons to their targets [83].

Integration and therapeutic implications

Integrating these molecular mechanisms provides a comprehensive framework for developing targeted interventions in peripheral nerve repair. Combinatorial regimens that couple transcriptional activation with epigenetic modulation and metabolic priming— delivered via advanced vector systems or smart biomaterials—have demonstrated synergistic restoration of muscle mass and function in preclinical models [10]. However, clinical translation must overcome challenges in delivery, including achieving tissue-specific targeting, minimizing immunogenicity, and avoiding off-target effects inherent to viral vectors and genome editors [84, 85]. Furthermore, patient-specific variables such as age-related declines in MuSC responsiveness and heterogeneity in injury severity necessitate personalized dosing and modality selection to optimize therapeutic outcomes [86].

Therapeutic applications of muscle reprogramming in peripheral nerve injury

Skeletal muscle reprogramming is a new way to treat peripheral nerve injury (PNI). It helps in three main ways: keeping muscles healthy, creating a better environment for healing, and improving the connection between nerves and muscles. Traditional treatments focus on the nerves, but this new approach works directly on the muscles that have lost their nerve connections. It makes the muscles not just something that nerves connect to, but an active part of the healing process.

Preservation of muscle mass and prevention of atrophy

One of the earliest and most severe consequences of PNI is muscle atrophy, driven by a disruption in neuromuscular signaling and sustained inactivity. Prompt initiation of reprogramming strategies is essential, as delayed intervention may lead to irreversible myofiber degeneration. By reactivating myogenic programs through overexpression of transcription factors such as MyoD and Pax7, satellite cells can be re-engaged to promote tissue regeneration even in non-myogenic compartments [87, 88]. In parallel, reprogramming approaches that inhibit catabolic pathways—including FOXO3, atrogin-1, and MuRF1— have been shown to effectively reduce proteolysis, thereby preserving muscle mass [89]. Enhancing mitochondrial function through NAD^+ supplementation and AMPK activation further supports oxidative metabolism and delays disuse atrophy [90, 91]. Preclinical studies in sciatic nerve transection models treated with small molecule cocktails have demonstrated sustained preservation of fiber cross-sectional area and contractile protein expression, even after prolonged denervation [92].

Anti-fibrotic and anti-adipogenic remodeling

Following chronic denervation, skeletal muscle undergoes fibrotic and adipogenic remodeling, compromising both tissue function and its capacity for reinnervation [93]. Fibro-adipogenic progenitors (FAPs), which initially support regeneration, become pathological if not properly regulated. Reprogramming during the early post-injury period takes advantage of a critical window in which FAPs remain plastic and responsive [94]. Targeted inhibition of TGF-β signaling in FAPs has been shown to redirect their differentiation toward a quiescent or pro-myogenic state, thereby mitigating fibrotic scarring [95]. Simultaneously, pharmacological agents that normalize extracellular matrix composition—such as inhibitors of collagen synthesis or enhancers of matrix metalloproteinase activity—contribute to structural recovery and tissue elasticity [11]. The use ofWnt agonists and HDAC inhibitors further blocks adipogenic transcription factors like PPARγ and C/EBPα, limiting ectopic fat deposition [96]. Collectively, these effects preserve structural integrity and create a more permissive environment for axonal regrowth and synapse formation [97].

Enhancement of neuromuscular junction (NMJ)

Following spinal cord injury, the neuromuscular junction (NMJ) is particularly vulnerable to denervation, leading to rapid disassembly characterized by fragmentation of acetylcholine receptor (AChR) clusters and degeneration of synaptic architecture [98]. However, reprogramming interventions, if implemented early—ideally within days of injury—can restore NMJ integrity [99]. This restoration involves the upregulation of synaptic scaffolding proteins such as Rapsyn and Dok-7 [100, 101], which stabilize AChR distribution across the postsynaptic membrane. Additionally, the restoration of agrin- MuSK signaling is crucial for accurate synaptogenesis, enabling regenerating axons to reform functional NMJs [102]. Furthermore, reprogramming indirectly benefits terminal Schwann cells, whose reactivation is essential for guiding axons back to their target zones [98]. Improved NMJ integrity, as demonstrated in multiple animal models, corresponds with better functional outcomes, including enhanced muscle responsiveness and coordination (Figure 3) [103].

Promotion of retrograde signaling and axonal regeneration

While axonal regeneration has been primarily attributed to neuron-intrinsic mechanisms, recent studies demonstrate that reprogrammed muscle actively participates via retrograd signaling [11]. Muscle fibers and satellite cells subjected to reprogramming secrete neurotrophic myokines—including IGF-1, CNTF, and BDNF—which collectively enhance neuronal survival and axonal elongation [11, 104, 105]. In addition, muscle-derived axon guidance molecules such as netrin-1, semaphorins, and ephrin ligands orchestrate axonal pathfinding, ensuring precise reinnervation of target muscle territories [106]. The release of synaptic attractants, notably agrin and laminins, further strengthens axon–muscle connectivity and promotes accurate synapse formation [107]. These insights reposition muscle tissue from a passive recipient to a dynamic signaling hub that supports and directs nerve regeneration.

Improvement of functional recovery and motor output

Ultimately, the success of any intervention for PNI hinges on its ability to restore motor function [14]. Skeletal muscle reprogramming improves functional outcomes by enhancing both structural and metabolic properties of the muscle. This approach upregulates key sarcomeric proteins, including myosin heavy chain and titin [108], which are essential for efficient force generation. It also counteracts denervation-induced fiber-type transitions by promoting a shift from fast glycolytic to oxidative phenotypes, thereby augmenting fatigue resistance and endurance [109]. Moreover, muscle reprogramming

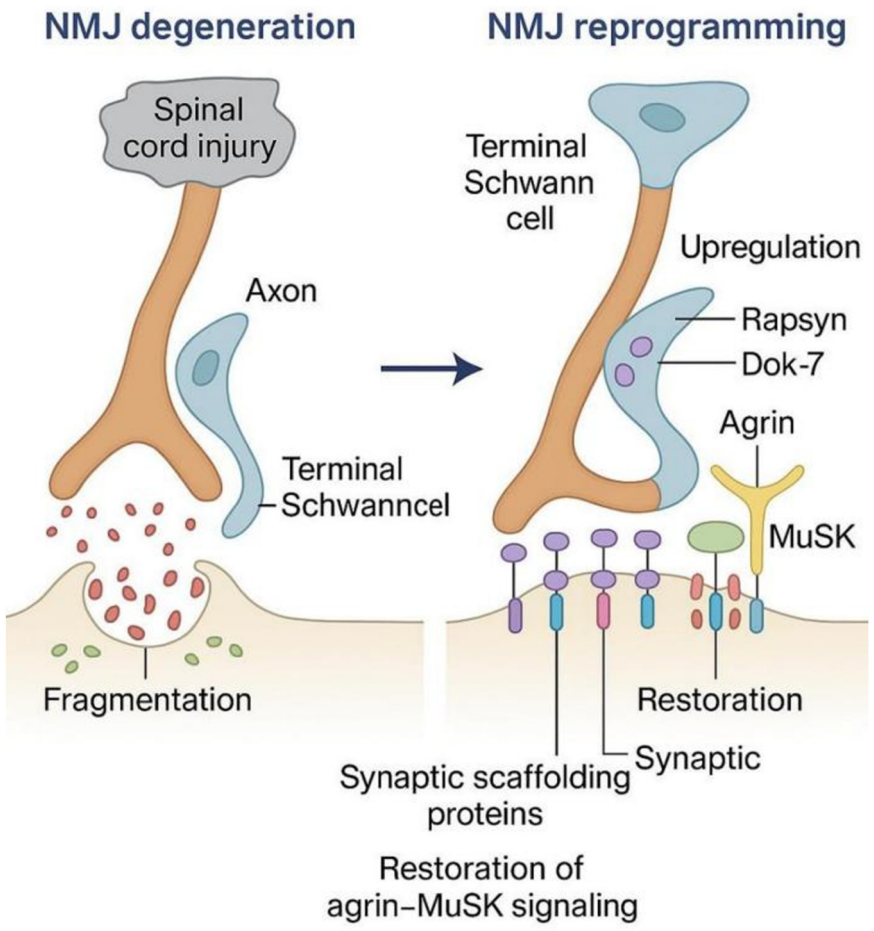

FIGURE 3
Neuromuscular Junction (NMJ) Disassembly and Reformation. This figure contrasts the disassembly of the neuromuscular junction (NMJ) following peripheral nerve injury with the process of precise reconstruction induced by muscle reprogramming. The left panel depicts the dispersal of acetylcholine receptor (AChR) clusters and the degradation of the postsynaptic membrane following denervation. The right panel illustrates the restoration of synaptic scaffolding proteins, such as Rapsyn and Dok-7, and the reactivation of the Agrin-MuSK signaling axis under reprogramming interventions. These mechanisms collectively promote functional synapse reformation and generate retrograde signals through the secretion of neurotrophic factors, such as IGF-1, BDNF, and GDNF, which enhance neuronal survival and guide regenerating axons back to their original target territories.

stabilizes the tendon–muscle interface and drives targeted ECM remodeling to restore effective force transmission across the myotendinous junction [110]. Functional benefits in rodent models—evidenced by enhanced EMG compound muscle action potentials, increased grip strength, and improved gait parameters—underscore the translational promise of these strategies [111].

Synergy with nerve-centered therapies

Although skeletal muscle reprogramming is not intended to replace conventional nerve repair, it functions as a powerful adjunct when combined with nerve-centered therapies [112]. Nerve-centered therapies encompass a range of strategies designed to restore or reconstruct damaged nerves, including nerve grafting, neurotrophic scaffolds, and cell-based interventions, such as the transplantation of induced pluripotent stem cell (iPSC)-derived motor neurons [113, 114]. These interventions primarily aim to promote axonal regrowth, restore neural continuity, and reestablish functional synapses with target muscles. Despite their utility, the clinical success of these therapies is often limited by challenges such as poor receptivity of target muscles, misdirected axonal growth, and insufficient trophic or structural support for regenerating neurons, particularly in cases involving long-gap peripheral nerve injuries or delayed surgical repair [115].

Integrating skeletal muscle-targeted reprogramming with these nerve-centered modalities can overcome many of these limitations, yielding regenerative outcomes superior to those achieved by either approach alone. For example, simultaneous nerve grafting and localized delivery of muscle reprogramming factors not only enhances the intrinsi regenerative capacity of grafts but also improves axonal targeting and synaptic specificity within reinnervated muscles [116]. By optimizing the distal muscle environment, reprogramming strategies facilitate the precise alignment of regenerating axons with neuromuscular junctions, thereby promoting stable and functional connectivity [117]. Additionally, co-delivery of reprogramming factors with iPSC-derived motor neurons has been shown to establish a supportive regenerative niche, enriched with trophic cues and extracellular matrix components, which promotes neuronal survival, integration, and synapse formation [118]. Beyond cellular co-therapies, bioengineered scaffolds seeded with reprogrammed muscle cells can serve as hybrid conduits that bridge the muscle–nerve interface, offering both physical alignment for axonal growth and biochemical conditioning of the muscle to sustain neural input. These constructs enable synchronized regeneration of nerve and muscle tissues, addressing one of the major barriers to full functional recovery [119]. Such integrated approaches hold particular promise for long-gap injuries and delayed repair contexts, where temporal and spatial coordination of proximal axonal outgrowth with distal muscle preservation is critical. By simultaneously supporting nerve regeneration and maintaining a receptive, functional muscle substrate, skeletal muscle reprogramming amplifies the therapeutic impact of nerve-centered interventions, ultimately driving more robust and durable functional recovery [120].

Clinical considerations and translational outlook

Despite encouraging preclinical outcomes, the translation of skeletal muscle reprogramming into clinical therapies faces multiple challenges [10]. Foremost are regulatory considerations for gene-modification and cell-transplantation approaches, including vector safety, manufacturing consistency, and long-term follow-up requirements [121]. Scaling protocols from rodent models to human patients necessitates optimizing dosage, delivery volumes, and accounting for slower regeneration kinetics and complex biomechanics in larger muscles [122]. Efficient, targeted delivery of reprogramming agents remains a pivotal hurdle, driving the development of minimally invasive modalities such as ultrasound-mediated injection and nanoparticle carriers [123]. Immune compatibility, particularly with viral vectors or allogeneic cells, further complicates clinical deployment and underscores the need for non-immunogenic delivery platforms [124]. Looking ahead, advances in biomaterials design, synthetic biology, and non-viral gene-delivery vectors hold promise to overcome these barriers. Rigorous clinical trials will be essential to evaluate the safety, efficacy, and durability of reprogramming-based interventions in diverse PNI patient populations.

Recent advances in reprogramming strategies

In recent years, muscle reprogramming has evolved from proof-of-concept studies using transcription factors or small molecules to sophisticated, translationally oriented platforms [125]. These strategies not only boost regenerative capacity but also tackle critical obstacles—off-target effects, immune responses, and scalability—that have impeded clinical translation. Below, we highlight the most impactful innovations in skeletal muscle reprogramming for peripheral nerve injury repair, respective translational bottlenecks provided in Table 2.

Single-cell multi-omics for target discovery

Recent single-cell RNA sequencing (scRNA-seq) and single-nucleus ATAC sequencing (snATAC-seq) studies have revealed extensive cellular heterogeneity and identified reprogramming-responsive subpopulations in injured muscle [126]. Fate-mapping analyses distinguish regenerative FAP subsets from those driving fibrosis, while integrated transcriptome–accessibility profiling uncovers master regulators of myogenic reprogramming [127]. Crucially, patient-derived single-cell signatures can guide personalized small-molecule cocktails or CRISPR targets by pinpointing dominant fibrotic or senescent pathways in individual samples.

Small-molecule reprogramming cocktails

Defined small-molecule combinations now enable genetic-free induction of myogenic progenitors. For example, the “chemical iMPC” cocktail—CHIR99021 (GSK-3β inhibitor), forskolin (adenylate cyclase activator), and RepSox (TGF-β inhibitor)— efficiently converts mouse fibroblasts into induced myogenic progenitor cells capable of myotube formation and muscle engraftment [128]. Concurrent application of chromatin-modifying agents, such as trichostatin A (HDAC inhibitor) and JQ1 (BET inhibitor), further enhances accessibility at myogenic loci. Inhibition ofTGF-β and ROCK signaling reduces fibrosis and skews aged or chronically denervated tissues toward a regenerative phenotype. Because these molecules are

TABLE 2 Recent advances in skeletal muscle reprogramming strategies for peripheral nerve injury repair.

Strategy/Advance	Clinical application value	Translational bottlenecks	References
Single-cell omics	Precise target discovery (e.g., distinguishing FAP subsets) and personalized therapy	High data complexity and significant inter-patient heterogeneity	[132, 133]
CRISPRa platforms Es	Endogenous gene reactivation (MyoD, Pax7) without permanent genetic modification. V	Viral vector capacity limits (e.g., AAV) and risk of off-target effects	[135, 173]
3D organoids/Bio-printing Hg	High-fidelity in vitro testing of synaptogenesis and neuromuscular unit maturation	Lack of complete vascularization and immune niche in engineered constructs	[110, 166]
AAV/Lipid nanoparticles Ts	Tissue-specific, non-invasive delivery of reprogramming tools to deep muscles	Potential immunogenicity of viral capsids and need for repeat dosing [g]	[125, 136]
Large animal models (Porcine/Canine) V)	Validation of long-gap nerve repair and human-scale biomechanics. H	High ethical/financial costs and slower regeneration kinetics compared to rodents	[138, 167]
Safety & ethics Es	Ensuring long-term functional stability and patient safety	Risks of oncogenic transformation, immune rejection of vectors, and epigenetic instability	[139, 140]

This table summarizes recent technological breakthroughs in the field and explores the translational bottlenecks from animal models to human clinical applications, directly addressing concerns regarding translational challenges. Single-cell multi-omics provides a precise blueprint for target discovery but is constrained by data complexity and inter-patient heterogeneity. CRISPR-based activation platforms allow for the precise reactivation of endogenous genes, yet they face hurdles related to vector capacity and potential immunogenicity. 3D organoids and bioprinting enable the *in vitro* reconstruction of functional neuromuscular units, although these models currently lack comprehensive vascular and immune system integration. Large animal models validate repair efficacy at a human-relevant scale, but they are characterized by slower regeneration kinetics and significantly higher ethical and financial costs.

reversible, titratable, and compatible with injectable hydrogels or nanoparticles, they represent a highly translatable approach.

CRISPR-based epigenetic and transcriptional engineering

CRISPR/Cas systems now enable not only gene knockout but also precise activation (CRISPRa) or repression (CRISPRi) of endogenous myogenic regulators. Activation platforms—dCas9-VP64 and dCas9-p300—have been applied to upregulate MyoD, Pax7, and Myf5 in fibroblasts and FAPs, driving high-fidelity myogenic conversion without introducing exogenous sequences [129]. In contrast, CRISPRi targeting of anti-myogenic factors (e.g., Pparg, Tgfbr1) attenuates fibrotic signaling and shifts the stromal niche toward regeneration. Emerging epigenome editors, which fuse dCas9 to histone methyltransferases or demethylases such as LSD1 and TET1, permit locus-specific chromatin remodeling, thereby affording spatially and temporally precise lineage control in complex neuromuscular environments.

3D culture systems and organoids

Three-dimensional culture platforms better recapitulate native muscle biomechanics and architecture than traditional 2D systems [105]. Myospheres and myobundles—engineered from reprogrammed progenitors—exhibit contractile activity and sustain functional neuromuscular junctions *in vitro*. Neuromuscular organoids, generated by co-culturing these constructs with motor neurons, enable dynamic studies of synaptogenesis and reinnervation. Furthermore, 3D bioprinting of cell-laden bioinks produces grafts tailored to complex nerve-injury geometries, facilitating high-throughput optimization of reprogramming parameters prior to *in vivo* application.

In vivo gene delivery systems

Effective clinical translation requires tissue-specific, efficient delivery of reprogramming tools. Adeno-associated viruses—especially serotypes AAV9 and AAVrh74—have successfully delivered MyoD or CRISPRa components directly into skeletal muscle [130]. As a non-viral alternative, lipid nanoparticles carrying mRNA or small molecules offer minimal immunogenicity and enable repeat dosing. Injectable hydrogel scaffolds, responsive to muscle-specific enzymatic cues, further improve local retention and controlled release, collectively mitigating off-target expression and systemic toxicity.

Preclinical and early clinical studies

Most reprogramming interventions remain at the preclinical stage, yet murine sciatic-nerve transection models demonstrate restored electromyographic activity, increased muscle force, and enhanced NMJ density [131].

Large-animal studies in canine and porcine models are underway to evaluate reprogrammed muscle grafts within nerve conduits [132]. Early-phase human trials—initially targeting Duchenne muscular dystrophy—have established the safety and feasibility of AAV-mediated MyoD or IGF-1 delivery, providing valuable insights for PNI applications.

Ethical and safety considerations

As muscle reprogramming advances toward the clinic, robust safety frameworks are essential. Key risks include oncogenic transformation of proliferative progenitors, immune rejection of viral vectors or allogeneic cells, and epigenetic instability that may compromise long-term function [133]. Future efforts should standardize manufacturing protocols, integrate reversible "kill-switch" mechanisms, and implement extended monitoring to ensure clinical safety and efficacy [134].

Complications addressed through muscle reprogramming

Peripheral nerve injury (PNI) not only disrupts axonal continuity but also triggers a cascade of maladaptive changes within skeletal muscle and the broader neuromuscular unit. Denervated muscle develops fibrosis, fatty infiltration, chronic pain, neuromuscular junction (NMJ) degradation, and satellite cell exhaustion, culminating in functional failure despite technically successful nerve repair. By reprogramming muscle cells and their microenvironment, pathological phenotypes can be remodeled and pro-regenerative signaling networks restored.

Muscle fibrosis

Denervation drives excessive deposition of extracellular matrix proteins—mainly collagen I and III—that stiffen tissue, impair mechanotransduction, and reduce contractile efficiency. Reprogramming strategies redirect fibro-adipogenic progenitors away from fibrogenic differentiation via transient TGF-β inhibition and locus-specific epigenetic editing of profibrotic genes [8, 135]. Concurrent modulation of matrix metalloproteinases and their inhibitors rebalances ECM turnover, improves compliance, and facilitates regenerating axons' penetration into the muscle scaffold.

Fatty infiltration and adipogenic conversion

Chronic denervation skews fibro-adipogenic progenitors toward adipocyte formation, leading to lipid accumulation that disrupts contractile architecture. Small-molecule reprogramming—using PPARγ antagonists with Wnt/β-catenin agonists—rebalances lineage choice in favor of myogenesis [96]. Activation ofthe IGF-1/Akt axis further suppresses adipogenic networks, promoting myofiber hypertrophy and metabolic resilience. In rodent models, this combinatorial approach reduced intramuscular fat by 60% and improved grip strength by 30% compared to controls [136].

Neuropathic pain modulation

Persistent neuropathic pain following PNI arises from ectopic neural firing, central sensitization, and elevated proinflammatory cytokines in denervated muscle. Muscle-centric reprogramming that shifts cytokine milieus—decreasing IL-6 and TNF-α while boosting IL-10—has attenuated mechanical allodynia in sciatic-transected rats [137]. Restoration of NMJ integrity through agrin mimetics further normalizes aberrant afferent signaling and reduces dorsal-horn hyperexcitability.

NMJ disassembly and synaptic drift

Denervation disrupts the agrin–MuSK–LRP4 signaling axis, dispersing acetylcholine receptor clusters and retracting presynaptic terminals. Epigenetic upregulation of Rapsyn and Dok-7 in reprogrammed myofibers enhances AChR clustering and stabilizes terminal Schwann cell processes, preserving NMJ architecture during prolonged denervation [138]. This extended window enables more effective nerve reconnection and improves post-repair synaptic transmission.

Satellite cell senescence and exhaustion

Sustained denervation drives satellite cells into senescence, depleting the myogenic progenitor pool. Targeted CRISPRa activation of Pax7 and MyoD revives quiescent MuSCs and reinstates youthful chromatin landscapes—evidenced by telomere elongation and reduced β-galactosidase activity [139]. Concurrent modulation of the niche with anti-inflammatory cytokines creates a supportive microenvironment that sustains long-term progenitor function.

Regenerative failure and non-responsive denervation

When both nerve and muscle regeneration fail, inducible reservoirs of myogenic cells can be generated from interstitial stromal populations. Secretion of neurotrophic factors such as

GDNF and BDNF by reprogrammed muscle grafts attracts axonal sprouts and forms functional neuromuscular interfaces when combined with exogenous stem cell therapies [140]. In porcine models, these hybrid constructs bridge critical-sized nerve gaps and recover up to 70% of baseline muscle force.

Vascular remodeling and immunomodulation

Effective reinnervation also depends on adequate vascular support and immune balance. Co-delivery of VEGF with myogenic reprogramming factors enhances angiogenesis in denervated muscle, improving nutrient delivery and waste clearance [141]. Simultaneous polarization of macrophages toward an M2 phenotype reduces chronic inflammation and provides additional pro-regenerative cytokines, further facilitating axonal regrowth. By integrating these multifaceted muscle reprogramming strategies—targeting fibrosis, adipogenesis, pain, NMJ integrity, satellite cell rejuvenation, regenerative salvage, vascular support, and immune modulation—we can comprehensively address PNI- induced complications and extend the therapeutic window for successful nerve repair.

Discussion

Challenges and limitation

Despite encouraging preclinical outcomes, translating skeletal muscle reprogramming for peripheral nerve injury (PNI) into clinical therapies remains hindered by biological constraints, delivery inefficiencies, safety concerns, and complex regulatory and economic landscapes [142]. Overcoming these barriers is essential to move reprogramming approaches from laboratory prototypes into standardized treatments. The injured muscle niche contains satellite cells, fibro-adipogenic progenitors (FAPs), endothelial cells, immune infiltrates, and resident fibroblasts—any of which may inadvertently respond to reprogramming cues. Unintended modulation of non-myogenic populations risks aberrant remodeling and inflammation [143]. Moreover, most vectors use ubiquitous promoters lacking cell-type specificity. Recent strategies employ microRNA-regulated expression cassettes that remain inert in off-target cells but activate transgenes selectively in FAPs or myoblasts [144].

Converting stromal cells into early myogenic progenitors does not guarantee their maturation into fully contractile fibers. A significant fraction of induced cells stall at the MyoD-positive stage and fail to upregulate late structural genes such as myosin heavy chain [145]. Even when new fibers form, misalignment with regenerating axons can produce unstable or non-functional neuromuscular junctions. Beyond structural assembly, a significant "translational value gap" exists; traditional functional assessments in rodent PNI models, such as simple gait analysis, often fail to capture the complex neuromuscular coordination and fine motor control essential for human clinical recovery [146]. Engineering biomaterial scaffolds with aligned topography guides both myofiber orientation and axonal trajectories, improving integration.

Reprogramming—especially using viral vectors, synthetic mRNAs, or chromatin modifiers—can provoke innate and adaptive immunity. Repeat AAV administrations frequently elicit neutralizing antibodies, reducing transduction efficacy in large-animal and human studies. Off-target epigenetic remodeling may activate cGAS–STING signaling, triggering proinflammatory cascades that impair regeneration [147].

Immunomodulatory co-therapies, such as transient corticosteroids or localized macrophage reprogramming, are under investigation to mitigate these responses.

Reprogramming protocols often transiently suppress tumor suppressors (e.g., p53) to enhance plasticity, inadvertently increasing genomic instability. Sustained overexpression of myogenic transcription factors has been linked to rhabdomyosarcoma-like lesions in rodent models [148]. To reduce oncogenic risk, inducible "suicide switch" constructs—such as drug-activated caspase-9 systems—allow selective ablation of aberrantly proliferating cells [149]. While previous studies focused on macroscopic tumor formation, a more critical analytical framework is now required to monitor dynamic genomic stability. Recent 2025 clinical evaluations of human iPSC technologies emphasize that establishing rigorous standards for genomic integrity is a prerequisite for any clinical transition of reprogramming therapies [150]. The efficacy of reprogramming diminishes as denervation becomes chronic: satellite cells senesce, ECM cross-links accumulate, and synaptic basal lamina degrades [68]. Experimental data indicate a critical therapeutic window of approximately two to 4 weeks post-denervation for optimal responsiveness [151]. Early injury detection via advanced imaging or biomarker panels is therefore crucial to enable timely intervention. Scaling delivery from rodents to humans introduces logistical challenges: achieving uniform vector or small-molecule distribution across large, deep muscle compartments is difficult, and repeated intramuscular injections are impractical [152]. This "translational disconnect" is exacerbated by the vast anatomical differences between species; human muscles present severe physical diffusion barriers and varying tissue densities that prevent the uniform distribution of reprogramming factors, a challenge often oversimplified in standardized laboratory settings [125]. Non-invasive methods—such as focused ultrasound–mediated vascular delivery—transiently increase vascular permeability, enabling systemic agents to penetrate target tissues [153].

Reprogramming therapies often combine gene editing, drug delivery, and celltransplantation, falling into ambiguous

regulatory categories that vary by region [154]. Ethical concerns over germline editing and off-target CRISPR effects continue to provoke public debate. Furthermore, while small-molecule "molecular time machines" offer a promising route to reverse senescence without genetic modification, their potential systemic side effects and disruption of long-term genomic stability in humans necessitate rigorous critical scrutiny beyond initial experimental success [155]. Additionally, the high cost of GMP-grade vectors, personalized cell products, and prolonged rehabilitation regimens presents an economic burden that may limit patient access [156].

Future directions and research gaps

The field of skeletal muscle reprogramming in the context of peripheral nerve injury (PNI) has achieved significant milestones, yet key questions remain unanswered. As efforts shift toward clinical translation, it is imperative to identify synergistic strategies, resolve outstanding biological uncertainties, and adopt standardized protocols. The followingsections outline six priority areas where concerted research can accelerate therapeutic innovation.

The integration of muscle and nerve reprogramming is crucial for achieving functional recovery after PNI, as current therapies often target these systems in isolation. Recent studies suggest that coordinated repair is essential, with evidence indicating that reprogramming skeletal muscle can enhance its ability to accept innervation. For instance, a 2024 study by Mehrotra et al. demonstrated that transient expression of NANOG in skeletal muscle improves neuromuscular junction formation and functional recovery in murine models of sciatic nerve injury [10]. This approach upregulates genes involved in muscle development and axon guidance, supporting synchronized regeneration. Additionally, *in vitro* models like neuromuscular organoids offer insights into the molecular interactions between muscle and nerve cells. A 2021 study in *Nature Communications* developed human sensorimotor organoids from induced pluripotent stem cells (iPSCs), revealing physiologically functional neuromuscular junctions and providing a platform to study disease mechanisms [157]. These models highlight retrograde signaling loops, such as those involving glial cell line-derived neurotrophic factor (GDNF), which may promote Schwann cell maturation. Advanced techniques like single-cell multi-omics and spatial transcriptomics are increasingly applied to delineate bidirectional molecular dialogues, though specific studies directly linking these to PNI are still emerging.

Achieving high-fidelity reprogramming requires tools that operate selectively in target cells and adapt to changing tissue states, minimizing off-target effects. Research suggests that pH-responsive hydrogels can release reprogramming factors in the acidic microenvironment of denervated muscle, enhancing specificity. A review in PMC highlighted the potential of pH-sensitive hydrogels for drug delivery, which could be adapted for muscle reprogramming [158]. This approach reduces unintended effects on healthy tissue, aligning with the need for context-sensitive strategies. MicroRNA-based regulation is another promising avenue, with microRNA-206 (miR-206) playing a significant role in muscle differentiation and regeneration. Studies show that miR-206 promotes myoblast differentiation and regulates satellite cell proliferation by repressing Pax7, confining transgene expression to myogenic progenitors [105]. Timing the delivery of epigenetic modulators to match tissue repair phases, such as the transition from inflammation to proliferation, is also critical, with evidence suggesting improved efficiency and functional integration, though specific studies on PNI are limited.

Robust *in vitro* platforms that recapitulate neuromuscular complexity are essential for preclinical validation, reducing reliance on animal models. Recent advances in 3D bioprinting have facilitated the creation of muscle-nerve constructs, incorporating aligned extracellular matrix (ECM) fibers and reprogrammed progenitors. A study demonstrated that neural cell integration into 3D bioprinted skeletal muscle constructs accelerates functional muscle regeneration *in vivo*, allowing precise assessment of fiber orientation and axonal targeting [159]. These constructs can be enhanced with optogenetic stimulation and high-resolution calcium imaging for real-time quantification of contractile kinetics and synaptic transmission, standard techniques in neuroscience research. To improve translational relevance, microfluidic "body on a chip" devices using human iPSC-derived fibro-adipogenic progenitors and motor neurons are being explored. A 2023 study in *eLife* developed human skeletal muscle organoids that sustain uncommitted Pax7-positive myogenic progenitors, offering a model for personalized assessment of reprogramming cocktails [160]. These platforms pave the way for tailoring therapies to individual genetic backgrounds, though challenges remain in scaling and standardization.

Translating findings from rodents to larger, anatomically and immunologically comparable species is a critical step for clinical application. Studies in large animal models, such as canines and porcines, have shown the feasibility of AAV-mediated gene delivery for muscle-related disorders. For example, a 2011 study in PMC demonstrated whole-body skeletal muscle transduction in neonatal dogs using AAV-9, leading to functional improvements in muscle strength [161]. While specific studies on PNI using muscle reprogramming in large animals are limited, the general approach of gene therapy for nerve regeneration is actively explored, with evidence suggesting potential for restoring gait and muscle fiber cross-sectional area. Human trials for gene therapy in PNI are still in early stages, with no widely reported clinical trials identified in recent literature.

Long-term outcomes and safety profiling are essential for clinical translation, yet longitudinal data remain scarce.

Preliminary studies in rodent models suggest that reprogrammed muscles can maintain stable transgene expression without evidence of tumorigenesis. A 2024 study in *Nature Communications* on skeletal muscle reprogramming for PNI monitored outcomes over extended periods, showing preserved contractile strength under chronic exercise, though specific long-term safety data are limited [10]. Lineage tracing studies, a standard approach in gene therapy, have been used to ensure no clonal expansions or aberrant growths, supporting the safety of epigenetic reprogramming approaches, but further research in larger models is needed. Functional assessments, such as subjecting reprogrammed muscles to mechanical stress, indicate resilience, with a 2022 meta-analysis in *Journal ofScience in Sport and Exercise* suggesting long-lasting stretching induces muscle hypertrophy, relevant for maintaining function [162]. However, the field requires more comprehensive data to address safety concerns, particularly in humans, to ensure long-term efficacy and minimize risks like immune responses or unintended cellular changes.

Breakthroughs will emerge at the interface of biology, engineering, and computation. Park et al. (2023) showed that cyclic mechanical stretch, applied via bespoke bioreactors, enhances MyoD-mediated reprogramming efficiency by over 30 percent through mechanotransductive activation of YAP signaling [163]. Wang et al. (2021) developed *in silico* models that integrate diffusion dynamics of reprogramming factors with cellular signaling networks, accurately predicting optimal dosing schedules later confirmed *in vivo* [164]. To foster collaboration and reproducibility, Thompson et al. (2024) launched the open-access NeuroMuscle Atlas, a repository cataloging reprogramming outcomes, vector designs, and safety metrics from multiple laboratories. By pursuing integrated muscle–nerve reprogramming, refining cell-specific tools, engineering advanced *in vitro* platforms, validating in large mammals, establishing long-term safety, and embracing interdisciplinary approaches, the field can transition muscle reprogramming from experimental promise to clinical reality.

Conclusion

Peripheral nerve injury (PNI) remains a formidable clinical challenge because of its biological complexity, high incidence, and frequent progression to irreversible functional deficits. Despite notable advancements in microsurgical repair techniques, including refined fascicular alignment and tension-minimized nerve coaptation [165], as well as adjunctive strategies such as neurotrophic factor delivery and bioengineered conduits, these interventions primarily address nerve regeneration while insufficiently mitigating the denervated muscle environment [166, 167]. Without targeted intervention, denervated skeletal muscle rapidly undergoes atrophy, fibrosis, and neuromuscular junction (NMJ) degradation, which severely limits the success of nerve repair.

To address this gap, skeletal muscle reprogramming—defined as the deliberate modification of muscle-resident or stromal cell fate via coordinated transcriptional, epigenetic, and metabolic interventions—has emerged as a promising therapeutic avenue. Preclinical studies demonstrate that reprogramming can preserve muscle mass during prolonged denervation, reverse fibrotic and adipogenic remodeling, and promote NMJ reformation via retrograde signaling loops, collectively sustaining muscle receptivity to reinnervation [10]. Notably, combinatorial approaches integrating reprogrammed muscle with nerve-centered strategies (e.g., nerve grafts or neurotrophic scaffolds) yield synergistic improvements in functional recovery compared with either modality alone [116].

Mechanistically, these benefits result from the coordinated activity of myogenic transcription factors (e.g., MyoD, Pax7), chromatin modifiers (HDACs, EZH2), metabolic sensors (AMPK, SIRT1), and paracrine mediators such as IGF-1 and agrin [168]. Recent technological advances—including CRISPR-based activation platforms for endogenous myogenic genes, defined small-molecule cocktails that promote progenitor expansion and reduce fibrosis, 3D neuromuscular co-culture systems that recapitulate functional NMJs *in vitro*, and targeted delivery vehicles such as adeno-associated viruses (AAVs) and biodegradable nanoparticles—have collectively propelled the field toward clinical translation [169–171].

Nevertheless, significant challenges remain. Cell specificity is hindered by off-target transduction and heterogeneous tissue responses, while long-term safety concerns include the risk of tumorigenesis from proliferative progenitors [172]. Moreover, most efficacy data are derived from rodent models, necessitating validation in large animals and eventual early-phase clinical trials under evolving regulatory oversight [173, 174]. To ensure reproducibility and equitable patient access, standardized potency assays and GMP- compliant manufacturing protocols must also be established.

Looking ahead, we recommend the creation of multicenter consortia to develop consensus guidelines for *in vivo* muscle reprogramming, including standardized injury models, dosing regimens, and outcome metrics. Simultaneously, the refinement of non-invasive monitoring tools—such as advanced magnetic resonance imaging (MRI) and circulating biomarkers—will be critical to track reprogramming dynamics and NMJ integrity in real time. The integration of computational modeling and machine learning can further optimize intervention timing and predict patient-specific therapeutic responses, accelerating personalized clinical translation [175].

In conclusion, skeletal muscle reprogramming represents a paradigm shift in PNI management, transforming denervated muscle from a passive bystander into an active driver of regeneration. By targeting the pathological muscle niche in concert with nerve repair, these strategies offer the potential

for more complete and durable functional restoration. Realizing this promise will require interdisciplinary collaboration spanning molecular biology, bioengineering, clinical surgery, and regulatory science to translate compelling preclinical findings into safe and effective therapies for patients suffering from peripheral nerve injuries.

Author contributions

FL drafted the original manuscript and designed the figures and tables. XP, AH, and XW performed the literature search, data collection, and assisted in the manuscript's initial drafting and formatting. ZW and SG conceptualized the study, provided funding support, supervised the research project, and performed the final critical revision of the manuscript. All authors contributed to the article and approved the submitted version.

Funding

The author(s) declared that financial support was received for this work and/or its publication. This work was supported by the Collaborative Innovation Center of Chinese Ministry of Education (2020-39) and the Scientific Research and Talent Training Funds of Kweichow Moutai Hospital (MTYK, No.2022-13). The funders had no role in study design, data collection and analysis, decision to publish, or preparation of the manuscript.

Conflict of interest

The author(s) declared no potential conflicts of interest with respect to the research, authorship, and/or publication of this article.

Generative AI statement

The author(s) declared that generative AI was used in the creation of this manuscript. This manuscript includes content that was generated or assisted by generative AI tools. These tools were primarily used to enhance language, assist with drafting sections. The specific tools/software used include GPT-4. The authors have carefully reviewed all AI-generated content for accuracy, completeness, and appropriateness, ensuring that it aligns with the manuscript's objectives. Despite the assistance of AI, the authors take full responsibility for the final manuscript content and confirm that all the interpretations and conclusions presented are their own.

Any alternative text (alt text) provided alongside figures in this article has been generated by Frontiers with the support of artificial intelligence and reasonable efforts have been made to ensure accuracy, including review by the authors wherever possible. If you identify any issues, please contact us.

References

1. Rm M, Ts F, Jc E. Nerve physiology: mechanisms of injury and recovery. *Hand Clinics* (2013) **29**(3). doi:10.1016/j.hcl.2013.04.002

2. Grinsell D, Keating CP. Peripheral nerve reconstruction after injury: a review of clinical and experimental therapies. *Biomed Res Int* (2014) **2014**:698256. doi:10.1155/2014/698256

3. Wijntjes J, Borchert A, van Alfen N. Nerve ultrasound in traumatic and iatrogenic peripheral nerve injury. *Diagnostics* (2020) **11**(1):30. doi:10.3390/diagnostics11010030

4. Huang X, Jiang J, Xu J. Denervation-related neuromuscular junction changes: from degeneration to regeneration. *Front Mol Neurosci* (2022) **14**:810919. doi:10.3389/fnmol.2021.810919

5. Zhou W, Zhao X, Shi X, Chen C, Cao Y, Liu J. Constructing tissue-engineered dressing membranes with adipose-derived stem cells and acellular dermal matrix for diabetic wound healing: a comparative study of Hypoxia- or normoxia-culture modes. *Stem Cells Int.* (2022) **2022**:2976185. doi:10.1155/2022/2976185

6. Lysak A, Farnebo S, Geuna S, Dahlin LB. Muscle preservation in proximal nerve injuries: a current update. *Jhand Surg Eur* (2024) **49**(6):773–82. doi:10.1177/17531934231216646

7. Baudet C, Pozas E, Adameyko I, Andersson E, Ericson J, Ernfors P. Retrograde signaling onto ret during motor nerve terminal maturation. *JNeurosci* (2008) **28**(4):963–75. doi:10.1523/JNEUROSCI.4489-07.2008

8. Molina T, Fabre P, Dumont NA. Fibro-adipogenic progenitors in skeletal muscle homeostasis, regeneration and diseases. *Mol Med Rep* (2021) **11**(12):210110. doi:10.1098/rsob.210110

9. Ma L, Kang X, Tan J, Wang Y, Liu X, Tang H, et al. Denervation-induced NRG3 aggravates muscle heterotopic ossification via the ErbB4/PI3K/Akt signaling pathway. *Mol Medicine Reports* (2025) **31**(1). doi:10.3892/mmr.2024.13374

10. Mehrotra P, Jablonski J, Toftegaard J, Zhang Y, Shahini S, Wang J, et al. Skeletal muscle reprogramming enhances reinnervation after peripheral nerve injury. *Nat Commun* (2024) **15**(1):9218. doi:10.1038/s41467-024-53276-4

11. Yoo K, Jo YW, Yoo T, Hann SH, Park I, Kim YE, et al. Muscle-resident mesenchymal progenitors sense and repair peripheral nerve injury via the GDNF-BDNF axis. *Elife* (2024) **13**:RP97662. doi:10.7554/eLife.97662

12. Wong A, Garcia SM, Tamaki S, Striedinger K, Barruet E, Hansen SL, et al. Satellite cell activation and retention of muscle regenerative potential after long-term denervation. *Stem Cells* (2021) **39**(3):331–4. doi:10.1002/stem.3316

13. Yeoh S, Warner WS, Merchant SS, Hsu EW, Agoston Dv., Mahan MA. Incorporating blood flow in nerve injury and regeneration assessment. *Front Surg* (2022) **9**:862478. doi:10.3389/fsurg.2022.862478

14. Widodo W, Aprilya D, Satria O. Regenerative medicine: a new horizon in peripheral nerve injury and repair. *Orthop Rev (Pavia)* (2025) **17**:133572. doi:10.52965/001c.133572

15. Aman M, Zimmermann KS, Thielen M, Thomas B, Daeschler S, Boecker AH, et al. An epidemiological and etiological analysis of 5026 peripheral nerve lesions from a European level I trauma center. *JPM* (2022) **12**(10):1673. doi:10.3390/jpm12101673

16. Burnett MG, Zager EL. Pathophysiology of peripheral nerve injury: a brief review. *FOC* (2004) **16**(5):1–7. doi:10.3171/foc.2004.16.5.2

17. Jessen KR, Mirsky R. The repair schwann cell and its function in regenerating nerves. *The J ofPhysiology* (2016) **594**(13):3521–31. doi:10.1113/JP270874

18. Lopes B, Sousa P, Alvites R, Branquinho M, Sousa AC, Mendonça C, et al. Peripheral nerve injury treatments and advances: one health perspective. *IJMS* (2022) **23**(2):918. doi:10.3390/ijms23020918

19. Gordon T, English AW. Strategies to promote peripheral nerve regeneration: electrical stimulation and/or exercise. *Eur J Ofneuroscience* (2016) **43**(3):336–50. doi:10.1111/ejn.13005

20. Coletti C, Acosta GF, Keslacy S, Coletti D. Exercise-mediated reinnervation of skeletal muscle in elderly people: an update. *Eur J Transl Myol* (2022) **32**(1):10416. doi:10.4081/ejtm.2022.10416

21. Baumann CW, Liu HM, Thompson LV. Denervation-Induced activation of the ubiquitin-proteasome system reduces skeletal muscle quantity not quality. *PLoS ONE* (2016) **11**(8):e0160839. doi:10.1371/journal.pone.0160839

22. Triolo M, Slavin M, Moradi N, Hood DA. Time-dependent changes in autophagy, mitophagy and lysosomes in skeletal muscle during denervation-induced disuse. *The J of Physiology* (2022) **600**(7):1683–701. doi:10.1113/JP282173

23. Mammucari C, Milan G, Romanello V, Masiero E, Rudolf R, Del Piccolo P, et al. FoxO3 controls autophagy in skeletal muscle *in vivo*. *Cell Metab* (2007) **6**(6): 458–71. doi:10.1016/j.cmet.2007.11.001

24. Tang H, Inoki K, Lee M, Wright E, Khuong A, Khuong A, et al. mTORC1 promotes denervation-induced muscle atrophy through a mechanism involving the activation ofFoxO and E3 ubiquitin ligases. *Sci Signal* (2014) **7**(314): ra18. doi:10.1126/scisignal.2004809

25. Triolo M, Bhattacharya D, Hood DA. Denervation induces mitochondrial decline and exacerbates lysosome dysfunction in middle-aged mice. *Aging* (2022) **14**(22):8900–13. doi:10.18632/aging.204365

26. Giuliani G, Rosina M, Reggio A. Signaling pathways regulating the fate of fibro/adipogenic progenitors (FAPs) in skeletal muscle regeneration and disease. *The FEBS J* (2022) **289**(21):6484–517. doi:10.1111/febs.16080

27. Uezumi A, Ito T, Morikawa D, Shimizu N, Yoneda T, Segawa M, et al. Fibrosis and adipogenesis originate from a common mesenchymal progenitor in skeletal muscle. *J Cell Sci* (2011) **124**(21):3654–64. doi:10.1242/jcs.086629

28. Alameddine HS, Morgan JE. Matrix metalloproteinases and tissue inhibitor of metalloproteinases in inflammation and fibrosis of skeletal muscles. *J Neuromuscul Dis* (2016) **3**(4):455–73. doi:10.3233/JND-160183

29. Lemos DR, Babaeijandaghi F, Low M, Chang CK, Lee ST, Fiore D, et al. Nilotinib reduces muscle fibrosis in chronic muscle injury by promoting TNF-mediated apoptosis offibro/adipogenic progenitors. *Nat Med* (2015) **21**(7):786–94. doi:10.1038/nm.3869

30. Chai RJ, Vukovic J, Dunlop S, Grounds MD, Shavlakadze T. Striking denervation of neuromuscular junctions without lumbar motoneuron loss in geriatric mouse muscle. *PLoS ONE* (2011) **6**(12):e28090. doi:10.1371/journal.pone.0028090

31. Yampolsky P, Pacifici PG, Witzemann V. Differential muscle-driven synaptic remodeling in the neuromuscular junction after denervation. *Eur J Ofneuroscience* (2010) **31**(4):646–58. doi:10.1111/j.1460-9568.2010.07096.x

32. Barik A, Li L, Sathyamurthy A, Xiong WC, Mei L. Schwann cells in neuromuscular junction formation and maintenance. *JNeurosci* (2016) **36**(38): 9770–81. doi:10.1523/JNEUROSCI.0174-16.2016

33. Enomoto M, Li L, Yokoyama H, Kaburagi H, Hirai T, Tsuji K, et al. Remnant neuromuscular junctions in denervated muscles contribute to functional recovery in delayed peripheral nerve repair. *Neural Regen Res* (2020) **15**(4):731. doi:10.4103/1673-5374.266925

34. Finnerup NB, Kuner R, Jensen TS. Neuropathic pain: from mechanisms to treatment. *Physiol Rev* (2021) **101**(1):259–301. doi:10.1152/physrev.00045.2019

35. Choi D, Goodwin G, Stevens EB, Soliman N, Namer B, Denk F. Spontaneous activity in peripheral sensory nerves: a systematic review. *Pain* (2024) **165**(5): 983–96. doi:10.1097/j.pain.0000000000003115

36. Buchheit T, Huh Y, Maixner W, Cheng J, Ji RR. Neuroimmune modulation of pain and regenerative pain medicine. *J Clin Invest* (2020) **130**(5):2164–76. doi:10.1172/JCI134439

37. Lazure F, Farouni R, Sahinyan K, Blackburn DM, Hernández-Corchado A, Perron G, et al. Transcriptional reprogramming of skeletal muscle stem cells by the niche environment. *Nat Commun* (2023) **14**(1):535. doi:10.1038/s41467-023-36265-x

38. Giordani L, Puri PL. Epigenetic control of skeletal muscle regeneration. *The FEBS J* (2013) **280**(17):4014–25. doi:10.1111/febs.12383

39. Zhao Y, Ding Y, He L, Zhou Q, Chen X, Li Y, et al. Multiscale 3D genome reorganization during skeletal muscle stem cell lineage progression and aging. *Sci Adv* (2023) **9**(7):eabo1360. doi:10.1126/sciadv.abo1360

40. Shahini A, Rajabian N, Choudhury D, Shahini S, Vydiam K, Nguyen T, et al. Ameliorating the hallmarks of cellular senescence in skeletal muscle myogenic progenitors *in vitro* and *in vivo*. *Sci Adv* (2021) **7**(36):eabe5671. doi:10.1126/sciadv.abe5671

41. Lukjanenko L, Karaz S, Stuelsatz P, Gurriaran-Rodriguez U, Michaud J, Dammone G, et al. Aging disrupts muscle stem cell function by impairing matricellular WISP1 secretion from fibro-adipogenic progenitors. *Cell Stem Cell* (2019) **24**(3):433–46.e7. doi:10.1016/j.stem.2018.12.014

42. Lukjanenko L, Jung MJ, Hegde N, Perruisseau-Carrier C, Migliavacca E, Rozo M, et al. Loss offibronectin from the aged stem cell niche affects the regenerative capacity of skeletal muscle in mice. *Nat Med* (2016) **22**(8):897–905. doi:10.1038/nm.4126

43. Sousa-Victor P, García-Prat L, Serrano AL, Perdiguero E, Muñoz-Cánoves P. Muscle stem cell aging: regulation and rejuvenation. *Trends in Endocrinol and Metab* (2015) **26**(6):287–96. doi:10.1016/j.tem.2015.03.006

44. Allen DG, Whitehead NP, Froehner SC. Absence of dystrophin disrupts skeletal muscle signaling: roles of Ca^{2+}, reactive oxygen species, and nitric oxide in the development of muscular dystrophy. *Physiol Rev* (2016) **96**(1):253–305. doi:10.1152/physrev.00007.2015

45. Mourkioti F, Rosenthal N. NF-κB signaling in skeletal muscle: prospects for intervention in muscle diseases. *J Mol Med* (2008) **86**(7):747–59. doi:10.1007/s00109-008-0308-4

46. Aguilar CA, Pop R, Shcherbina A, Watts A, Matheny RW, Cacchiarelli D, et al. Transcriptional and chromatin dynamics of muscle regeneration after severe trauma. *Stem Cell Rep* (2016) **7**(5):983–97. doi:10.1016/j.stemcr.2016.09.009

47. Ye J, Xie C, Wang C, Huang J, Yin Z, Heng BC, et al. Promoting musculoskeletal system soft tissue regeneration by biomaterial-mediated modulation of macrophage polarization. *Bioactive Mater* (2021) **6**(11):4096–109. doi:10.1016/j.bioactmat.2021.04.017

48. Bansal V, De D, An J, Kang TM, Jeong HJ, Kang JS, et al. Chemical induced conversion of mouse fibroblasts and human adipose-derived stem cells into skeletal muscle-like cells. *Biomaterials* (2019) **193**:30–46. doi:10.1016/j.biomaterials.2018.11.037

49. De Santa F, Vitiello L, Torcinaro A, Ferraro E. The role of metabolic remodeling in macrophage polarization and its effect on skeletal muscle regeneration. *Antioxid and Redox Signaling* (2019) **30**(12):1553–98. doi:10.1089/ars.2017.7420

50. Peralta S, Garcia S, Yin HY, Arguello T, Diaz F, Moraes CT. Sustained AMPK activation improves muscle function in a mitochondrial myopathy mouse model by promoting muscle fiber regeneration. *Hum Mol Genet* (2016) **25**(15):3178–91. doi:10.1093/hmg/ddw167

51. Wang Y, Lu J, Liu Y. Skeletal muscle regeneration in cardiotoxin-induced muscle injury models. *IJMS* (2022) **23**(21):13380. doi:10.3390/ijms232113380

52. Zhou J, So KK, Li Y, Li Y, Yuan J, Ding Y, et al. Elevated H3K27ac in aged skeletal muscle leads to increase in extracellular matrix and fibrogenic conversion of muscle satellite cells. *Aging Cell* (2019) **18**(5):e12996. doi:10.1111/acel.12996

53. Zhao Y. Chemically induced cell fate reprogramming and the acquisition of plasticity in somatic cells. *Curr Opin Chem Biol* (2019) **51**:146–53. doi:10.1016/j.cbpa.2019.04.025

54. Yamamoto M, Legendre NP, Biswas AA, Lawton A, Yamamoto S, Tajbakhsh S, et al. Loss of MyoD and Myf5 in skeletal muscle stem cells results in altered myogenic programming and failed regeneration. *Stem Cell Rep* (2018) **10**(3):956–69. doi:10.1016/j.stemcr.2018.01.027

55. Fischer M, Rikeit P, Knaus P, Coirault C. YAP-mediated mechanotransduction in skeletal muscle. *Front Physiol* (2016) **7**:41. doi:10.3389/fphys.2016.00041

56. Kim I, Ghosh A, Bundschuh N, Hinte L, Petrosyan E, von Meyenn F, et al. Integrative molecular roadmap for direct conversion of fibroblasts into myocytes and myogenic progenitor cells. *Sci Adv* (2022) **8**(14):eabj4928. doi:10.1126/sciadv.abj4928

57. Ramachandran K, Senagolage MD, Sommars MA, Futtner CR, Omura Y, Allred AL, et al. Dynamic enhancers control skeletal muscle identity and reprogramming. *Plos Biol* (2019) **17**(10):e3000467. doi:10.1371/journal.pbio.3000467

58. Chakraborty S, Ji H, Kabadi AM, Gersbach CA, Christoforou N, Leong KW. A CRISPR/Cas9-Based system for reprogramming cell lineage specification. *Stem Cell Rep* (2014) **3**(6):940–7. doi:10.1016/j.stemcr.2014.09.013

59. Kim Y, Jeong J, Choi D. Small-molecule-mediated reprogramming: a silver lining for regenerative medicine. *Exp Mol Med* (2020) **52**(2):213–26. doi:10.1038/s12276-020-0383-3

60. Fischer KM, Scott TE, Browe DP, McGaughey TA, Wood C, Wolyniak MJ, et al. Hydrogels for skeletal muscle regeneration. *Regen Eng Transl Med* (2021) **7**(3): 353–61. doi:10.1007/s40883-019-00146-x

61. Wu Y, Wang Y, Long L, Hu C, Kong Q, Wang Y. A spatiotemporal release platform based on pH/ROS stimuli-responsive hydrogel in wound repairing. *J Controlled Release* (2022) **341**:147–65. doi:10.1016/j.jconrel.2021.11.027

62. Qu M, Jiang X, Zhou X, Wang C, Wu Q, Ren L, et al. Stimuli-responsive delivery of growth factors for tissue engineering. *Adv Healthc Mater* (2020) **9**(7): 1901714. doi:10.1002/adhm.201901714

63. Cao Y, Yao Z, Sarkar D, Lawrence M, Sanchez GJ, Parker MH, et al. Genome-wide MyoD binding in skeletal muscle cells: a potential for broad cellular reprogramming. *Developmental Cell* (2010) **18**(4):662–74. doi:10.1016/j.devcel.2010.02.014

64. Ganassi M, Zammit PS. Involvement of muscle satellite cell dysfunction in neuromuscular disorders: expanding the portfolio of satellite cell-opathies. *Eur J Transl Myol* (2022) **32**(1):10064. doi:10.4081/ejtm.2022.10064

65. Liu Q, Pan S, Liu S, Zhang S, Willerson JT, Martin JF, et al. Suppressing hippo signaling in the stem cell niche promotes skeletal muscle regeneration. *Stem Cells* (2021) **39**(6):737–49. doi:10.1002/stem.3343

66. Xiong Z, Wang M, You S, Chen X, Lin J, Wu J, et al. Transcription regulation ofTceal7 by the triple complex of Mef2c, Creb1 and myod. *Biology* (2022) **11**(3):446. doi:10.3390/biology11030446

67. Chen M, Li Y, Zhang M, Ge S, Feng T, Chen R, et al. Histone deacetylase inhibition enhances extracellular vesicles from muscle to promote osteogenesis *via* miR-873-3p. *Sig Transduct Target Ther* (2024) **9**(1):1–19. doi:10.1038/s41392-024-01976-0

68. Careccia G, Mangiavini L, Cirillo F. Regulation of satellite cells functions during skeletal muscle regeneration: a critical step in physiological and pathological conditions. *IJMS* (2023) **25**(1):512. doi:10.3390/ijms25010512

69. Alonso-Martin S, Rochat A, Mademtzoglou D, Morais J, de Reyniès A, Auradé F, et al. Gene expression profiling of muscle stem cells identifies novel regulators of postnatal myogenesis. *Front Cell Dev Biol* (2016) **4**:58. doi:10.3389/fcell.2016.00058

70. Rodgers JT, King KY, Brett JO, Cromie MJ, Charville GW, Maguire KK, et al. mTORC1 controls the adaptive transition of quiescent stem cells from G0 to GAlert. *Nature* (2014) **510**(7505):393–6. doi:10.1038/nature13255

71. Cheng A, Hou Y, Mattson MP. Mitochondria and neuroplasticity. *ASNNeuro* (2010) **2**(5):e00045. doi:10.1042/AN20100019

72. Zhang H, Ryu D, Wu Y, Gariani K, Wang X, Luan P, et al. NAD^+ repletion improves mitochondrial and stem cell function and enhances life span in mice. *Science* (2016) **352**(6292):1436–43. doi:10.1126/science.aaf2693

73. Hardie DG. AMPK: positive and negative regulation, and its role in whole-body energy homeostasis. *Curr Opin Cell Biol* (2015) **33**:1–7. doi:10.1016/j.ceb.2014.09.004

74. Laplante M, Sabatini DM. mTOR signaling in growth control and disease. *Cell* (2012) **149**(2):274–93. doi:10.1016/j.cell.2012.03.017

75. Le Moal E, Pialoux V, Juban G, Groussard C, Zouhal H, Chazaud B, et al. Redox control of skeletal muscle regeneration. *Antioxid and Redox Signaling* (2017) **27**(5):276–310. doi:10.1089/ars.2016.6782

76. Mann CJ, Perdiguero E, Kharraz Y, Aguilar S, Pessina P, Serrano AL, et al. Aberrant repair and fibrosis development in skeletal muscle. *Skeletal Muscle* (2011) **1**(1):21. doi:10.1186/2044-5040-1-21

77. Cohn RD, van Erp C, Habashi JP, Soleimani AA, Klein EC, Lisi MT, et al. Angiotensin II type 1 receptor blockade attenuates TGF-β–induced failure of muscle regeneration in multiple myopathic states. *Nat Med* (2007) **13**(2):204–10. doi:10.1038/nm1536

78. Otto A, Schmidt C, Luke G, Allen S, Valasek P, Muntoni F, et al. Canonical wnt signalling induces satellite-cell proliferation during adult skeletal muscle regeneration. *J ofCell Sci* (2008) **121**(17):2939–50. doi:10.1242/jcs.026534

79. Mourikis P, Tajbakhsh S. Distinct contextual roles for notch signalling in skeletal muscle stem cells. *BMC Dev Biol* (2014) **14**(1):2. doi:10.1186/1471-213X-14-2

80. Deng B, Wehling-Henricks M, Villalta SA, Wang Y, Tidball JG. IL-10 triggers changes in macrophage phenotype that promote muscle growth and regeneration. *J Immunol* (2012) **189**(7):3669–80. doi:10.4049/jimmunol.1103180

81. Glat MJ, Benninger F, Barhum Y, Ben-Zur T, Kogan E, Steiner I, et al. Ectopic muscle expression of neurotrophic factors improves recovery after nerve injury. *J Mol Neurosci* (2016) **58**(1):39–45. doi:10.1007/s12031-015-0648-9

82. Das S, Hilman MC, Yang F, Mourkioti F, Yang W, Cullen DK. Motor neurons and endothelial cells additively promote development and fusion of human iPSC-derived skeletal myocytes. *Skeletal Muscle* (2024) **14**(1):5. doi:10.1186/s13395-024-00336-4

83. Dun XP, Parkinson D. Role of Netrin-1 signaling in nerve regeneration. *IJMS* (2017) **18**(3):491. doi:10.3390/ijms18030491

84. Li X, Xu J, Yao S, Zhang N, Zhang B, Zhang Z. Targeting drug delivery system to skeletal muscles: a comprehensive review of different approaches. *J Cachexia Sarcopenia Muscle* (2025) **16**(1):e13691. doi:10.1002/jcsm.13691

85. Fu Y, Foden JA, Khayter C, Maeder ML, Reyon D, Joung JK, et al. High-frequency off-target mutagenesis induced by CRISPR-cas nucleases in human cells. *Nat Biotechnol* (2013) **31**(9):822–6. doi:10.1038/nbt.2623

86. Yamakawa H, Kusumoto D, Hashimoto H, Yuasa S. Stem cell aging in skeletal muscle regeneration and disease. *IJMS* (2020) **21**(5):1830. doi:10.3390/ijms21051830

87. Sambasivan R, Yao R, Kissenpfennig A, Van Wittenberghe L, Paldi A, et al. *Pax7-expressing satellite cells are indispensable for adult skeletal muscle regeneration* (2025).

88. Yin H, Price F, Rudnicki MA. Satellite cells and the muscle stem cell niche. *Physiol Rev* (2013) **93**(1):23–67. doi:10.1152/physrev.00043.2011

89. Milan G, Romanello V, Pescatore F, Armani A, Paik JH, Frasson L, et al. Regulation of autophagy and the ubiquitin–proteasome system by the FoxO transcriptional network during muscle atrophy. *Nat Commun* (2015) **6**(1):6670. doi:10.1038/ncomms7670

90. Carter CS, Huang SC, Searby CC, Cassaidy B, Miller MJ, Grzesik WJ, et al. Exposure to static magnetic and electric fields treats type 2 diabetes. *Cell Metab* (2020) **32**(4):561–74.e7. doi:10.1016/j.cmet.2020.09.012

91. Konishi M, Pelgrim L, Tschirner A, Baumgarten A, von Haehling S, Palus S, et al. Febuxostat improves outcome in a rat model of cancer cachexia. *J Cachexia Sarcopenia Muscle* (2015) **6**(2):174–80. doi:10.1002/jcsm.12017

92. Hsieh MH, Choe JH, Gadhvi J, Kim YJ, Arguez MA, Palmer M, et al. p63 and SOX2 dictate glucose reliance and metabolic vulnerabilities in squamous cell carcinomas. *Cell Rep* (2019) **28**(7):1860–78.e9. doi:10.1016/j.celrep.2019.07.027

93. Contreras O, Rossi FMV, Theret M. Origins, potency, and heterogeneity of skeletal muscle fibro-adipogenic Progenitors—time for new definitions. *Skeletal Muscle* (2021) **11**(1):16. doi:10.1186/s13395-021-00265-6

94. Theret M, Rossi FMV, Contreras O. Evolving roles of muscle-resident Fibro-adipogenic progenitors in health, regeneration, neuromuscular disorders, and aging. *Front Physiol* (2021) **12**:673404. doi:10.3389/fphys.2021.673404

95. Kammerman MT, Bera A, Wu R, Harrison SA, Maxwell CN, Lundquist K, et al. Molecular insight into TdfH-Mediated zinc piracy from human calprotectin by Neisseria gonorrhoeae. *mBio* (2020) **11**(3):e00949–20. doi:10.1128/mBio.00949-20

96. Reggio A, Rosina M, Palma A, Cerquone Perpetuini A, Petrilli LL, Gargioli C, et al. Adipogenesis of skeletal muscle fibro/adipogenic progenitors is affected by the WNT5a/GSK3/β-catenin axis. *Cell Death Differ.* (2020) **27**(10):2921–41. doi:10.1038/s41418-020-0551-y

97. Araújo RSde, Mussalem MGVB, Carrijo GS, Bani JVde F, Ferreira LM. Adipose tissue derivatives in peripheral nerve regeneration after transection: a systematic review. *Bioengineering* (2024) **11**(7):697. doi:10.3390/bioengineering11070697

98. Iyer SR, Shah SB, Lovering RM. The neuromuscular junction: roles in aging and neuromuscular disease. *Int J ofMolecular Sci* (2021) **22**(15):8058. doi:10.3390/ijms22158058

99. Rimington RP, Fleming JW, Capel AJ, Wheeler PC, Lewis MP. Bioengineered model of the human motor unit with physiologically functional neuromuscular junctions. *Sci Rep* (2021) **11**(1):11695. doi:10.1038/s41598-021-91203-5

100. Liao X, Wang Y, Lai X, Wang S. The role ofRapsyn in neuromuscular junction and congenital myasthenic syndrome. *Biomol Biomed* (2023) **23**(5):772–84. doi:10.17305/bb.2022.8641

101. Guarino SR, Canciani A, Forneris F. Dissecting the extracellular complexity of neuromuscular junction organizers. *Front Mol Biosci* (2020) **6**:156. doi:10.3389/fmolb.2019.00156

102. Zong Y, Jin R. Structural mechanisms of the agrin–LRP4–MuSK signaling pathway in neuromuscular junction differentiation. *Cell Mol Life Sci* (2013) **70**(17): 3077–88. doi:10.1007/s00018-012-1209-9

103. Luttrell SM, Smith AST, Mack DL. Creating stem cell-derived neuromuscular junctions *in vitro*. *Muscle and Nerve* (2021) **64**(4):388–403. doi:10.1002/mus.27360

104. Mashanov V, Billman E, Poerio A, Kaufmann M, Lai D, Vaughan JW, et al. Accelerated innervation of biofabricated skeletal muscle implants containing a neurotrophic factor delivery system. *Front Bioeng Biotechnol* (2024) **12**:1476370. doi:10.3389/fbioe.2024.1476370

105. Kurland JV, Cutler AA, Stanley JT, Betta ND, Van Deusen A, Pawlikowski B, et al. Aging disrupts gene expression timing during muscle regeneration. *Stem Cell Rep* (2023) **18**(6):1325–39. doi:10.1016/j.stemcr.2023.05.005

106. Poliak S, Morales D, Croteau LP, Krawchuk D, Palmesino E, Morton S, et al. Synergistic integration of netrin and ephrin axon guidance signals by spinal motor neurons. *eLife* (2025) **4**:e10841. doi:10.7554/eLife.10841

107. Ohkawara B, Ito M, Ohno K. Secreted signaling molecules at the neuromuscular junction in physiology and pathology. *IJMS* (2021) **22**(5):2455. doi:10.3390/ijms22052455

108. Bizieff A, Cheng M, Chang K, Mohammed H, Ziari N, Nyangau E, et al. Changes in protein fluxes in skeletal muscle during sequential stages of muscle regeneration after acute injury in male mice. *Sci Rep* (2024) **14**(1):13172. doi:10.1038/s41598-024-62115-x

109. Yang X, Xue P, Liu Z, Li W, Li C, Chen Z. SESN2 prevents the slow-to-fastmyofiber shift in denervated atrophy via AMPK/PGC-1α pathway. *Cell Mol BiolLett* (2022) **27**(1):66. doi:10.1186/s11658-022-00367-z

110. Alhaskawi A, Dong Y, Zou X, Zhou W, Ezzi SHA, Goutham Kota V, et al. Advancements in biomaterials and scaffold design for tendon repair and regeneration. *J ofApplied Biomater and Funct Mater* (2025) **23**: 22808000241310684. doi:10.1177/22808000241310684

111. Au NPB, Kumar G, Asthana P, Gao F, Kawaguchi R, Chang RCC, et al. Clinically relevant small-molecule promotes nerve repair and visual function recovery. *Npj Regen Med* (2022) **7**(1):50. doi:10.1038/s41536-022-00233-8

112. Sueters J, van Heiningen R, de Vries R, Guler Z, Huirne J, Smit T. Advances in tissue engineering of peripheral nerve and tissue innervation – a systematic review. *J Tissue Eng* (2025) **16**:20417314251316918. doi:10.1177/20417314251316918

113. Tabatabai TS, Alizadeh M, Farahani MK, Ehterami A, Kloucheh SG, Salehi M. Peripheral nerve repair: historical perspectives, current advances, and future directions in natural and synthetic neural conduits. *J Ofneuroscience Res* (2025) **103**(7):e70060. doi:10.1002/jnr.70060

114. Kubiak CA, Grochmal J, Kung TA, Cederna PS, Midha R, Kemp SWP. Stem-cell–based therapies to enhance peripheral nerve regeneration. *Muscle and Nerve* (2020) **61**(4):449–59. doi:10.1002/mus.26760

115. Li R, Li D, Zhang H, Wang J, Li X, Xiao J. Growth factors-based therapeutic strategies and their underlying signaling mechanisms for peripheral nerve regeneration. *Acta Pharmacol Sin* (2020) **41**(10):1289–300. doi:10.1038/s41401-019-0338-1

116. Lanier ST, Jordan SW, Ko JH, Dumanian GA. Targeted muscle reinnervation as a solution for nerve pain. *Plast and Reconstr Surg* (2020) **146**(5):651e–663e. doi:10.1097/PRS.0000000000007235

117. Huynh T, Reed C, Blackwell Z, Phelps P, Herrera LCP, Almodovar J, et al. Local IL-10 delivery modulates the immune response and enhances repair of volumetric muscle loss muscle injury. *Sci Rep* (2023) **13**(1):1983. doi:10.1038/s41598-023-27981-x

118. Aldali F, Yang Y, Deng C, Li X, Cao X, Xu J, et al. Induced pluripotent stem cell-derived exosomes promote peripheral nerve regeneration in a rat sciatic nerve crush injury model: a safety and efficacy study. *Cells* (2025) **14**(7):529. doi:10.3390/cells14070529

119. Abalymov A, Parakhonskiy B, Skirtach A. Polymer- and hybrid-based biomaterials for interstitial, connective, vascular, nerve, visceral and musculoskeletal tissue engineering. *Polymers* (2020) **12**(3):620. doi:10.3390/polym12030620

120. Chen Y, Xu Y, Ramakrishna S. Electromagnetic-responsive targeted delivery scaffold technology has better potential to repair injured peripheral nerves: a narrative review. *Adv Technology Neurosci* (2024) **1**(1):51–71. doi:10.4103/ATN.ATN-D-24-00002

121. Wang C, Pan C, Yong H, Wang F, Bo T, Zhao Y, et al. Emerging non-viral vectors for gene delivery. *J Nanobiotechnol* (2023) **21**(1):272. doi:10.1186/s12951-023-02044-5

122. Tasset A, Bellamkonda A, Wang W, Pyatnitskiy I, Ward D, Peppas N, et al. Overcoming barriers in non-viral gene delivery for neurological applications. *Nanoscale* (2022) **14**(10):3698–719. doi:10.1039/D1NR06939J

123. Zhang W, Hou Y, Yin S, Miao Q, Lee K, Zhou X, et al. Advanced gene nanocarriers/scaffolds in nonviral-mediated delivery system for tissue regeneration and repair. *J Nanobiotechnol* (2024) **22**(1):376. doi:10.1186/s12951-024-02580-8

124. Li Y, Ji RR. Gene therapy for chronic pain management. *Cell Rep Med* (2024) **5**(10):101756. doi:10.1016/j.xcrm.2024.101756

125. Qi L, Zhang F, Wang K, Chen B, Li X, Xu J, et al. Advancements in skeletal muscle tissue engineering: strategies for repair and regeneration of skeletal muscle beyond Self-repair. *Regenerative Biomater* (2025) **12**:rbaf050. doi:10.1093/rb/rbaf050

126. Giannakis N. Data integration from multi-omics approaches reveal inflammation dynamics upon muscle tissue injury and regeneration (2020). Available online at: http://hdl.handle.net/2437/300926 (Accessed June 15, 2025).

127. Cai S, Hu B, Wang X, Liu T, Lin Z, Tong X, et al. Integrative single-cell RNA-seq and ATAC-seq analysis of myogenic differentiation in pig. *BMC Biol* (2023) **21**(1):19. doi:10.1186/s12915-023-01519-z

128. Biswas D, Jiang P. Chemically induced reprogramming of somatic cells to pluripotent stem cells and neural cells. *IJMS* (2016) **17**(2):226. doi:10.3390/ijms17020226

129. Kwon JB, Gersbach CA, 626. Directing skeletal myogenic progenitor cell lineage specification with CRISPR/Cas9 transcriptional activators. *Mol Ther* (2016) **24**:S248. doi:10.1016/S1525-0016(16)33434-7

130. Kagiava A, Karaiskos C, Richter J, Tryfonos C, Jennings MJ, Heslegrave AJ, et al. AAV9-mediated schwann cell-targeted gene therapy rescues a model ofdemyelinating neuropathy. *Gene Ther* (2021) **28**(10-11):659–75. doi:10.1038/s41434-021-00250-0

131. Hadzimustafic N, D'Elia A, Shamoun V, Haykal S. Human-induced pluripotent stem cells in plastic and reconstructive surgery. *IJMS* (2024) **25**(3):1863. doi:10.3390/ijms25031863

132. Angius D, Wang H, Spinner RJ, Gutierrez-Cotto Y, Yaszemski MJ, Windebank AJ. A systematic review of animal models used to study nerve regeneration in tissue-engineered scaffolds. *Biomaterials* (2012) **33**(32):8034–9. doi:10.1016/j.biomaterials.2012.07.056

133. Khandia R, Gurjar P, Priyanka RV, Al-Hussain SA, Zaki MEA. Recent advances in stem cell therapy: efficacy, ethics, safety concerns, and future directions focusing on neurodegenerative disorders – a review. *Int J Surg* (2024) **110**(10):6367–81. doi:10.1097/JS9.0000000000001609

134. Kato Y, Mori H. Genetically stable kill-switch using "demon and angel" expression construct of essential genes. *Front Bioeng Biotechnol* (2024) **12**:1365870. doi:10.3389/fbioe.2024.1365870

135. Gu H, Zhou Y, Yang J, Li J, Peng Y, Zhang X, et al. Targeted overexpression of PPARγ in skeletal muscle by random insertion and CRISPR/Cas9 transgenic pig cloning enhances oxidative fiber formation and intramuscular fat deposition. *FASEBj* (2021) **35**(2):e21308. doi:10.1096/fj.202001812RR

136. Lin H, Peng H, Sun Y, Si M, Wu J, Wang Y, et al. Reprogramming of cis-regulatory networks during skeletal muscle atrophy in Male mice. *Nat Commun* (2023) **14**(1):6581. doi:10.1038/s41467-023-42313-3

137. Pellett S, Yaksh T, Ramachandran R. Current status and future directions of botulinum neurotoxins for targeting pain processing. *Toxins* (2015) **7**(11):4519–63. doi:10.3390/toxins7114519

138. Gessler L, Huraskin D, Jian Y, Eiber N, Hu Z, Prószyński TJ, et al. The YAP1/TAZ-TEAD transcriptional network regulates gene expression at neuromuscular junctions in skeletal muscle fibers. *Nucleic Acids Res* (2024) **52**(2):600–24. doi:10.1093/nar/gkad1124

139. Jing Y, Jiang X, Ji Q, Wu Z, Wang W, Liu Z, et al. Genome-wide CRISPR activation screening in senescent cells reveals SOX5 as a driver and therapeutic target of rejuvenation. *Cell Stem Cell* (2023) **30**(11):1452–71.e10. doi:10.1016/j.stem.2023.09.007

140. Burrell JC, Browne KD, Dutton JL, Laimo FA, Das S, Brown DP, et al. A porcine model of peripheral nerve injury enabling. *Neurosurgery* (2025). Available online at: http://ral_nerve_injury.28.aspx/ (Accessed June 15, 2025).

141. Cai CW, Grey JA, Hubmacher D, Han WM. Biomaterial-based regenerative strategies for volumetric muscle loss: challenges and solutions. *Adv Wound Care* (2025) **14**(3):159–75. doi:10.1089/wound.2024.0079

142. Judson RN, Rossi FMV. Towards stem cell therapies for skeletal muscle repair. *Npj Regen Med* (2020) **5**(1):10. doi:10.1038/s41536-020-0094-3

143. Qazi TH, Duda GN, Ort MJ, Perka C, Geissler S, Winkler T. Cell therapy to improve regeneration of skeletal muscle injuries. *J Cachexia Sarcopenia Muscle* (2019) **10**(3):501–16. doi:10.1002/jcsm.12416

144. Consalvi S, Sandoná M, Saccone V. Epigenetic reprogramming of muscle progenitors: inspiration for clinical therapies. *Stem Cells Int* (2016) **2016**(1):6093601. doi:10.1155/2016/6093601

145. Zhang YX, Chen SL, Li YM, Zheng YW. Limitations and challenges of direct cell reprogramming *in vitro* and *in vivo*. *Histol Histopathol* (2022) **37**(08):723–37. doi:10.14670/HH-18-458

146. Viezuină DM, Burlacu IM, Greşiţă A, Matache IM, Târtea EA, Muşat MI, et al. Phase-specific evaluation of sciatic nerve regeneration in preclinical studies: a review of functional assessment, emerging therapies, and translational value. *Int J Mol Sci* (2025) **27**(1):419. doi:10.3390/ijms27010419

147. Calcedo R, Franco J, Qin Q, Richardson DW, Mason JB, Boyd S, et al. Preexisting neutralizing antibodies to Adeno- associated virus capsids in large animals other than monkeys may confound *in vivo* gene therapy studies. *Hum Gene Ther Methods* (2015) **26**(3):103–5. doi:10.1089/hgtb.2015.082

148. Tenente IM, Hayes MN, Ignatius MS, McCarthy K, Yohe M, Sindiri S, et al. Myogenic regulatory transcription factors regulate growth in rhabdomyosarcoma. *eLife* (2017) **6**:e19214. doi:10.7554/eLife.19214

149. Zhou X, Naik S, Dakhova O, Dotti G, Heslop HE, Brenner MK. Serial activation of the inducible caspase 9 safety switch after human stem cell transplantation. *Mol Ther* (2016) **24**(4):823–31. doi:10.1038/mt.2015.234

150. Dhaiban S, Chandran S, Noshi M, Sajini AA. Clinical translation of human iPSC technologies: advances, safety concerns, and future directions. *Front Cell Dev Biol* (2025) **13**:1627149. doi:10.3389/fcell.2025.1627149

151. Kostrominova TY. Skeletal muscle denervation: past, present and future. *IJMS* (2022) **23**(14):7489. doi:10.3390/ijms23147489

152. Le Guen YT, Le Gall T, Midoux P, Guégan P, Braun S, Montier T. Gene transfer to skeletal muscle using hydrodynamic limb vein injection: current applications, hurdles and possible optimizations. *The J ofGene Med* (2020) **22**(2): e3150. doi:10.1002/jgm.3150

153. Krut Z, Gazit D, Gazit Z, Pelled G. Applications of ultrasound-mediated gene delivery in regenerative medicine. *Bioengineering* (2022) **9**(5):190. doi:10.3390/bioengineering9050190

154. Maciulaitis R, D'Apote L, Buchanan A, Pioppo L, Schneider CK. Clinical development of advanced therapy medicinal products in Europe: evidence that regulators must be proactive. *Mol Ther* (2012) **20**(3):479–82. doi:10.1038/mt.2012.13

155. Tang C, Zhang Z, Yang C, Li L, Li J, Cheng X, et al. Molecular time machines unleashed: small-molecule-driven reprogramming to reverse the senescence. *Stem Cells Transl Med* (2026) **15**(1):szaf069. doi:10.1093/stcltm/szaf069

156. Harrison RP, Ruck S, Medcalf N, Rafiq QA. Decentralized manufacturing of cell and gene therapies: overcoming challenges and identifying opportunities. *Cytotherapy* (2017) **19**(10):1140–51. doi:10.1016/j.jcyt.2017.07.005

157. Pereira JD, DuBreuil DM, Devlin AC, Held A, Sapir Y, Berezovski E, et al. Human sensorimotor organoids derived from healthy and amyotrophic lateral sclerosis stem cells form neuromuscular junctions. *Nat Commun* (2021) **12**(1):4744. doi:10.1038/s41467-021-24776-4

158. Vegad U, Patel M, Khunt D, Zupančič O, Chauhan S, Paudel A. pH stimuli-responsive hydrogels from non-cellulosic biopolymers for drug delivery. *Front Bioeng Biotechnol* (2023) **11**:1270364. doi:10.3389/fbioe.2023.1270364

159. Kim JH, Kim I, Seol YJ, Ko IK, Yoo JJ, Atala A, et al. Neural cell integration into 3D bioprinted skeletal muscle constructs accelerates restoration of muscle function. *Nat Commun* (2020) **11**(1):1025. doi:10.1038/s41467-020-14930-9

160. Mavrommatis L, Jeong HW, Kindler U, Gomez-Giro G, Kienitz MC, Stehling M, et al. Human skeletal muscle organoids model fetal myogenesis and sustain uncommitted PAX7 myogenic progenitors. *eLife* (2023) **12**:RP87081. doi:10.7554/eLife.87081

161. Yue Y, Shin JH, Duan D. Whole body skeletal muscle transduction in neonatal dogs with AAV-9. *Methods Mol Biol* (2011) **709**:313–29. doi:10.1007/978-1-61737-982-6_21

162. Warneke K, Freund PA, Schiemann S. Long-lasting stretching induces muscle hypertrophy: a meta-analysis of animal studies. *J Ofsci IN SPORT and EXERCISE* (2023) **5**(4):289–301. doi:10.1007/s42978-022-00191-z

163. Park SM, Lee JH, Ahn KS, Shim HW, Yoon JY, Hyun J, et al. Cyclic stretch promotes cellular reprogramming process through cytoskeletal-nuclear mechano-coupling and epigenetic modification. *Adv Sci (Weinh)* (2023) **10**(32):e2303395. doi:10.1002/advs.202303395

164. Wang H, Yang Y, Liu J, Qian L Direct cell reprogramming: approaches, mechanisms and progress. *Nat Rev Mol Cell Biol* (2021) **22**(6):410–424. doi:10.1038/s41580-021-00335-z

165. Pereira CT, Hill EE, Stasyuk A, Parikh N, Dhillon J, Wang A, et al. Molecular basis of surgical coaptation techniques in peripheral nerve injuries. *JCM* (2023) **12**(4):1555. doi:10.3390/jcm12041555

166. El Ouaamari Y, Van den Bos J, Willekens B, Cools N, Wens I. Neurotrophic factors as regenerative therapy for neurodegenerative diseases: current status, challenges and future perspectives. *IJMS* (2023) **24**(4):3866. doi:10.3390/ijms24043866

167. Stocco E, Barbon S, Emmi A, Tiengo C, Macchi V, De Caro R, et al. Bridging gaps in peripheral nerves: from current strategies to future perspectives in conduit design. *IJMS* (2023) **24**(11):9170. doi:10.3390/ijms24119170

168. Massenet J, Gardner E, Chazaud B, Dilworth FJ. Epigenetic regulation of satellite cell fate during skeletal muscle regeneration. *Skeletal Muscle* (2021) **11**(1):4. doi:10.1186/s13395-020-00259-w

169. Hsu MN, Liao HT, Truong VA, Huang KL, Yu FJ, Chen HH, et al. CRISPR-Based activation of endogenous neurotrophic genes in adipose stem cell sheets to stimulate peripheral nerve regeneration. *Theranostics* (2019) **9**(21):6099–111. doi:10.7150/thno.36790

170. Mikhailova MM, Klein OI, Patsaev TD, Panteleyev AA. Co-culture of postnatal mouse spinal cord and skeletal muscle explants as an experimental model of neuromuscular interactions. *Histochem Cell Biol* (2025) **163**(1):15. doi:10.1007/s00418-024-02343-4

171. Andreana I, Repellin M, Carton F, Kryza D, Briançon S, Chazaud B, et al. Nanomedicine for gene delivery and drug repurposing in the treatment of muscular dystrophies. *Pharmaceutics* (2021) **13**(2):278. doi:10.3390/pharmaceutics13020278

172. Dou D, Lu J, Dou J, Huo Y, Gong X, Zhang X, et al. Global regulatory considerations and practices for tumorigenicity evaluation of cell-based therapy. *Regul Toxicol Pharmacol* (2025) **156**:105769. doi:10.1016/j.yrtph.2024.105769

173. Li A, Pereira C, Hill EE, Vukcevich O, Wang A. Vitro, *in vivo* and *Ex Vivo* models for peripheral nerve injury and regeneration. *Curr Neuropharmacol* (2022) **20**(2):344–61. doi:10.2174/1570159X19666210407155543

174. Moffit JS, Blanset DL, Lynch JL, MacLachlan TK, Meyer KE, Ponce R, et al. Regulatory consideration for the nonclinical safety assessment of gene therapies. *Hum Gene Ther* (2022) **33**:1126–41. doi:10.1089/hum.2022.090

175. Novoa JJ, Westra IM, Steeneveld E, Fonseca Neves N, Arendzen CH, Rajaei B, et al. Good manufacturing Practice– compliant human induced pluripotent stem cells: from bench to putative clinical products. *Cytotherapy* (2024) **26**(6):556–66. doi:10.1016/j.jcyt.2024.02.021

EBM Experimental Biology and Medicine

TYPE Brief Communication
PUBLISHED 23 January 2026
DOI 10.3389/ebm.2026.10856

OPEN ACCESS

*CORRESPONDENCE
Csaba Szabo,
csaba.szabo@unifr.ch

RECEIVED 10 October 2025
REVISED 14 November 2025
ACCEPTED 08 January 2026
PUBLISHED 23 January 2026

CITATION
Kieronska-Rudek A, Petrosino M, Zuhra K and Szabo C (2026) Cyanide is an endogenous stimulator of endothelial cell proliferation, migration and differentiation.
Exp. Biol. Med. 251:10856.
doi: 10.3389/ebm.2026.10856

Cyanide is an endogenous stimulator of endothelial cell proliferation, migration and differentiation

Anna Kieronska-Rudek, Maria Petrosino, Karim Zuhra and Csaba Szabo*

Section of Pharmacology, Department of Oncology, Microbiology and Immunology, Faculty of Science and Medicine, University of Fribourg, Fribourg, Switzerland

Abstract

Cyanide is generally considered a cytotoxic molecule. However, recent studies have shown that mammalian cells — including endothelial cells — can produce cyanide from glycine via a lysosomal pathway. Studies in hepatocytes indicated that cyanide, when administered at low concentrations, or when generated from endogenous sources, exerts regulatory, rather than cytotoxic effects. Here we show that human umbilical vein endothelial cells produce detectable levels of cyanide (~0.1 nmoles/mg protein/h), and this is enhanced by administration of glycine (1 mM). Glycine stimulates endothelial cell proliferation, migration and tube formation. Low concentrations of the cyanide releasing molecules amygdalin or mandelonitrile (100 μM) exert similar effects. On one hand, cyanide induces the upregulation of VEGF protein in endothelial cells, while on the other hand, VEGF stimulates the generation of cyanide by endothelial cells, suggesting a positive feedback. VEGF-stimulated endothelial cell ATP generation, proliferation and migration is inhibited by the cyanide scavenger hydroxycobalamin (10 μM) as well as by pharmacological agents that prevent lysosomal acidification and thus inhibit cyanide formation by the endothelial cells. In conclusion, cyanide, at low concentrations, generated by endothelial cells, acts as a proangiogenic mediator, via stimulation of the VEGF pathway and the maintenance of cellular bioenergetics.

KEYWORDS

vascular, endothelial, proliferation, migration, blood vessels

Impact statement

This study identifies cyanide as an endogenous signaling molecule that promotes endothelial cell proliferation, migration, and differentiation. By demonstrating a physiological role for low-level cyanide generation in vascular biology, the work challenges the traditional view of cyanide solely as a toxicant and reveals a previously

unrecognized regulatory pathway with broad implications for endothelial function and angiogenesis.

Introduction

Cyanide is primarily recognized as a cytotoxic agent, which inhibits mitochondrial electron transport through binding to the heme a3 group in mitochondrial Complex IV (Cytochrome C oxidase, CCOx) [1]. However, a separate body of evidence suggests that cyanide, at low concentrations, can also exert various cytoprotective or regulatory actions [2–4]. Most recently, an endogenous cyanide generating pathway has been demonstrated in mammalian cells and tissues. According to this pathway, cyanide is produced from glycine within lysosomes under acidic conditions and cyanide biogenesis supports cellular bioenergetics and proliferation and exerts cytoprotective effects in hepatocytes [4]. Although this recent report was primarily focusing on hepatocytes, a survey of various cell lines and primary cells also demonstrated that endothelial cells also produce detectable levels of cyanide, and this cyanide generation can be stimulated by increasing the extracellular glycine concentration [4]. However, the functional role of cyanide generation by endothelial cells has not yet been elucidated; the available body of literature on the effects of cyanide in this cell type focuses on the toxicological context [5].

Here we demonstrate that cyanide generation in endothelial cells, at low concentrations, stimulates cell proliferation and angiogenesis. The current findings put cyanide in a physiological, regulatory context within the cardiovascular system.

Materials and Methods

Materials

Mandelonitrile (#116025), amygdalin (#A6005), glycine (#G7126), hydroxychloroquine (#H0915), Vitamin B12a (#H1428000), vascular endothelial growth factor (VEGF, #SRP3182), Corning® Matrigel® Basement Membrane Matrix (#CLS354234) and β-actin antibody (#A1978) were purchased from Sigma-Aldrich (Buchs, Switzerland). LysoTracker™ Bafilomycin A1 (J61835) was purchased from Alfa Aesar/ ThermoFisher (Haverhill, MA, United States). Deep Red (#L12492) was purchased from ThermoFisher Scientific/ Invitrogen. The anti-VEGF antibody (#ab51745) was purchased from Abcam (Cambridge, UK). The cyanide detection probe Chemosensor P (2-amino-3-((5-(benzothiazol-2-yl)-2-hydroxybenzylidene)amino) maleonitrile) [6] was a kind gift of Dr. Sait Malkondu (Giresun University, Giresun, Turkey).

Cell culture

Human umbilical vein endothelial cells (HUVECs, CC-2519) were purchased from Lonza (Basel, Switzerland). Cells were maintained in EGM®-2 Endothelial Cell Growth Medium-2 BulletKit® (CC-3162; Lonza, Basel, Switzerland) at 37 °C in a humidified atmosphere containing 5% CO_2. Cells up to the 5th passage were used.

Electrochemical analysis of cyanide production

Electrochemical detection of cyanide was performed following a previously described protocol [4], with minor modifications. Briefly, cells were seeded in 24-well plates and allowed to adhere overnight. Depending on the experimental conditions, cells were then incubated for 72 h in medium supplemented with VEGF (20 ng/mL) or control medium without VEGF.

To assess cyanide generation, cells were treated for 16 h with the cyanide-releasing compound: glycine (1 mM), amygdalin (100 μM), or mandelonitrile (100 μM) or control vehicle. In another experiment, cells were incubated in the absence or presence of VEGF for 72 h (see below). Following the various treatments, culture media were collected and mixed immediately in a 1:1 ratio with 1 M NaOH to stabilize released hydrogen cyanide (HCN) as CN^-. The samples were incubated at room temperature for 30 min to ensure complete conversion of HCN to CN^-. A standard curve was generated using potassium cyanide (KCN). Cyanide production rates were normalized to total protein content, which was determined using the BCA protein assay (Thermo Scientific, #23225). Results were expressed as nanomoles of cyanide per milligram of protein per hour. The specificity of this method has previously been validated [4].

Western blotting

Cell lysates were prepared using RIPA Lysis and Extraction Buffer (Thermo Fisher Scientific), supplemented with Halt™ Protease and Phosphatase Inhibitor Cocktail (Thermo Fisher Scientific). Total protein concentrations were determined using the Pierce™ BCA Protein Assay Kit (Thermo Fisher Scientific). Western blot analysis was performed according to a previously described protocol [7]. VEGF protein expression was detected using a primary antibody against VEGF (1:1,000), followed by incubation with a horseradish peroxidase-conjugated secondary antibody (Cell Signalling Technology, Danvers, MA, United States). After VEGF detection, membranes were stripped using Restore™ PLUS Western Blot Stripping Buffer (#10016433, Thermo Fisher Scientific) and incubated with primary antibody against β-actin (1:15,000) as a loading control. Blots were developed using Radiance Plus

Chemiluminescence Substrate (#AC2103, Azure Biosystems, Dublin, CA, United States). Densitometric analysis was performed using the ImageJ software (NIH, Bethesda, MD, United States). Protein levels were normalized to β-actin.

Confocal microscopy-based detection of cyanide

Cells were seeded in 4-chamber glass-bottom dishes (pre-coated with rat tail collagen, #354236, Corning) at a density of 2.5×10^4 cells per compartment. Cells were incubated overnight at 37 °C in a humidified incubator (5% CO_2) to allow attachment. Cells were then incubated in EGM-2 media with or without VEGF for 72 h.

Cyanide levels were assessed using a previously established protocol [4, 8] with slight modifications. Briefly, cells were incubated for 1 h with 10 μM of the cyanide-selective fluorescent probe CSP. After probe incubation, cells were stained with LysoTracker™ Deep Red (50 nM) for 10 min to label lysosomes. Cells were then washed 3x with Hank's Balanced Salt Solution (Thermo Fisher Scientific) to remove excess dye. Confocal imaging was performed using a Leica SP5 microscope equipped with a ×40 oil-immersion objective. For each condition, three images per well were acquired from five independent biological replicates. Fluorescence intensity was quantified using the ImageJ software. The specificity of this method has previously been validated [4].

Cell proliferation assay

Cells were seeded in 96-well plates at a density of 4×10^3 cells per well and incubated overnight at 37 °C in a humidified incubator to allow cell adhesion. The following day, the culture medium was replaced with medium containing various pharmacological agents including glycine (1 mM), or amygdalin (100 μM), or mandelonitrile (100 μM). Immediately after treatment, the plate was placed in the BioTek Cytation 5 Cell Imaging Multimode Reader (Agilent) [4]. Live-cell imaging was performed every 4 h over 48 h, with four images captured per well at ×100 magnification.

In another set of experiments, cells were placed either in a modified EGM-2 BulletKit® (Lonza) medium which excluded all growth factors and contained a reduced amount of FBS (0.5% FBS) with or without VEGF (20 ng/mL) supplementation in the presence or absence of hydroxocobalamin (B12a, 10 μM), hydroxychloroquine (HCQ, 10 μM) or bafilomycin (30 nM) and cell proliferation was monitored for 48 h as described above.

Wound healing assay

Cells were seeded in 96-well plates at a density of 2.5×10^4 cells per well and incubated overnight to allow for cell adherence. The following day, scratch wounds were generated using the Essen BioScience WoundMaker (4563; Essen BioScience Inc., Hertfordshire, UK). Cells were then gently washed with PBS to remove debris resulting from the scratch. The medium was subsequently replaced with treatment medium containing either glycine (1 mM), or amygdalin (100 μM) or mandelonitrile (100 μM). The plate was then placed in a BioTek Cytation 5 Cell Imaging Multimode Reader, and images were captured every 4 h over 20 h. Four images per well were acquired at ×100 magnification.

Tube formation assay

Prior to cell seeding, a 96-well plate was coated with 60 μL of Matrigel per well and incubated at 37 °C for 1 h to allow the matrix to polymerize. Cells were then seeded at a density of 1.5×10^4 cells per well in 100 μL of EBM-2. The plate was returned to the incubator for 2 h to allow for cell attachment, minimizing potential interference from treatment compounds during the adhesion phase. Following this initial incubation, test compounds were added to the appropriate wells to achieve final concentrations of 1 mM glycine and 100 μM amygdalin or mandelonitrile. Incubation continued for an additional 14–16 h at 37 °C when analysis was conducted as described [9]. Four representative images per well were captured using a BioTek Cytation 5 Cell Imaging Multi-Mode Reader at ×100 magnification. Image analysis was performed using the Angiogenesis Analyzer plugin for ImageJ. Quantitative assessment of angiogenesis was based on key morphological parameters, including total tube length, number of segments, and number of junctions.

Adenosine triphosphate (ATP) production

ATP levels were measured using the CellTiter-Glo® Luminescent Cell Viability Assay (Promega, Madison, WI, United States) as described [10]. Luminescence was measured using a Infinite 200 Pro plate reader (Tecan).

Statistical analysis

Unless otherwise stated, data are presented as mean values ± SEM of several independent experiments where an independent experiment is defined as an experiment performed on a different experimental day, representing a biological replicate (as opposed to technical replicates). No statistical methods were used to pre-determine sample sizes, but our sample sizes are similar to those reported in previous publications [4, 8]. Data are presented as mean ± SEM of 4-5 biological experiments, where the average of a

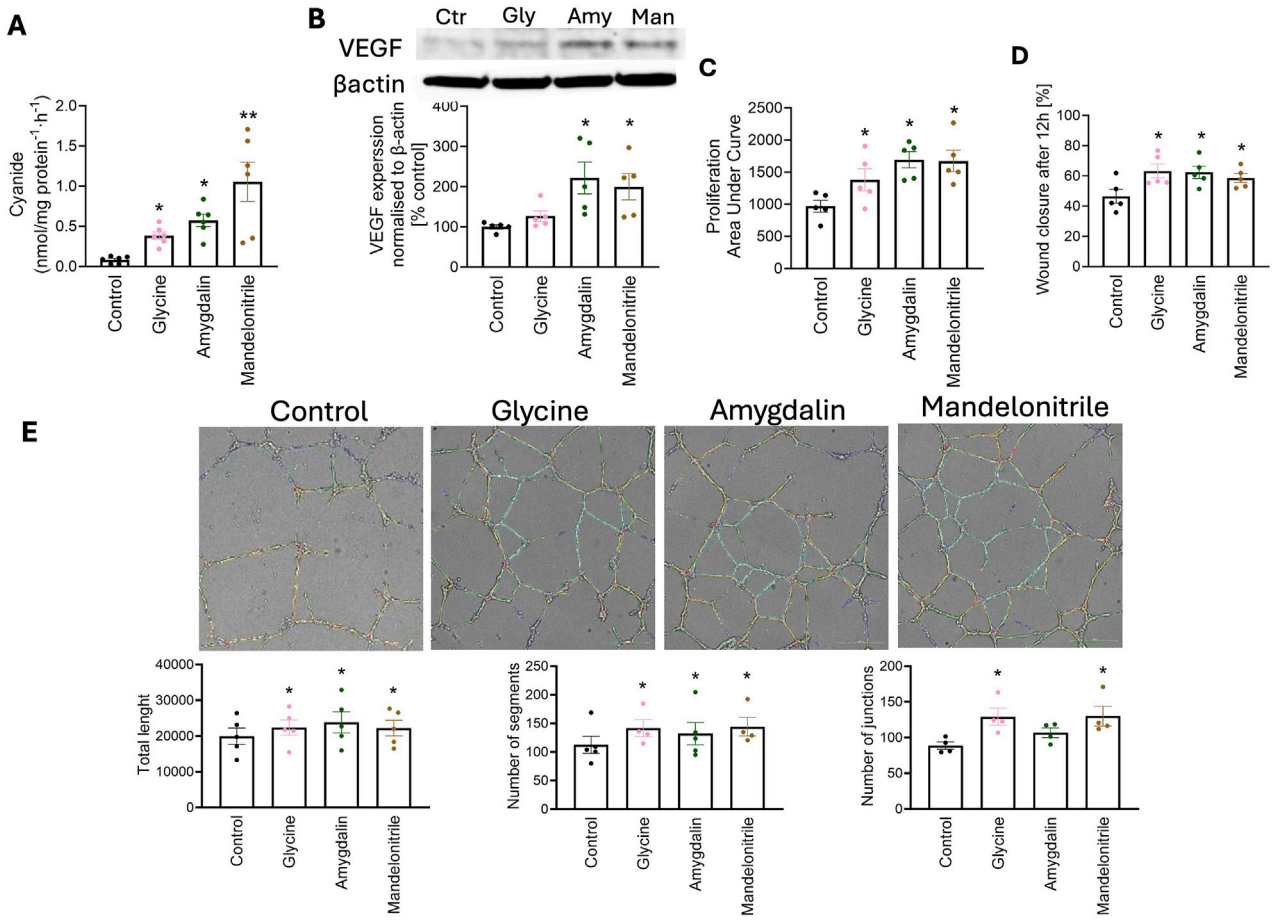

FIGURE 1
Low levels of cyanide promote endothelial cell proliferation, migration and differentiation. **(A)** Detection of cyanide generation **(B)**, induction of VEGF expression **(C)**, proliferation **(D)**, wound healing and **(E)** tube formation in HUVECs in response to incubation with glycine (Gly) (1 mM), amygdalin (Amy) (100 μM) or mandelonitrile (Man) (100 μM). For **(E)**, representative images as well as statistical analysis of the data are shown. Data are presented as mean ± SEM. Individual data points represent independent biological replicates. Statistical analysis was performed as described in the Materials and Methods section; significance is indicated as follows: *p < 0.05, **p < 0.01.

minimum of three technical replicates is calculated and entered as a single value. Paired or unpaired Student's t-test was used to compare 2 groups, as appropriate. For multiple comparisons, one or two-way ANOVA followed by post-hoc analysis by Dunnett or Fisher LSD test, respectively. Differences among groups are considered statistically significant for p values of ≤0.05. Statistical analysis was performed using GraphPad Prism 10.2 (GraphPad Software Inc., San Diego, California, United States).

Results

HUVECs grown in culture in Vascular Cell Basal Medium (which contains 30 μM glycine) produce detectable levels of cyanide (0.1 nmoles/mg protein/h); cyanide generation was enhanced by approximately 4-fold when the medium was supplemented with glycine (1 mM) to 0.4 nmoles/mg protein/h (Figure 1A). Glycine induced a trend toward increased expression of vascular endothelial growth factor (VEGF) (Figure 1B) and stimulated cell proliferation (Figure 1C), migration (Figure 1D) and tube formation (Figure 1E). A stimulatory effect on VEGF expression was also observed after treatment of the cells with low concentrations of the cyanogenic molecules amygdalin (100 μM) or mandelonitrile (100 μM) (Figure 1B); both of these compounds–which release cyanide at a comparable rate as the endogenous cyanide generation rates [4] – mimicked the effect of glycine and stimulated endothelial cell proliferation, migration and tube formation (Figures 1C-E). These compounds, when added to HUVECs, generate cyanide at rates of 0.5–1 nmoles/mg protein/h (Figure 1A).

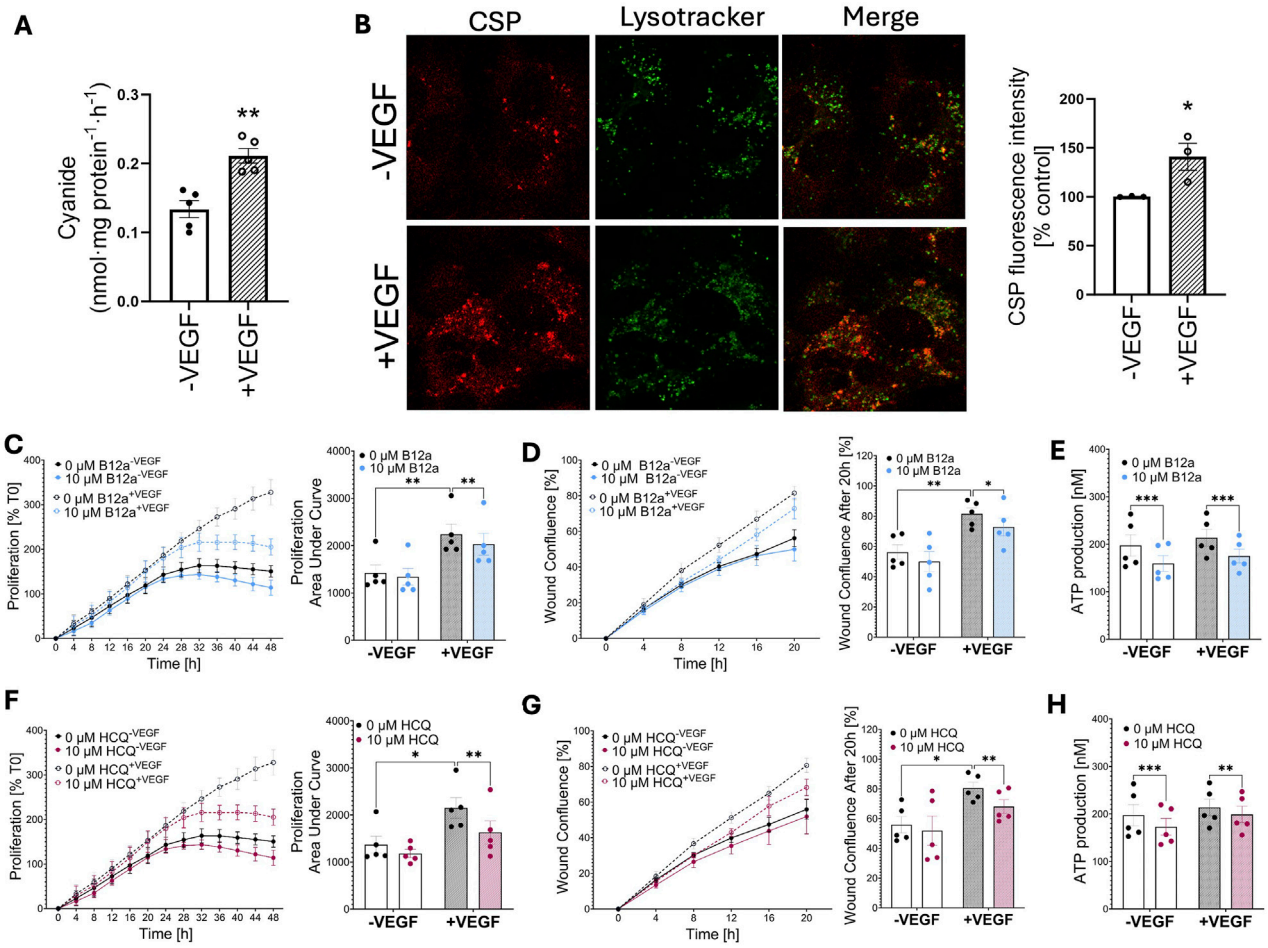

FIGURE 2
Endogenous cyanide generation supports endothelial cell proliferation, migration and differentiation. **(A)** Detection of cyanide generation by the electrochemical method and **(B)** confocal microscopy using the cyanide-specific probe CSP in HUVECs incubated with or without VEGF for 72 h. Effect of cyanide scavenger Vitamin B12a (B12a) **(C–E)** or hydroxychloroquine (HCQ) **(F–H)** in HUVECs in the presence of absence of 20 ng/mL VEGF on **(C,F)** cell proliferation, **(D,G)** wound healing, and **(E,H)** ATP production. Data are presented as mean ± SEM. Individual data points represent independent biological replicates. Statistical analysis was performed as described in the Materials and Methods section; significance is indicated as follows: *p < 0.05, **p < 0.01, ***p < 0.001.

Administration of VEGF stimulated the generation of cyanide by endothelial cells (Figures 2A,B); confocal imaging studies localized cyanide primarily to the lysosomes (Figure 2B) — consistently with the prior findings in hepatocytes and fibroblasts [4, 8]. A less pronounced cyanide signal was also detected in the cytosolic compartment of the cells (Figure 2B).

Scavenging of cyanide with hydroxocobalamin (Vitamin B12a, 10 μM) reduced the VEGF-induced cell proliferation (Figure 2C), migration (Figure 2D) and ATP production (Figure 2E). The lysosomal deacidification agent hydroxychloroquine, which inhibits cyanide generation by shifting the pH optimum of the reaction in the lysosomes [4], also inhibited VEGF-stimulated proliferation (Figure 2F), migration (Figure 2G) and ATP production (Figure 2H); similar inhibitory effect was also detected by treatment of the cells with the lysosomal proton pump inhibitor bafilomycin, which attenuated basal and VEGF-stimulated proliferation by 21 ± 4 and 45 ± 3%, respectively (n = 4, <0.05).

Discussion

With recent data demonstrating its lysosomal generation from glycine in mammalian cells [4], cyanide can be classified as a gasotransmitter: a diffusible, endogenous mediator that is produced in mammalian cells to serve regulatory functions [4, 11]. Importantly, several gasotransmitters have previously been shown to be produced in endothelial cells. NO, produced from L-arginine, is responsible for endothelium-dependent vascular relaxations, and serves as a pro-angiogenic agent

[12–16]. CO from heme oxygenase serving as an endothelial cell protective mediator [17–19], and H_2S exerts vasorelaxant and proangiogenic effects [20–23]. The current report adds cyanide as a pro-angiogenic molecule. Interestingly, prior reports have made important connections of VEGF to the NO and H_2S systems. VEGF has been shown to induce both the generation of NO and H_2S in endothelial cells, and these two mediators [24, 25] — in a synergistic manner [26] — are important effectors of VEGF's proangiogenic effect. In addition, H_2S has also been shown to upregulate VEGF and VEGF receptor expression and activation [27–30].

The current findings indicate that cyanide, when produced at low levels by endothelial cells, exerts similar regulatory actions: it supports cell proliferation, migration and differentiation. The effects of cyanide biogenesis could be mimicked by exposure of the cells to low levels of the cyanogenic compounds amygdalin or mandelonitrile, which generated comparable, or slightly higher levels of cyanide, than the cyanide generation rate observed in response to addition of glycine. (The concentration of glycine, used at 1 mM in this study, is slightly above its physiological plasma levels, which are in the 0.2–0.5 μM range).

The current report demonstrates that Vitamin B12a (a potent scavenger of cyanide [31]), as well as hydroxychloroquine and bafilomycin (compounds that inhibits cyanide generation via inhibiting lysosomal acidification) reduce the VEGF-induced proliferative response in HUVECs. Although all of these pharmacological agents have several different pharmacological actions — for instance, Vitamin B12 can scavenge H_2S and other reactive species too [31] — the above findings, coupled with the effect of two structurally different cyanide-releasing molecules, which mimic the effect of glycine, point to the role of the endogenous cyanide pathway in the observed actions. Moreover, the upregulation of VEGF in response to cyanogenic compounds suggests a potential positive feedback cycle between VEGF and cyanide.

Confocal imaging of HUVECs produced data that are consistent with the lysosomal cyanide generation pathway already demonstrated in various cell types, including hepatocytes, fibroblasts and various cancer cells [4]. According to this pathway, glycine is taken up into the lysosomes, and reacts with HOCl to generate various short-lived intermediary species, which, in turn, decompose to yield cyanide and CO_2. Indeed, prior studies have already demonstrated all of the relevant [4] components of the glycine/cyanide biogenetic system in endothelial cells, including peroxidase activity, HOCl generation, uptake of glycine from the extracellular space as well as the serine/glycine conversion system governed by the intracellular enzyme serine hydroxymethyl transferase [32–35].

Importantly, prior studies have already demonstrated that glycine can stimulate endothelial cell proliferation and angiogenesis, and attributed its effects to a bioenergetic stimulatory response [36]. Likewise, at relatively low concentrations (1–10 mM), glycine was found to stimulate angiogenesis and vascular development in zebrafish embryos [37]. There are also several lines of data demonstrating cytoprotective effects of glycine in endothelial cells [38]. The current findings are consistent with the above findings. We suggest that — similar to what was demonstrated in hepatocytes and hepatoma cells — also in HUVECs, low concentrations of endogenously generated cyanide stimulate mitochondrial electron transport and ATP generation, which supports the energy requirement of proliferation, migration and differentiation.

Cyanide is known as a potent inhibitor of Complex IV (cytochrome c oxidase), and this effect is primarily attributed to its cytotoxic actions. This effect, however, is expected to be less relevant in endothelial cells for two reasons: (a) the levels of cyanide generated are rather low, and we have found no evidence of cytotoxic or cytostatic effects, and, in fact, a stimulatory effect on bioenergetics was noted; (b) endothelial cells tend to utilize glycolysis, rather than oxidative phosphorylation to meet their energetic demands [39]. It is interesting to notice that in the zebrafish study mentioned earlier, at higher concentrations (100–400 mM), the stimulatory effect of glycine was diminished and the amino acid inhibited vascular development [37]. Based on prior data — in cells overproducing cyanide due to silencing of the cyanide degradation pathway governed by rhodanese [4], or cells that exhibit genetic mutations in the glycine degradation pathway [4], or cells that contain high levels of cyanide due to inhibition of rhodanese [11] — such a biphasic concentration-response is consistent with the action of cyanide as an endogenous mediator.

The data presented in this article indicate that cyanide production exerts regulatory roles in endothelial cells, and promotes endothelial cell proliferation, migration and differentiation. Although the underlying effects remain to be further characterized, the data presented in this report point, in part, to a potential VEGF-related mechanism, and in part to stimulation of cellular bioenergetics. A limitation of the current study is that cellular bioenergetic parameters (e.g., oxidative phosphorylation, glycolysis) have not been measured; such measurements would further expand on the underlying mechanisms of cyanide's action. Given the fact that cyanide is an endogenous molecule, which is present in the blood at detectable levels (basally, in approximately 300–600 nM) [1, 4], the current report raises the possibility that low levels of cyanide may contribute to the maintenance of endothelial and cardiovascular homeostasis. It is noteworthy in this respect that there are several reports showing that the cyanide metabolite 2-aminothiazoline-4-carboxylic acid correlates with various clinical parameters in cardiovascular disease and aging [40, 41].

Author contributions

CS initiated and conceptualized the study, and contributed to the experimental design and data interpretation. AK-R, MP, and KZ conducted experiments. AK-R and CS drafted and wrote the paper. All authors contributed to the article and approved the submitted version.

Data availability

The original contributions presented in the study are publicly available. The data can be found here: https://doi.org/10.5281/zenodo.18154411.

Funding

The author(s) declared that financial support was received for this work and/or its publication. This work was supported by the Swiss National Research Foundation: Grant 310030L_204371 to CS and Grant CRSK-3_221109 grant to KZ.

Conflict of interest

The author(s) declared no potential conflicts of interest with respect to the research, authorship, and/or publication of this article.

Generative AI statement

The author(s) declared that generative AI was not used in the creation of this manuscript.

Any alternative text (alt text) provided alongside figures in this article has been generated by Frontiers with the support of artificial intelligence and reasonable efforts have been made to ensure accuracy, including review by the authors wherever possible. If you identify any issues, please contact us.

References

1. Zuhra K, Szabo C. The two faces of cyanide: an environmental toxin and a potential novel mammalian gasotransmitter. *FEBS J* (2022) **289**:2481–515. doi:10.1111/febs.16135

2. Correia SC, Santos RX, Cardoso SM, Santos MS, Oliveira CR, Moreira PI. Cyanide preconditioning protects brain endothelial and NT2 neuron-like cells against glucotoxicity: role of mitochondrial reactive oxygen species and HIF-1α. *Neurobiol Dis* (2012) **45**:206–18. doi:10.1016/j.nbd.2011.08.005

3. Randi EB, Zuhra K, Pecze L, Panagaki T, Szabo C. Physiological concentrations of cyanide stimulate mitochondrial complex IV and enhance cellular bioenergetics. *Proc Natl Acad Sci U S A.* (2021) **118**:e2026245118. doi:10.1073/pnas.2026245118

4. Zuhra K, Petrosino M, Janickova L, Petric J, Ascenção K, Vignane T, et al. Regulation of mammalian cellular metabolism by endogenous cyanide production. *Nat Metab* (2025) **7**:531–55. doi:10.1038/s42255-025-01225-w

5. Alan-Albayrak E, Simonsen U. Cyanide beyond toxicity: a systematic review of its effects on vascular function. *Basic Clin Pharmacol Toxicol* (2025) **137**:e70124. doi:10.1111/bcpt.70124

6. Malkondu S, Erdemir S, Karakurt S. Red and blue emitting fluorescent probe for cyanide and hypochlorite ions: biological sensing and environmental analysis. *Dyes Pigm* (2020) **174**:108019. doi:10.1016/j.dyepig.2019.108019

7. Ascenção K, Dilek N, Augsburger F, Panagaki T, Zuhra K, Szabo C. Pharmacological induction of mesenchymal–epithelial transition via inhibition of H_2S biosynthesis and consequent suppression of ACLY activity in colon cancer cells. *Pharmacol Res* (2021) **165**:105393. doi:10.1016/j.phrs.2020.105393

8. Petrosino M, Zuhra K, Kieronska-Rudek A, Janickova L, Bremer O, Khalaf M, et al. Cyanide overproduction impairs cellular bioenergetics in Down syndrome. *Neurotherapeutics* (2025) **22**:e00719. doi:10.1016/j.neurot.2025.e00719

9. Kubota Y, Kleinman HK, Martin GR, Lawley TJ. Role of laminin and basement membrane in the morphological differentiation of human endothelial cells into capillary-like structures. *J Cell Biol* (1988) **107**:1589–98. doi:10.1083/jcb.107.4.1589

10. Kieronska-Rudek A, Zuhra K, Ascenção K, Chlopicki S, Szabo C. The PARP inhibitor olaparib promotes senescence in murine macrophages. *GeroScience* (2025). doi:10.1007/s11357-025-01679-6

11. Grimmett ZW, Schindler JC, Stamler JS. Gases define redox signalling: NO, H_2S, O_2 and cyanide. *Nat Metab* (2025) **7**:444–6. doi:10.1038/s42255-025-01229-6

12. Ignarro LJ. Nitric oxide as a unique signaling molecule in the vascular system: a historical overview. *J Physiol Pharmacol* (2002) **53**:503–14.

13. Morbidelli L, Donnini S, Ziche M. Role of nitric oxide in the modulation of angiogenesis. *Curr Pharm Des* (2003) **9**:521–30. doi:10.2174/1381612033391405

14. Moncada S, Higgs EA. Nitric oxide and the vascular endothelium. *Handb Exp Pharmacol* (2006) **176**:213–54. doi:10.1007/3-540-32967-6_7

15. Pacher P, Beckman JS, Liaudet L. Nitric oxide and peroxynitrite in health and disease. *Physiol Rev* (2007) **87**:315–424. doi:10.1152/physrev.00029.2006

16. Napoli C, Ignarro LJ. Nitric oxide and pathogenic mechanisms involved in the development of vascular diseases. *Arch Pharm Res* (2009) **32**:1103–8. doi:10.1007/s12272-009-1801-1

17. Calay D, Mason JC. The multifunctional role and therapeutic potential of HO-1 in the vascular endothelium. *Antioxid Redox Signal* (2014) **20**:1789–809. doi:10.1089/ars.2013.5659

18. Choi YK, Kim YM. Regulation of endothelial and vascular functions by carbon monoxide via crosstalk with nitric oxide. *Front Cardiovasc Med* (2021) **8**:649630. doi:10.3389/fcvm.2021.649630

19. Vu GH, Kim CS. Redox regulation of endogenous gasotransmitters in vascular health and disease. *Int J Mol Sci* (2025) **26**:9037. doi:10.3390/ijms26189037

20. Szabo C. Hydrogen sulfide, an enhancer of vascular nitric oxide signaling: mechanisms and implications. *Am J Physiol Cell Physiol* (2017) **312**:C3–C15. doi:10.1152/ajpcell.00282.2016

21. Wang R, Szabo C, Ichinose F, Ahmed A, Whiteman M, Papapetropoulos A. The role of H_2S bioavailability in endothelial dysfunction. *Trends Pharmacol Sci* (2015) **36**:568–78. doi:10.1016/j.tips.2015.05.007

22. Szabo C, Papapetropoulos A. International union of basic and clinical pharmacology. CII: pharmacological modulation of H_2S levels: H_2S donors and H_2S biosynthesis inhibitors. *Pharmacol Rev* (2017) **69**:497–564. doi:10.1124/pr.117.014050

23. Cirino G, Szabo C, Papapetropoulos A. Physiological roles of hydrogen sulfide in Mammalian cells, tissues, and organs. *Physiol Rev* (2023) **103**:31–276. doi:10.1152/physrev.00028.2021

24. Papapetropoulos A, García-Cardeña G, Madri JA, Sessa WC. Nitric oxide production contributes to the angiogenic properties of vascular endothelial growth factor in human endothelial cells. *J Clin Invest* (1997) **100**:3131–9. doi:10.1172/JCI119868

25. Papapetropoulos A, Pyriochou A, Altaany Z, Yang G, Marazioti A, Zhou Z, et al. Hydrogen sulfide is an endogenous stimulator of angiogenesis. *Proc Natl Acad Sci U S A.* (2009) **106**:21972–7. doi:10.1073/pnas.0908047106

26. Coletta C, Papapetropoulos A, Erdelyi K, Olah G, Módis K, Panopoulos P, et al. Hydrogen sulfide and nitric oxide are mutually dependent in the regulation of angiogenesis and endothelium-dependent vasorelaxation. *Proc Natl Acad Sci U S A.* (2012) **109**:9161–6. doi:10.1073/pnas.1202916109

27. Wang MJ, Cai WJ, Li N, Ding YJ, Chen Y, Zhu YC. The hydrogen sulfide donor NaHS promotes angiogenesis in a rat model of hind limb ischemia. *Antioxid Redox Signal* (2010) **12**(9):1065–77. doi:10.1089/ars.2009.2945

28. Potenza DM, Guerra G, Avanzato D, Poletto V, Pareek S, Guido D, et al. Hydrogen sulphide triggers VEGF-induced intracellular Ca^{2+} signals in human endothelial cells but not in their immature progenitors. *Cell Calcium* (2014) **56**: 225–34. doi:10.1016/j.ceca.2014.07.010

29. Tao BB, Cai WJ, Zhu YC. H_2S is a promoter of angiogenesis: identification of H_2S "receptors" and its molecular switches in vascular endothelial cells. *Handb Exp Pharmacol* (2015) **230**:137–52. doi:10.1007/978-3-319-18144-8_6

30. Zhang YX, Jing MR, Cai CB, Zhu SG, Zhang CJ, Wang QM, et al. Role of hydrogen sulphide in physiological and pathological angiogenesis. *Cell Prolif* (2023) **56**:e13374. doi:10.1111/cpr.13374

31. Chan A, Balasubramanian M, Blackledge W, Mohammad OM, Alvarez L, Boss GR, et al. Cobinamide is superior to other treatments in a mouse model of cyanide poisoning. *Clin Toxicol (Phila).* (2010) **48**:709–17. doi:10.3109/15563650.2010.505197

32. Sagné C, Agulhon C, Ravassard P, Darmon M, Hamon M, El Mestikawy S, et al. Identification and characterization of a lysosomal transporter for small neutral amino acids (LYAAT-1/PAT1). *Proc Natl Acad Sci U S A.* (2001) **98**: 7206–11.

33. Aratani Y, Koyama H, Nyui S, Suzuki K, Kura F, Maeda N. β_2 integrin-mediated cell–cell contact transfers active myeloperoxidase to endothelial cells. *J Biol Chem* (2012) **287**:1061–9.

34. Cheng G, Salerno JC, Cao Z, Pagano PJ. Vascular peroxidase-1 catalyzes the formation of hypohalous acids. *Free Radic Biol Med* (2013) **53**:1958–65.

35. Vandekeere S, Dubois C, Kalucka J, Carmeliet P, Schoors S, Goveia J, et al. Serine synthesis via PHGDH is essential for heme production in endothelial cells. *Cell Metab.* (2018) **28**:573–87. doi:10.1016/j.cmet.2018.06.009

36. Su L, Kong X, Loo SJ, Gao Y, Kovalik JP, Su X, et al. Diabetic endothelial cells differentiated from patient iPSCs show dysregulated glycine homeostasis and senescence-associated phenotypes. *Front Cell Dev Biol* (2021) **9**:667252. doi:10.3389/fcell.2021.667252

37. Tsuji-Tamura K, Sato M, Fujita M, Tamura M. Glycine exerts dose-dependent biphasic effects on vascular development of zebrafish embryos. *Biochem Biophys Res Commun* (2020) **527**:539–44. doi:10.1016/j.bbrc.2020.04.098

38. Van den Eynden J, Ali SS, Horwood N, Carmans S, Brône B, Hellings N, et al. Glycine and glycine receptor signalling in non-neuronal cells. *Front Mol Neurosci* (2009) **2**:9. doi:10.3389/neuro.02.009.2009

39. Li X, Sun X, Carmeliet P. Hallmarks of endothelial cell metabolism in health and disease. *Cell Metab.* (2019) **30**:414–33. doi:10.1016/j.cmet.2019.08.011

40. Meng L, Wang Y, Wang X, Mu M, Zheng H. Association between exposure to volatile organic compounds and atherogenic index of plasma in NHANES 2011–2018. *Environ Sci Pollut Res* (2025) **15**:9024. doi:10.1038/s41598-025-93833-5

41. Cao Q, Song Y, Huan C, Jia Z, Gao Q, Ma X, et al. Biological aging mediates the association between volatile organic compounds and cardiovascular disease. *BMC Public Health* (2024) **24**:2928. doi:10.1186/s12889-024-20349-4

EBM Experimental Biology and Medicine

TYPE Original Research
PUBLISHED 24 February 2026
DOI 10.3389/ebm.2026.10788

OPEN ACCESS

*CORRESPONDENCE
Qiang Gu,
guqiang106@sina.com
Bo Sun,
bsun@shmu.edu.cn

RECEIVED 12 August 2025
REVISED 18 December 2025
ACCEPTED 20 January 2026
PUBLISHED 24 February 2026

CITATION
Zhuang G, Gu Q, Xie S, Guo X and Sun B (2026) Intra- and extrapulmonary lipopolysaccharides-induced acute lung injury and pharmacotherapeutic response patterns in ventilated 7-day-old rabbits.
Exp. Biol. Med. 251:10788.
doi: 10.3389/ebm.2026.10788

Intra- and extrapulmonary lipopolysaccharides-induced acute lung injury and pharmacotherapeutic response patterns in ventilated 7-day-old rabbits

Guiyin Zhuang[1], Qiang Gu[1]*, Siyu Xie[1], Xiaojing Guo[2] and Bo Sun[2]*

[1]Department of Pediatrics, The First Affiliated Hospital of Shihezi University, Shihezi, Xinjiang, China, [2]Department of Pediatrics, National Health Commission Laboratory of Neonatal Diseases, National Children's Medical Center and Children's Hospital of Fudan University, Shanghai, China

Abstract

We explored pharmacotherapeutic response patterns of lipopolysaccharides (LPS)-induced pneumonia and sepsis as direct and indirect acute lung injury (ALI), and efficacy of a combined surfactant (S) and inhaled nitric oxide (iNO), simulating critical care, in rabbits of post-neonatal infancy. Anaesthetized 7-day-old healthy rabbits were injected intratracheally (IT) or intravenously (IV) with LPS (15–20–25 mg/kg, L) or saline as a control (C), and subjected to initial 2-hour mechanical ventilation (MV) with standardized tidal volume to induce ALI. They were then treated with S (200 mg/kg) and iNO (10 ppm, N), or not, thereby allocating to 6 groups (ITC, ITL, ITLSN, IVC, IVL, IVLSN) for another 8 h. Survival time/rate (ST), and variables as biomarkers in lung physiology, histopathology, biochemistry, and pathophysiology were measured. The survival was LPS-route, but not dosing, dependent. Compared to the IVL, ITL had relatively higher ST, lung injury score (LIS), lower intrapulmonary phospholipid pools, mRNA expressions in surfactant proteins (SPs) and pulmonary vascular endothelial cell injury (VEI)-related variables. ITLSN had higher phospholipid pools but no improvement in ST, lung mechanics, LIS or mRNA expression of SPs, proinflammatory mediators and VEI-related variables. IVLSN had improved lung mechanics, LIS, phospholipid pools, and SP-A mRNA expression, but worse ST, metabolic acidosis, higher interleukin mRNA expression in the lungs, liver and kidney, suspected as sepsis-associated multiorgan involvement. Using the infant rabbit LPS-ALI model, we characterized the survival as LPS-route dependent, the lung impairment and response pattern in surfactant

and iNO treatment ineffectiveness/failure, as pharmacotherapeutic response patterns, with causal implication pertinent to the underlying pathophysiology of experimental pediatric ARDS.

KEYWORDS

ARDS, infection, inhaled nitric oxide, lipopolysaccharides, pulmonary surfactant

Impact statement

Pathophysiology and pharmacotherapeutic efficacies of ARDS requiring critical care in neonatal and post-neonatal infancy are unclear. In ventilated 7-day-old rabbits, direct (intratracheal) LPS-induced ALI was associated with severe pneumonia but moderate death risks whereas indirect (intravenous) LPS-ALI was with moderate lung injury but high deaths due to sepsis associated multiorgan impairment. Surfactant and inhaled NO failed to improve the survival, associated with highly provoked mRNA expression of proinflammatory mediators as multiorgan involved septic lung damage pattern. The pathophysiological and pharmacotherapeutic response patterns of LPS-route dependent worse outcome implicates causal relations underlying the mortality of experimental pediatric ARDS.

Background

Acute respiratory distress syndrome (ARDS) as a severe and persistent hypoxemic respiratory failure (PHRF) is characterized by pulmonary infection, inflammation, high vascular-to-alveolar permeability and ventilation/perfusion mismatching. Its initial stage is acute lung injury (ALI) or mild-to-moderate ARDS. Current knowledge of etiology, pathogenesis and pathophysiology of ALI and PHRF is focused on direct and indirect assaults to the lungs, also known as pulmonary and extrapulmonary causes. These involve bacterial and viral pneumonia, lung abscess, contusion, airway obliteration, sepsis, acute pancreatitis, acid aspiration of gastric regurgitation, or embolism of bone fracture, etc.; and hemodynamic derangement as sepsis and septic shock with multiorgan system dysfunction/failure [1–4]. Its clinical definition has been modified several times, and response to oxygenation, high positive end-expiratory pressure (PEEP) and restricted tidal volume (V_T) in mechanical ventilation (MV) are considered protective as mainstay [5].

There are differences in pathogenesis, pathophysiology, respiratory mechanics, histological and biochemical alterations for triggers attributable to pulmonary ($ARDS_p$) and extrapulmonary ARDS ($ARDS_{exp}$) [6, 7]. In $ARDS_p$, the primary attack is due mainly to pathogen-associated response pattern in alveolar epithelial and capillary endothelial cells, causing wide spread activation of alveolar macrophages and the inflammatory response, confined mainly in the alveoli and small airway compartment [8, 9]. The damage to alveolar epithelial cells leads to decreased clearance of edema fluid from the alveolar space of injured blood-gas barrier, inactivation or depressed production of pulmonary surfactant (PS) by type II alveolar epithelial cells (ATII), with degenerative, suppurative and necrotic bronchiolitis and alveolitis, and ultimately remodeling with cystic pulmonary fibrosis. In contrast, $ARDS_{exp}$ is caused by the release of inflammatory mediators from extrapulmonary assaults and organ tissue lesions, which primarily affect pulmonary capillary endothelial cells, then to ATs. The triggers cause massive production of inflammatory cells and mediators into the bloodstream leading to inflammatory cascade and aggregation of inflammatory cells, resulting in an increased permeability in blood-gas barrier, intrapulmonary edema, and microvascular tone dysregulation [8, 9]. Regarding the lung mechanics in $ARDS_p$, dynamic compliance of respiratory system (Cdyn) is generally reduced even if high PEEP is applied whereas in $ARDS_{exp}$ Cdyn would be more associated with the management of high permeability of blood-gas barrier and systemic hemodynamic derangement to assist in lung protective ventilation [10].

Postnatal maturation of lung structure and immune system likely influence the age-related response differences in lung and systemic infection susceptibility. This pertains to mechanisms of pulmonary inflammation, injury, reparation and remodeling in pediatric and infant patients to bacterial, viral and other pathogen induced ALI and PHRF, especially in late neonatal and postneonatal infancy [4, 11]. Moreover, it is unclear how the underlying mechanisms of pharmacotherapeutic action would be, with regard to ancillary respiratory medications in critical care for pediatric and neonatal patients at high death risk of ARDS. The consensus agreement on the definition of pediatric ARDS (pARDS), by the Pediatric Acute Lung Injury Consensus Conference (PALICC) clarified incidence, epidemiology, management, prognosis and outcome assessment [4, 5]. Surfactant therapy is recognized as an optimal treatment in lung protective ventilation strategies for neonatal respiratory distress syndrome (RDS) of prematurity [12]. However, in those from late neonatal to early post-neonatal infancy, there is insufficient evidence supporting the therapeutic efficacy of surfactant treatment for ALI and PHRF, even contradictory in interpretation of its efficacy [13]. Similarly, the existing evidence on the effectiveness of inhaled nitric oxide (iNO) in treatment of

pARDS is also in debate due to transient improvement in oxygenation without reducing mortality but raised concerns on the extrapulmonary organ system safety [14]. Therefore, we speculate that patients diagnosed as pARDS may differ from adult ARDS, especially in the lung impairment and treatment response patterns with sensitive pathobiological biomarkers as phenotypes to predict outcome and prognosis [11, 14, 15].

In this study, we aimed to establish a high dose lipopolysaccharides (LPS)-induced ALI model, in rabbits at post-neonatal infancy, with two different administration routes, of etiological distinction, by intratracheal or intravenous injection of LPS with MV, to simulate critical care for neonatal and pediatric patients in early infancy. We first hypothesized that severity of ALI should be associated with LPS route and dosage to lead a survival rate or median survival time (ST_{50}) in reasonable length (within 10 h) of V_T-restricted MV [16]. This should enable characterizing the severity of septic ALI as in pARDS, with survival status as a key outcome linking the two different etiologies and associated damage response patterns. We then hypothesized that a combined PS and iNO regimen would exert better effects compared to MV alone [16], and explored their mechanisms of pharmacotherapeutic action. With unexpected outcome thereof, we managed to explain mechanisms of ineffectiveness/failure similar in the pARDS trials [17–19].

Materials and methods

Experimental ethics, protocol and animal management

The study protocol was approved by the Ethics Committee of the Children's Hospital of Fudan University (No. 2023350). Healthy New Zealand White rabbits, 7-day-old in early infancy, were provided by Shanghai Songlian Experimental Animal Center. The rabbit pups' age for developmental stage was estimated, by body weight (BW) gain, corresponding to human infant around 2-month of age, assuming an infant rabbit around 40–50 postnatal days at weaning with BW gain corresponding to approximately 1 year-old human infant. The animals care followed the institutional laboratory routine management, according to Chinese regulations for experimental animal care and welfare in the medical research and ethics requirement.

The pups were allocated to 7 groups: non-ventilated (C0), intratracheal saline (ITC), intratracheal LPS (ITL), intratracheal LPS + intratracheal PS + iNO (ITLSN), intravenous saline (IVC), intravenous LPS (IVL), and intravenous LPS + PS + iNO (IVLSN) (for pups' average body weight and gender see Table 1). The experiments were conducted in two phases. In phase I, experiments were focused on direct, pulmonary ALI, simulating pneumonia-associated pARDS ($pARDS_p$) as in the ITC, ITL and ITLSN groups. In phase II, experiments were focused on indirect, extrapulmonary-associated ALI, simulating sepsis-associated pARDS ($pARDS_{exp}$), involving the IVC, IVL and IVLSN groups (Figure 1a).

After weighing BW, pups were injected intraperitoneally with 3% sodium pentobarbital (1.5 mL/kg), and intratracheally intubated. In the phase I experiments, 2 mL/kg of saline was injected intratracheally in the ITC. *E. coli* (serotype 0111 B4, cat. No. L2630, Sigma-Aldrich, St. Louis, MO, USA)-derived LPS was dissolved in sterile saline to 7.5, 10 and 12.5 mg/mL, 2 mL/kg (corresponding to 15, 20 and 25 mg/kg, or 20 mg/kg in average, see below) was injected intratracheally into each pup lungs to induce ALI in the ITL and ITLSN groups. After LPS or saline injection, all the pups were connected to ventilator for MV. Two hours after the LPS injection and MV, pups in the ITLSN were intratracheally injected with 2.5 mL/kg of PS (200 mg/kg) and iNO (10 parts per million in volume, ppm), through inspiratory limb of the ventilator circuit and MV was resumed [20]. In the phase II experiment, each pup in the IVC received 2 mL/kg of saline injected through external cervical vein. For the pups in the IVL and IVLSN, each was injected intravenously with the same dose of LPS as used in the phase I. Two hours after LPS injection and MV, each pup in IVLSN received the same dose of PS and iNO as in ITLSN. After the administration of saline or LPS, the pups in both phases were subjected to the identical MV settings throughout. In each phase, several pups were immediately euthanized by intracranial injection of an overdose of 3% sodium pentobarbital to cause heart arrest, and served as a non-ventilated control group (C0). Thus, there were totally 186 rabbit pups enrolled, 12 each in the C0, IVC and ITC, 51 each in the IVL and ITL, and 24 each in the IVLSN and ITLSN groups.

Mechanical ventilation, measurement of lung mechanics, and survival time

A multi-plethysmograph-ventilator system was used to enable a parallel MV, which consisted of specially designed 10 plexiglass boxes and a Servo ventilator (900C, Siemens-Elema, Solna, Sweden) to ventilate ten rabbits simultaneously [21]. The system also consisted of a pneumotachometer (RSS100-HR, Hans Rudolph Inc., Kansas City, KA), a pressure transducer (Shanghai Yangfan Electronic, Shanghai, China), and a bioelectric signal amplifier. Variables of lung mechanics were monitored and recorded by an automated physiologic monitoring system (PowerLab, ADInstruments Pty Ltd, New South Wales, Australia) with an electrocardiogram (ECG) module. Tidal volume (Vt), positive end-expiratory pressure (PEEP), and peak insufflation pressure (PIP) were measured through individual adjustment of PIP to achieve designated Vt in pups. Pressure-control mode was chosen with a fraction of

TABLE 1 Basic information of experimental animals.

Group	N	Body weight (g)	Male n (%)
C0	12	118 ± 3.8	7 (58.3)
ITC	12	117 ± 5.8	3 (25.0)
ITL	51	114 ± 6.0	22 (43.1)
ITLSN	24	108 ± 4.4	5 (20.8)
IVC	12	115 ± 3.8	7 (58.3)
IVL	51	116 ± 5.5	25 (49.0)
IVLSN	24	108 ± 5.1	6 (25.0)

Group definitions and abbreviations: IT, intratracheal; IV, intravenous; C, control; L, lipopolysaccharides (15, 20, 25 mg/kg); S, pulmonary surfactant (200 mg/kg); N, inhaled nitric oxide (10 ppm); C0, non-ventilated control. Values are means ± standard deviation.

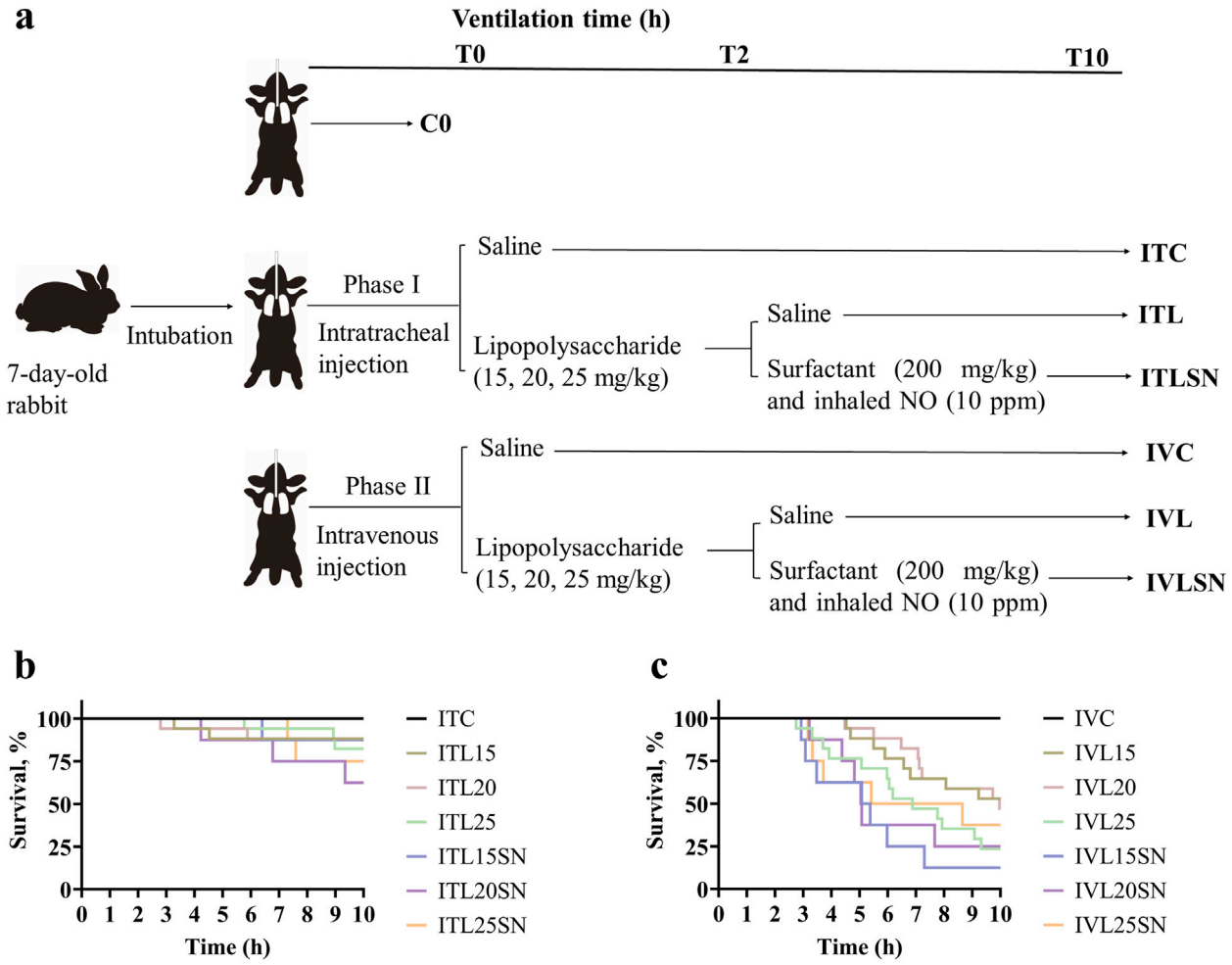

FIGURE 1
The study design and animal survival curves in Phase I and II experiments with different dosages and routes of lipopolysaccharides (LPS) administration. **(a)** Flow chart of the two phases of experiments with different LPS dosage and route of administration; **(b)** Survival curves of the animals receiving different dosage of LPS in the Phase I experiment (n = 8–17, ITC n = 12, ITL15/20/25 n = 17, ITLSN15/20/25 n = 8); **(c)** Survival curves of the animals receiving different dosages of LPS in the Phase II experiment (n = 8–17, IVC n = 12, IVL15/20/25 n = 17, IVLSN15/20/25 n = 8). Group definitions and abbreviations: C, control; IT, intratracheal; IV, intravenous; L, lipopolysaccharides (15, 20, 25 mg/kg body weight); N, inhaled nitric oxide (10 ppm); S, surfactant (200 mg/kg).

inspired oxygen (FiO_2) at 1.0, a respiratory rate of 40 beats/minute, an inspiratory to expiratory time ratio of 1:2, and Vt targeted at 4–6 mL/kg [22]. Dynamic compliance of respiratory system (Cdyn) was derived from Vt/(PIP-PEEP) corrected by BW, and expressed as mL/kg/cmH_2O. During MV, 3% sodium pentobarbital was injected intraperitoneally as required to maintain analgesia while a stable spontaneous breathing was maintained. Throughout the MV, the rabbits were kept in the boxes on a 37 °C heating pad, and intraperitoneally injected per pup with 0.3 mL/kg mixed solution (10% dextrose and 5% sodium bicarbonate in the ratio of 6:4) every 1–2 h where necessary to counter balance acidosis and maintain basal metabolism. The time 0 was when the rabbits completed tracheal intubation and connected to the ventilator through the multi-plethysmograph system. Measurements of PIP, PEEP and Vt values were at initial 15–60 min, and every half hour thereafter, or as frequently as needed, until death or per protocol termination of the ventilation. The maximum time of MV was 10 h. During the ventilation, we carefully observed the face and body color of pups and their respiratory effort. If the animal appeared cyanotic or pale, heart rate was checked with electrocardiograph (ECG) (Supplementary Figure 1). At the termination of ventilation, pups were euthanized with an overdose of 3% sodium pentobarbital till heart arrest. Blood samples from the left heart ventricle was immediately withdrawn from left heart ventricle for blood gas analysis. The diagnostic criteria for ALI as early stage of ARDS were mainly characterized by deterioration of Cdyn by 30% from control level [23]. By histopathological features under light microscopy, there was a massive infiltration of inflammatory cells, widening of alveolar septa, alveolar atelectasis, and damage of alveolar septa, causing high vascular-to-alveolar permeability, as verified after initial 2-h of MV in additionally a few animals from both ITL and IVL groups [23, 24].

Lung tissue sample processing

We used the same rabbits to undergo histopathological examination (right upper and lower lobes), and biochemical analysis (both lobes of left side), or quantitative PCR (qPCR) measurement of fresh tissue of right middle lobe. The lung accessory lobe was excised to determine the wet-to-dry weight ratio (W/D), which was used to assess the lung tissue fluid content. First, we ligated the right middle lobe to obtain lung tissue for qPCR or transmission electron microscopy. Next, we ligated the lung accessory lobe to obtain tissue for W/D ratio determination. Then, we ligated the right hilum and performed biochemical analysis on the left lung lobes. Finally, we ligated the left hilum and performed pressure fixation and sampling for histopathology (right upper and lower lobes). In some animals in each group, middle liver and cortical kidney tissues were collected for qPCR examination.

Lung histopathology and morphometry

The lungs designated for histopathological analysis (n = 8–30 per group) were prepared for fixation by lung perfusion through a catheter placed in the pulmonary artery through right heart ventricle. Concurrently, a constant gas flow with pressure of 30 cmH_2O was delivered via the intratracheal tube by the ventilator for 1 minute, then reduced to 10 cmH_2O as the deflation pressure to maintain continuous alveolar expansion, approximating the functional residual volume. Lung tissue was perfused with a 4% paraformaldehyde solution for 30-min fixation, followed by further fixation in 4% paraformaldehyde, embedding in paraffin, sectioning, and staining with hematoxylin-eosin (H-E) to assess alveolar expansion (Vv), coefficient of variance of Vv [CV (Vv)], and lung injury score (LIS), with morphometry. Vv and CV (Vv) were counted in 30–40 fields using a light microscope (magnification ×200) and an IMS image analysis system (Leica, Wetzlar, Germany). The LIS was determined based on the severity of four items: edema, hemorrhage, inflammatory cell infiltration, and alveolar injury. The scale assigned a score of 0 for each injury item found areas less than 1%, 1 for 1%–25%, 2 for 25%–50%, 3 for 50%–75%, and 4 for >75% within the field. The LIS_{total} was calculated individually by summing up the four injury item scores [20].

Ultrastructural morphology of the lungs

The lung tissue from the right middle lobe was freshly excised and trimmed to 1 mm^3. It was then fixed in glutaraldehyde for 24 h at 4 °C and osmium, followed by dehydration, embedding, sectioning, staining, and examination with a transmission electron microscope (FEI Tecnai G2 Spirit TWIN, ThermoFisher Scientific, Boston, MA, USA).

Biochemical analysis of phospholipids and proteins

For the left lung lobes subjected to biochemical analysis (n = 8–30 per group), by clamping right hilar, bronchoalveolar lavage (BAL) was performed with cold saline each time till full lung lobe expansion, followed by gentle withdrawal. Collected BAL fluid (BALF) was recorded. This procedure was repeated three times which yielded a total volume as recovered BALF, and subjected to measurement of total phospholipids (TPL) and disaturated phosphatidylcholine (DSPC) [25, 26]. Total proteins (TP) in BALF were determined using BCA kit (Thermo Fisher Scientific, Waltham, MA). When performing whole-lung lavage, the volume of normal saline instilled was 30 mL/kg; for a single lung, the volume was 15 mL/kg. In our experiment, only the left lung was lavaged. Therefore, to calculate whole-lung TPL or DSPC content, all the measurements were corrected for both

lungs (as divided by 0.45), and its amount is expressed as mg/kg BW [27].

Wet to dry weight ratio (W/D) determination

For W/D determination, the lung accessory lobe was weighed within 10 min of collection: surface moisture was gently removed with filter paper, and the wet weight (W) was recorded to 0.1 mg on a high-precision balance. The lung accessory lobe was then dried in a forced-air oven at 60 ˚C for ≥24 h until consecutive weighings were constant. Its final value was taken as dry weight (D, to 0.1 mg) and used to calculate W/D.

Quantitative PCR of mRNAs

For the lung, liver, kidney tissue samples from the rabbits allocated to qPCR analysis (n = 5–40 per group), mRNA in fresh organ (lung, liver, kidney) tissue samples were extracted using RNAex Pro Reagent (Accurate Biotechnology CO., LTD, Changsha, China) following the manufacturer's instructions. Total RNA was reverse-transcribed into single-stranded cDNA using Evo M-MLV PrimeScript RT reagent kit, following the manufacturer's instructions. Total RNA levels were measured with an SYBR green detection system using a Roche LightCycler 480 II system (Roche, Basel, Switzerland). The target genes were categorized as follows: surfactant proteins (SP)-A, SP-B, SP-C, nuclear transcript factor kappa B (NF-κB), tumor necrosis factor (TNF)-α, interleukin (IL)-1β, IL-6, IL-8, tyrosine kinase receptor (Tie)-2, angiopoietin (Ang)-1 and Ang-2. The mRNA levels of each gene were standardized against β-actin expression, employing $2^{-\triangle\triangle Ct}$ formula to determine average fold change in reference to the control (C0) group. Primer sequences are provided in the Supplementary Table 1.

Statistics and data analysis

Statistical analyses were performed using SPSS version 26.0 (IBM, Armonk, NY), and figures were produced by GraphPad Prism 9.0 (GraphPad Software, La Jolla, CA). For survival analysis, the Kaplan-Meier survival curve was applied, complemented by log-rank test. Median survival time (ST_{50}) is expressed as the survival length of 50th percentile in a group number, denoting as median survival time, and corresponding interquartile range (IQR as 75th and 25th percentiles), in minutes. Quantitative data were presented as means ± standard deviation (SD). Proportional data, including survival rate, were presented as number (n) and percentage (%). For quantitative data, One-way ANOVA F test with Bonferroni *post hoc* test, or Kruskal-Wallis H test with Wilcoxon-Mann-Whitney U test, was utilized, depending on the continuity, distribution characteristics, variance homogeneity of data, and repeated measures. P value <0.05 was considered statistically significant for the difference.

Results

In the initial experiment (ITL and IVL) (Supplementary Figures 2, 3; Supplementary Tables 2, 3), we found that the LPS induced ALI severity was not dose-dependent, neither were the survival, phospholipid content in BALF, or the mRNA expression of pro-inflammatory cytokines and mediators in lung tissue. Therefore, to facilitate data analysis and presentation, the groups of different doses of LPS were combined, hence the number of animals, and designated as 20 mg/kg of LPS in average in the ITL, ITLSN, IVL and IVLSN groups, respectively, in the main results for easy comprehension (Figures 1b,c). Average BW was around 115 g, which was approximately doubled from that at term birth (31 days of gestation, with birth weight of 55–65 g in average), and male-to-female was 4:6. Values of W/D were significantly lower in the IVL than in the ITL (Table 2).

Phase I experiment: IT-LPS

Survival status and blood gas analysis

There were no deaths in the ITC during the 10-h MV period. The survival rates in ITL and ITLSN groups were low, however both being above 50% (Figures 1b, 2a; Table 2), and not the LPS-dose dependent. No significant differences in pH, PCO_2 or lactate levels were observed among the ITC, ITL and ITLSN groups (Table 2). By subgroup analysis for the early death survived less than 10 h, those from ITL and ITLSN were more acidotic and had higher lactate in the blood (Table 3), denoting metabolic acidosis.

Measurement of lung mechanics

During the MV period, Cdyn values were lower in ITL and ITLSN groups than in the ITC throughout. At the end, values of Cdyn of both groups were still 20% lower than that of the ITC group ($P < 0.05$, Figure 2b; Supplementary Table 4). Representative data of Cdyn are presented in Supplementary Table 4.

Lung histopathology and morphometry

The lung histopathology and morphometry of each group in the phase I are shown in Figures 2c,d, 4 (see below). The lungs from ITL and ITLSN groups demonstrated pronounced alveolar destruction alternatively with moderate alveolar septa thickening, and wide spread alveolar inflammatory cell infiltration, epithelial damage, along with overt infill of both alveoli and small airways, by exudative cells and fluid, supposedly from capillary lumen. Compared with the ITC, the ITL group had 20% lower Vv ($P < 0.01$) and 17% higher CV (Vv) values,

TABLE 2 General status of the experimental animals in various groups.

Group	N	Survival (%)	pH	PCO_2 (mmHg)	Lactate (mmol/L)	W/D
C0	12		7.20 ± 0.12	74.3 ± 15.9	5.1 ± 3.5	5.06 ± 0.42
ITC	12	12 (100)	7.29 ± 0.18	65.2 ± 11.1	3.6 ± 2.7	5.33 ± 0.52
ITL	51	44 (86.3)	7.25 ± 0.18	63.8 ± 17.8	4.4 ± 5.0	5.48 ± 0.41
ITLSN	24	18 (75)	7.28 ± 0.14	56.9 ± 19.6	6.8 ± 6.2	5.51 ± 0.43
IVC	12	12 (100)	7.30 ± 0.06	62.4 ± 16.7	4.1 ± 3.3	5.51 ± 0.30
IVL	51	21 (41.2)	7.19 ± 0.15	$43.5 \pm 21.7^{\dagger\###}$	$12.5 \pm 5.8^{\dagger\dagger\dagger\###}$	$5.25 \pm 0.32^{\#}$
IVLSN	24	6 (25)	7.20 ± 0.20	37.0 ± 21.1	13.0 ± 6.0	5.26 ± 0.43

Group definitions and abbreviations: IT, intratracheal; IV, intravenous; C, control; L, lipopolysaccharides (15, 20, 25 mg/kg); S, pulmonary surfactant (200 mg/kg); N, inhaled nitric oxide (10 ppm); C0, non-ventilated control. Values are means ± standard deviation. W/D, wet/dry lung weight ratio. $^{\#}P < 0.05$, $^{\###}P < 0.001$ vs. ITL, $^{\dagger}P < 0.05$, $^{\dagger\dagger\dagger}P < 0.001$ vs. IVC.

whereas that in the ITLSN were even worse, both groups showing a significantly higher grade of inflammation, alveolar injury, and LIS_{total} values (all $P < 0.001$).

Ultrastructural observation of the lungs

With transmission electron microscopy observation, in the normal saline group, there were lamellar bodies (LBs) in clean and well aerated alveolar spaces (Figure 5a) and type I and II alveolar epithelial cells (ATI, ATII, respectively) with abundant capillaries. Tubular myelin is readily discernible at high magnification. In contrast, the alveolar spaces of the LPS-treated group were filled with many scattered cells and loosened ATI, ATII with fewer LB, and many interstitial cells with intensified lysosomes in cytoplasm, denoting inflammatory response to LPS (Figures 5b–e). In the alveolar space of the ITLSN, among scattered LB, there were ring-shaped membrane layers, much exceeding the adjacent epithelial cell size, likely exogenous surfactant phospholipids (Figure 5f). Tension expanded alveolar septa with surface fluid layer containing cell debris and LB alternative with infilled polymorphonucleated cells are present in alveolar space.

Biochemical analysis of phospholipids and proteins in BALF and lung homogenate (LH)

The TPL and DSPC levels in BALF were lower, and TP higher, in the ITL than in the ITC. The DSPC/TP in ITL was significantly lower. In the ITLSN, TPL and DSPC levels were more than 100% higher than the ITL (all $P < 0.001$), with 24% increment in TP, and 76% increment in DSPC/TP (ITL: TPL 7.24 ± 3.26, DSPC 3.73 ± 2.11, TP 9.30 ± 3.25, DSPC/TP 0.41 ± 0.21; ITLSN: TPL 16.5 ± 5.34, DSPC 8.28 ± 3.97, TP 11.5 ± 2.75 and DSPC/TP 0.72 ± 0.26) (Figures 2e,f; Table 4). DSPC/TPL was around 40–50% with no significant difference among the three IT-groups. In the total lung phospholipid pool (BALF + LH) of the C0, ITC and ITL groups, TPL were around 140–180 mg/kg, DSPC 35–50 mg/kg, and DSPC/TPL 25–29%, in average (Table 4). For TPL and DSPC in the ITLSN, there were 233 and 70 mg/kg in the total pools, which derives net increments by approximately 72 and 28 mg/kg, or 45% and 66%, in average over the TPL and DSPC of the ITC and ITL groups, respectively. Notably, there were ratios of 13 and 7 between LH and BALF (i.e. 216 vs. 16.5 and 62 vs. 8.3 mg/kg, Table 4) for TPL or DSPC, respectively, in the ITLSN.

Measurement of mRNA expression in the lung tissue

The IL-1β mRNA expression was increased in ITL, and even higher in ITLSN, whereas that for IL-8 and Ang-2 in both groups had similar but moderately enhanced expression. That for SP-A, -B, -C were mildly enhanced in the ITC but significantly depressed in SP-C for ITLSN (Figures 2g–i).

Comparison of mRNA expression of pro-inflammatory cytokines in liver and kidney tissues

In general, the magnitudes of mRNA expression of IL-1β, IL-6 and IL-8 in the liver tissue of ITC, ITL and ITLSN groups were not enhanced or lower (Figure 2j). And for kidney, in the ITLSN there was a modest increment in IL-1β and moderate decrement in IL-6 and IL-8 expression (Figure 2k).

Phase II experiment: IV-LPS

Survival status and blood gas analysis

Like that in the phase I, there were no death in the IVC whereas the survival rates in the IVL and IVLSN groups were significantly decreased and below 50% ($P < 0.01$) (Figure 3a). The ST_{50} of the IVL was around 545 min, along with a survival rate of 41.2% at 10 h. There were further shortened ST_{50} at 314 min and an even lower survival rate of 25% in the IVLSN (Figure 3a) in contrast to ITLSN (Figure 2a; Table 2). By subgroup analysis for the early deaths (Table 3), those survived less than 10 h from the IVL and IVLSN groups had lower average PCO_2 (30 mmHg) and high lactate (16–17 mmol/L) in contrast to those survived 10 h (60 mmHg, 7 mmol/L), respectively.

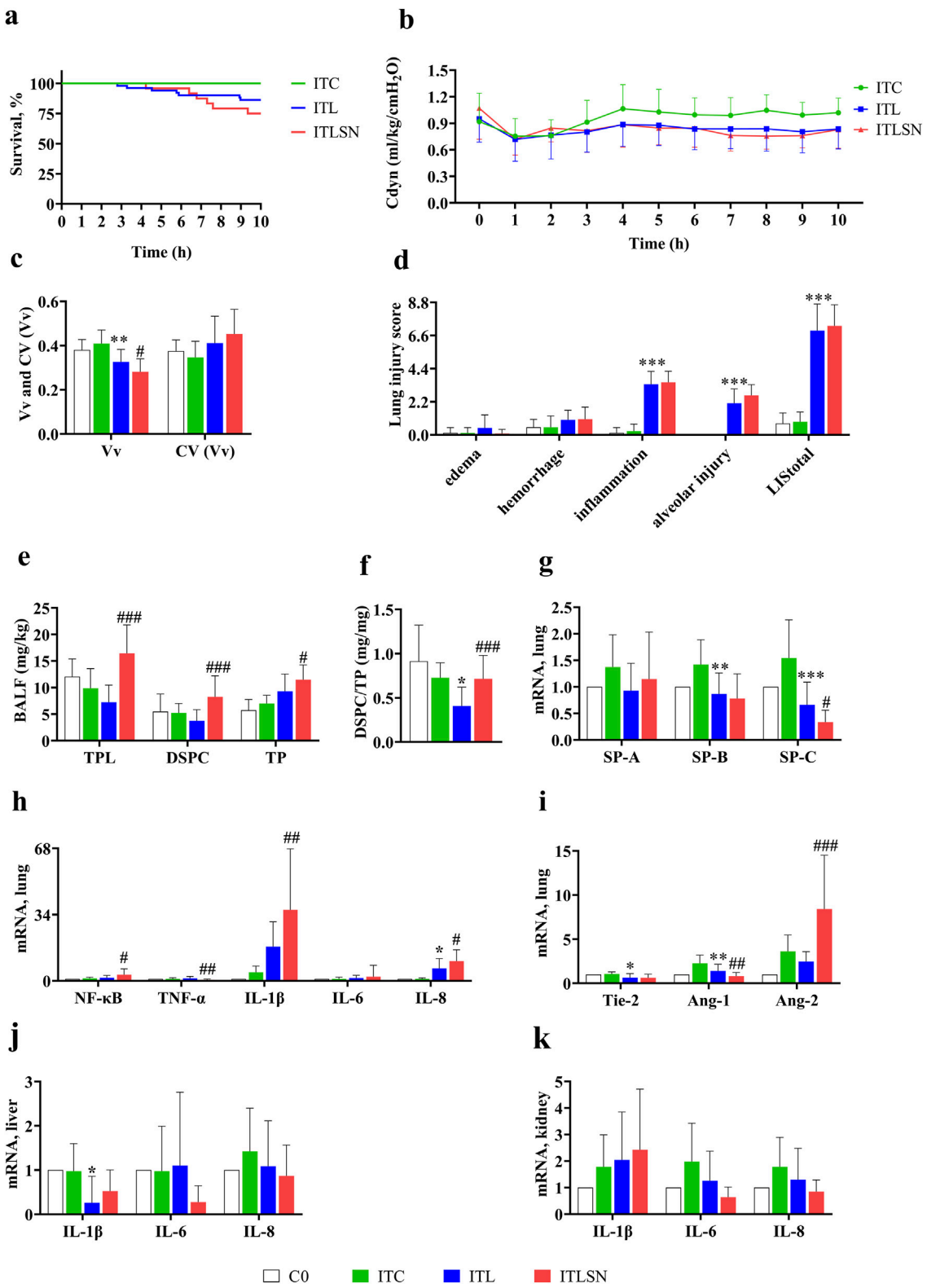

FIGURE 2
Major results of 7-day old rabbits in Phase I experiment. **(a)** Kaplan-Meier survival curves (ITC n = 12, ITL n = 51, ITLSN n = 24), ITC, saline control; ITL, combined intratracheal LPS 15–25 mg/kg; ITLSN, ITL with surfactant and iNO treatment; **(b)** Trend of dynamic compliance of respiratory system (Cdyn) during ventilation (for details with sample size, see Supplementary Table 4) (ITC n = 12, ITL n = 51, ITLSN n = 24). **(c)** Alveolar expansion (Vv) and

(*Continued*)

FIGURE 2 (Continued)
variation of alveolar aeration (CV(Vv)) (C0 n = 8, ITC n = 8, ITL n = 30, ITLSN n = 24); **(d)** Lung injury score (LIS) (C0 n = 8, ITC n = 8, ITL n = 30, ITLSN n = 24); **(e)** Total phospholipids (TPL), disaturated phosphatidylcholine (DSPC) and total proteins (TP) in bronchoalveolar lavage fluid (BALF) (C0 n = 8, ITC n = 7, ITL n = 30, ITLSN n = 24); **(f)** DSPC/TP ratio; **(g)** mRNA expression of surfactant proteins (SP) in lung tissue (C0 n = 8, ITC n = 8, ITL n = 30, ITLSN n = 24); **(h)** mRNA expression of pro-inflammatory mediators in lung tissue (C0 n = 8, ITC n = 8, ITL n = 30, ITLSN n = 24); NF-κB, nuclear transcription factor-κB; TNF-α, tumor necrosis factor-α; IL, interleukin; **(i)** mRNA expression of the injury marker of endothelial cells in lung tissue: Tie-2, tyrosine kinase receptor-2; Ang, angiopoietin; **(j)** mRNA expression of pro-inflammatory mediators in liver tissue (C0 n = 5, ITC n = 6, ITL n = 40, ITLSN n = 19); **(k)** mRNA expression of pro-inflammatory mediators in kidney tissue (C0 n = 5, ITC n = 6, ITL n = 40, ITLSN n = 19). For group definitions see Figure 1 legends. Values are mean ± standard deviation. $^{*}P < 0.05$, $^{**}P < 0.01$, $^{***}P < 0.001$ vs. ITC, $^{\#}P < 0.05$, $^{\#\#}P < 0.01$, $^{\#\#\#}P < 0.001$ vs. ITL (Due to the very small mean ± standard deviation of the control group, the value levels are almost imperceptible in the figure d and h).

TABLE 3 General status of the experimental animals. Stratified analysis of early death and 10-h survivors on blood gas and W/D.

Group	Survival h (n)	pH	PCO_2 (mmHg)	Lactate (mmol/L)	W/D
ITL	<10 (6)	7.17 ± 0.18	45.7 ± 23.0^{a}	14.1 ± 6.4^{aaa}	5.31 ± 0.45
ITL	10 (39)	7.26 ± 0.18	66.5 ± 15.4	3.0 ± 2.6	5.50 ± 0.41
ITLSN	<10 (6)	7.13 ± 0.20^{b}	43.8 ± 26.7	15.2 ± 4.2^{bbb}	5.40 ± 0.49
ITLSN	10 (17)	7.34 ± 0.04	61.5 ± 14.8	3.8 ± 3.3	5.55 ± 0.42
IVL	<10 (26)	7.21 ± 0.15	29.8 ± 13.9^{ccc}	16.6 ± 3.0^{ccc}	5.21 ± 0.32
IVL	10 (22)	7.17 ± 0.16	59.6 ± 18.0	7.6 ± 4.4	5.30 ± 0.33
IVLSN	<10 (18)	7.18 ± 0.20	28.9 ± 13.2^{ddd}	15.1 ± 4.4^{ddd}	5.17 ± 0.30
IVLSN	10 (6)	7.25 ± 0.21	61.6 ± 22.3	6.7 ± 5.9	5.55 ± 0.66

Group definitions and abbreviations: IT, intratracheal; IV, intravenous; C, control; L, lipopolysaccharides (15, 20, 25 mg/kg); S, pulmonary surfactant (200 mg/kg); N, inhaled nitric oxide (10 ppm); C0, non-ventilated control. Values are means ± standard deviation. W/D, wet/dry lung weight ratio. $^{a}P < 0.05$, $^{aaa}P < 0.001$ vs. ITL (10 h), $^{b}P < 0.05$, $^{bbb}P < 0.001$ vs. ITLSN (10 h), $^{ccc}P < 0.001$ vs. IVL (10 h), $^{ddd}P < 0.001$ vs. IVLSN (10 h).

Measurement of lung mechanics

During the whole 10-h MV period, Cdyn in IVC was around 1.0 mL/kg/H_2O with no deterioration. In IVL in the initial 5 h, Cdyn was very close to that of IVC, and in the late 5 h, it fell by 10–15% and ended at 0.82 in average. That for IVLSN an upward trend was observed during the late 5-h around 1.0, close to that of the IVC (Figure 3b; Table 4). The IVL and IVLSN had the lowest ST_{50}, survival rate, pH and the highest lactate of the blood sample at termination of MV (Table 2).

Lung histopathology and morphometry

Figure 4 contains representative photomicrographs of the Phase I and II groups. No significant damage alterations were observed in the lungs of ITC groups. Both IVL and IVLSN groups exhibited moderate to severe lung pathologic changes compared with those in the ITL, as more aerated alveoli are seen, as measured by V_V and LIS in both IVL and IVLSN groups compared to that of ITL and ITLSN groups (Supplementary Figures 4a,b). Compared with the IVC, IVL did not show significant differences in Vv, CV (Vv), edema or hemorrhage scores, but had significant increases in inflammation, alveolar injury scores, and LIS_{total}. No significant differences in Vv and CV (Vv) were observed between the IVL and IVLSN groups (Figures 3c,d). Compared with the IVL, the IVLSN had lower inflammation scores but not LIS_{total}, whereas LIS items and LIS_{total} in both IVL and IVLSN groups were markedly lower than that in the corresponding groups of phase I (Supplementary Figures 4a,b).

Ultrastructural morphology of the lungs

Similar features, but less in severity, of the microstructures of alveoli and bronchioles were seen compared to that in the phase I under the transmission electron microscopy. Ultrastructural morphology of the IVL group revealed interstitial edema, detached and loosely arranged ATII cells sloughing into the alveolar lumen, and markedly increased lysosomes (Figures 5d–f). Ultrastructural morphology of the IVLSN group (not shown) mirrored the ITLSN picture: surfactant-phospholipid lamellae and tubular myelin occupied the alveolar spaces, while interstitial infiltrates of inflammatory cells were again conspicuous.

Biochemical analysis of phospholipids and proteins in BALF and LH

The levels of TPL and DSPC in BALF were more than 2 folds, and TP and DSPC/TP more than 50% and 100%, higher

TABLE 4 Analysis of lung phospholipid pools.

Group	N	TPL_{BALF} (mg/kg)	$DSPC_{BALF}$ (mg/kg)	$DSPC/TPL_{BALF}$ (%)	TP_{BALF} (mg/kg)	$DSPC/TP_{BALF}$ (mg/mg)
C0	8	12.1 ± 3.34	5.50 ± 3.30	42.6 ± 18.3	5.74 ± 2.03	0.91 ± 0.41
ITC	7	9.89 ± 3.69	5.23 ± 1.77	55.2 ± 20.9	7.00 ± 1.56	0.73 ± 0.17
ITL	30	7.24 ± 3.26	3.73 ± 2.11	49.9 ± 19.9	9.30 ± 3.25	0.41 ± 0.21*
ITLSN	24	16.5 ± 5.34###	8.28 ± 3.97###	50.3 ± 13.7	11.5 ± 2.75#	0.72 ± 0.26###
IVC	8	8.48 ± 2.97	4.32 ± 2.24	49.1 ± 17.5	6.51 ± 1.89	0.65 ± 0.26
IVL	30	8.79 ± 2.30	4.26 ± 1.89	48.1 ± 16.4	6.15 ± 2.03###	0.69 ± 0.21###
IVLSN	24	32.2 ± 12.6^^^	15.1 ± 5.96^^^	47.0 ± 5.90	10.5 ± 4.20^^^	1.51 ± 0.51^^^

Group	N	TPL_{LH} mg/kg	$DSPC_{LH}$ mg/kg	$DSPC/TPL_{LH}$ %	$TPL_{BALF+LH}$ mg/kg	$DSPC_{BALF+LH}$ mg/kg	$DSPC/TPL_{BALF+LH}$ %
C0	8	146 ± 24.2	37.1 ± 15.2	25.8 ± 9.70	158 ± 26.5	42.6 ± 13.4	27.3 ± 7.64
ITC	7	167 ± 46.0	44.1 ± 18.5	26.8 ± 9.78	177 ± 48.0	49.3 ± 18.8	28.2 ± 9.38
ITL	30	138 ± 45.4	31.9 ± 15.3	23.1 ± 8.32	145 ± 45.1	35.6 ± 15.2	24.7 ± 7.78
ITLSN	24	216 ± 62.7###	62.0 ± 33.5###	28.7 ± 11.9	233 ± 64.9###	70.3 ± 36.5###	30.0 + 11.5
IVC	8	123 ± 35.9	29.0 ± 9.61	25.1 ± 10.1	131 ± 34.0	33.3 ± 9.43	26.9 ± 10.5
IVL	30	152 ± 47.6	35.0 ± 15.8	23.7 ± 10.4	160 ± 48.1	39.3 ± 16.2	25.1 ± 9.61
IVLSN	24	240 ± 71.5^^^	71.5 ± 36.3^^^	28.6 ± 9.00	272 ± 68.3^^^	86.6 ± 36.8^^^	31.1 ± 7.75

Values are means ± standard deviation. TPL, Total phospholipid; DSPC, Disaturated phosphatidylcholine. TP, Total proteins. BALF, Bronchoalveolar lavage fluid; LH, Lung homogenate. *$P < 0.05$ vs. ITC, #$P < 0.05$, ###$P < 0.001$ vs. ITL, ^^^$P < 0.001$ vs. IVL. For group definitions see Table 1 legends.

in the IVLSN than in the IVL group, respectively (IVL: TPL 8.79 ± 2.30, DSPC 4.26 ± 1.89, TP 6.15 ± 2.03, DSPC/TP 0.69 ± 0.21; IVLSN: TPL 32.2 ± 12.6, DSPC 15.1 ± 5.96, TP 10.5 ± 4.20 and DSPC/TP1.51 ± 0.51) (Figures 3e,f; Table 4). DSPC/TPL was around 40–50% with no significant difference among the four groups. In the total lung phospholipid pool, i.e., in BALF + lung tissue homogenate, of the IVC and IVL groups, TPL were around 130–160 mg/kg, DSPC 33–40 mg/kg, and DSPC/TPL 25–27%, in average. For TPL and DSPC in BALF + lung tissue homogenate in the IVLSN, there were 270 and 87 mg/kg, which were 9 and 6 times that in the BALF (32 and 15 mg/kg in average) (Figure 3e; Table 4), respectively, with 31% of DSPC/TPL. It also derives net increments by approximately 126 and 50 mg/kg, or 86% and 138%, respectively, over the average TPL and DSPC in the IVC and IVL. Likewise, there were ratios of 8 and 5 between LH and BALF (i.e. 240 vs. 32.2 and 71.5 vs. 15.1 mg/kg, Table 4) for TPL or DSPC, respectively, in the IVLSN, denoting relatively enriched DSPC in both BALF and LH, compared with that of the ITLSN.

Measurement of mRNA expression in lung tissues (and in both phases of experiments)

In both IVC and IVL groups, there were no significant differences in the mRNA expression of SP-A, SP-B, and SP-C. Compared with the IVC group, the mRNA expression of NF-κB, TNF-α, IL-1β, IL-6, and IL-8 were upregulated in the IVL, and even higher in the IVLSN. The mRNA expression of Tie-2, Ang-1 and Ang-2 of both ITC and IVC had modest increment compared with that of C0, and ITL and IVL had approximately 40% depression compare to the corresponding ITC and IVC. The ITLSN and IVLSN had even lower expression of Tie-2 and Ang-1, but markedly enhanced expression of Ang-2 by three folds in both ITLSN and IVLSN (Figures 2g–i, 3g–i).

Comparison of mRNA expression of pro-inflammatory cytokines in liver and kidney tissues

In general, compared to the IVC, the IVL had 1-10 folds increments in the mRNA expression of ILs in both liver and kidney tissues. In contrast, the IVLSN had even more folds of increments than that of the IVL (Figures 3j,k).

Comparison of ITL and IVL

In Supplementary Figure 5, a direct comparison between ITC and IVC, or ITL and IVL in the Figures 2, 3 and Tables 4, 5 is provided. It facilitates comprehension of baseline characteristics between any two of the four groups in the two phases of experiments excluding both ITLSN and IVLSN groups (see above "Measurement of mRNA expression in lung tissues").

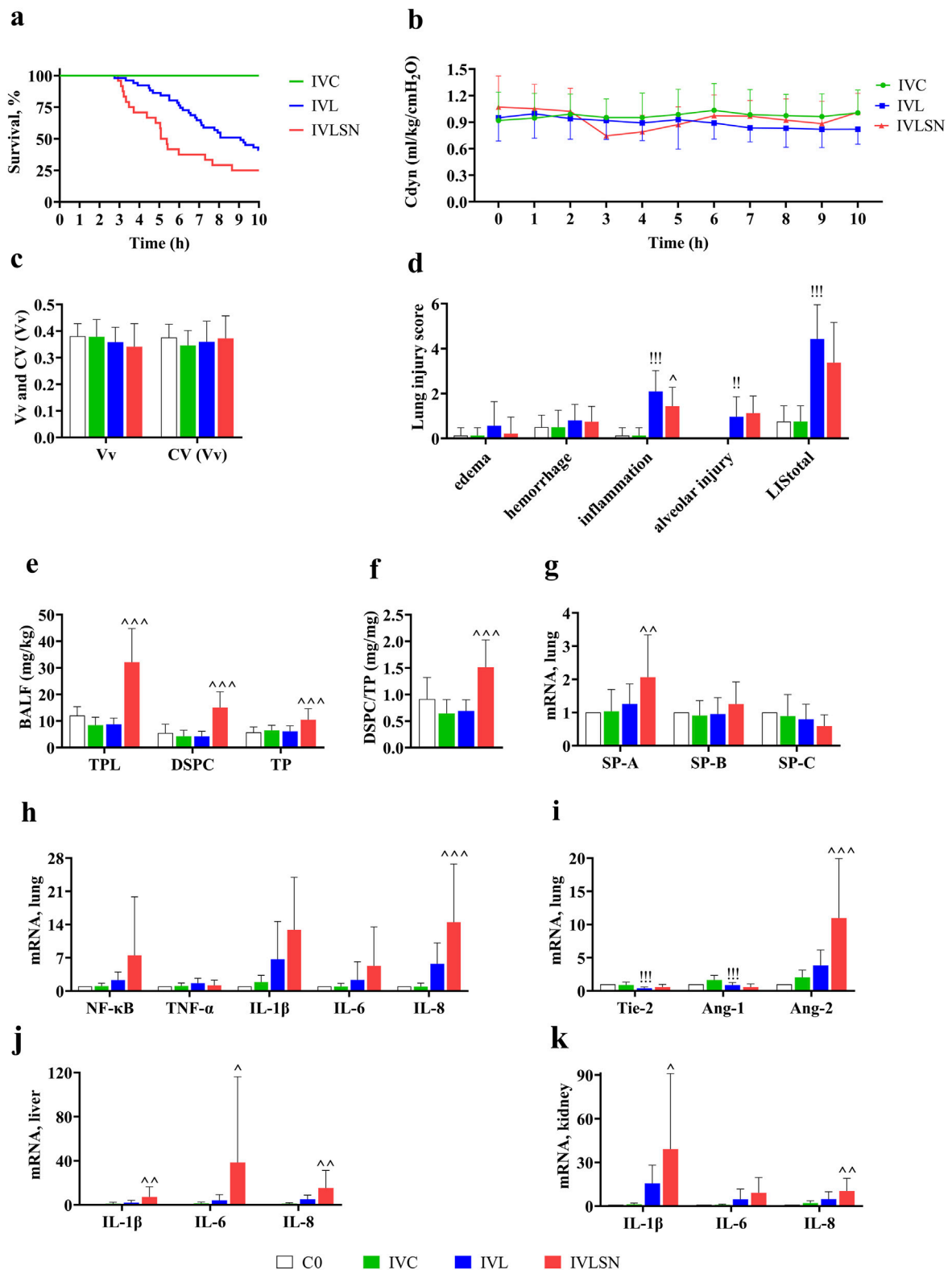

FIGURE 3
Major results of 7-day old rabbits in Phase II experiment. **(a)** Kaplan-Meier survival curves (IVC n = 12, IVL n = 51, IVLSN n = 24); IVC, saline control; IVL, combined intravenous LPS 15–25 mg/kg; IVLSN, IVL with surfactant and iNO treatment; **(b)** Trend of Cdyn during ventilation (for details with sample size, see Supplementary Table 4) (IVC n = 12, IVL n = 51, IVLSN n = 24); **(c)** Vv and CV(Vv) (C0 n = 8, IVC n = 8, IVL n = 30, IVLSN n = 24); **(d)** LIS
(*Continued*)

FIGURE 3 (Continued)
(C0 n = 8, IVC n = 8, IVL n = 30, IVLSN n = 24); **(e)** TPL, DSPC and TP in BALF (C0 n = 8, IVC n = 8, IVL n = 30, IVLSN n = 24); **(f)** DSPC/TP ratio; **(g)** mRNA expression of SP (C0 n = 8, IVC n = 8, IVL n = 30, IVLSN n = 24); **(h)** mRNA expression of pro-inflammatory mediators in lung tissue (NF-κB, TNF-α, IL) (C0 n = 8, IVC n = 8, IVL n = 30, IVLSN n = 24); **(i)** mRNA expression of the injury markers of endothelial cells in lung tissue (Tie-2, Ang) (C0 n = 8, IVC n = 8, IVL n = 30, IVLSN n = 24); **(j)** mRNA expression of pro-inflammatory mediators in liver tissue (C0 n = 5, IVC n = 5, IVL n = 36, IVLSN n = 24); **(k)** mRNA expression of pro-inflammatory mediators in kidney tissue (C0 n = 5, IVC n = 5, IVL n = 36, IVLSN n = 24). For group definitions see Figure 1 legends; and for abbreviations see Figures 1, 2. Legends. Values are mean ± standard deviation. $^{!!}P < 0.01$, $^{!!!}P < 0.001$ vs. IVC, $^{\wedge}P < 0.05$, $^{\wedge\wedge}P < 0.01$, $^{\wedge\wedge\wedge}P < 0.001$ vs. IVL. (Due to the very small mean ± standard deviation of the control group, the value levels are almost imperceptible in the figure **d**, **j** and **k**).

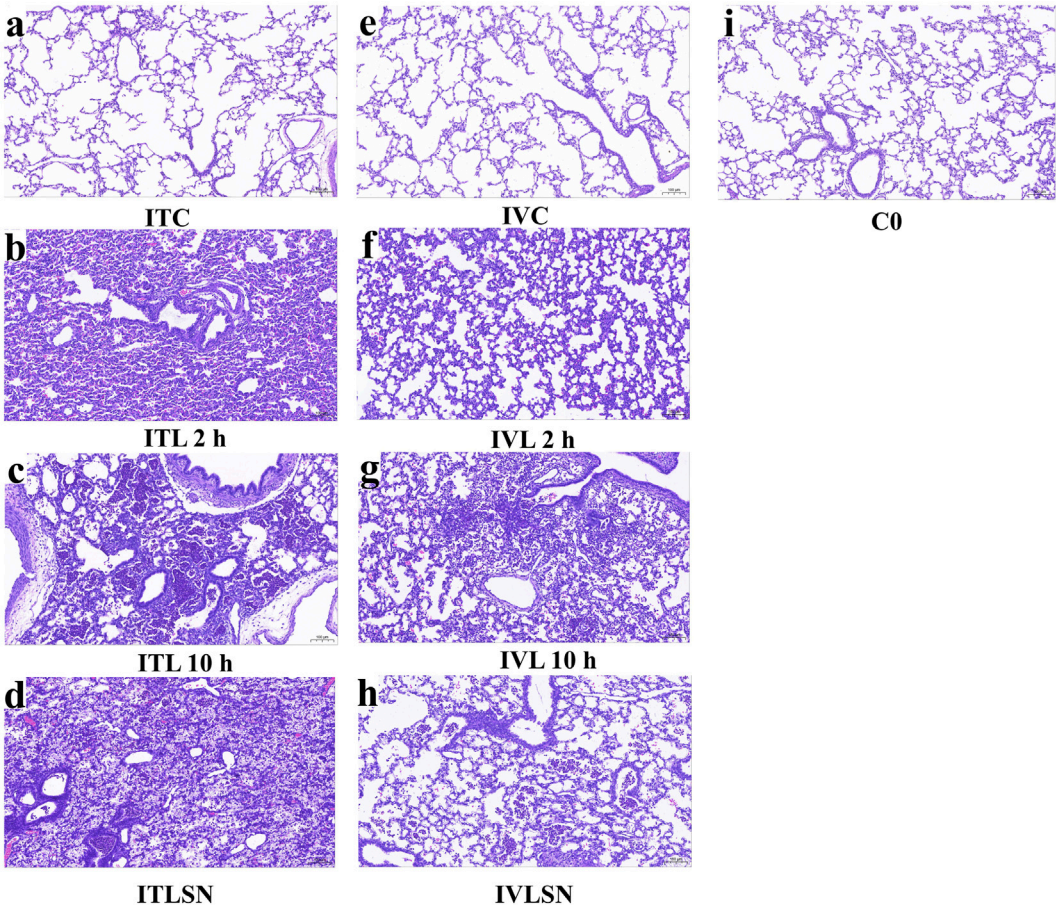

FIGURE 4
Representative photomicrographs of the lungs at different ventilation time. **(a)** ITC; **(b)** ITL 2 h; **(c)** ITL 10 h; **(d)** ITLSN; **(e)** IVC; **(f)** IVL 2 h; **(g)** IVL 10 h; **(h)** IVLSN; **(i)** C0. Scale bar = 100 μm. For group definitions see Figure 1 legends.

Discussion

Despite decades of efforts to bridge the knowledge gap, effective respiratory therapies with MV and ancillary medications for rescue purpose in pARDS remain to be limited, with high mortality risks to be solved [28]. The strength of current LPS-ALI model in 7-day old rabbits at their early post-neonatal infancy is characterized as simulating the $pARDS_p$ and $pARDS_{exp}$ by LPS-route associated different lung damage patterns, as shown in the survival length, LIS and pulmonary and extrapulmonary organ impairment. In neonatal and pediatric critical care, as we chose this animal age in maturation, it often faces with severe pneumonia and sepsis as underlying morbidities, with lung functional failure in ALI, PHRF and septic shock as the most fatal situation. The pharmacotherapeutic response patterns observed herewith may not readily explain the complex pathophysiology of pARDS in humans. However, the outcome was verified by

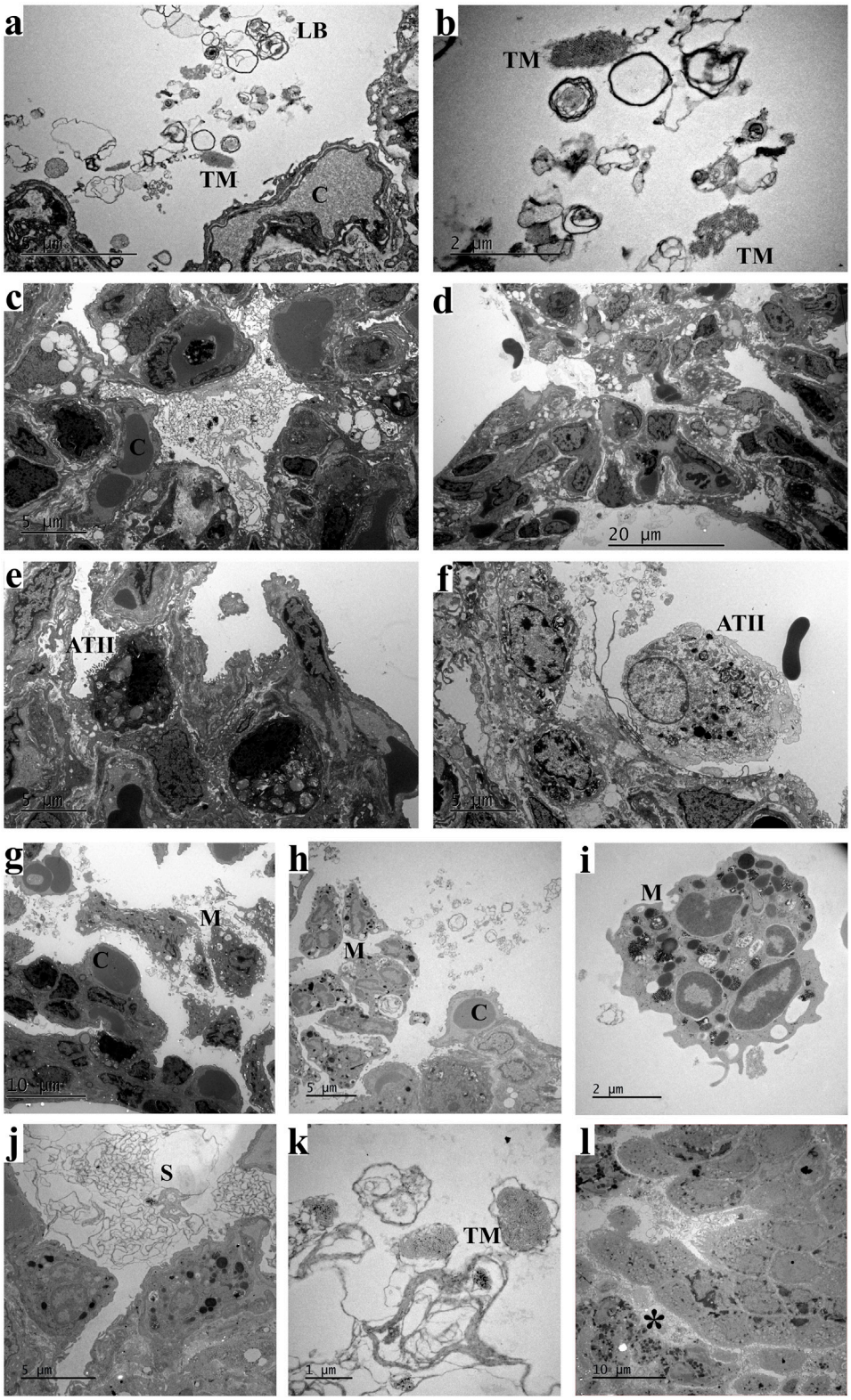

FIGURE 5
Ultrastructure of alveoli in 7-day old rabbit lungs. **(a,b)** IVC, loosen lamellar body and tubular myelin in alveolar space; **(c)** ITL, fluid infiltration in alveolar space and loosen ATII; **(d–f)** IVL, interstitial edema and loosen ATII with few lamellar bodies but intensified lysosome; **(g–i)** ITLSN, alveolar microphages; **(j,k)** ITLSN, surfactant phospholipid layers and tubular myelin in alveolar space; **(l)** ITLSN, interstitial inflammatory cells. For group
(*Continued*)

FIGURE 5 (Continued)
definitions see Figure 1 legends. Scale bar size: **d** = 20 μm; **g** and **l** = 10 μm; **a**,**c**, **e**,**f**,**h** and **j** = 5 μm; **b** and **i** = 2 μm; **k** = 1 μm. Abbreviations: ATII, type II alveolar epithelial cell; C, capillary; LB, lamellar body; M, macrophage; S, surfactant phospholipid membrane layers; TM, tubular myelin. *, inflammatory cell. For group definitions see Figure 1 legends.

TABLE 5 Stratified analysis of early death and 10-h survivors on lung surfactant phospholipid pools.

Group	Survival h (n)	TPL_{BALF} mg/kg	$DSPC_{BALF}$ mg/kg	TP_{BALF} mg/kg	TPL_{LH} mg/kg	$DSPC_{LH}$ mg/kg
ITL	<10 (1)	3.68	1.15	7.41	125	42.8
ITL	10 (29)	7.36 ± 3.24	3.82 ± 2.09	9.36 ± 3.29	138 ± 46.1	31.5 ± 15.4
ITLSN	<10 (6)	21.0 ± 2.49^{bb}	11.0 ± 2.44^{b}	12.4 ± 1.93	242 ± 45.3	88.2 ± 38.3^{bb}
ITLSN	10 (18)	15.0 ± 5.20	7.35 ± 4.00	11.2 ± 2.96	208 ± 66.4	53.3 ± 27.6
IVL	<10 (13)	8.79 ± 2.22	4.90 ± 2.00	6.43 ± 2.24	145 ± 48.0	32.2 ± 16.0
IVL	10 (17)	8.79 ± 2.43	3.77 ± 1.69	5.96 ± 1.91	156 ± 48.2	37.2 ± 15.8
IVLSN	<10 (18)	35.5 ± 11.4^{dd}	16.3 ± 5.31^{d}	9.99 ± 4.01	236 ± 69.9	75.5 ± 38.9^{dd}
IVLSN	10 (6)	22.3 ± 11.6	11.4 ± 6.74	11.9 ± 4.82	250 ± 81.8	59.5 ± 26.5

Group	Survival h (n)	$TPL_{BALF+LH}$ mg/kg	$DSPC_{BALF+LH}$ mg/kg
ITL	<10 (1)	129	44.0
ITL	10 (29)	145 ± 45.8	35.3 ± 15.4
ITLSN	<10 (6)	263 ± 45.7	99.3 ± 40.5^{bb}
ITLSN	10 (18)	223 ± 68.2	60.7 ± 30.5
IVL	<10 (13)	154 ± 48.6	37.1 ± 16.1
IVL	10 (17)	165 ± 48.6	41.0 ± 16.6
IVLSN	<10 (18)	272 ± 68.6	91.8 ± 39.4
IVLSN	10 (6)	273 ± 73.9	70.9 ± 24.1

Values are means ± standard deviation. $^{b}P < 0.05$, $^{bb}P < 0.01$ vs. ITLSN (10 h), $^{d}P < 0.05$, $^{dd}P < 0.01$ vs. IVLSN (10 h). For group definitions see Table 1 legends.

Cdyn, survival rate and ST_{50} (for survival length), LIS, and the surfactant phospholipid metabolic pools. The key variables as biomarkers strengthened understanding of the underlying morbidities and applicability of pharmacotherapeutic action by surfactant and iNO treatment. It is therefore of causal implication as highly clinical problems oriented, in quest of rescue solution for prediction of pARDS outcome, despite there was an ineffectiveness/failure with the combined surfactant and iNO treatment [17].

From the lung damage patterns shown in the two phases of experiments, the direct ALI was associated with severe pneumonia and higher LIS, but moderate death risks; whereas the indirect ALI was with moderate LIS but high death risks due to sepsis associated multiorgan impairment in the lung, liver and kidney. The combined surfactant and iNO failed to improve the survival, associated with highly provoked mRNA expression of proinflammatory mediators as multiorgan involved septic lung damage patterns, especially in the IVLSN. These suggest imbalanced efficacies of the two combined respiratory ancillary medications when the lung impairment severity, hypotension and septic shock compromised ventilation/perfusion matching as underlying pathophysiologic, causative risks.

In addition, improper and insufficient surfactant dosage, surface activity, composition of phospholipids and hydrophobic proteins, SP-B and SP-C, its anti-inhibition potential and metabolic characteristics, partially associated with manufacturing process, may also determine as covariate towards the worse outcome. These issues should be explored to enrich our knowledge based on the current concept and recommendation for pARDS [29, 30]. This LPS-ALI model should be eligible for investigation of any new invention of surfactant preparation in novel components, manufacturing process improvement, or treatment response which would be associated with timing and dosing (loading and repeat doses) and

delivery techniques (bolus, diluted lavage, or both), and interaction with other medications in critical care, in combination with pathobiological variables as phenotypic and sub-phenotypic indicators [31].

We found those of the IVLSN group had the shortest average survival time but with higher TPL and DSPC total pools (BALF + lung tissue) (Tables 4, 5). These findings may also be corroborated by sub-group data analysis for that of the 10-h survivors (Tables 4, 5). It is thereon estimated, approximately 63% and 36% of full dose surfactant TPL in the IVLSN and ITLSN groups, respectively, remaining in the whole lung metabolic pool at the end of MV, over the ensuing 7 h MV, or shorter for those of early death, and that the TPL being supposedly catabolized at a rate of 5%/h or 9%/h in average in the IVLSN or ITLSN lungs, respectively. Thus, these findings may be regarded as baseline evidences concerning the surfactant phospholipid metabolism in ALI for future investigation with stable isotope labeled phospholipids to estimate pharmacokinetic and pharmacodynamic efficiency as well. The presence of supposedly exogenous surfactant phospholipid membrane layers with no overt TM in adjacent alveolar space were in contrast to that of the controls (Figure 5). Given that the lung injury patterns (Figures 2–4), and phospholipid pools in those of early deaths and 10-h survivors (Tables 4, 5), the exogenous surfactant should be distributed in the injured lung alveoli, and taken up by ATII in reference to the control group (ITC, IVC). Whether it follows the re-synthesis and secretion by ATII, as reutilization, in the severely injured lungs is questionable and needs deliberate design of experiment to verify.

The histopathological features of lung impairment in ITL and ITLSN groups attained wide spread purulent and necrotic alveolitis and bronchiolitis, in contrast to mild and moderate inflammation in those of the IVL and IVLSN. However, there were disparities in the death risks, with mild-to-moderate deterioration in the lung mechanics measured by Cdyn in both ITL and IVL, but improved only in the IVLSN group but with higher early deaths. These discrepancies may account for the surfactant and iNO treatment ineffectiveness/failure, and should be of clinical implication in using MV-centered approaches to predict risks in immediate progression [12]. Another potentially eligible approach is to use surfactant lavage and subsequently with the bolus surfactant regimen, as we did in a meconium-induced lung injury model of near-term newborn rabbit model with good efficacy [16]. Repeated dosing is a third option, however, it would incur a decrease of already impaired functional residual lung volume, simply due to the presence of lung edema and consolidation. This was evidenced by higher LIS for alveolar injury and inflammation, and TP in BALF of both ITLSN and IVLSN groups, though their DSPC/TP levels were also elevated. As these animals had metabolic acidosis with low pH and very high lactate in the blood at the end of MV, their early death might be related to impaired hypoxemia-associated hemodynamic condition when intravenous volume expander and vasopressor were not applicable due to the small animal body size restriction.

This LPS-ALI model rendered a suitable approach in search of relevant pharmacotherapeutic products alleviating the severity of pARDS in neonates and infants. The treatment response pattern by the combined surfactant and iNO treatment, to the two different routes of LPS administration, was not expected in the original design. However, the resulting therapeutic response patterns with both physiological and pathobiological variables, underscored the disparities of outcome. Notably, by sub-group analysis, it revealed that those in the ITLSN and IVLSN with short survival length had nearly normal PCO_2 but lower pH and very high lactate in blood at the end of MV (Table 3). Nevertheless, those in the ITLSN, IVL and IVLSN subgroups with short survival length had variable total surfactant phospholipid pools (Table 5).

To our surprise, under the high dose of LPS exposure, there were limited elevation in the mRNA expression of pro-inflammatory cytokines and mediators. In general, being a hallmark feature of septic ALI ($ARDS_{exp}$), alveolar macrophages, as an innate immune cell type, are engaged in the maintenance of pulmonary homeostasis of immune response [32]. The classic NF-κB pathway activated pro-inflammatory cytokines, such as TNF-α, IL-1β, IL-6, IL-8, inducing neutrophil chemotaxis and activation in alveolar space, ultimately leading to the necrosis and purulent damages of alveolar structure, causing ALI and ARDS [33]. The evolving permeability as main pathological change in the course of lung damage may be centered in the pulmonary vascular endothelia, in which IL-1β, −6 and −8 play important roles through a number of vascular endothelial cell associated mediators [34]. This may be the next target to investigate for understanding the injury severity and protective ventilation strategy.

The unexpected high early death due to suspected hemodynamic derangement in the IVLSN was based solely on the evidence of enhanced mRNA expression in the liver and kidney as extrapulmonary organ injury, to link that in the clinical findings [35, 36]. In the study design, there was no measurement of extrapulmonary organ system for multiorgan dysfunction/failure. Therefore, current study was an attempt of reverse translation to explain mechanisms behind the clinical trial limitation, or failure, specifically for surfactant and/or iNO in pARDS [15, 37]. The biomarkers for defining the lung injury and alleviation by intervention, such as Ang-1, Ang-2, Tie-2 for vascular endothelial cell injury, and those for lung fluid clearance, surfactant production and metabolism, integrity and proliferation of ATs may be extended to understanding the pathogenesis and mechanistic roles underlying the pathophysiology and pharmacotherapeutic action [38].

Nitric oxide (NO) plays a pivotal role in modulating both intrapulmonary vascular tone and inflammatory responses. The concrete evidence of iNO in alleviating the lung parenchymal injury in ARDS is not clear yet [39, 40], and its off-label use in

very preterm infants at risk of early bronchopulmonary dysplasia (BPD), tended to be safe and assumed to be active in modulation of inflammation and coagulation [41, 42]. Moreover, our own experience in experimental bacterial ALI and that of clinical report, suggest safety and optimal to the effectiveness of iNO with 30–50% oxygen [43] which may mitigate hyperoxic hazard. Like the off-label use in surfactant, the ancillary pharmacotherapeutic strategies in pARDS deserve their systematic investigation to reach consensus agreement. We thereby speculate it be different from the conventions of surfactant therapy in neonatal RDS of prematurity.

The most prominent limitation was the lack of direct evidence regarding the SN failure in both ITLSN and IVLSN groups. We consider the following indirect evidence to account for the SN failure, especially in IVLSN. First, the LIS_{total} values in IVL and IVLSN groups were lower than that of ITL and ITLSN, coinciding with that of Figure 4 at 2 and 10 h. It implied that the lung infection and inflammation as well as the treatment response patterns were not the same due to LPS route, representing a timely cause-effect from the commence of SN treatment to the end of ventilation between the two group. These were in contrary to the respective survival curves as shown in Figures 2a, 3a. We therefore infer that the survival discrepancy between these two groups, as were for ITLSN vs. ITL or IVLSN vs. IVL, should be impacted by factors other than the lung injury severity, very probably associated with systemic hypotension and septic shock in the treatment of SN. Although we implemented intermittent ECG monitoring, there had no intravenous infusion, vasopressor use, and blood pressure monitoring, due to tiny vasculature of the animals. Second, through examination of qPCR results, marked over-expression of mRNA of ANG-2, IL-1, -6 and 8 in the lungs, liver and kidney in IVLSN, implying multiple organ dysfunction. These phenomena were modest or moderate in ITLSN group. Third, by comparing the ultrastructure images, and the surfactant phospholipid pools in BALF + LH, of injured lungs in Figures 2, 3, the concurrent composite images in Figure 5 mainly represent lung maturation (as day 7 of postnatal life) with lamellar bodies and tubular myelin in alveolar space of unaffected lungs (ITC, IVC). In LPS group, the alveolar structure with inflammatory epithelial and interstitial cells, alveolar macrophages, often with prominent intracellular lysosomes, showing infection in the LPS-injured lungs. In ITLSN and IVLSN group, the large ring-like phospholipids in alveolar space as considered exogenous surfactant, with the ring diameter much exceeding that of the alveolar epithelial cells, were not found in the control animal lungs (ITC, IVC). Moreover, Figures 4, 5 revealed that the alveolar space and bronchiolar lumen in the LPS group were often filled with protein-rich exudate. This protein-and-cell debris was likely to sequester or inactivate endogenous and exogenous surfactant, thereby jeopardize the latter therapeutic action. In our previous preterm and near-term rabbit study, a porcine lung natural surfactant isolated SP-A strengthened biophysical and physiological properties of a porcine lung derived surfactant phospholipid preparation (Curosurf®, with SP-B and C), by reversing inactivation and inhibition from blood plasma proteins (fibrinogen/fibrin, albumin) and meconium [44]. Thus, this study did not have sufficient evidence to explain the mechanisms of exogenous surfactant therapeutic function in counterbalance inactivation/dysfunction, and iNO safety inferential in hemodynamic homeostasis. It remains a crucial and imperative knowledge gap in comprehension of LPS-ALI injury model simulating neonatal and pediatric critical care.

In addition to above strengths and limitations, there are other limitations to address. For the three different LPS dosing groups in the initial experiment, we did not have discerned the LPS dose dependent lung injury by severity and survival status, but found LPS route-dependent effects in survival. Neither did we found any marked benefits of combined PS and iNO in both ITLSN and IVLSN, with IVLSN the worst in survival, though surfactant phospholipid pool and Cdyn seem to be potentially optimal in the 10-h survivors. It was quite different from our previous experiments in adult or young animals at the expectation to find therapeutic efficacy by MV and ancillary medications with PS and iNO [24, 45]. Another weak point is the lack of intravenous fluid maintenance as the fragile vasculature for indwelling intubation. The intraperitoneal injection followed our previous experience with ventilated near-term rabbits that may in part counter balance acidosis and basal metabolism requirement [16, 20, 46]. In future study, these problems may be dealt with deliberate fluid injection and altering of PS dosage, along with other medications, such as intratracheal glucocorticosteroids, or vasopressors, to maintain a longer survival. The route and dose of LPS may still be an important issue for pharmacotherapeutic efficacy in parallel comparison of $ARDS_p$ and $ARDS_{exp}$. This may need a framework to standardize the LPS, or other inducing chemicals, with dosing regimen, more measurement of multiorgan functioning variables including sensitive biomarkers to define. Besides, the high LPS doses used in this study may induce a hyper-acute, fulminant lung injury that does not fully recapitulate the subacute phase of human pARDS. Therefore, the model may be best suited for studying early ALI, rather than its chronic or reparative phases.

Conclusion

This study successfully established pulmonary and extrapulmonary ARDS models induced by a high dose range of LPS, in 7-day-old rabbits, explicitly depicting the distinct pathophysiological mechanisms underlying the pharmacotherapeutic action using the combined surfactant and iNO. The impact was with the disparities of LPS route dependent lung injury and survival patterns, underscoring the pathobiological phenotypes of associated pulmonary impairment and inflammatory responses versus the extrapulmonary

multiorgan involvement. The model and concept deserve further validation in the overall and specific efficacy assessment for rescue of $pARDS_p$ and $pARDS_{exp}$.

Author contributions

QG and BS, study design, experimental protocol and conducting, data analysis and interpretation, and manuscript revision; GZ, animal care, major experimental execution, data analysis and interpretation, manuscript draft and revision; SX, animal care, experimental assistance, data analysis; XG, coordination, data analysis. All authors contributed to the article and approved the submitted version.

Data availability

The original contributions presented in the study can be found via NutStore link: Dr. Zhuang G data files https://www.jianguoyun.com/p/DeoOWs0Q6pX-DRia56EGIAA (accession number: YQMQeY) PWD: YQMQeY. Further inquiries can be directed to the corresponding authors.

Ethics statement

The study protocol was approved by the Ethics Committee of the Children's Hospital of Fudan University (No. 2023350).

Funding

The author(s) declared that financial support was received for this work and/or its publication. This study was supported by the National Natural Science Foundation of China (No. 82360315, QG) and the Talent Development Fund (CZ001209) for the Key Laboratory of Clinical Medical Research Center for Children's Diseases.

Acknowledgements

We are very grateful for the technical assistance provided by Ni Qin and Jiangang Lao.

Conflict of interest

The author(s) declared no potential conflicts of interest with respect to the research, authorship, and/or publication of this article.

Generative AI statement

The author(s) declared that generative AI was not used in the creation of this manuscript.

Any alternative text (alt text) provided alongside figures in this article has been generated by Frontiers with the support of artificial intelligence and reasonable efforts have been made to ensure accuracy, including review by the authors wherever possible. If you identify any issues, please contact us.

Supplementary material

The Supplementary Material for this article can be found online at: https://www.ebm-journal.org/articles/10.3389/ebm.2026.10788/full#supplementary-material

References

1. Lu Y, Song Z, Zhou X, Huang S, Zhu D, Yang CBX, et al. A 12-month clinical survey of incidence and outcome of acute respiratory distress syndrome in Shanghai intensive care units. *Intensive Care Med* (2004) **30**:2197–203. doi:10.1007/s00134-004-2479-y

2. Sapru A, Flori H, Quasney MW, Dahmer MK, Pediatric Acute Lung Injury Consensus Conference Group. Pediatric acute lung injury consensus conference. Pathobiology of acute respiratory distress syndrome. *Pediatr Crit Care Med* (2015) **16**:S6–22. doi:10.1097/PCC.0000000000000431

3. Zhu T, Zhang W, Feng SJ, Yu HP. Emodin suppresses LPS-induced inflammation in RAW264.7 cells through a PPARγ-dependent pathway. *Int Immunopharmacol* (2016) **34**:16–24. doi:10.1016/j.intimp.2016.02.014

4. Khemani RG, Smith LS, Zimmerman JJ, Erickson S. Pediatric acute lung injury consensus conference. Pediatric acute respiratory distress syndrome: definition, incidence, and epidemiology: proceedings from the pediatric acute lung injury consensus conference. *Pediatr Crit Care Med* (2015) **16**:S23–40. doi:10.1097/PCC.0000000000000432

5. Ranieri VM, Rubenfeld GD, Thompson BT, Ferguson ND, Caldwell E, Fan E, et al. Acute respiratory distress syndrome: the Berlin definition. *JAMA* (2012) **307**:2526–33. doi:10.1001/jama.2012.5669

6. Zhu YF, Xu F, Lu XL, Wang Y, Chen JL, Chao JX, et al. Mortality and morbidity of acute hypoxemic respiratory failure and acute respiratory distress syndrome in infants and young children. *Chin Med J (Engl)* (2012) **125**:2265–71. doi:10.3760/cma.j.issn.0366-6999.2012.13.005

7. Engel M, Nowacki RME, Jonker EM, Ophelders D, Nikiforou M, Kloosterboer N, et al. A comparison of four different models of acute respiratory distress syndrome in sheep. *Respir Res* (2020) **21**:209. doi:10.1186/s12931-020-01475-0

8. Rocco PR, Zin WA. Pulmonary and extrapulmonary acute respiratory distress syndrome: are they different? *Curr Opin Crit Care* (2005) **11**:10–7. doi:10.1097/00075198-200502000-00003

9. Pelosi P, D'Onofrio D, Chiumello D, Paolo S, Chiara G, Capelozzi VL, et al. Pulmonary and extrapulmonary acute respiratory distress syndrome are different. *Eur Respir J Suppl* (2003) **42**:48s–56s. doi:10.1183/09031936.03.00420803

10. Shaver CM, Bastarache JA. Clinical and biological heterogeneity in acute respiratory distress syndrome: direct versus indirect lung injury. *Clin Chest Med* (2014) **35**:639–53. doi:10.1016/j.ccm.2014.08.004

11. Smith LS, Zimmerman JJ, Martin TR. Mechanisms of acute respiratory distress syndrome in children and adults: a review and suggestions for future research. *Pediatr Crit Care Med* (2013) **14**:631–43. doi:10.1097/PCC.0b013e318291753f

12. Sweet DG, Carnielli VP, Greisen G, Hallman M, Klebermass-Schrehof K, Ozek E, et al. European consensus guidelines on the management of respiratory distress syndrome: 2022 update. *Neonatology* (2023) **120**:3–23. doi:10.1159/000528914

13. Willson DF, Notter RH. The future of exogenous surfactant therapy. *Respir Care* (2011) **56**:1369–86. ; discussion 86-8. doi:10.4187/respcare.01306

14. Gebistorf F, Karam O, Wetterslev J, Afshari A. Inhaled nitric oxide for acute respiratory distress syndrome (ARDS) in children and adults. *Cochrane Database Syst Rev* (2016) **2016**:Cd002787. doi:10.1002/14651858.CD002787.pub3

15. Willson DF, Thomas NJ, Tamburro R, Truemper E, Truwit J, Conaway M, et al. Pediatric calfactant in acute respiratory distress syndrome trial. *Pediatr Crit Care Med* (2013) **14**:657–65. doi:10.1097/PCC.0b013e3182917b68

16. Xu Y, Guo X, Chen M, Ricci F, Salomone F, Murgia X, et al. Efficacy of synthetic surfactant (CHF5633) bolus and/or lavage in meconium-induced lung injury in ventilated newborn rabbits. *Pediatr Res* (2023) **93**:541–50. doi:10.1038/s41390-022-02152-2

17. Rowan CM, Randolph AG, Iyer NP, Korang SK, Kneyber MCJ. Pulmonary specific ancillary treatment for pediatric acute respiratory distress syndrome: from the second pediatric acute lung injury consensus conference. *Pediatr Crit Care Med* (2023) **24**:S99–s111. doi:10.1097/pcc.0000000000003162

18. De Luca D, Cogo P, Kneyber MC, Biban P, Semple MG, Perez-Gil J, et al. Surfactant therapies for pediatric and neonatal ARDS: ESPNIC expert consensus opinion for future research steps. *Crit Care* (2021) **25**:75. doi:10.1186/s13054-021-03489-6

19. Taylor G, Jackson W, Hornik CP, Koss A, Mantena S, Homsley K, et al. Surfactant administration in preterm infants: drug development opportunities. *J Pediatr* (2019) **208**:163–8. doi:10.1016/j.jpeds.2018.11.041

20. Chen M, Xu Y, Guo X, Sun B. Efficacy of perinatal pharmacotherapeutic actions for survival of very preterm newborn rabbits at 26-day gestation. *J Appl Physiol (1985)* (2023) **134**:558–68. doi:10.1152/japplphysiol.00606.2022

21. Sun B, Kobayashi T, Cursted T, Grossmann G, Robertson B. Application of a new ventilator-multi-plethysmograph system for testing efficacy of surfactant replacement in newborn rabbits. *Eur Respir J* (1991) **4**:364–70. doi:10.1183/09031936.93.04030364

22. Guo X, Luo S, Amidani D, Rivetti C, Pieraccini G, Pioselli B, et al. *In vitro* characterization and *in vivo* comparison of the pulmonary outcomes of Poractant alfa and Calsurf in ventilated preterm rabbits. *PLoS One* (2020) **15**:e0230229. doi:10.1371/journal.pone.0230229

23. Zhu Y, Guo C, Cao L, Gong X, Wang C, Sun B. Different effects of surfactant and inhaled nitric oxide in modulation of inflammatory injury in ventilated piglet lungs. *Pulm Pharmacol Ther* (2005) **18**:303–13. doi:10.1016/j.pupt.2005.01.005

24. Zhou ZH, Sun B, Lin K, Zhu LW. Prevention of rabbit acute lung injury by surfactant, inhaled nitric oxide, and pressure support ventilation. *Am J Respir Crit Care Med* (2000) **161**:581–8. doi:10.1164/ajrccm.161.2.9901048

25. Mason RJ, Nellenbogen J, Clements JA. Isolation of disaturated phosphatidylcholine with osmium tetroxide. *J Lipid Res* (1976) **17**:281–4. doi:10.1016/S0022-2275(20)36986-8

26. Bartlett GR. Phosphorus assay in column chromatography. *J Biol Chem* (1959) **234**:466–8. doi:10.1016/S0021-9258(18)70226-3

27. Miedema M, de Jongh FH, Frerichs I, van Veenendaal MB, van Kaam AH. Changes in lung volume and ventilation during surfactant treatment in ventilated preterm infants. *Am J Respir Crit Care Med* (2011) **184**:100–5. doi:10.1164/rccm.201103-0375OC

28. Orloff KE, Turner DA, Rehder KJ. The current state of pediatric acute respiratory distress syndrome. *Pediatr Allergy Immunol Pulmonol* (2019) **32**:35–44. doi:10.1089/ped.2019.0999

29. Cañadas O, Olmeda B, Alonso A, Pérez-Gil J. Lipid-protein and protein-protein interactions in the pulmonary surfactant system and their role in lung homeostasis. *Int J Mol Sci* (2020) **21**. doi:10.3390/ijms21103708

30. Loney RW, Panzuela S, Chen J, Yang Z, Fritz JR, Dell Z, et al. Location of the hydrophobic surfactant proteins, SP-B and SP-C, in fluid-phase bilayers. *J Phys Chem B* (2020) **124**:6763–74. doi:10.1021/acs.jpcb.0c03665

31. Dushianthan A, Cusack R, Goss V, Postle AD, Grocott MP. Clinical review: exogenous surfactant therapy for acute lung injury/acute respiratory distress syndrome--where do we go from here? *Crit Care* (2012) **16**:238. doi:10.1186/cc11512

32. Wang J, Peng X, Yuan N, Wang B, Chen S, Wang B, et al. Interplay between pulmonary epithelial stem cells and innate immune cells contribute to the repair and regeneration of ALI/ARDS. *Transl Res* (2024) **272**:111–25. doi:10.1016/j.trsl.2024.05.012

33. Sapra L, Saini C, Das S, Mishra PK, Singh A, Mridha AR, et al. Lactobacillus rhamnosus (LR) ameliorates pulmonary and extrapulmonary acute respiratory distress syndrome (ARDS) via targeting neutrophils. *Clin Immunol* (2024) **258**:109872. doi:10.1016/j.clim.2023.109872

34. Xu H, Sheng S, Luo W, Xu X, Zhang Z. Acute respiratory distress syndrome heterogeneity and the septic ARDS subgroup. *Front Immunol* (2023) **14**:1277161. doi:10.3389/fimmu.2023.1277161

35. Siuba M, Duggal A. Nonpulmonary organ failure in ards: what can we modify? *Respir Care* (2019) **64**:610–1. doi:10.4187/respcare.07008

36. Khadaroo RG, Marshall JC. ARDS and the multiple organ dysfunction syndrome. Common mechanisms of a common systemic process. *Crit Care Clin* (2002) **18**:127–41. doi:10.1016/s0749-0704(03)00069-1

37. Afshari A, Brok J, Møller AM, Wetterslev J. Inhaled nitric oxide for acute respiratory distress syndrome (ARDS) and acute lung injury in children and adults. *Cochrane Database Syst Rev* (2010):Cd002787. doi:10.1002/14651858.CD002787.pub2

38. Vassiliou AG, Kotanidou A, Dimopoulou I, Orfanos SE. Endothelial damage in acute respiratory distress syndrome. *Int J Mol Sci* (2020) **21**. doi:10.3390/ijms21228793

39. Payen DM. Inhaled nitric oxide and acute lung injury. *Clin Chest Med* (2000) **21**:519–29. doi:10.1016/s0272-5231(05)70163-5

40. Kang JL, Park W, Pack IS, Lee HS, Kim MJ, Lim CM, et al. Inhaled nitric oxide attenuates acute lung injury via inhibition of nuclear factor-kappa B and inflammation. *J Appl Physiol (1985)* (2002) **92**:795–801. doi:10.1152/japplphysiol.00202.2001

41. Bronicki RA, Fortenberry J, Schreiber M, Checchia PA, Anas NG. Multicenter randomized controlled trial of inhaled nitric oxide for pediatric acute respiratory distress syndrome. *J Pediatr* (2015) **166**:365–9.e1. doi:10.1016/j.jpeds.2014.10.011

42. Ellsworth MA, Harris MN, Carey WA, Spitzer AR, Clark RH. Off-label use of inhaled nitric oxide after release of NIH consensus statement. *Pediatrics* (2015) **135**:643–8. doi:10.1542/peds.2014-3290

43. Rayhrer CS, Edmisten TD, Cephas GA, Tribble CG, Kron IL, Young JS. Nitric oxide potentiates acute lung injury in an isolated rabbit lung model. *Ann Thorac Surg* (1998) **65**:935–8. doi:10.1016/s0003-4975(98)00119-2

44. Sun B, Curstedt T, Lindgren G, Franzén B, Alaiya AA, Calkovská A, et al. Biophysical and physiological properties of a modified porcine surfactant enriched with surfactant protein A. *Eur Respir J* (1997) **10**:1967–74. doi:10.1183/09031936.97.10091967

45. Zhao DH, Sun B, Wu ZH, Lindwall R, Robertson B. Mitigation of endotoxin-induced acute lung injury in ventilated rabbits by surfactant and inhaled nitric oxide. *Intensive Care Med* (2000) **26**:229–38. doi:10.1007/s001340050052

46. Luo S, Guo X, Xu Y, Dong Y, Rehan VK, Sun B. Comparison of survival of preterm newborn rabbits at 25-28 days of gestation with perinatal therapies at birth transition. *J Appl Physiol (1985)* (2021) **131**:220–8. doi:10.1152/japplphysiol.00027.2021

EBM Experimental Biology and Medicine

TYPE Original Research
PUBLISHED 24 February 2026
DOI 10.3389/ebm.2026.10755

OPEN ACCESS

*CORRESPONDENCE
Paula Peixoto Campos,
paulapc@ufmg.br

RECEIVED 17 July 2025
REVISED 15 January 2026
ACCEPTED 06 February 2026
PUBLISHED 24 February 2026

CITATION
Heleno JFG, dos Santos LCC, Fontes IC, Paiva Silva MRA, Correia LB, Silva NDG, Prazeres PHDM, Goulart Guimarães PP, Gilroy DW, Andrade SP and Campos PP (2026) L-Glutamine attenuates peritoneal fibrosis developed in 5-Fluorouracil-treated mice.
Exp. Biol. Med. 251:10755.
doi: 10.3389/ebm.2026.10755

L-Glutamine attenuates peritoneal fibrosis developed in 5-Fluorouracil-treated mice

Juliana Francisca Grossi Heleno[1,2], Leticia Cristine Cardoso dos Santos[1], Igor Campos Fontes[1], Mirielly Ranny Almeida Paiva Silva[1], Lucas Barbosa Correia[1], Nayma Drielly Granato Silva[1], Pedro Henrique Dias Moura Prazeres[1], Pedro Pires Goulart Guimarães[3], Derek W. Gilroy[4], Silvia Passos Andrade[3] and Paula Peixoto Campos[1]*

[1]General Pathology Department, Biological Science Institute, Federal University of Minas Gerais, Belo Horizonte, Brazil, [2]Benjamin Guimarães Foundation, Hospital of Baleia, Department of Hospital Dentistry, Belo Horizonte, Minas Gerais, Brazil, [3]Department of Physiology and Biophysics, Institute of Biological Sciences, Federal University of Minas Gerais, Belo Horizonte, Minas Gerais, Brazil, [4]Department of Ageing, Rheumatology and Regenerative Medicine, University College London, London, United Kingdom

Abstract

Peritoneal fibrosis is an adverse effect of cancer therapy leading to progressive organ failure. L-Glutamine supplementation has been shown to attenuate fibrosis and improve wound healing in several types of tissue injuries. The aim of this study was to evaluate the effects of this supplementation on key components of the peritoneal fibrovascular tissue induced by implants in mice treated with 5-Fluorouracil (5-FU) C57BL/6 mice received three intraperitoneal doses of immunosuppressant (60, 40, and 40 mg/kg) on non-consecutive days prior to implantation of polyether-polyurethane sponges into the peritoneal cavity. The group treated with L-Glutamine received 150 mg/kg/day for 7 days (oral gavage) starting 24 h after implantation and the control group received filtered water. Eight days after implantation, implants were removed and processed for inflammatory, angiogenic, and fibrogenic markers. Flow cytometry results showed that L-Glutamine decreased (48%) the frequency/influx of total intra-implant cells. The remaining cell population in the treated group had more neutrophils, lymphocytes, and macrophages than in the control. Immunohistochemistry analysis showed fewer Caspase-3-positive cells in the treated group. Myeloperoxidase (MPO) and N-acetyl-β-D-glucosaminidase (NAG) activities, TNF-α levels, and mast cell numbers were decreased in the implants of the L-Glutamine-treated group compared with the control. Similarly, angiogenesis (VEGF levels and number of blood vessels) was attenuated by L-Glutamine. Supplementation also decreased the amount of intra-implant collagen and TGF-β1 levels. These results indicate that L-Glutamine attenuates critical inflammatory-angiogenesis and profibrotic

pathways involved in fibrosis development in immunosuppression conditions, supporting its potential as an adjunct therapeutic strategy for managing peritoneal healing in cancer.

KEYWORDS

angiogenesis, fibrogenesis, immunonutrient, inflammation, repair

Impact statement

Adverse healing (fibrosis/adhesion) in the peritoneal cavity occurs after traumatic surgical procedures, injection and cancer treatments, impairing the function of visceral organs. Effective prevention and therapeutic management strategies are needed, especially under immunosupression. L-Glutamine (GLN), an aminoacid used as a nutritional supplement, has been shown to modulate inflammation, angiogenesis and fibrosis, key components of the wound healing process. Our data provides important information on the effects of oral L-Glutamine supplementation on the development of fibrovascular tissue in a model of implant induced peritoneal adhesion in mice treated with 5-Fluoracil (5-FU). The aminoacid was able to differentially modulate the recruitment/activation of inflammatory cells of the myeloid lineage towards a predominantly anti-inflammatory, anti-angiogenic and anti-fibrogenic phenotype on the peritoneal fibrovascular tissue under immunosupression. By targeting multiple axes involved in peritoneal fibrosis, our findings advance the knowledge on the mechanisms of action of L-Glutamine controlling wound healing in the abdominal cavity.

Introduction

Peritoneal adhesions are characterized by the abnormal formation of fibrous connections between tissues and organs within the abdominal cavity due to dysregulated wound healing processes such as excessive collagen deposition and inflammatory cytokine release. They develop in 75%–90% of patients following abdominal surgery, infection, irradiation, or the introduction of foreign materials like surgical sutures and meshes [1–3]. These adhesions can lead to significant health complications, including bowel obstruction, chronic abdominal pain, and female infertility, resulting in substantial economic burdens due to increased hospitalizations, repeat surgical interventions, and reduced patient productivity [3–6]. Peritoneal injury disrupts the mesothelial layer triggering a cascade of events such as coagulation, inflammation, fibrinolysis, angiogenesis, extracellular matrix deposition. These events are orchestrated by an influx of various cell types, immune cells, endothelial cells, mast cells and stromal fibroblasts that, in turn release their products at the site of the injury resulting in a fibrous exudate [4–7]. When fibrinolytic imbalance occurs, this exudate may develop into fibrous tissue, as mesothelial cells, fibroblasts, and myofibroblasts contribute to the extracellular matrix deposition, accompanied by the prolonged activation of inflammatory and angiogenic processes [4–7]. The newly formed tissue is a dysmorphic connective structure composed of a dense, disorganized extracellular matrix, highly vascularized, differentiated, innervated, and populated with a variety of cell types [4–7]. This adverse healing process (fibrosis/abdominal adhesion) is responsible for impairing the functionality of visceral organs, constituting a major cause of morbidity and mortality [1–3]. Despite ongoing research, the precise mechanisms underlying adhesion formation remain incompletely understood, and effective preventive and therapeutic strategies are still needed [8, 9].

L-Glutamine, the most abundant free amino acid in the human body, is a crucial cellular substrate, not only as an amino acid, but also as a source of energy, nitrogen and carbon for macrophages, lymphocytes and other cells (enterocytes, fibroblasts) [10–13]. Thus, L-Glutamine is directly involved in the process of immunological cell division, in acid-base balance, in the transport of ammonia between tissues, in the donation of carbon skeletons for gluconeogenesis and participates in the processes of recovery from physiological stress due to harmful and/or catabolic events [10, 14]. The reduction in the availability of L-Glutamine appears to influence several functions, whether in the immune system, antioxidant action or inflammation induced by physical exercise or disease. Other studies have attributed the improvement of tissue repair processes in wounds with increased catabolism to oral supplementation with L-Glutamine, such as in seriously ill, burned, cancer or critical patients, where L-Glutamine consumption exceeds the body's synthesis capacity [13, 15]. In 1999, it was reported that total parenteral nutrition with glutamine shortened hospital stays and improved immunity after major abdominal surgery [16]. However, the effects of this supplementation are far from clear cut. It has been reported that this amino acid exerted both anti- and pro- inflammatory, angiogenic and fibrogenic effects on various damaged/injured tissues, with improvement in the quality of remodeling [17–21]. For instance, it has been reported that inhibition of L-Glutamine metabolism by an analogue, 6-diazo-5-oxo-L-norleucine, accelerated the resolution and repair of acute lung injury induced by intratracheal lipopolysaccharide (LPS) instillation [18]. In contrast, L-Glutamine supplementation was able to decrease the expression of various pro-inflammatory mediators in rat osteoarthritis [17, 18]. In the angiogenic process, glutamine has been shown to play a key role in endothelial cell sprouting and blood vessel formation [19, 20, 22].

However, different results have been obtained for migration experiments performed under glutamine withdrawal, depending on the endothelial cell types used [19, 20, 22]. Glutamine has been shown to either down or up regulate fibrosis in several experimental/human conditions. The use of L-Glutamine enema reduced inflammation and fibrosis in experimental diversion colitis in Wistar rats [23]. Oral administration of glutamine promoted faster skin healing by acting on several stages of healing, such as collagen synthesis, wound contraction and epithelialization in a rat wound model [24]. However, pro-fibrotic effects of L-Glutamine have been reported. Patients with severe fibrosis exhibit elevated serum glutamine levels and increased expression of kidney glutamine synthetase. Deprivation of glutamine metabolism *in vitro* and *in vivo* inhibits fibroblast activation, ameliorating renal fibrosis [22]. Furthermore, inhibition of glutamine metabolism suppressed activation of hepatic stellate cells attenuating liver fibrosis [25]. Thus, further investigation is needed to advance our knowledge on the effects of glutamine on various components of fibroproliferative conditions (inflammation, angiogenesis and fibrogenesis).

We hypothesized that this amino acid might modulate these components on our murine model of peritoneal fibrosis induced by the synthetic matrix of polyether-polyurethane. In this model, surgical implantation of the matrix elicited the formation of an adhesion-like tissue in which inflammation, angiogenesis and fibrosis are identified [26–29]. Given that L-Glutamine supplementation is recommended to patients undergoing chemotherapy, and this population is prone to have simultaneous medical interventions and/or tissue damage (surgery, tissue replacement, fibrosis), the animals in this study were also treated with 5-FU. This drug is one of the most widely employed antimetabolite chemotherapeutic used as a first line antineoplastic agent in the treatment of several cancers in humans, such as colorectal, breast, head and neck, pancreas and stomach cancers [30]. The reported adverse side effects of this drug in humans and experimental animal models, includes immunosuppressive and catabolic actions that directly influence wound repair processes [31, 32]. Due to these actions, this drug has been extensively used as a pharmacological model/tool to study several types of injuries and diseases in experimental animals and *in vitro* systems [31–33]. This study is the first, to our knowledge, to investigate the effects of L-Glutamine on peritoneal fibrosis in immunosuppressed animals.

Materials and methods

Animals

In this study, male C57BL/6 mice (7–8 weeks old weighing 17–21 g, n = 25 per group) were obtained from the Animal House (Bioterio Central) of Federal University of Minas Gerais (UFMG)-Brazil. The animals in each experimental group were allocated to distinct and non-overlapping analyses, including flow cytometry (10 animals), biochemical assays and cytokines (10 animals), and histological evaluation (5 animals), according to the specific processing requirements of each tissue. The mice were housed individually, with free access to standard chow and water, and maintained at 12:12 h light/dark cycle (lights on at 7: 00 a.m.). To ensure ethical treatment, all procedures were designed to minimize animal distress and were performed in compliance with the UFMG Institutional Animal Committee guidelines (CEUA no 204/2022).

Administration of chemotherapeutic drug (5-FU)

The animals were prepared to receive intraperitoneal injections of 5-FU for 3 non-consecutive days (at the doses of 60 mg/kg, on day 1 and 40 mg/kg on days 3 and 5). These days, in the timeline of the experiment, they were denoted as day −5, −3 and −1, respectively. The doses were chosen according to the protocol established by Sonis et al., 1990 and 2004 [31, 33]. Before 5-FU administration the animals were weighed and blood samples collected for quantitative determination of leukocytes, which was used as a reference to establish leukopenia at the time of euthanasia (n = 10 for each group). An overdose of the anesthetics (10 x the anesthetic dose) was used to euthanize the animals. At the time of euthanasia (day 13 after the first dose of 5-FU) an overdose of the anesthetics (10 x the anesthetic dose), blood samples were collected to confirm leukopenia (n = 10) and body weight evaluated.

Implantation of synthetic matrix implants

Polyether-polyurethane sponges (Vitafoam Ltd., Manchester, UK) were used as the implanted material. The implants were disc-shaped (cut from a plate using a surgical punch) measuring 5 mm in thickness and 8 mm in diameter. Prior to surgery, the sponge discs were immersed in 70% v/v ethanol overnight and subsequently sterilized by boiling in distilled water for 30 min. Anesthesia was induced using a bolus of ketamine (150 mg/kg) and xylazine (10 mg/kg). The ventral hair was shaved and the exposed skin wiped with 70% v/v ethanol. The sponge discs were aseptically implanted intraperitoneally, through a 1-cm long ventral midline incision. Post-operatively, the animals were monitored for any signs of infection at the surgical site, discomfort, or distress; any animal showing such signs was promptly euthanized.

Administration of oral L-Glutamine

The treated group received L-Glutamine at a dose of 150 mg/kg/day, diluted in 100 μL of filtered water (oral

gavage) once daily for 7 consecutive days, starting the day after surgery. The dosage was selected based on previously published experimental studies in animals [31, 33]. The control group received an equal volume of filtered water (oral gavage) for the same duration. Animals were withheld from food and water for 30 min to prevent interference with substance absorption.

Histological analysis

Implants from each group of mice (n = 5) were carefully excised, dissected free of adherent tissue, and fixed in formalin (10% v/v in isotonic saline) and used for all histological analyses. Sections (5 μm) were stained with Hematoxylin and Eosin (H&E) for evaluation of the fibrovascular tissue, inflammatory cells counting and blood vessels determination. Images of 20 fields per slide of each implant were captured for data analysis with an objective lens (×40) on an optical microscope (final magnification of ×400). Dominici staining (a mast cell marker) was employed to quantify this cell population. A countable mast cell was defined as a structure with metachromasia. Images of 20 fields from histological cross-sections from each implant were captured with a panchromatic objective lens (×40) in an optical microscope (final magnification ×400).

Picrosirius-red staining was used followed by polarized light microscopy to identify and quantify collagen fibers. To carry out this analysis, images of sequential cross-sections of each implant were obtained from 20 fields, and images of histological cross-sections (area = 4,795 μm^2) of the implants were captured using a panchromatic objective lens (×40) on an Olympus BX43 light microscope (final magnification = ×400).

All the images were digitized and analyzed using Image Pro-Plus 7.0 software with a final resolution of 2,560 × 1920 pixels (Media Cybernetics Inc., USA).

Immunohistochemistry (IHC)

IHC reaction for the detection of Caspase-3 was performed using mouse anti-primary antibody Caspase-3 (1:300; #9662 Cell Signaling). Tissue sections (5 μm) were dewaxed, and a heat-induced antigen retrieval was performed using a pressure cooker with citrate buffer (pH 6), the slides were then cooled for 20 min in the same buffer. Sections were incubated for 15 min with Peroxidase Blocker from Novolink Polymer Detection Systems (Leica) and protein blocking was performed with solution from the same IHC kit. The slides were then incubated overnight at 4 °C with the primary antibody: caspase (1:300); followed by incubation with Post Primary and Polymer solutions. Peroxidase activity was visualized using DAB chromogen. The absence of staining in negative controls, where the primary antibody was omitted, confirmed specificity. Sections were then counterstained with hematoxylin. Protein expression was quantified by measuring the stained area within the implants, regardless of staining intensity. For morphometric analysis, images of stained cells from all cross-sectional fields using a ×100 planapochromatic objective (final magnification = ×1000) in light microscopy. The Caspase-3 images were digitized through an Olympus microcamera and transferred to an analyzer (QCapture). The results are presented as the number of Caspase-3 positive cells per field.

Flow cytometry analysis

Intra-implant leukocytes were quantified by flow cytometry. The following monoclonal panel of fluorescent antibodies were used: anti-CD45 (fluorochrome Pe-Cy5), anti-CD11c (fluorochromeViviD/eF450), anti-CD3 (fluorochrome PE), anti-F4/80 (fluorochrome FITC), anti-MHC-ll (fluorochrome Cy7PE), anti-GR-1 (fluorochrome APC). Ten implants from each group were evaluated. The implants were shred with scissors in 1 mL of HBSS, then 2.5 mL of filtered and sterilized type 1 collagenase (Sigma Chemicals, St Louis, MO, USA) and trypsin were added to the fragments. After incubation for 30 min at 37 °C, the cells were washed and centrifuged (500 g for 10 min at 4 °C). The cells isolated from implants were suspended in a staining buffer (0.1% BSA in PBS). Subsequently, the cells were washed with FACS buffer, flushed to surface molecules for 20 min at 4 °C. At least 50,000 blocked -events were acquired for analysis using FACSCanto-ll (BD Biosciences, San Jose, CA, USA).

The data were analyzed using FlowJo Version 9.7.5 (TreeStar, Carrum Downs, Australia). Direct dispersion (FSC-A) and lateral dispersion (SSC-A) were used to initially remove debris and capture leukocytes. Leukocytes were quantified based on CD45 expression, and then T lymphocytes were quantified based on CD45 + CD3 expression. From the $CD45^+$ cells, the expression of GR1 versus F4/80 was evaluated to select monocytes (GR1 + and GR1Low) and neutrophils (GR1 + F4/80Neg). The F4/80 High GR1Low/Neg port was used to characterize macrophages.

Determination of myeloperoxidase and N-acetyl-β-DGlucosaminidase activities

Neutrophil infiltration into the implants was assessed indirectly by analyzing MPO activity, a lysosomal hemoprotein found in the azurophilic granules in neutrophil as previously described [34, 35]. Pellets from centrifugation of implants homogenates were divided into two portions, a part of the corresponding pellet was weighed, homogenized in pH 4.7 buffer (0.1M NaCl, 0.02M $NaPO_4$, 0.015M NaEDTA), and centrifuged at 12,000 × g for 10 min. The pellets

were then resuspended in 0.05M $NaPO_4$ buffer (pH 5.4) containing 0.5% hexadecyltrimethylammonium bromide (HTAB) followed by three freeze thaw cycles using liquid nitrogen. MPO activity in the supernatant samples was assayed by measuring the change in absorbance (optical density; OD) at 450 nm using tetramethylbenzidine (1.6 mM) and H_2O_2 (0.3 mM). The reaction was terminated by adding 50 mL of H_2SO_4 (4M). Results were expressed as a change in OD per g of wet tissue. No standard curve was used; therefore, this represents a semi-quantitative measure of MPO activity. The remaining part of the pellet was used to quantify the extent of mononuclear cells accumulation in the implants by measuring the levels of the lysosomal enzyme NAG present in high levels in activated macrophages [34–36]. Briefly, these pellets were weighed, homogenized in NaCl solution (0.9% w/v) containing 0.1% v/v Triton X-100 (Promega, Madison, WI, USA), and centrifuged (3000 × g; 10 min at 4 °C). Samples (100 µL) of the resulting supernatant were incubated for 10 min with 100 µL of p-nitrophenyl-Nacetyl-β-D-glucosaminide (Sigma-Aldrich, St. Louis, MO, USA) prepared in citrate/phosphate buffer (0.1M citric acid, 0.1M Na_2HPO_4; pH 4.5) to yield a final concentration of 2.24 mmol. The reaction was stopped by the addition of 100 µL of 0.2-M glycine buffer (pH 10.6). Hydrolysis of the substrate was determined by measuring the absorption at 400 nm. Results are expressed as nmol per g of wet tissue.

Measurement of TNF-α, VEGF and TGF-β1 production

In the remaining supernatants of the implants used for inflammatory enzymes, production of the cytokines were evaluated (n = 10). They were homogenized in PBS pH 7.4 containing 0.05% Tween, and centrifuged at 10,000 x g for 30 min. The levels of the cytokines in the supernatant from each implant (50 µL) were measured using Immunoassay Kits (R and D Systems, USA) and following the manufacturer's protocol to each cytokine. Briefly, dilutions of cell-free supernatants were added in duplicate to ELISA plates coated with a specific murine monoclonal antibody against cytokine, followed by the addition of a second horseradish peroxidase-conjugated polyclonal antibody, also against cytokine.

After washing to remove any unbound antibody-enzyme reagent, a substrate solution (50 µL of a 1:1 solution of hydrogen peroxide and tetramethylbenzidine 10 mg/mL in DMSO) was added to the wells. Color development was halted after 20 min incubation with 2M sulfuric acid (50 µL), and the intensity of the color was measured at 540 nm on a spectrophotometer (Thermoplate). Standards were 0.5-log10 dilutions of recombinant murine cytokines from 7.5 ρg mL^{-1} to 1000 ρg mL^{-1} (100 µL). The threshold of sensitivity for each chemokine is 15.625 ρg/mL. The results were expressed as ρg cytokine per mg wet tissue.

Statistical analysis

All data are presented as mean ± SEM for normally distributed variables. The normality of the data was assessed using the Shapiro–Wilk test, and homogeneity of variances was evaluated with Levene's test. When the assumptions of normality and homoscedasticity were met, parametric tests were applied (Student's *t*-test for comparisons between two groups, two-way ANOVA followed by appropriate post-hoc tests for multiple groups). Data are presented as mean ± SEM, and $p < 0.05$ was considered statistically significant. Outliers were identified and excluded using the ROUT method (Q = 1%) through the "Identify Outliers" function in GraphPad Prism 8.2.1 (GraphPad Software, San Diego, CA, USA).

Results

The protocol used to induce immunosuppression (3 doses of 5-FU) resulted in a decrease in the number of leukocytes, p = 0.014 (n = 10). The initial counting in the blood samples, before 5-FU, was 4,209 ± 506 leukocytes. On day 8 post implantation, when the animals were euthanized, the leukocyte number was 2,388 ± 265 (Figure 1a). In relation to body weight (Figure 1b), there was a significant difference between the animal's weight of the two groups. The control group lost more weight compared with the treated group (p = 0.014 days 4 and p = 0.098 days 8) (n = 10). Oral administration of L-Glutamine (150 mg/kg/day) did not show signs of toxicity, dietary restrictions or changes in the animals' motor activity. The synthetic matrix was well tolerated by all animals. No signs of infection or rejection were observed at the implant site during the period of the experiment.

Histopathological analysis - macro and microscopic evaluation of the implant

In situ images of the implants showed that they were firmly fixed in abdominal organs, liver and intestines. In the macroscopic analysis, the implants in the control group apparently showed a greater quantity of red blood cells, visibly evidenced by the color of the implants (Figures 2a–c). Histological analysis (H&E staining) was employed to evaluate the fibroproliferative tissue formed within and around the synthetic matrix. In both groups (control and treated), it was observed that the newly formed tissue was composed of inflammatory cells, blood vessels, extracellular matrix and an eosinophilic transudate (Figures 3a,b). However, in the control group the number of these features was higher. The mean number of inflammatory cells per field (n = 5) in the control group was 322 ± 11 versus 186 ± 23, p = 0.029 in the treated group (Figure 3c).

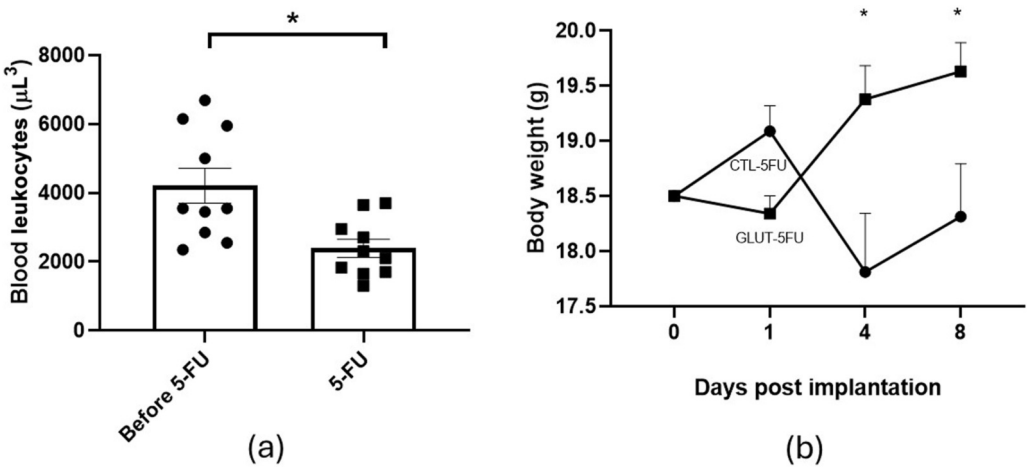

FIGURE 1
Effects of 5-FU on blood leukocytes number and body weight. Administration of the chemotherapeutic agent caused a decrease in blood leukocytes (48.8%) compared with the samples before 5-FU administration **(a)**. There was a progressive weight gain in the L-Glutamine treated group compared with a loss in body weight was observed in the control group **(b)**. Values are means ± SEM of 10 animals in each group. *p < 0.05. Body weight over time and between groups was analyzed by two-way ANOVA, while paired leukocyte counts before and after treatment were analyzed by paired Student's t-test.

Flow cytometry analysis

Using flow cytometry, we were able to analyze specific populations of inflammatory cells in the fibrovascular tissue. Our results showed that L-Glutamine was effective in reducing the overall frequency of $CD45^+$ cells (40.87%; p = 0.031). However, when immune cell subsets were analyzed as relative frequencies with the $CD45^+$ population, L-Glutamine group exhibited higher proportions of neutrophils (3-fold; p = 0.046; n = 7–9), macrophages by (3-fold; p = 0.032; n 7-9, and lymphocytes by (5-fold; p = 0.014; n = 7–9), than control group (Figures 4a–e).

Immunohistochemistry for Caspase-3

The number of Caspase-3 positive cells (marked in brown) was higher in the control group 6.5 ± 0.9 compared with the treated group 4.0 ± 0.5, p = 0.044 (n = 5 for both groups). This indicates that L-Glutamine supplementation exerted an anti-apoptotic effect in our adhesion model (Figures 5a–c).

Measurement of MPO, NAG, TNF-alpha and mast cells

Further analysis of the inflammatory components of implant-induced fibrovascular tissue were determined by evaluating MPO and NAG activities, and TNF-alpha levels (Figures 6a–c). In addition, the number of mast cells was quantified (Figures 6d–f). L-Glutamine was able to attenuate all the parameters evaluated. The values for MPO were 3.6 ± 0.42 in control versus 1.5 ± 0.42 (O.D/g wet tissue) in the treated group p = 0.010 (n = 9), and NAG values were 1.2 ± 0.16 control versus 0.5 ± 0.15 (nmol/g wet tissue) in L-Glutamine group, p = 0.009 (n = 9). Furthermore, the treatment lowered TNF-α production (pg/mg tissue) in the treatment group (control 3.4 ± 0.47 versus 1.6 ± 0.6; p = 0.025 (n = 9). The number of mast cells/slide was also lower in the treated group, 104 ± 16.5 (n = 5) versus 203 ± 37.0 in the control group, p = 0.041.

Evaluation of angiogenesis

The supplementation was able to reduce the angiogenic markers evaluated (number of blood vessels, VEGF levels). Histological analysis (H&E) showed that in implants of control animals the number of newly formed vessels was 11 ± 0.5/field (n = 5) versus 7 ± 0.3/field in the treated group (p = 0.0001). VEGF levels were significantly lower in the L-Glutamine-treated group (1.9 ± 0.43 pg/mg, n = 9) compared to the control group (4.9 ± 0.7 pg/mg, n = 9) p = 0.003 (Figures 7a–d).

Analysis of fibrogenic markers

L-Glutamine supplementation was able to attenuate the fibrogenic parameters analyzed (collagen deposition and TGF-

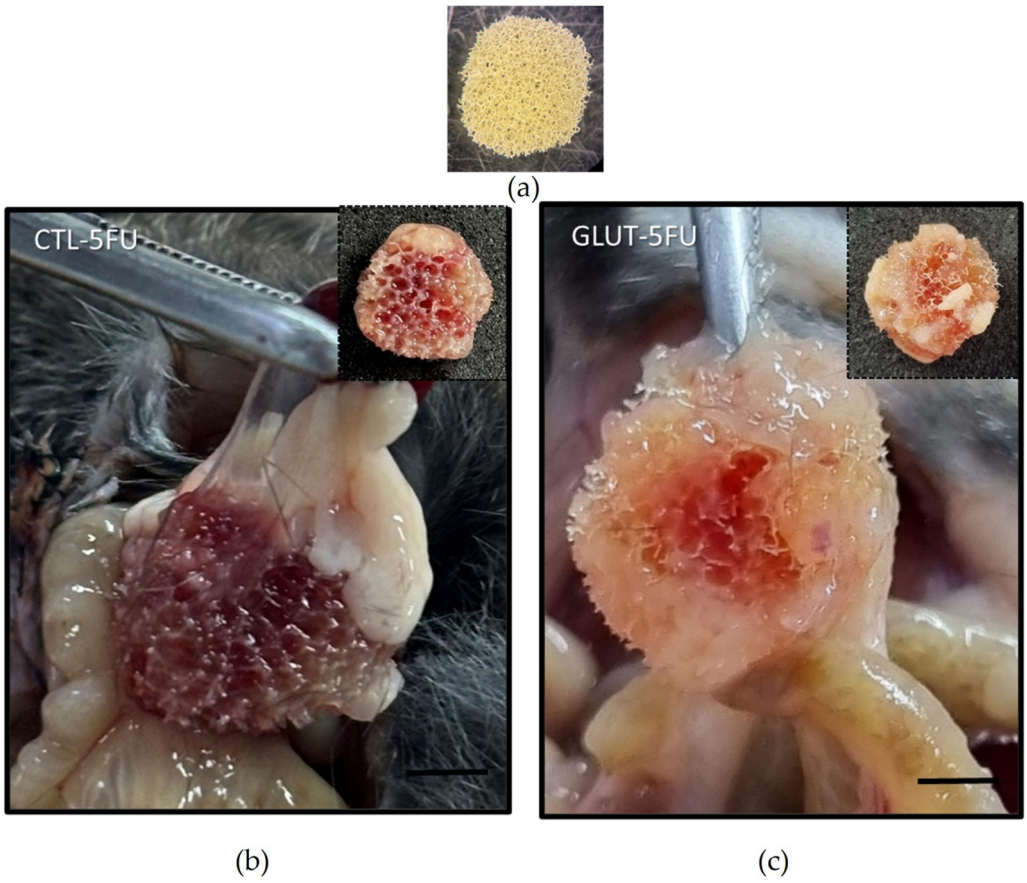

FIGURE 2
In situ images of polyether–polyurethane intraperitoneal implants. Image of the sponge disc before implantation **(a)**. Representative images of implants adhered to intestines through a band of fibrous tissue and removed from the peritoneal cavity at day 8 (Control **(b)**; Treated **(c)**). Scale bar, 50 μm.

β levels). Interestingly, collagen type III (greenish color) was predominant in the treated group. In this group, the fibers had a more fragmented appearance with greater spacing among the fibers compared with the control group (Figures 8a–c). Less total collagen area (Picrosirius red staining) in the treated group was observed 12.10 ± 3.54 versus 26.72 ± 2.35 μm^2 in the control group $p = 0.009$ ($n = 5$) (Figure 8c). The L-Glutamine was effective in reducing the levels of the pro-fibrogenic cytokine TGF-β (control 4.6 ± 0.5 pg/mg) versus 2.8 ± 0.9 in the treated group, $p = 0.0156$ ($n = 9$) (Figure 8d).

Discussion

Peritoneal adhesions, adverse healing processes, are serious medical conditions and major challenges for the health system [1–3]. Although several surgical and pharmacological interventions have been able to attenuate the burden of this condition, none seems to prevent/treat this pathological condition completely. Thus, the search for new therapeutic approaches is warranted [8, 9].

Physiologically, L-Glutamine is directly involved in immunological cell division, acid-base balance, transport of ammonia between tissues, donation of carbon skeletons for gluconeogenesis and participates in processes of recovery from physiological stress and/or catabolic events [10, 14, 37]. It has been reported that this amino acid exerted both anti- and pro-inflammatory, angiogenic and fibrogenic effects on several damaged/injured tissues, thus improving the quality of remodeling in randomized clinical studies [37, 38]. In clinical conditions with high metabolic demand and immunosuppression, such as chemotherapy treatments, burn and critical patients, the body needs a large amount of this amino acid, but its availability is limited. Thus, oral or enteral supplementation of L-Glutamine through diet has been recommended, turning it into a potential therapeutic agent [38–40]. Our objective was to investigate whether this amino acid supplementation would modulate the healing process after

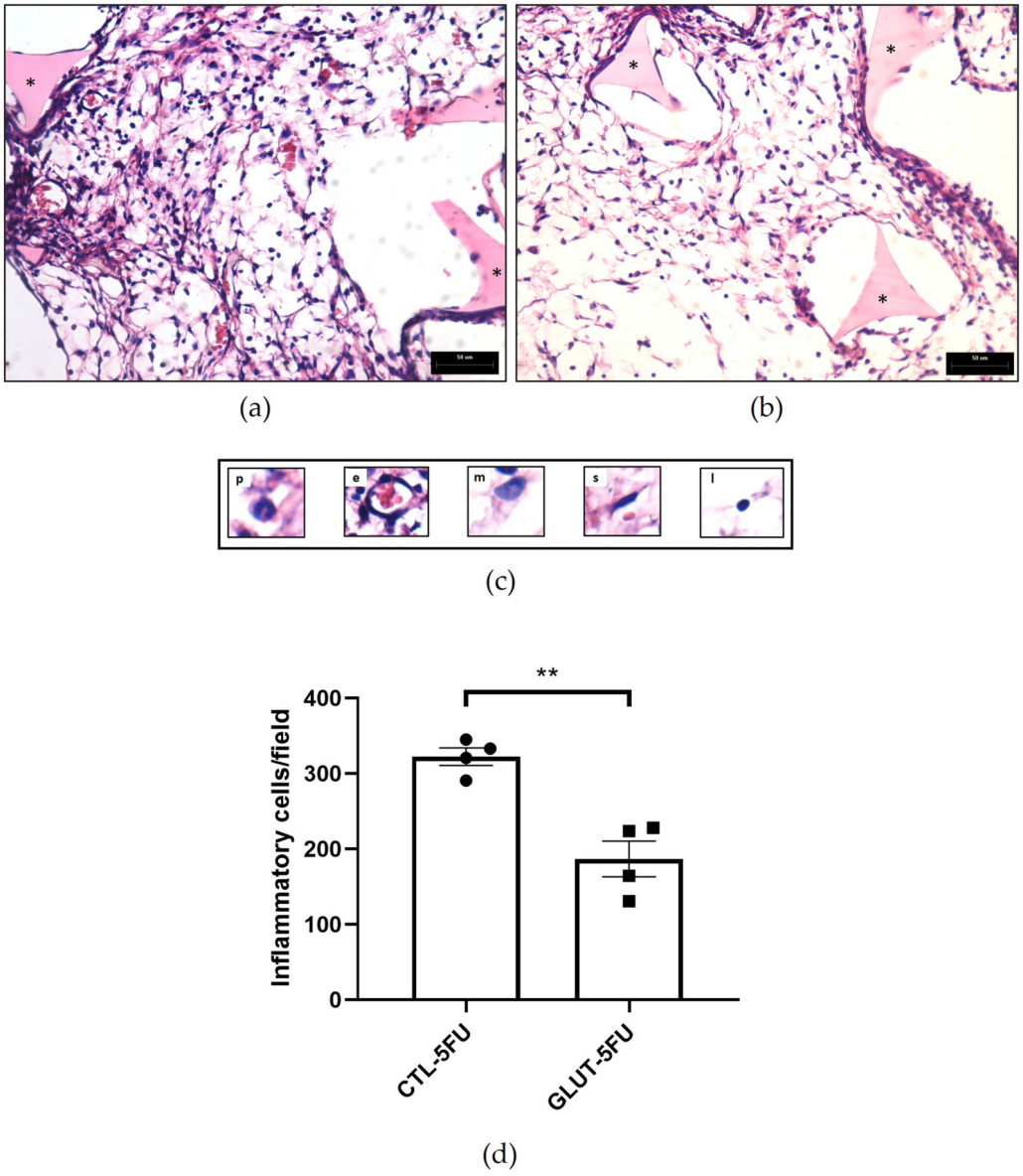

FIGURE 3
Representative histological sections of intraperitoneal implants stained with Haematoxylin and Eosin (H&E). In the fibrovascular tissue a greater number of cells and vessels are seen in implants of control mice compared with the implants of treated animals (control **(a)**; treated **(b)**). Different cell types were identified morphologically: polymorphonuclear cells (p), endothelial cells (e), mononuclear cells (m), spindle cells (s) and lymphocytes (l). The number of cells in control is higher than in the treated group **(c)**. Inflammatory cells **(d)** counting (n=5) were lower in the implants after the treatment. *Sponge matrix, arrows; blood vessels. Values are means ± SEM of five animals in each group. **p < 0.001, Student unpaired t-test. Planapochromatic objective (×40) in light microscopy (final magnification = ×400). Scale bar, 50 μm.

peritoneal injury in immunosuppressed mice. The effects of L-Glutamine supplementation were evaluated on mice submitted to chemotherapy (5-FU) and surgical implantation of polyether polyurethane matrix in the abdominal cavity, simultaneously. Both approaches are likely to reflect the clinical scenario of cancer patients that undergo peritoneal surgery with consequent adverse healing. The experimental procedures inflict local and systemic tissue damage requiring further energy supply to comply with the metabolic demand. As reported in previous publications, implantation of the matrix elicited formation of peritoneal fibrosis in which inflammation, angiogenesis and fibrosis were identified [25–28]. The use of 5-FU in our study, based on the work by [31, 33], resulted in a fall of leukocytes (48%), confirming the immunosuppressive effect of

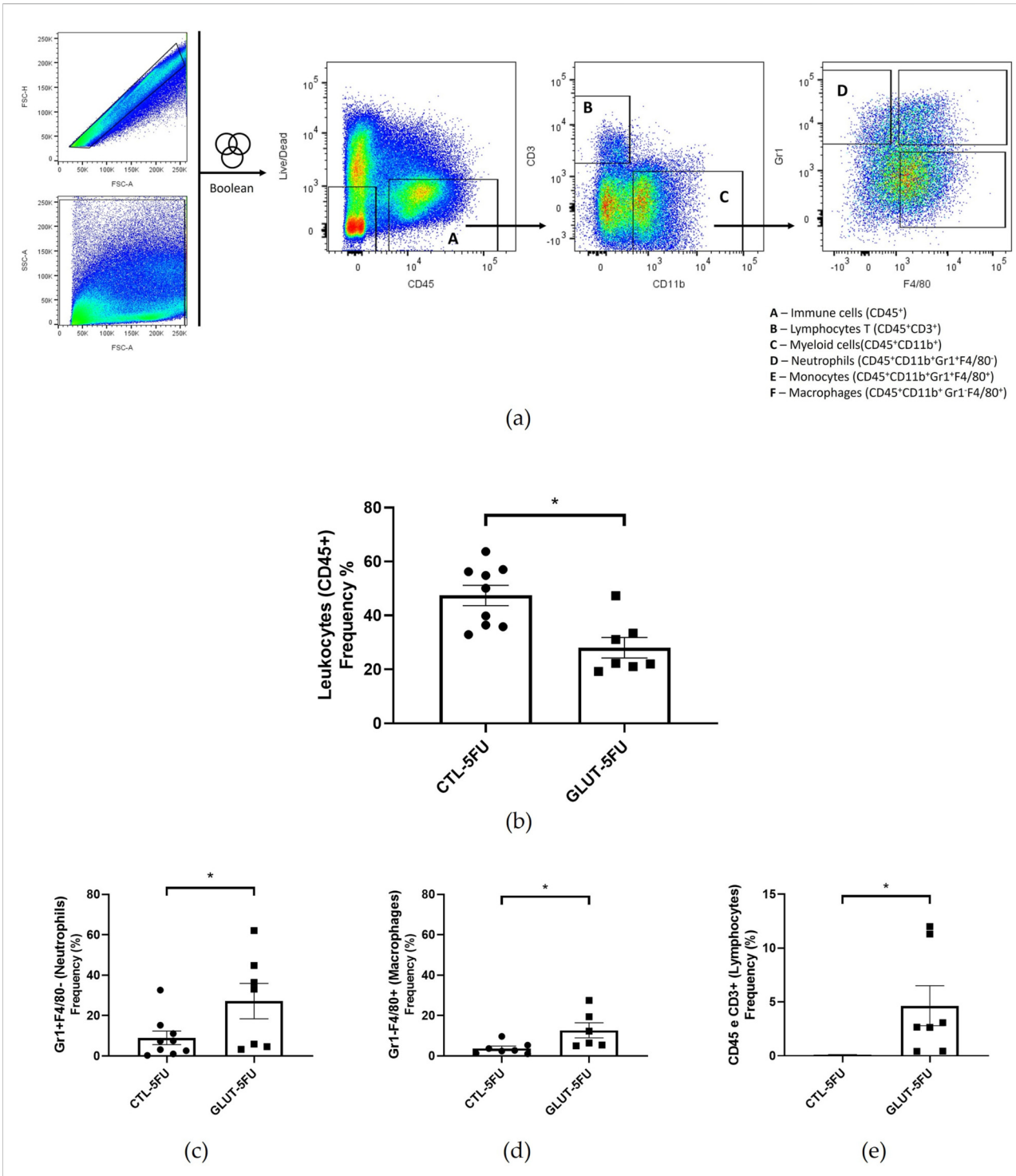

FIGURE 4
Effects of L-Glutamine on the recruitment of different cell types intra-implant (flow cytometry). Represented in **(a)** is the strategy of analysis in dot plots identifying the infiltration of neutrophils, macrophages and T lymphocytes, inside the implant. In **(b)**, the frequency of total immune cells and **(c–e)** the total count of neutrophils, macrophages and lymphocytes were compared in both groups, and the results are expressed as the mean ± SEM. *p < 0.05; Student's unpaired t-test, n = 7-9 animals per group.

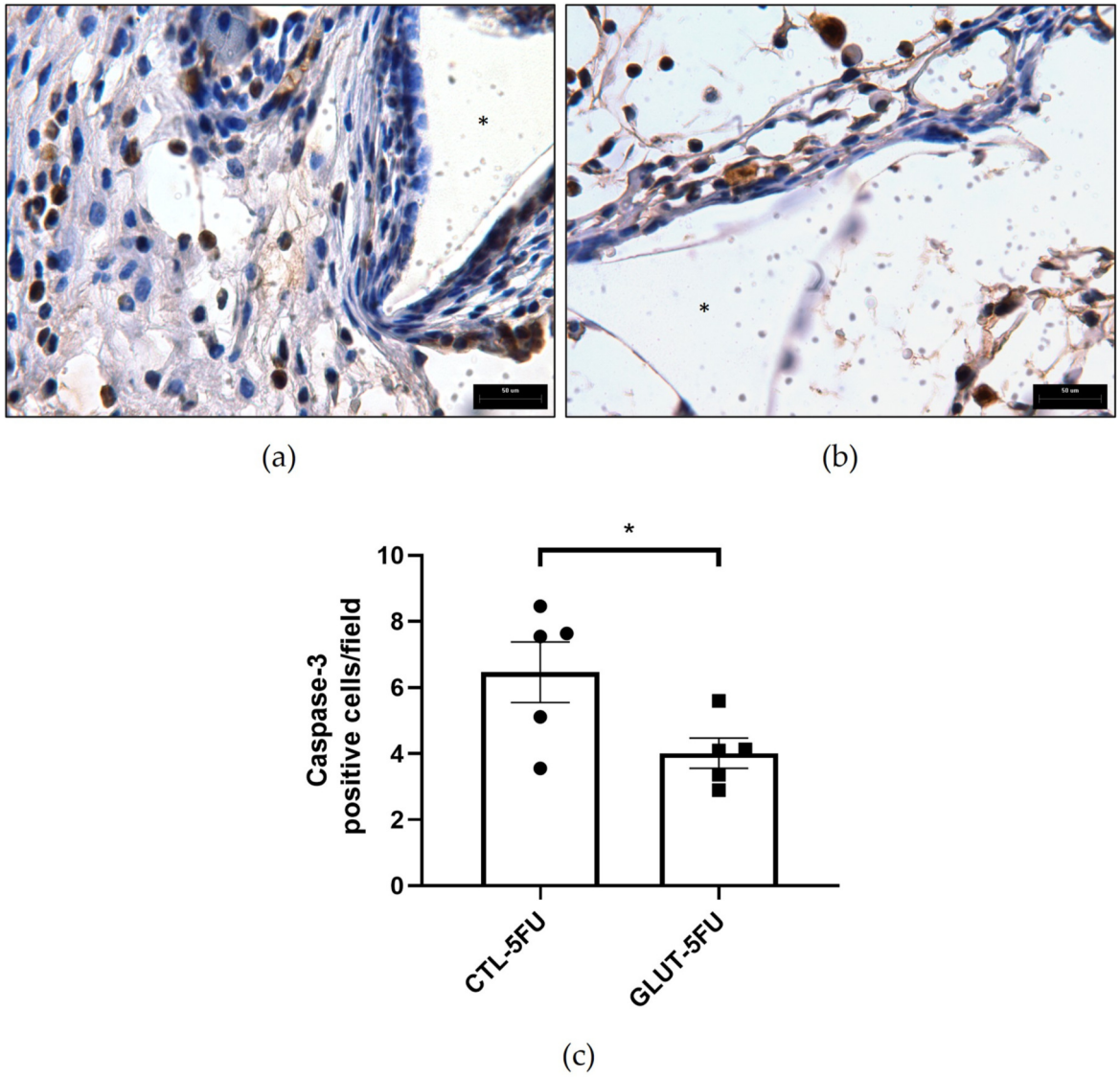

FIGURE 5
Effect of L-Glutamine on the apoptotic marker. Representative micrographs of intraperitoneal implants (**(a)**, control; **(b)**, treated) immunostained with Caspase-3. More positive cells were observed in the control implant compared with the treated **(c)**. Values are means ± SEM; *$p < 0.05$, Student's unpaired t-test, n = 5. Planapochromatic objective (×100) in light microscopy (final magnification = ×1000). Scale bar, 50 μm.

the chemotherapeutic agent observed in both humans and experimental animals. It was interesting to observe a progressive body weight gain in the L-Glutamine treated animals whereas body weight loss was seen in the control group, during the time of the experiments. These findings confirm the beneficial effects of L-Glutamine supplementation on systemic metabolism and body weight control [41].

There were also striking differences between the two groups regarding the formation of peritoneal adhesion-like tissue. Visually, the amount of red blood cells was less in the treated group as indicated by the color of the implants (macro analysis). Histological analysis of the implants revealed that the newly formed peritoneal fibrovascular tissue that formed in and around the implants, during the time period examined (8 days), was composed of inflammatory cells, blood vessels, and extracellular matrix proteins. This observation confirms our previous reports that described this model of intra-peritoneal adhesion based on the implantation of polyether-polyurethane sponge matrix [26–29]. However, the number of total cells was less in implants of the animals supplemented with L-Glutamine. These data were corroborated by flow cytometry that demonstrated a marked reduction in the overall frequency of

10.3389/ebm.2026.10755

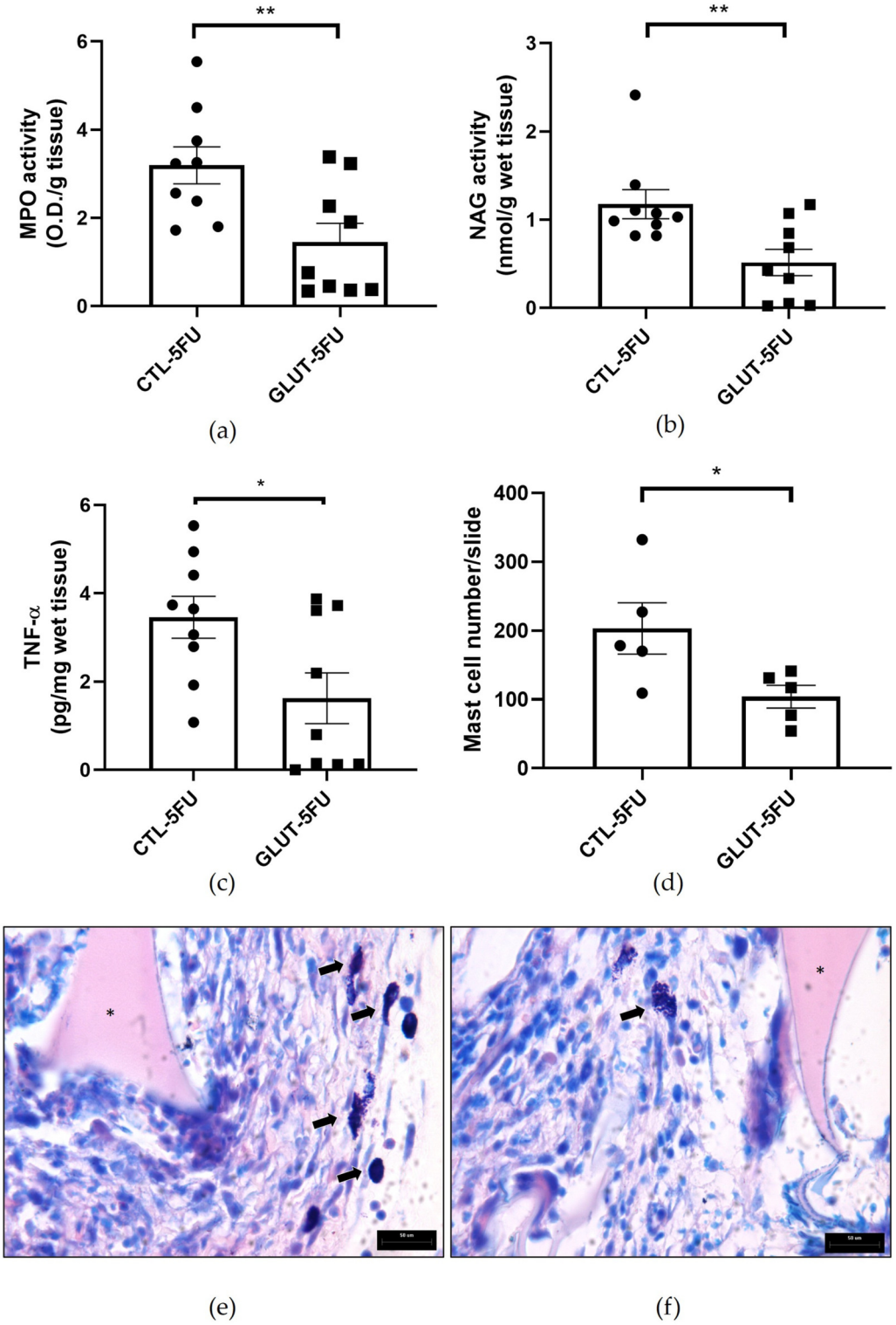

FIGURE 6
Effects of L-Glutamine on inflammatory markers. The production of all inflammatory markers myeloperoxidase- MPO **(a)**; N-acetyl-β-d-glucosaminidase-NAG **(b)**; tumor necrosis factor alpha- TNF-α **(c)** (n = 9); and Mast cells **(d)** counting (n = 5) were lower in the implants after the treatment. Representative photomicrograph of histological sections of the implants control **(e)** versus treated **(f)** stained with Dominici. Values are means ± SEM; *p < 0.05, **p < 0.001, Student's unpaired t-test. Planapochromatic objective (×100) in light microscopy (final magnification = ×1000). Scale bar, 50 μm.

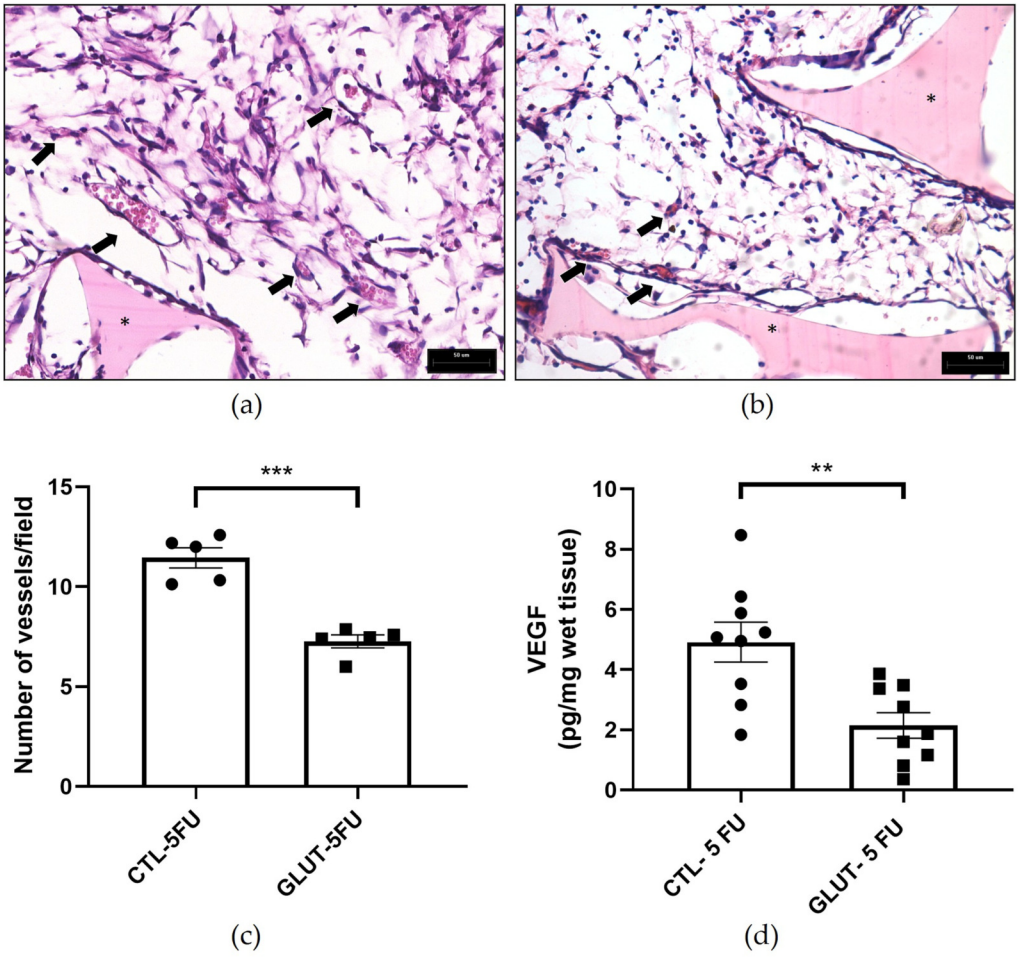

FIGURE 7
Effects of L-Glutamine on angiogenesis. Photomicrographs of the sponge implant stained with H&E are shown; (**(a)**, control and **(b)**, treated); magnification. Figure 6 **(c,d)** shows the number of blood vessels (n = 5 animals) and VEGF levels (n = 9 animals), respectively. Arrows: intra-implant vessels. The results are expressed as means ± SEM. **p < 0.001, ***p < 0.0001; Student unpaired t test. Planapochromatic objective (×40) in light microscopy (final magnification = ×400), Scale bar, 50 μm.

CD45 cells, a 48% reduction in the implants of the treated group. It was interesting that in the remaining leukocyte population in this group, neutrophils, lymphocytes and macrophages represented a higher relative proportion compared with the control group. It has been demonstrated that L-Glutamine exerts anti-apoptotic activity in small intestine injury [42]. This effect may have occurred in our experiments. The number of Caspase-3 positive cells in the control group was higher than in the treated group indicating an anti-apoptotic effect L-Glutamine which may have contributed to the increased number of the inflammatory cell populations in the treated group. The other factor that may have favored the increased number of these cells in the implant of the treated group was availability of amino acid. *In vitro* studies showed that glutamine potentiates the activity of inflammatory cells, promoting activation and function of neutrophils and macrophages and proliferation and differentiation of lymphocytes [43–47]. The other inflammatory parameters analyzed MPO and NAG activities, TNF-alpha levels and mast cell number were decreased in the implants after L-Glutamine supplementation. These soluble and cellular markers are relevant components of the inflammatory response to a number of stimuli, including implantation techniques [26, 27, 29]. Thus, this amino acid favored the anti-inflammatory phenotype observed in our model. The apparent discrepancy between the presence of higher neutrophil/macrophage/lymphocyte infiltration in the peritoneal fibrotic tissue and reduced MPO, NAG, and TNF-α production may suggest immune reprogramming. It has been reported that glutamine shifts polarized inflammatory cells, particularly macrophages and neutrophils, towards their phenotypes and functions [48, 49]. Our results are in line with several reports that demonstrated the anti-inflammatory

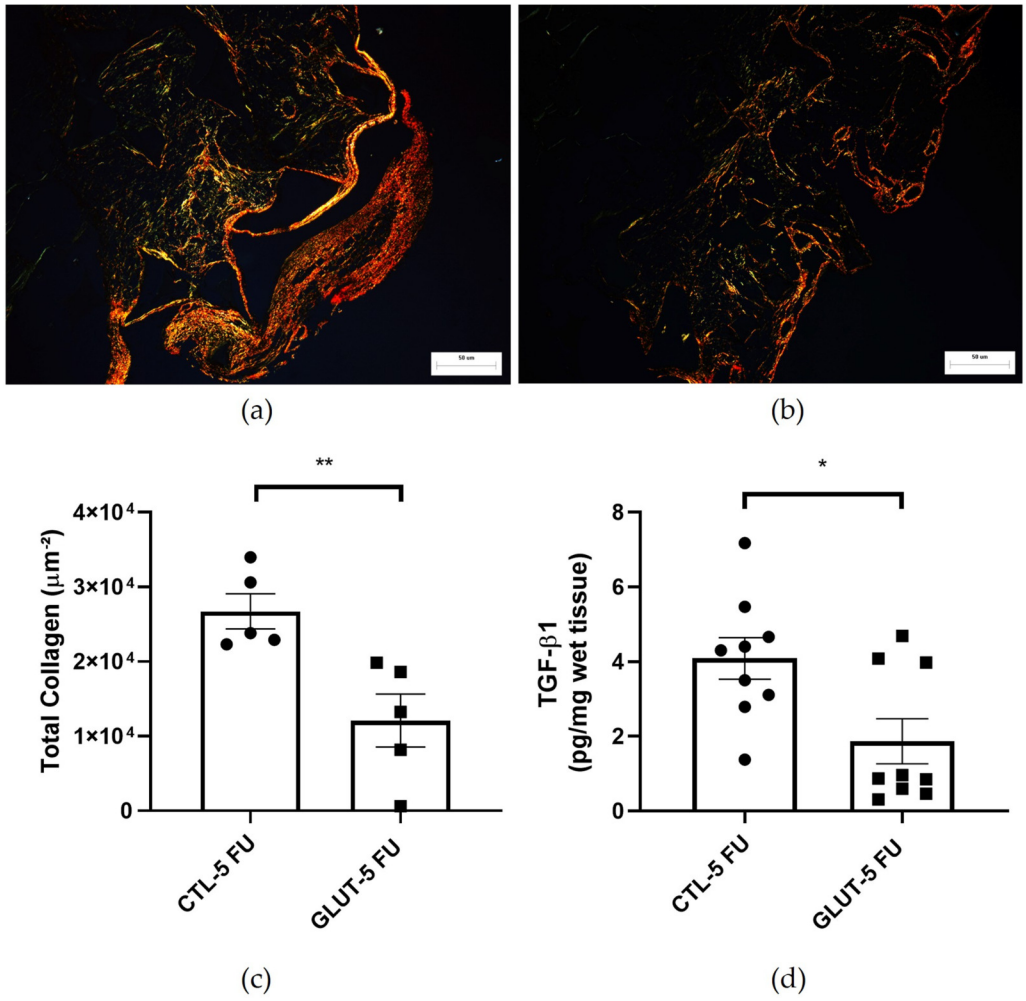

FIGURE 8
Effects of L-Glutamine on collagen fiber deposition. Representative photomicrographs of intra-implant collagen fibers visualized by Picrosirius red staining showing the control **(a)** and the L-Glutamine-treated **(b)** n = 5 animals. There was a significant reduction in the area of collagen fibers between the groups **(c)**. TGF-β1 levels were lower in the L-Glutamine treated group relative to the control group **(d)** n = 9 animals. Results are expressed as mean ± SEM. *p < 0.05, **p < 0.01, Student's unpaired t-test. Planapochromatic objective (×20) in light microscopy (final magnification = ×200). Scale bar = 50 µm.

effects of L-Glutamine supplementation *in vitro* and *in vivo* systems [16, 17, 50, 51].

However, it has been reported that inhibition of L-Glutamine metabolism by an analogue, 6-diazo-5-oxo-L-norleucine, and not its supplementation, accelerated the resolution and repair of acute lung injury induced by intratracheal lipopolysaccharide (LPS) instillation [18].

Furthermore, while L-Glutamine can enhance glutathione production and attenuate oxidative stress, thereby reducing inflammation, it can also serve as a fuel source for rapidly proliferating immune cells, potentially exacerbating inflammatory responses in critical systemic conditions [11, 13, 37]. These seemingly contradictory results are likely to depend on various factors such as, type of injury, phase of the injury, experimental model used. Further investigation will be necessary to establish mechanisms by which L-Glutamine exerted its anti-inflammatory effects on our model.

The anti-inflammatory effects of L-Glutamine supplementation observed in the peritoneal fibrotic tissue occurred in immunodepressed animals. It is well established that early inflammation is essential for tissue clearance and repair initiation and that excessive immune suppression could potentially impair healing. However, the fact that various inflammatory cells (neutrophils, macrophages and lymphocytes) were in higher frequency in the treated group, suggest that L-Glutamine promoted immune reprogramming. Activation and function of these cell populations towards a pro-repair phenotype in immunosuppressed state. Exogenous

glutamine has been shown to augment the functions of neutrophils, lymphocytes and macrophages in a rat peritonitis model [52]. Thus, the treatment appeared to have promoted a more balanced immune response, facilitating inflammatory cells reprogramming toward a pro-repair phenotype and supporting physiological tissue remodeling.

Another component of the peritoneal adhesion-like tissue evaluated was angiogenesis. L-Glutamine supplementation was able to decrease the number of blood vessels, and levels of VEGF (key pro-angiogenic molecule). Because in our model, blood vessel formation and inflammation are co-existing processes and L-Glutamine attenuated the latter, down regulation of angiogenesis was expected to occur. Whether this effect was a direct action of L-Glutamine or a consequence of decreased inflammatory process in the implants remains to be determined.

It is clear from the literature that glutamine metabolism is a key factor in angiogenesis. However, its effects on this process are far from clear cut. For instance, pharmacological blockade of glutamine metabolism has been shown to reduce pathological and developmental angiogenesis *in vivo* and endothelial sprouting *in vitro* indicating that endothelial cells depend on extracellular glutamine for proliferation and viability [18, 19]. Our finding showed that rather than stimulating the angiogenic parameters analyzed, L-Glutamine promoted inhibition of VEGF levels and blood vessels number. This discrepant result may be attributed to the type of angiogenesis models used. It is also relevant to consider that the immunosuppression caused by 5-FU may have altered the pattern of glutamine metabolism in our model. However, given that we only studied inflammatory angiogenesis, analysis of angiogenesis in other experimental models is warranted in the future.

Fibroblast activation, proliferation and the products of its activities are essential phases of physiological wound healing, but it is also a process involved in progression of pathological healing and tissue fibrosis. The fibrogenic component of the peritoneal fibrovascular tissue was evaluated through TGF-β production and total collagen (Picrosirious red staining). These markers were reduced by L-Glutamine treatment indicating the anti fibrogenic activity of the amino acid. Picrosirius polarization method is simple, sensitive and specific for collagen staining, particularly useful to reveal the molecular order, organization and/or heterogeneity of collagen fiber orientation in different connective tissues [53]. However, it is not sensitive enough to differentiate collagens subtypes. Thus, further investigation using specific antibodies or molecular markers for collagens types may reveal whether L-Glutamine supplementation modulated the deposition of distinct types of collagen in peritoneal fibrosis. Glutamine has been shown to either up or down regulate fibrosis in several pathological conditions. For instance, the use of L-Glutamine enema reduced inflammation and fibrosis in experimental diversion colitis in Wistar rats [23]. Furthermore, oral administration of glutamine promoted faster skin healing by acting on several stages of healing, such as collagen synthesis, wound contraction and epithelialization, in excision wound model [23]. Several studies, however, have evidenced pro-fibrotic effects of L-Glutamine. One such study revealed that patients with severe fibrosis exhibit elevated serum glutamine levels and increased expression of kidney glutamine synthetase. Deprivation of glutamine metabolism *in vitro* and *in vivo* inhibits fibroblast activation, ameliorating renal fibrosis [21]. Furthermore, inhibition of glutamine metabolism could suppress the activation of hepatic stellate cells attenuating liver fibrosis [25]. It has also been demonstrated that glutamine and its conversion to glutamate by glutaminase are required for TGF-β–induced collagen protein production in lung fibroblasts [54]. A number of factors may explain the divergent and opposing effects of L-Glutamine on fibrosis. One possibility is that in our study, the animals were immunosuppressed, therefore, the cells involved in the fibrogenic response were not under normal physiological state. It is possible that the diversity of tissues, models and experimental protocols used to evaluate the effects of L-Glutamine on fibrosis has contributed to the distinct responses reported.

In our study, using a range of histological and biochemical markers, we demonstrated the efficacy of L-Glutamine supplementation attenuating key components (inflammation, blood vessel formation and collagen deposition) of implant-induced peritoneal fibrosis in 5-FU-treated mice. Glutamine actions in regulating the peritoneal fibrovascular tissue growth is likely to have occurred through activation/inhibition/regulation of a range of molecular signaling pathways. In inflammatory processes, for instance, L-Glutamine has been shown to induce MAPK phosphatase, to inhibit NF-kB and to regulate TGF-B1/SMAD2/3 pathways [17, 50, 55]. In several angiogenic assays, glutamine has been shown to act through mTOR and EGFR/ERK signaling pathways [56]. Potential signaling pathways activated by glutamine such as TGF-β/Smad or mTOR/MTFP1/DRP1 are involved in fibroblast activation in fibrotic diseases [21]. However, we do not provide direct evidence of glutamine actions in our model through these pathways which constitutes a limitation of this study. Certainly, identification of signaling pathways and their specific roles mediating glutamine actions will be necessary for developing glutamine-based therapies in peritoneal fibrosis in immunosuppression conditions.

Another limitation of this study was the fact that we did not include a healthy control group (non-5-FU). This would be relevant to examine the effects of L-Glutamine on fibroproliferative processes in norm-immune animals to rule out the systemic effect of 5-FU on peritoneal fibrosis. However, our main focus was to examine specifically the potential therapeutic effect of L-Glutamine during antineoplastic treatment. In the course of chemotherapy, very often humans and/or animals endures simultaneous tissue damage such as surgeries, tissue replacement, and inflammatory processes. Thus, by inflicting two challenging

conditions (immunosuppression and fibrosis) to the animals and examining their systemic and local response to L-Glutamine supplementation, our results clearly show that the supplementation acted systemically by improving body weight (metabolic parameter) and locally by down regulating inflammation, angiogenesis and fibrosis in peritoneal healing tissue in immunosuppressed mice. Thus, our study design was effective in demonstrating, for the first time, the beneficial effects of L-Glutamine on attenuating peritoneal fibrosis in immunosuppressed conditions.

Altogether, our results and published reports highlight the importance of L-Glutamine metabolism on fibrovascular tissue remodeling and the need for further investigation to understand the role of this amino acid in physiological and pathological wound healing.

Conclusion

In our study, the presence of polyether–polyurethane implants in the peritoneal cavity resulted in the formation of an adhesion-like tissue in mice treated with 5-FU. Oral supplementation of L-Glutamine was able to differentially modulate inflammatory cells of the myeloid lineage towards a predominant anti-inflammatory, anti-angiogenic and anti-fibrogenic phenotype of the peritoneal fibrovascular tissue. These findings suggest that L-Glutamine holds promise for translation into clinical trials as a potential adjuvant therapy in the management of peritoneal fibrosis in immunosuppressed states.

Author contributions

JH, PC and SA participated in the design, interpretation of the studies and analysis of the data and review of the manuscript; JH, LS, IF, MS, LC, NS, PP and PG conducted the experiments, PC, JH, DG, and SA wrote the manuscript, PC funding acquisition. All authors contributed to the article and approved the submitted version.

Funding

The author(s) declared that financial support was received for this work and/or its publication. This work was supported by the Minas Gerais Research Support Foundation (FAPEMIG RED-00570-16, RED-00213-23) and Benjamin Guimarães Foundation, Teaching and Research Center at Hospital of Baleia, Minas Gerais, Brazil. The funders had no role in the design of the study; in the collection, analyses, or interpretation of data; in the writing of the manuscript; or in the decision to publish the results.

Data availability

The original contributions presented in the study are included in the article/Supplementary Material, further inquiries can be directed to the corresponding author.

Ethics statement

The animal study was approved by Biological Institute of Biological Science Institutional Animal Welfare Committee (process number: CEUA no 204/2022). The study was conducted in accordance with the local legislation and institutional requirements.

Acknowledgements

The authors would like to thank Fundação de Amparo à Pesquisa do Estado de Minas Gerais - Support Foundation of the State of Minas Gerais (FAPEMIG-MG/Brazil), Coordenação de Aperfeiçoamento de Pessoal de Nível Superior (CAPES – Coordination for the Improvement of Higher Education Personnel), and Conselho Nacional de Desenvolvimento Científico e Tecnológico - National Council for Scientific and Technological Development (CNPq-Brazil) for supporting this study through scholarships.

Conflict of interest

The author(s) declared no potential conflicts of interest with respect to the research, authorship, and/or publication of this article.

Generative AI statement

The author(s) declared that generative AI was not used in the creation of this manuscript.

Any alternative text (alt text) provided alongside figures in this article has been generated by Frontiers with the support of artificial intelligence and reasonable efforts have been made to ensure accuracy, including review by the authors wherever possible. If you identify any issues, please contact us.

Supplementary material

The Supplementary Material for this article can be found online at: https://www.ebm-journal.org/articles/10.3389/ebm.2026.10755/full#supplementary-material

References

1. Chegini N. Peritoneal molecular environment, adhesion formation and clinical implication. *Front Biosci* (2002) **7**:e91–115. doi:10.2741/A911

2. Capella-Monsonís H, Kearns S, Kelly J, Zeugolis DI. Battling adhesions: from understanding to prevention. *BMC Biomed Eng* (2019) **1**:5. doi:10.1186/s42490-019-0005-0

3. Herrick SE, Wilm B. Post-surgical peritoneal scarring and key molecular mechanisms. *Biomolecules* (2021) **11**(5):692. doi:10.3390/biom11050692

4. Cheong YC, Laird SM, Li TC, Shelton JB, Ledger WL, Cooke ID. Peritoneal healing and adhesion formation/reformation. *Hum Reprod Update* (2001) **7**(6): 556–66. doi:10.1093/humupd/7.6.556

5. Ozel H, Avsar FM, Topaloglu S, Sahin M. Induction and assessment methods used in experimental adhesion studies. *Wound Repair Regen* (2005) **13**(4):358–64. doi:10.1111/j.1067-1927.2005.130402.x

6. Hellebrekers BWJ, Kooistra T. Pathogenesis of postoperative adhesion formation. *Br J Surg* (2011) **98**(11):1503–16. doi:10.1002/bjs.7657

7. Tsai JM, Shoham M, Fernhoff NB, George BM, Marjon KD, McCracken MN, et al. Neutrophil and monocyte kinetics play critical roles in mouse peritoneal adhesion formation. *Blood Adv* (2019) **3**(18):2713–21. doi:10.1182/bloodadvances.2018024026

8. van Steensel S, van den Hil LCL, Schreinemacher MHF, Ten Broek RPG, van Goor H, Bouvy ND. Adhesion awareness in 2016: an update of the national survey of surgeons. *PLoS One* (2018) **13**(8):e0202418. doi:10.1371/journal.pone.0202418

9. Fatehi HA, Zarzycki AN, Jeon K, Dundas JA, Vasanthan V, Deniset JF, et al. Prevention of post-operative adhesions: a comprehensive review of present and emerging strategies. *Biomolecules* (2021) **11**(7):1027. doi:10.3390/biom11071027

10. Tanaka Y, Takeuchi H, Nakashima Y, Nagano H, Ueno T, Tomizuka K, et al. Effects of an elemental diet to reduce adverse events in patients with esophageal cancer receiving docetaxel/cisplatin/5-fluorouracil: a phase III randomized controlled trial-EPOC 2 (JFMC49-1601-C5). *ESMO Open* (2021) **6**(5):100277. doi:10.1016/j.esmoop.2021.100277

11. Newsholme P, Procopio J, Lima MMR, Pithon-Curi TC, Curi R. Glutamine and glutamate—their central role in cell metabolism and function. *Cell Biochem Funct* (2003) **21**(1):1–9. doi:10.1002/cbf.1003

12. Rogero MM, Tirapegui J, Pedrosa RG, De Castro IA, De Oliveira Pires IS. Effect of alanyl-glutamine supplementation on plasma and tissue glutamine concentrations in rats submitted to exhaustive exercise. *Nutrition* (2006) **22**(5): 564–71. doi:10.1016/j.nut.2005.11.002

13. Leite JSM, Cruzat VF, Krause M, Homem De Bittencourt PI. Physiological regulation of the heat shock response by glutamine: implications for chronic low-grade inflammatory diseases in age-related conditions. *Nutrire* (2016) **41**:17. doi:10.1186/s41110-016-0021-y

14. Tapiero H, Mathé G, Couvreur P, Tew KD. II. Glutamine and glutamate. *Biomed Pharmacother* (2002) **56**(9):446–57. doi:10.1016/s0753-3322(02)00285-8

15. Cruzat V, Macedo Rogero M, Noel Keane K, Curi R, Newsholme P. Glutamine: metabolism and immune function, supplementation and clinical translation. *Nutrients* (2018) **10**(11):1564. doi:10.3390/nu10111564

16. Powell-Tuck J. Total parenteral nutrition with glutamine dipeptide shortened hospital stays and improved immune status and nitrogen economy after major abdominal surgery commentary by J powell-tuck. *Gut* (1999) **44**(2):155. doi:10.1136/gut.44.2.155

17. Ma X, Cai D, Zhu Y, Zhao Y, Shang X, Wang C, et al. L-Glutamine alleviates osteoarthritis by regulating lncRNA- NKILA expression through the TGF-β1/SMAD2/3 signalling pathway. *Clin Sci (Lond)* (2022) **136**(13):1053–69. doi:10.1042/CS20220082

18. Vigeland CL, Beggs HS, Collins SL, Chan-Li Y, Powell JD, Doerschuk CM, et al. Inhibition of glutamine metabolism accelerates resolution of acute lung injury. *Physiol Rep* (2019) **7**(5):e14019. doi:10.14814/phy2.14019

19. Kim B, Li J, Jang C, Arany Z. Glutamine fuels proliferation but not migration of endothelial cells. *The EMBO J* (2017) **36**(16):2321–33. doi:10.15252/embj.201796436

20. Huang H, Vandekeere S, Kalucka J, Bierhansl L, Zecchin A, Brüning U, et al. Role of glutamine and interlinked asparagine metabolism in vessel formation. *EMBO J* (2017) **36**(16):2334–52. doi:10.15252/embj.201695518

21. Cai Y, Tian B, Deng Y, Liu L, Zhang C, Peng W, et al. Glutamine metabolism promotes renal fibrosis through regulation of mitochondrial energy generation and mitochondrial fission. *Int J Biol Sci* (2024) **20**(3):987–1003. doi:10.7150/ijbs.89960

22. Ocaña MC, Martínez-Poveda B, Quesada AR, Medina MÁ. Highly glycolytic immortalized human dermal microvascular endothelial cells are able to grow in glucose-starved conditions. *Biomolecules* (2019) **9**(8):332. doi:10.3390/biom9080332

23. Pacheco RG, Esposito CC, Müller LC, Castelo-Branco MT, Quintella LP, Chagas VL, et al. Use of butyrate or glutamine in enema solution reduces inflammation and fibrosis in experimental diversion colitis. *World J Gastroenterol* (2012) **18**(32):4278–87. doi:10.3748/wjg.v18.i32.4278

24. Goswami S, Kandhare A, Zanwar AA, Hegde MV, Bodhankar SL, Shinde S, et al. Oral L-glutamine administration attenuated cutaneous wound healing in wistar rats. *Int Wound J* (2016) **13**(1):116–24. Epub 2014. doi:10.1111/iwj.12246

25. Du K, Hyun J, Premont RT, Choi SS, Michelotti GA, Swiderska-Syn M, et al. Hedgehog-YAP signaling pathway regulates glutaminolysis to control activation of hepatic stellate cells. *Gastroenterology* (2018) **154**(5):1465–79.e13. doi:10.1053/j.gastro.2017.12.022

26. Mendes JB, Campos PP, Ferreira MAND, Bakhle YS, Andrade SP. Host response to sponge implants differs between subcutaneous and intraperitoneal sites in mice. *J Biomed Mater Res B Appl Biomater* (2007) **83**(2):408–15. doi:10.1002/jbm.b.30810

27. Mendes JB, Campos PP, Rocha MA, Andrade SP. Cilostazol and pentoxifylline decrease angiogenesis, inflammation, and fibrosis in sponge-induced intraperitoneal adhesion in mice. *Life Sci* (2009) **84**(15-16):537–43. doi:10.1016/j.lfs.2009.01.023

28. Marques SM, Castro PR, Campos PP, Viana CTR, Parreiras PM, Ferreira MAN, et al. Genetic strain differences in the development of peritoneal fibroproliferative processes in mice. *Wound Repair Regen* (2014) **22**(3):381–9. doi:10.1111/wrr.12177

29. De Lazari MGT, Viana CTR, Pereira LX, Orellano LAA, Ulrich H, Andrade SP, et al. Sodium butyrate attenuates peritoneal fibroproliferative process in mice. *Exp Physiol* (2023) **108**(1):146–57. doi:10.1113/EP090559

30. Longley DB, Harkin DP, Johnston PG. 5-fluorouracil: mechanisms of action and clinical strategies. *Nat Rev Cancer* (2003) **3**:330–8. doi:10.1038/nrc1074

31. Sonis ST. The pathobiology of mucositis. *Nat Rev Cancer* (2004) **4**(4):277–84. doi:10.1038/nrc1318

32. Deptuła M, Zieliński J, Wardowska A, Pikuła M. Wound healing complications in oncological patients: perspectives for cellular therapy. *Postepy Dermatol Alergol* (2019) **36**(2):139–46. doi:10.5114/ada.2018.72585

33. Sonis ST, Tracey C, Shklar G, Jenson J, Florine D. An animal model for mucositis induced by cancer chemotherapy. *Oral Surg Oral Med Oral Pathol* (1990) **69**(4):437–43. doi:10.1016/0030-4220(90)90376-4

34. Orellano LAA, Almeida SA, Campos PP, Andrade SP. Angiopreventive versus angiopromoting effects of allopurinol in the murine sponge model. *Microvasc Res* (2015) **101**:118–26. doi:10.1016/j.mvr.2015.07.003

35. Pereira LX, Viana CTR, Orellano LAA, Almeida SA, Vasconcelos AC, Goes ADM, et al. Synthetic matrix of polyether-polyurethane as a biological platform for pancreatic regeneration. *Life Sci* (2017) **176**:67–74. doi:10.1016/j.lfs.2017.03.015

36. Viana CTR, Orellano LAA, Pereira LX, De Almeida SA, Couto LC, De Lazari MGT, et al. Cytokine production is differentially modulated in malignant and non-malignant tissues in ST2-Receptor deficient mice. *Inflammation* (2018) **41**(6): 2041–51. doi:10.1007/s10753-018-0847-y

37. Griffiths RD. The evidence for glutamine uses in the critically-ill. *Proc Nutr Soc* (2001) **60**(3):403–10. doi:10.1079/pns200197

38. Stehle P, Ellger B, Kojic D, Feuersenger A, Schneid C, Stover J, et al. Glutamine dipeptide-supplemented parenteral nutrition improves the clinical outcomes of critically ill patients: a systematic evaluation of randomised controlled trials. *Clin Nutr ESPEN* (2017) **17**:75–85. doi:10.1016/j.clnesp.2016.09.007

39. Bozzetti F, Biganzoli L, Gavazzi C, Cappuzzo F, Carnaghi C, Buzzoni R, et al. Glutamine supplementation in cancer patients receiving chemotherapy: a double-blind randomized study. *Nutrition* (1997) **13**(7-8):748–51. doi:10.1016/s0899-9007(97)83038-9

40. McClave SA, Taylor BE, Martindale RG, Warren MM, Johnson DR, Braunschweig C, et al. Guidelines for the provision and assessment of nutrition support therapy in the adult critically ill patient: society of critical care medicine (SCCM) and American society for parenteral and enteral nutrition (A.S.P.E.N.). *JPEN J Parenter Enteral Nutr* (2016) **40**(2):159–211. doi:10.1177/0148607115621863

41. Braha A, Albai A, Timar B, Negru Ş, Sorin S, Roman D, et al. Nutritional interventions to improve cachexia outcomes in Cancer-A systematic review. *Medicina (Kaunas)* (2022) **58**(7):966. doi:10.3390/medicina58070966

42. Wells SM, Kew S, Yaqoob P, Wallace FA, Calder PC. Dietary glutamine enhances cytokine production by murine macrophages. *Nutrition* (1999) **15**(11-12): 881–4. doi:10.1016/s0899-9007(99)00184-7

43. Furukawa S, Saito H, Inoue T, Matsuda T, Fukatsu K, Han I, et al. Supplemental glutamine augments phagocytosis and reactive oxygen

intermediate production by neutrophils and monocytes from postoperative patients *in vitro*. *Nutrition* (2000) **16**(5):323–9. doi:10.1016/s0899-9007(00)00228-8

44. Pithon-Curi TC, Schumacher RI, Freitas JJS, Lagranha C, Newsholme P, Palanch AC, et al. Glutamine delays spontaneous apoptosis in neutrophils. *Am J Physiol Cell Physiol* (2003) **284**(6):C1355–61. doi:10.1152/ajpcell.00224.2002

45. Carr EL, Kelman A, Wu GS, Gopaul R, Senkevitch E, Aghvanyan A, et al. Glutamine uptake and metabolism are coordinately regulated by ERK/MAPK during T lymphocyte activation. *J Immunol* (2010) **185**(2):1037–44. doi:10.4049/jimmunol.0903586

46. Nakaya M, Xiao Y, Zhou X, Chang JH, Chang M, Cheng X, et al. Inflammatory T cell responses rely on amino acid transporter ASCT2 facilitation of glutamine uptake and mTORC1 kinase activation. *Immunity* (2014) **40**(5):692–705. doi:10.1016/j.immuni.2014.04.007

47. Hu X, Ma Z, Xu B, Li S, Yao Z, Liang B, et al. Glutamine metabolic microenvironment drives M2 macrophage polarization to mediate trastuzumab resistance in HER2-positive gastric cancer. *Cancer Commun (Lond)* (2023) **43**(8):909–37. doi:10.1002/cac2.12459

48. Kim J-M, Na Im Y, Chung Y-J, Youm J-h, Young Im S, Han MK, et al. Glutamine deficiency shifts the asthmatic state toward neutrophilic airway. *Inflammation Allergy* (2021) **77**(4):1180–91. doi:10.1111/all.15121

49. Jeong SY, Im Y, Youm J, Lee HK, Im SY. l-Glutamine attenuates DSS-induced colitis *via* induction of MAPK Phosphatase-1. *Nutrients* (2018) **10**(3):288. doi:10.3390/nu10030288

50. Chiu YW, Lee CH, Lo HC. Oral post-treatment supplementation with a combination of glutamine, citrulline, and antioxidant vitamins additively mitigates jejunal damage, oxidative stress, and inflammation in rats with intestinal ischemia and reperfusion. *PLoS One* (2024) **19**(2):e0298334. doi:10.1371/journal.pone.0298334

51. Saito H, Furukawa S, Matsudaby T. Glutamine as an immunoenhancing nutrient JPEN. *J Parenter Enteral Nutr* (1999) **23**(5 Suppl. l):S59–61. doi:10.1177/014860719902300515

52. Lattouf R, Younes R, Lutomski D, Naaman N, Godeau G, Senni K, et al. Picrosirius red staining: a useful tool to appraise collagen networks in normal and pathological tissues. *J Histochem Cytochem* (2014) **62**(10):751–8. doi:10.1369/0022155414545787

53. Hamanaka RB, O'Leary EM, Witt LJ, Tian Y, Gökalp GA, Meliton AY, et al. Glutamine metabolism is required for collagen protein synthesis in lung fibroblasts. *Am J Respir Cell Mol Biol* (2019) **61**(5):597–606. doi:10.1165/rcmb.2019-0008OC

54. Wang B, Wu G, Zhou Z, Dai Z, Sun Y, Ji Y, et al. Glutamine and intestinal barrier function. *Amino Acids* (2015) **47**(10):2143–54. doi:10.1007/s00726-014-1773-4

55. Han T, Guo M, Zhang T, Gan M, Xie C, Wang JB. A novel glutaminase inhibitor-968 inhibits the migration and proliferation of non-small cell lung cancer cells by targeting EGFR/ERK signaling pathway. *Oncotarget* (2017) **8**(17):28063–73. doi:10.18632/oncotarget.14188

56. Klimberg VS, Souba WW, Dolson DJ, Salloum RM, Hautamaki RD, Plumley DA, et al. Prophylactic glutamine protects the intestinal mucosa from radiation injury. *Cancer* (1990) **66**(1):62–8. doi:10.1002/1097-0142(19900701)66:1<62::aid-cncr2820660113>3.0.co;2-e

EBM Experimental Biology and Medicine

EBM is the official journal of the Society for Experimental Biology and Medicine

Experimental Biology and Medicine (EBM) is a global, peer-reviewed journal dedicated to the publication of multidisciplinary and interdisciplinary research in the biomedical sciences.

Discover more of our Special Issues

See more →

Contact

development@ebm-journal.org

See more

ebm-journal.org

publishingpartnerships.frontiersin.org/our-partners